ROTOR-ROTOR INTERACTIONS IN THE DESIGN OF UNMANNED AERIAL SYSTEMS

A Dissertation
Presented to
The Academic Faculty

By

Jeremy Epps

In Partial Fulfillment
of the Requirements for the Degree
Doctor of Philosophy in the
School of Aerospace Engineering
Decision and Control Laboratory

Georgia Institute of Technology

August 2022

ROTOR-ROTOR INTERACTIONS IN THE DESIGN OF UNMANNED AERIAL SYSTEMS

Thesis committee:

Dr. Eric Feron
Electrical and Computer Engineering
King Abduallah University of Science and Technology

Dr. Eric Johnson
School of Aerospace Engineering
Pennsylvania State University

Dr. Marilyn Smith
School of Aerospace Engineering
Georgia Institute of Technology

Dr. Javier Irizarry
School of Building Constructions
Georgia Institute of Technology

Dr. Jonathan Rogers
School of Aerospace Engineering
Georgia Institute of Technology

Date approved: June 15, 2022

ACKNOWLEDGMENTS

I want to express my gratitude to my thesis committee members, Dr. Eric Feron, Dr. Eric Johnson, Dr. Marilyn Smith, Dr. Jonathan Rogers, and Dr. Javier Irizarry, for their guidance and wisdom throughout the preparation of this work. I would also like to thank the members of the Unmanned Aerial Vehicle Research Facility, namely Dmitry Bershadsky, Steven Haviland, and Lee Whitcher. This work would not have been possible without the effort of my colleagues Kevin Garanger, Thanakorn Khamvilai, Bilal Maassarani, and Obadah Wali.

I want to thank the sponsors who have supported me and funded the work presented in this thesis: The National Science Foundation, The National GEM Consortium, King Abdullah University of Science and Technology, and optimAero.

To all of my friends that I have met at Georgia Tech, thank you for the ongoing support throughout this process. I want to thank my friends from North Carolina AT SU and my fraternity brothers for their support and encouragement. To Dr. Kiper, whom I'm blessed to have in my life, thank you for your unwavering support. To my family, especially my mother, father, and brother, thank you for the endless emotional support throughout these years. Lastly, but certainly not least, I must thank God for not only answering my prayers but keeping me motivated even when I complained about the very thing I had prayed for.

TABLE OF CONTENTS

LIST OF TABLES

LIST OF FIGURES

SUMMARY

This dissertation investigates the impact of rotor-rotor interactions on small Unmanned Aerial System (UAS) design. This work aims to investigate the aerodynamic effects of two rotor configurations, the first being non-coplanar overlapping rotors, tandem-rotors, and the second being the semi-coaxial rotor configuration, which is an adaptation of the traditional coaxial rotor configuration. This work is motivated by three UAS, two of which, the Tetracopter and the Dodecacopter, are designed and developed as a part of the work presented in this dissertation. The Tetracopter and Dodecacopter are multi-agent vehicles that implement multiple layers of non-coplanar overlapping rotors. The goal of these two vehicles is to implement a design where a multi-agent UAS can have the structural rigidity to withstand carrying payloads, whether the payload is carried above or below the vehicle, while being as efficient as a multi-agent aircraft with coplanar rotors. The goal of the Y6sC is to show that the semi-coaxial rotor configuration allows a vehicle to be more efficient in hover than a traditional coaxial rotor configuration and that the semi-coaxial rotor configuration grants the vehicle more maneuverability than a traditional coaxial rotor configuration.

This dissertation can be separated into two halves; the first half begins with the presentation of a thrust stand fabricated to collect data on both rotor configurations. This half also discusses the methods used to conduct these thrust stand experiments, the methods used to analyze the data, and discussions about the results and their comparison to established theories that predict the performance of these rotor configurations. A rotor configuration performance estimation method that is based on the empirical data collected is also presented, and the accuracy of this estimation method is validated. This estimation method is then used to estimate the optimal design of the Tetracopter and Dodecacopter, which accounts for the vehicle's weight and the performance of the vehicle's rotors which may be impacted by rotor-rotor interactions.

The latter half of this dissertation discusses the design of the Dodecacopter along with the methods used to flight test the vehicle. The data produced from the flight tests are discussed, and estimations of the degradation in the performance of the vehicle due to the rotor-rotor interactions are presented and discussed. The dissertation concludes with a brief discussion on the design implications derived from the results of the work presented.

CHAPTER 1
INTRODUCTION AND BACKGROUND

1.1 Motivation

Over the past two decades, the technological advances in lithium-ion batteries and the miniaturization of inertial measurement units have led to the emergence of small multi-rotor aircraft. These smaller components have allowed for the creation of novel multi-rotor unmanned aerial systems (UAS) designs that have rotor configurations vastly different from traditional manned rotor-craft. Moreover, as the exploration of small multi-rotor UAS increases, more unique rotor configurations have been implemented to allow small UAS to maneuver in ways traditional quadcopters cannot [1, 2, 3] or to limit the size of the UAS [4]. Another advancement in the field of UAS is the introduction of modular or multi-agent UAS that can assemble into different airframes by attaching self-similar modules. Several researchers have explored the usefulness of multi-agent/modular systems by creating the Distributed Flight Array [5], Boeing's LIFT! project [6], and the ModQuad [7] as shown in Figs. 1.1 to 1.3.

Figure 1.1: ETH Zurich's Distributed Flight Array

Figure 1.2: Artist depiction of Boeing's LIFT! Project lifting an HVAC Unit.

Figure 1.3: The GRASP Lab's ModQuad assembled into two sub-modules

The work presented in this thesis focuses on UAS with oblique rotor configurations that enable UAS to perform unique maneuvers and multi-agent/modular UAS. More specifically, the goal of the work presented in this thesis is to understand the relationship between

the relative position of the rotors of these unique designs and the performance of those rotors due to the rotor-rotor interactions between them. This work is motivated by the creation of three unique UAS, the Tetracopter [8], the Y6sC [9] and the Tetrahedron Dodecacopter [10, 11], all depicted below in Fig. 1.4, respectively. These vehicles incorporate two rotor configurations, both of which can create rotor-rotor interactions. The first configuration, used by both the Tetracopter and the Tetrahedron Dodecacopter, is the tandem-rotor configuration, where the rotors are non-coplanar, yet the planes they operate in are parallel to one another, which forces the downstream rotor to operate in the slipstream or wake of the upstream rotor. Both the Tetracopter and the Tetrahedron Dodecacopter are designed to be modular UAS meaning that multiple Tetracopters or Tetrahedron Dodecacopters can be assembled to create larger multi-agent UAS as shown in Fig. 1.4d. The second-generation (Gen-2) of the Dodecacopter, which is an assembly of four first-generation Dodecacopters, has multiple layers of overlapping non-coplanar rotors. The effects of the overlap between these layers of rotors are investigated in this thesis by collecting flight test data of both the Gen-1 and Gen-2 Tetrahedron Dodecacopter. The second rotor configuration, which the Y6sC uses, is the semi-coaxial rotor configuration. This configuration is an adaptation to the traditional coaxial rotor system where two rotors are concentric [12]; however, the goal of this rotor system is to angle the rotors of a coaxial rotor system so that the downstream rotor is not engulfed in the wake of the upstream rotor as it is in a traditional coaxial rotor system.

(a) The Tetracopter

(b) The Y6sC

(c) Gen-1 Tetrahedron Dodecacopter

(d) Gen-2 Tetrahedron Dodecacopter

Figure 1.4: The different UAS designs that have motivated the work presented in this thesis.

1.2 Research Goals and Objectives

1.2.1 Research Goal

The goal of the presented work is to understand how the rotor-rotor interactions of a significantly spaced tandem-rotor configuration and the semi-coaxial rotor configuration impact the performance of a vehicle that uses these configurations and to understand the design implications of UAS that incorporate these rotor configurations. Once the relationship

between the performance of the rotors of these unique designs and the relative distance between them is known, this works aims to find the optimal configuration of the Tetrahedron Dodecacopter.

Tandem-rotor configurations for small UAS have been investigated in other works [13, 14, 15, 16]; however, the design space of the tandem rotor configurations studied in these works is not large enough for one to derive design implications of an UAS such as the Tetracopter or the Tetrahedron Dodecacopter. Empirical data of the performance of the semi-coaxial rotor configuration is scarce [17], which leads to the same issue of the inability of design implications to be derived from the existing data.

1.2.2 Research Objectives

The objectives of this work are as follows:

1. Design, fabricate, and fly a multi-agent/modular system that has the ability to be more structurally rigid than multi-agent UAS arrays.

2. Design and fabricate a thrust stand that allows for the performance data of tandem-rotor and semi-coaxial rotor configurations to be gathered.

3. Quantify the relationship between the vertical and horizontal separation of a tandem rotor system and the performance of the rotors in the system.

4. Develop a method that uses empirical data to optimize the design of the Tetracopter and the Tetrahedron Dodecacopter and find the optimal configuration of both vehicles.

5. Collect flight test data of the Tetrahedron Dodecacopter for the purpose of investigating if the performance impact of overlapping non-coplanar rotors is present during flight.

6. Compare the flight test data of the Tetrahedron Dodecacopter to the thrust stand data collected.

7. Perform a sensitivity analysis on the vertical separation and the angle of the rotors of a semi-coaxial rotor configuration.

1.3 Contributions

The contributions of this work is as follows:

1. The collection of data quantifying the relationship between the rotor position of a tandem rotor configuration and the performance of the rotors.

2. The development of a method that can be used to find the optimal configuration of the Tetracopter and the Tetrahedron Dodecacopter and estimate the performance of a tandem rotor configurations that experiences rotor-rotor interactions.

3. Flight test data that compares the efficiency of the Gen-1 Tetrahedron Dodecacopter to the Gen-2 Tetrahedron Dodecacopter for the purpose in investigating how the performance of the Tetrahedron Dodecacopter changes with its overall size.

4. Validating that the tetrahedron rotor configuration is a viable configuration for a UAS.

5. The collection of data quantifying the relationship between the rotor positions of a semi-coaxial rotor configuration and the performance of the rotors.

6. Discovery of a rotor configuration that is more efficient in hover than both the traditional coaxial rotor configuration and the previous semi-coaxial rotor configuration.

1.4 Thesis Summary

The remainder of this chapter covers the background and a detailed description of the Tetracopter, the Y6sC, and the Dodecacopter. The remainder of this thesis is as follows: Chap-

ter 2 covers the relevant analytical theory that can be applied to the tandem-rotor configurations, as well as a brief discussion of the theories used to describe parameters of a rotor's wake. Chapter 3 provides a discussion about previous works related to UAS with unique rotor configurations and past works that have investigated the performance of rotors that experience rotor-rotor interactions. Chapter 4 contains a description of the thrust stand used to gather the performance data on both the tandem-rotor configurations and the semi-coaxial rotor configurations. This chapter also discusses the precision of the thrust stand and the experimental methods used to gather the data of both rotor configurations. Chapter 5 begins with a discussion of the metrics used to quantify the performance changes due to rotor-rotor interactions of each rotor configuration, and then the results of each set of experiments are presented. This chapter ends with an in-depth discussion and validation of the estimation method used when calculating the optimum configuration of the Tetracopter and the Tetrahedron Dodecacopter. Chapter 6 discusses in detail the design of the Dodecacopter modules and both generations of the Tetrahedron Dodecacopter. This chapter then presents flight test data of both generations of the Tetrahedron Dodecacopter and compares this data to the thrust stand data collected. Lastly, Chapter 7 discusses UAS design implications derived from the results of the work presented in this thesis, along with a review of the contributions of the work presented in this thesis and how the work can be improved.

1.5 Background

The study of the rotor-rotor interactions discussed in this thesis is motivated by the design of the Tetracopter, Y6sC, and the Dodecacopter. The analysis of the performance data of the tandem-rotor and semi-coaxial rotor configurations will be discussed in the context of the design of these three multi-rotor UAS, which prompts a discussion of the goals and motivation of each UAS design.

1.5.1 The Tetracopter

The main goal of multi-agent/modular UAS is to combine the lifting force of all of its members to transport heavier payloads. The main benefit of a multi-agent UAS over a monolithic UAS is the ability of the multi-agent UAS to separate into smaller UAS that can navigate through tight spaces and then reassemble once the vehicles have reached their destination. Other advantages of multi-agent UAS include the ability to put in common the capabilities of its members, which could have, for example, different sensing capabilities. To date, the only multi-agent UAS created are designed as an array of singular rotorcrafts with co-planar rotors, as shown in Figs. 1.1 to 1.3, which becomes a disadvantage in the face of external forces that could cause structural deformations to the aggregate. These multi-agent arrays can experience high structural stresses caused by lifting heavy payloads, flying in turbulent air, or a loss in thrust generation of one or more of the systems' agents. The goal of the Tetracopter is to eliminate these issues with existing multi-agent/modular systems by incorporating an airframe that is inherently rigid in three dimensions while maintaining the efficiency of a multi-agent array. Vehicles that implement the Tetrahedron rotor configuration also have the added benefit of being able to carry payloads above their rotors as shown in Fig. 1.5. Loading a payload in this manner would obstruct the inflow of traditional UAS; however, a UAS implementing the Tetrahedron rotor configuration has the possiblity of having greater separation between the lower layer of rotors and the payload and can have numerous layers of rotors which would increase the separation between the payload and the lowest layer of rotors.

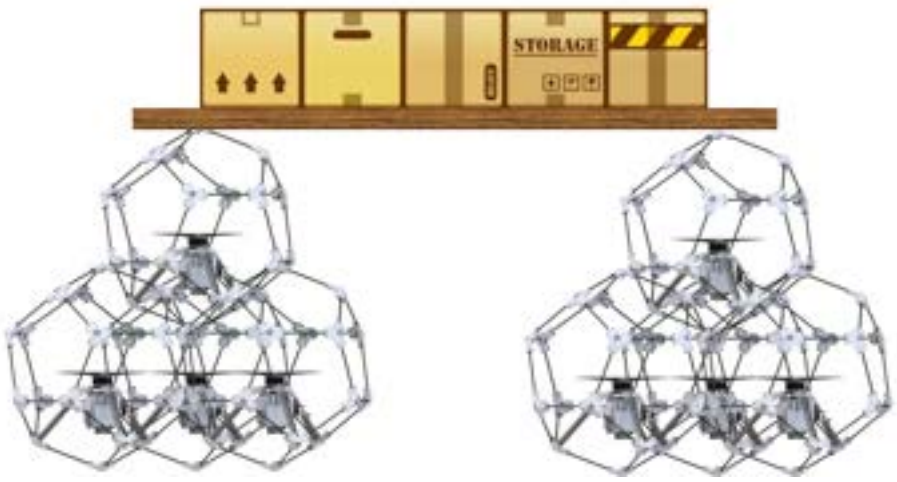

Figure 1.5: An example of the Dodecacopter carrying a payload above its rotors.

The Tetracopter, shown in Fig. 1.6, is designed to be an elementary module of a larger aircraft named the Fractal Tetrahedron Assembly (FTA) [18], which can be comprised of several elementary modules as shown in Fig. 1.7. The shape of the FTA is based on the Sierpinski tetrahedron [19], which is essentially an assembly of multiple regular tetrahedrons, which are inherently rigid. Each rotor of the Tetracopter is contained within one of these regular tetrahedrons. As previously mentioned, current multi-agent UAS are designed so that all of their rotors are co-planar, and as the array of vehicles increases, the severity of a structural, mechanical failure caused by one agent failing to carry its share of the payload increases. Designing the Tetracopter's airframe to mimic the Sierpinski tetrahedron mitigates the adverse structural effects of increasing its size and number of agents. The Tetracopter is made of four identical submodules, shown in Fig. 1.8, and a common payload, which includes the battery and avionics of the quad-rotorcraft. The submodules of the Tetracopter are not considered elementary modules because they cannot maintain a steady hover by themselves.

Figure 1.6: A model of the Tetracopter

Figure 1.7: The second generation of the Tetracopter

Figure 1.8: A submodule of the Tetracopter

The airframe of each submodule is constrained to a regular tetrahedron because of the shape's inherent strength and rigidity. It should be noted that the tetrahedron airframe has been used in past works as early as 1904 in Alexander Graham Bell's novel kite design [20, 21] depicted in Fig. 1.9. Bell stated that the fractal tetrahedron airframe was chosen because "the tetrahedral cell possesses rigidity or strength in three directions – that is to say, vertically, laterally, and longitudinally– so that internal bracing is entirely superfluous and is dispensed with.".

Figure 1.9: Bell fabricated several kites using the tetrahedral airframe; the kite depicted resembles the proposed UAS most closely.

Under the assumption that each submodule of the Tetracopter and the FTA are identical, the constraint on the airframe requires the rotor configuration of the Tetracopter to be in the shape of a regular tetrahedron, meaning that the center of each of the Tetracopter's rotors must be at the vertex of a regular tetrahedron, as shown in Fig. 1.10. These parameters overlaid on a tandem-rotor configuration are shown in Fig. 1.11. The constraint placed on the relative locations of the rotors of the Tetracopter and the FTA can be expressed as Eq. (1.1).

Figure 1.10: The rotor configuration parameters of the Tetracopter and the Tetrahedron Dodecacopter where the center of each rotor is coincident with a vertex of the regular tetrahedron.

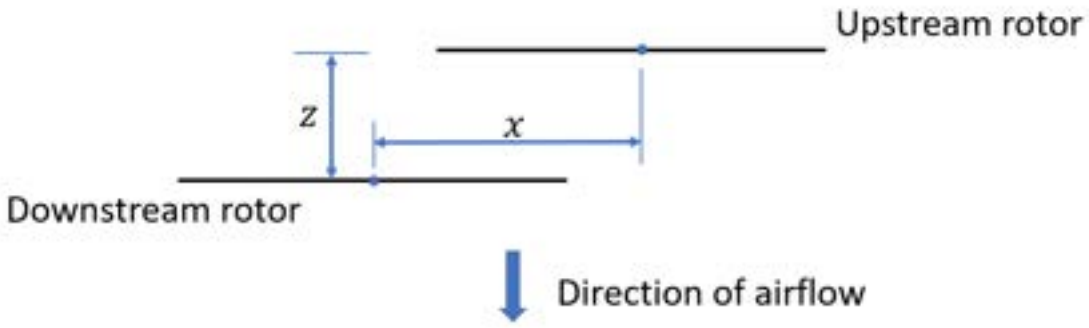

Figure 1.11: Parameters of a tandem rotor configuration

$$z = \sqrt{2}x \tag{1.1}$$

A top view showing the area of the rotors of the Gen-1 Tetracopter and the Gen-2 Tetracopter with and without overlapping rotors can be seen in Fig. 1.12. Depending on the separation of the rotors within the Gen-1 Tetracopter, there may be rotor overlap, which causes the Gen-2 Tetracopter to have four layers of overlapping rotors, as shown and labeled in Fig. 1.12c and Fig. 1.12d. It is well documented that a rotor operating in the slipstream or wake of another rotor will experience a degradation in performance [22]. For the Tetracopter to meet its goal of being as efficient as a traditional multi-rotor system that has an equivalent number of rotors, the magnitude of the performance degradation as a function of the vertical and horizontal separation between the downstream rotors and the upstream rotor must be understood. The trade-off between the increase in the airframe's weight and the increase in the separation of the rotors of the Tetracopter must also be understood so that an optimal configuration can be found. In essence, the question that must be answered is; "Is the Tetracopter more efficient if the weight and subsequently the size of the vehicle is reduced, which will drive the separation between the vehicle's rotors to be reduce causing overlap between the rotors and rotor-rotor interactions or are the rotor-rotor interactions between the rotors more degrading to the hover efficiency of the Tetracopter than the increase in vehicle weight needed to adequately separate the rotors of the vehicle to ensure there are no rotor-rotor interactions?"

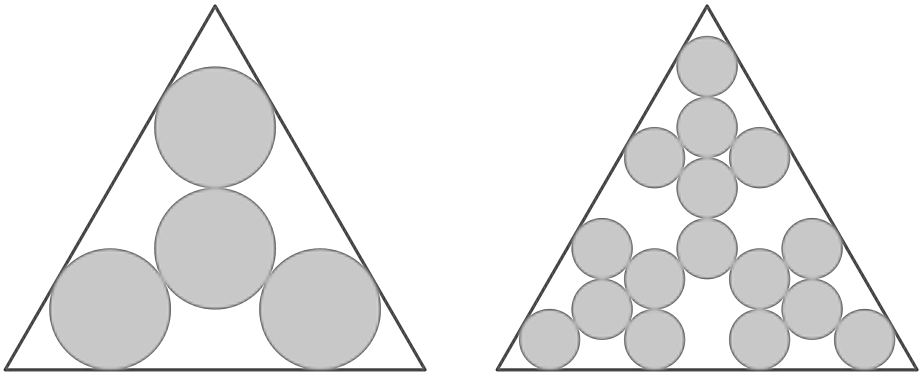

(a) Gen-1with no rotor overlap (b) Gen-2 with no rotor overlap

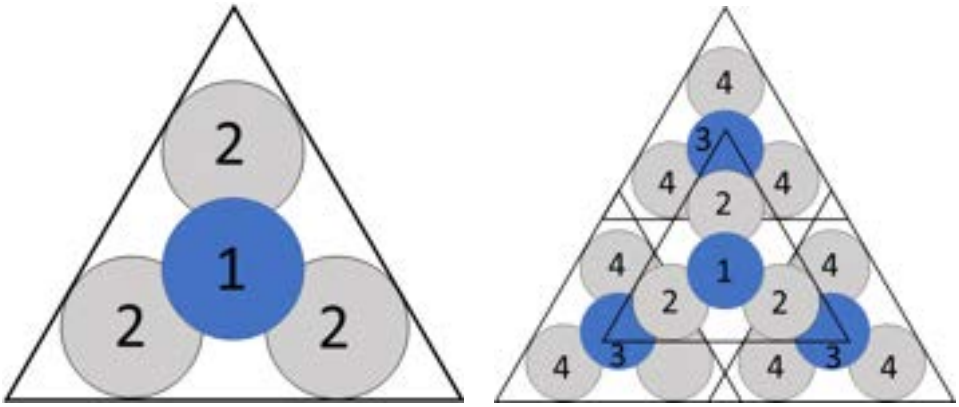

(c) Gen-1 with rotor overlap (d) Gen-2 with rotor overlap

Figure 1.12: The top view of the Gen-1 and Gen-2 Tetracotpers with and without rotor overlap. The planes that the rotors lay in are labeled in Figures (c) and (d), where the rotor on the upper most layer is labeled 1 and the rotors on lower layers are numbered accordingly.

1.5.2 The Y6sC

The *Y6sC* is an adaptation of the conventional Y6C, which uses three sets of coaxial rotors, as shown in Fig. 1.13a. Figure 1.13c shows the rotor configuration of the Y6sC, which has its downstream rotors mounted at the negative of the angle ζ, defined in Fig. 1.13d, of the upstream rotors. One advantage of the design is the gain of two degrees of freedom (DOF) for only a reorientation of the same propulsion system. Another advantage of the design is that the airflow from the upstream rotor is not perpendicular to the plane of the

downstream rotor, thus allowing the downstream rotor to avoid digesting the full slipstream of the upstream rotor. In theory, this should improve the efficiency of the rotor system in comparison to a coaxial rotor configuration. However, there are downfalls to the *Y6sC* design, the first being the weight of the motor mounts. Depending on the angle ζ of the motor mounts and the separation distance between the rotors, the weight of the motor mounts may offset the efficiency benefits created by angling the rotors. Another disadvantage is that there can be a significant decrease in the maximum thrust generation in the Z-axis (i.e., the force opposing gravity) that the rotor configurations can create due to the angle ζ of the rotors. Bershadsky et al. presented the first study of the *Y6sC*, which explores the unique maneuverability of the vehicle using Direct Force Control (DFC) and presents basic thrust stand results of the semi-coaxial rotor configuration [9]. However, the thrust stand used in that study had numerous limitations. Moreover, an alteration to Bershadsky's semi-coaxial design, which involves only changing the angle of the upstream rotor in comparison to a coaxial configuration, is introduced in this thesis. This alteration aims to alleviate the issue of the purely semi-coaxial rotor configuration (where $\zeta_U = \zeta_D$) in generating thrust in the Z-axis, hereinafter referred to as Z-Force. The work involving the semi-coaxial rotor configuration presented in this thesis aims to understand the relationship between the angles ζ_U and ζ_D of the semi-coaxial rotor configuration, the vertical separation of the rotors in the semi-coaxial configuration, and the efficiency of the configuration in producing Z-force.

(a) A multi-rotor using the Y6C configurtion

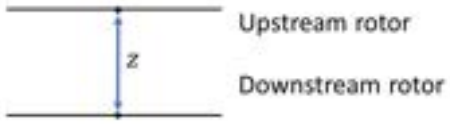

(b) Traditional coaxial configuration

(c) The *Y6sC*

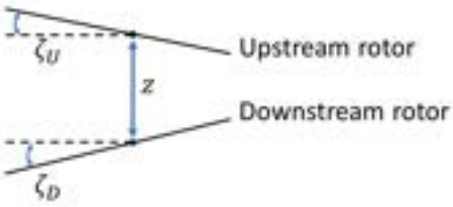

(d) The semi-coaxial rotor configuration

Figure 1.13: A UAS that uses the Y6C design (a) along with a diagram of the traditional coaxial rotor configuration (b). The *Y6sC* (c) along with an annotated diagram of the semi-coaxial configuration (d).

A second aerodynamic interaction may be indirectly created when implementing the semi-coaxial configuration onto a UAS. Depending on the vehicle that the semi-coaxial rotor configuration is placed on, there is a possibility that the slipstream and wake of the lower rotors of two pure semi-coaxial rotor configurations, which are illustrated in Fig. 1.14, interact with one another. Since there is a possibility that the wake of oblique rotors can change the performance of the rotors, thus affecting how the semi-coaxial rotor configuration should be implemented onto a vehicle, this rotor configuration is investigated. It should be noted that a similar rotor configuration is also used by vehicles that do not use the semi-coaxial rotor configuration but have rotor configurations where the planes of the rotors are oblique to one another, as shown in Fig. 1.15. This rotor configuration is usually placed on vehicles to increase maneuverability [23, 9, 24, 25]. In this thesis, the scope

of the work performed involving both the semi-coaxial rotor configuration and the oblique rotor configuration only includes the performance of the rotor configurations system and not the maneuverability enabled by the rotor configurations.

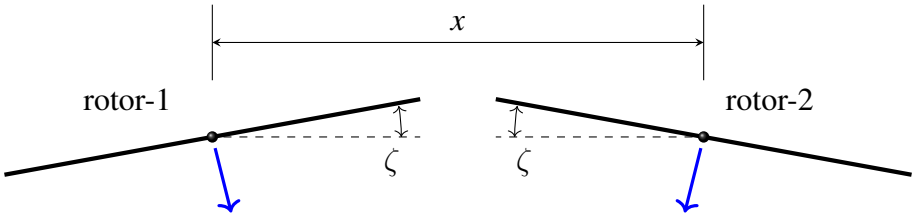

Figure 1.14: Oblique rotor configuration parameters.

Figure 1.15: A hexarotor UAS with oblique rotors

1.5.3 The Dodecacopter

The goal of the Tetrahedron Dodecacopter design is similar to that of the Tetracopter, and essentially the Tetrahedron Dodecacopter is an improvement of the Tetracopter. Unlike the Tetracopter, the Tetrahedron Dodecacopter is an assembly of single rotor modules that each have their own power source, power distribution board, electronic speed controller (ESC), and in most cases their own flight controller. A module of the Dodecacopter can be seen in Fig. 1.16.

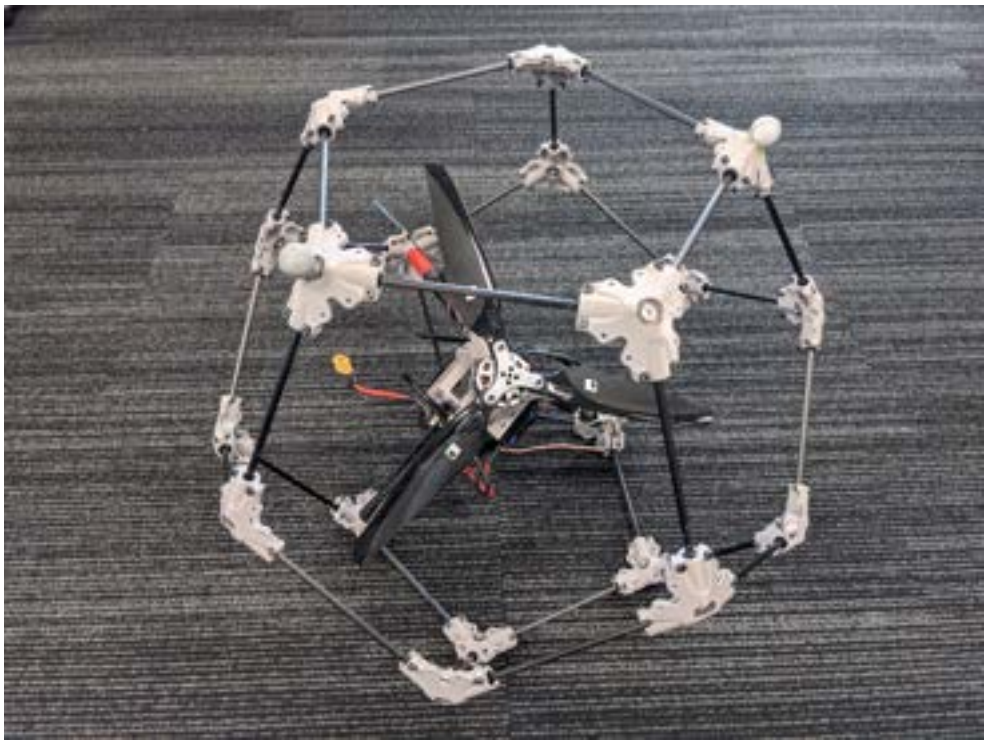

Figure 1.16: Dodecacopter Module

The airframe of each module is in the shape of a regular dodecahedron, which allows for the modules to be assembled into several configurations, such as a traditional quadrotor configuration where the rotors are coplanar, Fig. 1.17 and a hexarotor configuration as shown in Fig. 1.18. The dodecahedron airframe of each module allows for the assembly of configurations with non-coplanar rotor such as a hexarotor Dodecacopter, shown in Fig. 1.19, that allows for 6-DOF.

Figure 1.17: The quadrotor Dodecacopter

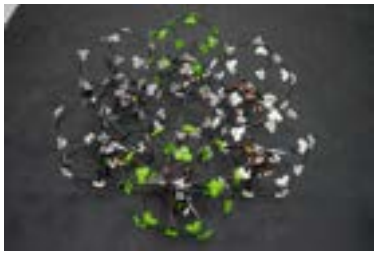

Figure 1.18: The hexarotor Dodecacopter

Figure 1.19: The 6-DOF hexarotor Dodecacopter

One can imagine the numerous other configurations that the dodecahedron modules

can be created. The work performed in this thesis focuses on the tetrahedron Dodecacopter and the second generation (Gen-2) Tetrahedron Dodecacopter as shown in Fig. 1.4c and Fig. 1.4d.

CHAPTER 2
RELEVANT THEORY

2.1 Summary

This chapter discusses the relevant theory that will be used to compare the empirical results presented in this thesis. This chapter covers the analytical theory that estimates the performance of isolated rotors and tandem-rotor systems and briefly discusses theories used to describe a rotor's wake. Section 2.2 provides a review of simple momentum theory applied to a single main rotor of a helicopter as well as a tandem-rotor system and introduces performance coefficients that will be used throughout this thesis. Section 2.3 provides a high-level discussion of the composition of a rotor's wake and methods used to predict certain aspects of the wake.

2.2 Rotor Performance

There are two well-known methods of predicting the performance of a helicopter rotor, Simple Momentum theory and Blade Element Theory (BET). These theories allow for relatively good predictions of the power consumption of a rotor at a given thrust value; however, depending on the assumptions made when applying these theories, the performance estimates can differ from empirical data. BET and Blade Element Momentum Theory (BEMT), a hybrid of both BET and simple momentum theory, are what most modern rotor performance prediction methods are based on; however, BET and BEMT are computational methods that require the blade to be discretized and the analysis to be completed for each segment of the rotor blade. The simple momentum theory is the most referenced analytical performance prediction method for tandem rotor systems. Because of this, the simple momentum theory of a single main rotor at hover and a tandem rotor system at hover will be

reviewed. An in-depth review of both theories can be found in [22].

2.2.1 Simple Momentum Theory

The simple momentum theory uses several assumptions, one of which is the assumption that the rotor can be thought of as an infinitesimally thin permeable actuator disk, thus allowing the existence of a pressure difference over the disk. The flow generated by the disk is assumed to be one-dimensional, incompressible, inviscid, and quasi-steady. Although these assumptions allow for the calculations within the theory to be tractable, several real-world effects are ignored; thus, the simple momentum theory is usually used as a first-order performance estimate or, in laymen's terms, a "sanity check". A thorough analysis of a rotor using the simple momentum theory can be found in [22]. A number of the conclusions from the simple momentum theory are used in defining the metrics used later in this thesis to analyze the empirical performance data collected as a result of thrust stand experiments, so a brief overview of the simple momentum theory must be given.

The simple theory is based on three conservation laws; the conservation of mass, momentum, and energy, each of which can be seen by using the theory to predict the power consumption of a rotor. Let the fluid surrounding a rotor, and its wake be thought of as a controlled volume, with a beginning, point 0, and an ending ∞, as labeled in Fig. 2.1. Let the area of the rotor be A and the thrust it produces at hover be T. Using the conservation of mass, the mass flow into the control volume must be equivalent to the mass flow rate exiting the control volume. Consider a circular cross-section of the rotor's wake at a distance z from the rotor. Let $r(z)$ be its radius and $v(z)$ the velocity of the air going through that cross-section, as shown in Fig. 2.1. Thus, the mass flow rate through the control volume is defined as $\dot{m} = \rho v(z)\pi r(z)^2$, where ρ is the air density, which is assumed to be constant. The conservation of momentum along with a constant value of ρ, implies that the quantity $\pi r(z)^2 v(z)$ is constant. By defining v_i as the incident velocity of the airflow through the rotor, v_∞ the final velocity of the airflow, and A_∞ the final area of the wake, Eq. (2.1) can

be generated.

$$Av_i = A_\infty v_\infty. \tag{2.1}$$

Using the conservation of fluid momentum, the produced thrust can be defined as the difference between the momentum of the fluid before the actuator disk and the momentum at the end of the wake. Since the velocity of the air at the beginning of the control volume is zero, the thrust generated can be written as Eq. (2.2).

$$T = \dot{m} v_\infty, \tag{2.2}$$

From the conservation of energy, the work done per unit time by the rotor, or in other words, the power, must be equal to the change in energy of the fluid per unit time, which can be seen in its final form as Eq. (2.3).

$$Tv_i = \frac{1}{2}\dot{m} v_\infty^2 \tag{2.3}$$

Using equations Eqs. (2.2) and (2.3), it can be seen that the velocity at the end of the control volume is twice the value of the incident velocity, as shown in Eq. (2.4). Expanding Eq. (2.2) using Eq. (2.4) and solving for the incident velocity, Eq. (2.5) can be formed. Using Eq. (2.5), the power required to hover can be defined as Eq. (2.6). Equation (2.6) is know as the *ideal power*. It should be noted that the *ideal power* does not account for viscous effects. The ideal power and how it is defined will be used in one of the metrics used to analyze the empirical data presented in this thesis.

$$v_\infty = 2v_i \tag{2.4}$$

$$v_i = \sqrt{\frac{T}{2\rho A}} \tag{2.5}$$

$$P = Tv_i = \frac{T^{3/2}}{\sqrt{2\rho A}}. \tag{2.6}$$

Along with estimating the performance of a rotor, the momentum theory also predicts the shape of a rotor's slipstream. Due to the increase in velocity of the air as it moves down the control volume, as shown in Eq. (2.4), a contraction of the wake, *vena contracta*, is observed as shown in Fig. 2.1. This can also be seen mathematically through the conservation of fluid mass in the control volume as derived in Eqs. (2.7) and (2.8). This contraction has an important role in this work. As one can imagine, in a tandem rotor configuration or a coaxial rotor configuration, operating a rotor inside of the slipstream of another rotor will change the performance of the former. This contraction also dictates how close, in both the vertical and horizontal directions, the downstream rotor of a tandem-rotor system can be to the upstream rotor without experiencing any performance impacts.

$$\rho A v_i = \rho A_\infty v_\infty = 2\rho A_\infty v_i \tag{2.7}$$

$$\frac{A}{2} = A_\infty \tag{2.8}$$

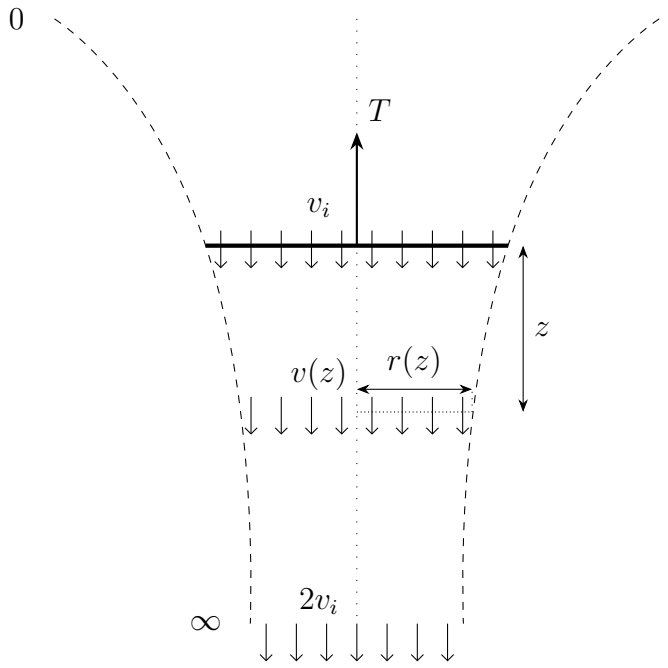

Figure 2.1: Illustration of the wake contraction under a single rotor.

2.2.2 Momentum Theory Applied to a Tandem Rotor System

Simple momentum theory can be applied to a tandem rotor system, and this derivation is detailed in [22]. However, there are several downfalls when using simple momentum theory to estimate power consumption. For this purpose, a brief discussion of how the simple momentum theory is applied to a tandem-rotor configuration is needed. There are two types of tandem rotor systems that the momentum theory can be extended to. *Case 1* consists of two non-concentric rotors virtually on the same plane with one another with some amount of overlap between them. *Case 2* involves a tandem rotor system where one rotor operates in almost the fully developed slipstream of the other rotor, meaning that there is a significant vertical separation between the two rotors, as shown in Fig. 2.2. The momentum theory quantifies the impact of the rotors being overlapped in both cases.

To begin, consider the top view of a tandem-rotor system as mentioned in Case 1, and let the system be broken into three areas, one for the area where the two rotors overlap and two for the area of each rotor that does not overlap with the other rotor. Let n be the ratio of

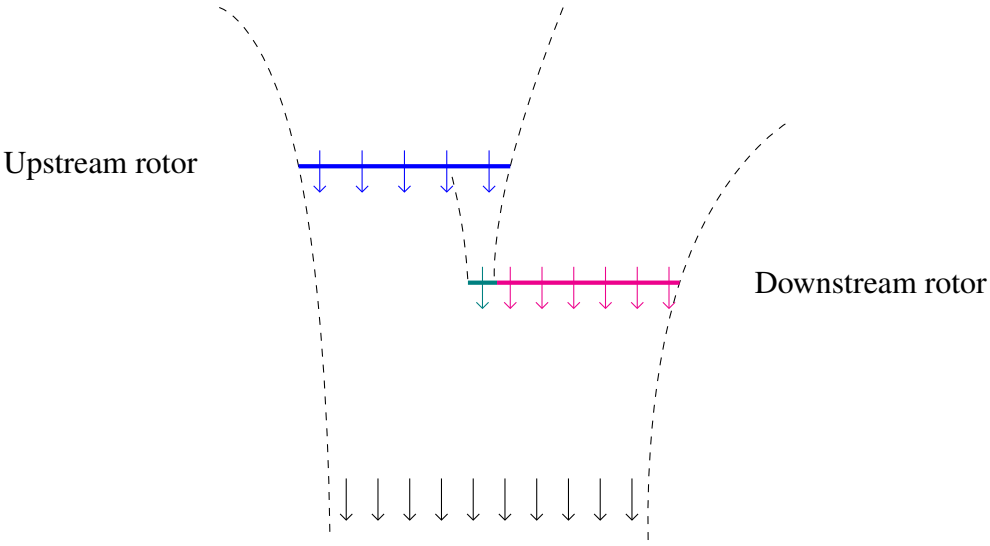

Figure 2.2: Illustration of the wake interaction between two overlapping rotors.

the overlapped area to the area of one of the rotors in the tandem-rotor assembly. Note that the overlap area used to define n does not include the overlapped area of both rotor discs, meaning the area is not counted twice due to there being two discs in the overlapped area. n can be found through a basic geometric calculation that is left to the reader. Using the ideal power found in Eq. (2.6), the power consumption of each of the two non-overlapping sections can be defined as Eq. (2.9), where the subscript i is an index for rotor 1 and rotor 2 of the tandem-rotor configuration. The ideal power of the overlapped area can be defined as Equation 2.10.

$$P_i = \frac{(1-n)T_i^{3/2}}{\sqrt{2\rho A}} \tag{2.9}$$

$$P_{ov} = \frac{n(T_1+T_2)^{3/2}}{\sqrt{2\rho A}} \tag{2.10}$$

To relate the induced power of a tandem rotor configuration to the induced power of two independent rotors, an induced power overlap interference factor is defined, as shown in Eq. (2.11). Suppose an assumption is made that both rotors are producing the same amount of thrust (i.e., $T_1 = T_2$), then the overlap interference factor can be expressed as Eq. (2.11),

which can be simplified to Eq. (2.12).

$$\kappa_{ov} = \frac{P_1 + P_2 + P_{ov}}{2P} \tag{2.11}$$

$$\kappa_{ov} = 1 + 0.4142n \tag{2.12}$$

The change in κ_{ov} as a function of the horizontal separation ratio $\frac{x}{D}$, where x is the horizontal distance between the centers of the two rotors and D is the diameter of one rotor, can be seen in Fig. 2.3. *Case 2* involves calculating n so that it accounts for the amount of overlap between the fully developed slipstream of the upstream rotor and the disc area of the downstream rotor. As a reminder, the area of the fully developed wake of the upstream rotor can be found using momentum theory as shown in Eq. (2.8). Momentum theory is applied to Case 2 as it is with a single main rotor. The full analysis can be viewed in [22]. The value of n can be calculated through the known geometric calculation of the overlapped area between two circles if different circumferences. As shown in Fig. 2.3, the momentum theory predicts κ_{ov} of Case 2 will always be lower than that of *Case 1* because the lower rotor of Case 2 will never be completely engulfed by the slipstream of the upstream rotor due to the size of the fully developed slipstream being half the area of either rotor disc.

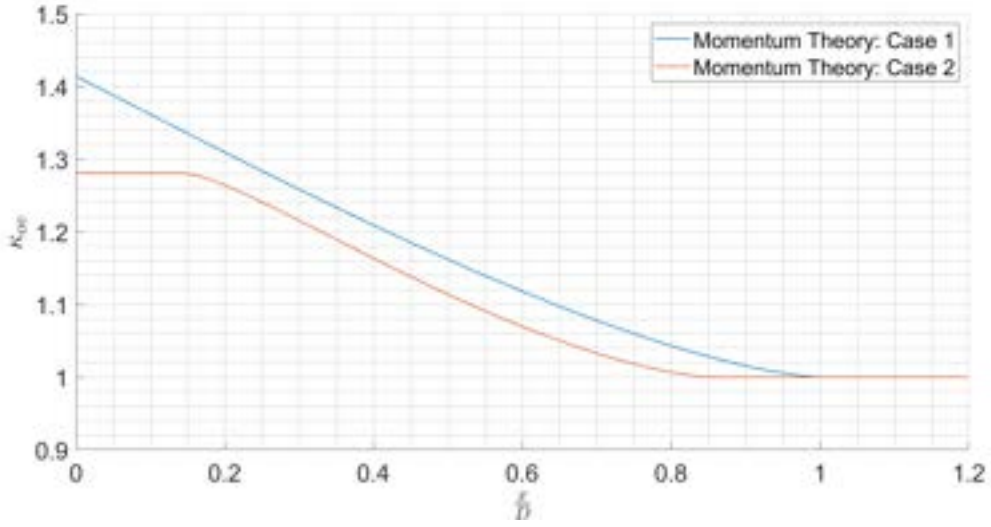

Figure 2.3: The induced power overlap interference factor versus the horizontal separation ratio of a tandem rotor system for both *Case 1* and *Case 2*

There are a few scenarios that momentum theory does not accurately capture, and empirical data from past works involving sub-scale models of helicopter rotors show that there is variability in the results compared to the momentum theory depending on the amount of vertical separation between the rotors. The majority of empirical data that has been compared to this momentum theory analysis are for rotors that operate at high Re, which is why the goal of this thesis is to collect empirical data on a rotor that operates at a relatively low Re, which are commonly used on small UAS. Throughout this thesis, the empirical data presented will be compared to the momentum theory analysis.

2.2.3 Nondimensionalization

Nondimensional coefficients are used throughout this thesis to analyze the performance of the rotor configurations discussed. The thrust generated by a rotor, its power consumption, and its torque generation can all be defined in nondimensional terms by dividing the value of interest by the area of the rotor disk (A), the density of the air (ρ), the radius of the rotor disc (R), and the rotational frequency of the rotor (Ω), as shown in Eq. (2.13), Eq. (2.14), and Eq. (2.15). For articulate rotors, these coefficients can change with a combination of a

change in the rotor blade's pitch and the rotor's angular velocity. However, in theory, for fixed-pitch rotors, which are the type of rotors used in the work presented in this thesis, these coefficients will remain relatively constant if the rotors operate in an isolated manner, meaning no external flows interact with the rotor. Since this thesis involves the aerodynamic interaction between rotors, these coefficients have an important role in quantifying the effects of the relative position between the rotors and their performance.

$$C_T = \frac{T}{\rho A(\Omega R)^2} \tag{2.13}$$

$$C_P = \frac{P}{\rho A(\Omega R)^3} \tag{2.14}$$

$$C_Q = \frac{Q}{\rho AR(\Omega R)^2} \tag{2.15}$$

2.3 Wake Structure

Although the work presented in this thesis focuses on the performance of specific rotor configurations and does not include flow visualization and the prediction of wake dynamics of rotors experiencing rotor-rotor interactions, the two are heavily dependent on one another. A brief, high-level discussion about the dynamics of a rotor's wake is needed to have an informed discussion about the related works and the results presented in this thesis.

From past flow visualization studies on helicopter rotors [26, 22], it is known that a rotor's wake is made of two main flow features, blade tip vortex cores, and vortex sheets. The tip vortex cores are caused by centrifugal forces, which are generated where local velocities are high. These vortex cores will move outward, away from the center of the rotor, until they reach a radial equilibrium caused by centrifugal force becoming equal with the pressure forces. The vortex sheet is formed from the boundary layers of the upper and lower surface of the rotor blade merging. There are several wake models ranging from

prescribed wake models [27, 28], rigid wake models, to free-vortex wake models [29, 30, 31], that are used to predict certain parameters of rotor wakes ranging from the inflow velocity of the rotor to vortex strengths and wake geometry. There have also been several studies that have collected empirical data on the dynamics of the vortex cores and vortex sheets created by a single main rotor [32, 33]. Another notable characteristic of rotor wakes that impact the research presented in this thesis is the aperiodicity of a rotor's wake as well as vortex disturbances and wake instabilities. Past works have shown that aperiodicity, vortex disturbances, and wake instabilities are related to the operating condition of the rotor, the number of blades on the rotor, the rotor's disk loading, and the geometry of the rotor blades [34, 35, 36]. These findings influence the experimental methods used in the work presented in this thesis. An overview of these methods can be found in [22].

2.4 Conclusion

The theories discussed in this chapter will be used throughout this thesis to describe the results of the experiments conducted and will allow the reader to understand conclusions derived from these results. The momentum theory prediction of the performance of tandem rotor systems is limited to two cases, one where the two rotors operate in the same plane and another where the downstream rotor operates in the fully developed slipstream of the upstream rotor. However, the possible rotor configurations of the Tetracopter and Tetrahedron Dodecacopter may place the rotors at varying distances from the upstream rotor, which include slightly before the fully developed slipstream, in the almost fully developed slipstream, and well after the fully developed slipstream of the upstream rotor. These limitations of using the momentum theory prompt the collection of empirical data on the tandem-rotor configurations that can be used on the Tetracopter and the Tetrahedron Dodecacopter. It should be noted that the momentum theory also uses several simplifying assumptions that ignore several non-ideal physical effects that a rotor experiences while generating thrust. There is no known application of an analytical rotor performance pre-

diction method such as the momentum theory on oblique rotors, such as the semi-coaxial rotor configuration. However, the contraction of a rotor's slipstream and knowledge of the components of a rotor's wake is still helpful in understanding the performance impact of rotor configurations such as the semi-coaxial configuration.

CHAPTER 3
RELEVANT LITERATURE

3.1 Summary

This chapter covers the relevant work involving multi-rotor systems, empirical and computational aerodynamic studies of rotors that operate a low rotor tip Reynolds numbers (*Re*) commonly used on commercial off the shelf (COTS) UAS, and preliminary studies performed by the author regarding the Tetracopter. Section 3.2 presents a discussion about novel rotorcraft with oblique rotor configurations as well as larger manned rotorcraft that experience rotor-rotor interactions. Relevant aerodynamic studies and their findings are discussed in Section 3.3 along with a preliminary study of the rotor configuration of the Tetracopter conducted by the author.

3.2 Novel Multi-rotors

The previously mentioned small UAS that are the focus of this thesis falls into two categories; multi-agent/modular UAS and UAS with oblique rotor configurations. These categories of UAS have rotor configurations that can involve rotor-rotor interactions, yet studies of how these interactions impact these vehicles' hover efficiency are scarce. The goal of these vehicles usually involves enabling the vehicle to maneuver in a unique manner, or the vehicles are a hardware platform for a unique method of network control. These vehicles are rarely if ever, commercialized, so their development ends after the goal of the vehicle design is achieved, which is usually completed without optimizing the vehicle for hover efficiency. The following subsections discuss several novel vehicles that are part of the two previously mentioned vehicle categories.

3.2.1 Aircraft with Oblique Rotors

Several small UAS designs incorporate oblique rotor configurations to increase their degrees of freedom (DoF). [37, 25, 38, 39, 40, 41, 42, 43, 44, 45]. Although these vehicles have the advantage of higher DoF, which can be used to withstand strong disturbances such as wind without a change in attitude, they're trading efficiency in producing vertical thrust for higher DoF. Not only are these vehicles reducing their hover efficiency by placing angles on their rotors, but they may also be reducing their efficiency by operating some of their rotors in the slipstream or wake of another. Bershadsky, created a rotor configuration that both gave the vehicle, the Y6sC [9], more DoF than a traditional drone and improved its efficiency compared to its predecessor, the Y6, which is equipped with three pairs of coaxial rotors. One set of experiments presented in this thesis investigates the efficiency of the rotor configuration used on the Y6sC, the semi-coaxial rotor configuration. This thesis also investigates the efficiency and feasibility of a new rotor configuration, the semi-coaxial-B configuration [46]. To the author's knowledge, the Y6sC is the only UAS that has flown using the semi-coaxial rotor configuration, so little information on the efficiency of the configuration is available. There is also no known information on the efficiency of the semi-coaxial-B configuration or any similar rotor configuration.

3.2.2 Multi-agent/Modular Multi-rotors

Empirical studies of the efficiency of multi-agent or modular UAS are seldomly performed. The main reason for this scarcity is that current multi-agent or modular UAS are arranged so that their rotors lie on the same plane, meaning that there are most likely no aerodynamic interactions. Another barrier to collecting empirical data on these vehicles is the time and amount of resources needed to design, build and fly these UAS. To date, not including the Tetracopter or Dodecacopter, there are only three other UAS that can be classified as either multi-agent UAS or modular UAS. These three include the ModQuad [7], the Distributed Flight Array (DFA) [5] and the Boeing LIFT! project [6].

Each of these designs has its unique purpose and functionality. The ModQuad is the only multi-agent vehicle that has been assembled while in flight and has been used as a flying manipulator to pick up items such as a coffee cup [47]. The DFA, has the capability of autonomously assembling several single rotor modules into several different shapes while on the ground and then taking off and maintaining a steady hover. The main purpose of the DFA is to be a testbed for distributed estimation and control algorithms. Lastly, the Boeing LIFT! project investigated the feasibility of using a modular UAS to lift heavy payloads such as HVAC systems and the ability to scale the cargo capacity of the aggregate by adding more modules. Although these vehicles are novel in their own manner, they all possess co-planar rotors. As previously mentioned, the goal of the Tetracopter and the Dodecacopter is to be a multi-agent/modular UAS that has the rigidity to maintain its structural integrity in the face of one or more modules failing. With the use of multiple vehicles, the design of the Tetracopter and the Dodecacopter also allows for the possibility of payloads being placed on top of the vehicles because the rotor configuration allows the inflow of the majority of the rotors not to be obstructed by the payload. However, as previously mentioned, the goal of both vehicles is to have these previously mentioned abilities while maintaining the efficiency of a traditional UAS with co-planar rotors.

3.3 Aerodynamic Studies

3.3.1 Computational Studies

Several studies have attempted to use a variety of computational fluid dynamic (CFD) methods to predict how the rotor-rotor interactions between tandem rotor configurations impact the performance of the rotors [48, 49, 50]. However, the interactions between a tandem-rotor configuration are extremely difficult to model, and the accuracy of the methods can vary depending on the parameters of the tandem-rotor configuration that is being studied. In [48], a free-vortex filament method is used to predict and analyze helicopter rotor wakes for single main rotor, coaxial rotor, side-by-side rotors, and tandem rotor configurations.

The parameters of the tandem-rotor configurations analyzed in this study have a vertical separation ranging from $0.05 < \frac{z}{D} < 0.2$ and span the entire range of horizontal separation ranging from $0.0 < \frac{x}{D} < 2.0$. The results of analyzing the tandem-rotor configuration using this method underpredict the overlap interference factor of a tandem-rotor configuration compared to a momentum theory analysis and suggests that tandem-rotor configurations with horizontal separation ratios ranging between $0.8 < \frac{x}{D} < 1.5$ are more efficient than two isolated rotors. The same effect is found in [49], where a modified free-wake method is used to predict and analyze rotor wakes of a tandem-rotor configuration. Both authors state that this happens because the close spacing of a tandem-rotor system causes the rotors' wakes to contract less. Based on momentum theory, if the contraction of the wake is not present, then the induced velocity at the rotor disk decreases, which reduces the induced power. Both authors also discuss the inability of the momentum theory to predict the performance of closely spaced tandem rotor configurations because momentum theory is based on the geometric overlap of the rotors or, in the case where the rotors are vertically separated, overlap between the slipstream of the upstream rotor and the disc area of the downstream rotor. These studies show that even computational methods have difficulty predicting the performance and wake deformation of tandem rotor configurations, thus influencing the work performed in this thesis to be based on empirical data rather than data gathered through computational methods.

3.3.2 Empirical Studies

Tandem Rotor Configurations

Tandem rotor configurations have been used by manned helicopters for decades [51] and aerodynamic studies of these configurations are usually for larger rotors that operate at higher *Re* [30, 52, 53]. Over time, advancements in battery technology, sensors, and processors reached the point where they are small enough and quick enough to meet the requirements needed to stabilize the flight of small UAS. These advancements allowed for the

design of unique aircraft that implement rotor configurations similar to a manned tandem-rotor aircraft. These designs include the unique rotor configurations previously discussed, which spurred research on the aerodynamic effects of propellers that operate at low *Re*. More specifically, the rotor-rotor interactions between propellers that operate at low *Re* (i.e., *Re*$< 250,000$) became a popular area of study [54, 13, 14].

Studies such as [13] sought to collect empirical data on tandem-rotor systems that are commonly used on small UAS. The work performed in [13] investigated the efficiency and thrust sharing of a tandem-rotor system at different horizontal separations ratios while maintaining a vertical separation ratio of $\frac{z}{D} = 0.05$. These tandem rotor configurations in these experiments were torque-balanced. The results of this study show that the lower rotor of the tandem rotor system is less efficient than the upstream rotor up until $\frac{x}{D} > 0.95$. Between the horizontal separation ratios of $0.95 < \frac{x}{D} < 1$, the lower rotor has a higher efficiency than the upstream rotor. The peak efficiency of the system is at $\frac{x}{D} = 0.97$; however, it is stated that the system is still 3 % less efficient than two isolated rotors. These efficiency changes in the downstream rotor were not observed when the total thrust of the system was increased to 15 N. This work also investigated the effects of varying the vertical separation ratio of a tandem-rotor system between $0.05 < \frac{z}{D} < 0.85$ while the horizontal separation ratio is maintained at $\frac{x}{D} = 0.85$. The results show an efficiency difference of roughly 2 %. The gains were mainly found when $\frac{z}{D} < 0.35$. This work provided some preliminary insights on what could be the optimum configuration of the Tetracopter and the Dodecacopter; however, due to the rigidity constraints on the airframe of the Tetracopter and the Dodecacopter, data for tandem-rotor configurations with varying horizontal and vertical separation ratios are needed.

In [14], performance and Particle Image Velocimetry (PIV) data are presented for tandem rotor configurations with a vertical separation ratio of $\frac{z}{D} = 0.125$ and $\frac{z}{D} = 0.20$ and a horizontal separation ratio ranging between $0.125 < \frac{x}{D} < 1$. In this study, the rotors have a diameter of roughly 10.7" and are operated at a *Re* of $40,000$ and $80,000$ while the system

is torque-balanced. The performance results from this study showed that the efficiency of the downstream rotor increased as the horizontal separation between the rotors increased. An interesting finding from this work is that the upstream rotor of a tandem-rotor system with overlap performed better than an isolated rotor when the rotors are operated at a *Re* of $40,000$. The author attributes this improvement in efficiency to swirl recovery. The PIV results from this study show that the tip vortices of each rotor can interact with one other in different manners depending on the relative position between the rotors.

Given that the rotor configuration of the Dodecacopter and the Tetracopter have both counter-rotating and co-rotating tandem rotor configurations, both spin directions are investigated in this thesis. However, there is little to no empirical data on co-rotating tandem rotor systems, which can most likely be attributed to the configuration not being useful in traditional aircraft design. The most relevant work is the difference between coaxial rotor systems and stacked (co-rotating) rotor systems. One performance phenomenon that is difference between these two systems is swirl recovery, which is created by the lower rotor of a coaxial rotor system. Swirl recovery is the reduction in the energy that a rotor loses from transferring angular momentum to the wake, creating a swirl within the wake. Since the downstream rotor of a coaxial rotor system is rotating in the opposite direction of the upstream rotor, in theory, some of power loss by the upstream rotor from creating the swirl is recovered due to the rotation of the downstream rotor. Johnson describes swirl loss in detail using momentum theory and concludes that the total power increase due to swirl recovery is roughly $1\,\%$ for a helicopter rotor with a typical thrust coefficient. Another detailed review of swirl loss using momentum theory is given in [55]. A more recent study presented empirical data of a coaxial rotor system that consisted of two 6.56' (2 m) diameter rotors. This study included the traditional coaxial rotor system as well as a stacked (co-rotating) rotor system. The results showed that the azimuth angle of the stacked rotor system is the main factor that determines whether the stacked rotor system performs better than a traditional coaxial rotor system. The results also showed that a traditional coaxial rotor system

has a nearly a 4 % efficiency increase over a stacked rotor system that had an azimuth angle of 90°. The coaxial rotor system was also compared to a stacked rotor system with a −50° azimuth angle between the upper and lower rotor. This comparison showed that the coaxial rotor system is 2.7 % more efficient than the stacked rotor system. Similar experiments that investigated the difference between coaxial and stacked rotor systems using rotors with a diameter of roughly $4.25'$, found that the coaxial rotor system experienced a 5 % reduction in induced power due to swirl recovery when compared to a stacked rotor system [52]. It should be noted that the ratio of the vertical separation between the rotors and the diameter of the rotors in these experiments is less than 0.1 Although these studies show a minor efficiency difference between a coaxial and stacked rotor system, it is unclear weather this difference in efficiency remains if the axes of the two rotors are not concentric, and at what horizontal distance does this efficiency increase becomes nonexistent. As previously mentioned, this phenomenon is stated to be present in tandem rotor systems operating at low *Re* [14]. One goal of the work presented in this thesis is to see if this effect is present at the *Re* that a small UAS typically operates at and at what values of vertical and horizontal separation are these effects present.

Oblique Rotor Configurations

Very few studies have investigated rotor configurations similar to the semi-coaxial configuration. Preliminary studies of the configuration performed by Bershadsky provided data that led to the conclusion that a purely semi-coaxial rotor configuration with both rotors placed at a 15° and 30° performs better than a traditional coaxial rotor configuration [9]. However, the thrust stand used in that study had several limitations that may have affected the results. Bennetts [17] designed and fabricated a thrust stand that allowed the performance for several non-coplanar rotor configurations with oblique flow interactions to be measured. He also performed flow visualization experiments on the configurations. This study shows that the downstream rotor of a semi-coaxial configuration performs better than

a coaxial rotor configuration because the downstream rotor does not ingest the entire wake of the upstream rotor due to the angles placed on the rotors. This study did not investigate the effects of the vertical separation of a semi-coaxial rotor configuration on the performance of the downstream rotor.

3.3.3 Preliminary Results

The author of this thesis also performed preliminary experiments on the tetrahedron rotor configuration before performing the work discussed in this thesis [56]. These experiments were conducted on a custom thrust stand, as shown in Fig. 3.1, which was equipped with smaller 5" polycarbonate tri-blade propellers than the propellers used in the experiments discussed later in this thesis. The propellers are rotated by Flywoo NIN 2207 2450KV motors and controlled by EMAX Formula Series 45A electronic speed controllers (ESCs).

The force created by the propellers was transferred through an aluminum shaft to four load cells, two of which were used to measure the thrust generated in the Z-axis, while the other two were used to measure the torque about the Z-axis generated by the four rotors.

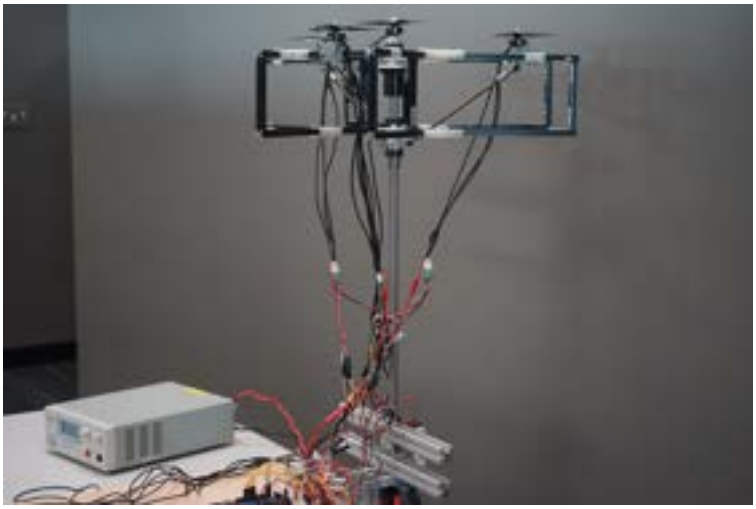

Figure 3.1: A custom thrust stand created to gather data on the tetrahedron rotor configuration.

Fig. 3.2 was developed by creating a polynomial fit of each configuration's 11 data points and evaluating the polynomial using an arbitrary thrust value of 1.4 kg. The summa-

tion of each isolated rotor's power consumption at a collective thrust value of 1.4 kg was found using the same method and is labeled as *Isolated Rotors* on Fig. 3.2. These preliminary results supported the results of applying the momentum theory to a tandem-rotor configuration. However, the sensors and design of the thrust stand had a number of flaws and limitations that reduced the accuracy of the results. These results and the limitations of this thrust stand motivated the development of the thrust stand presented in this thesis and the overall work performed.

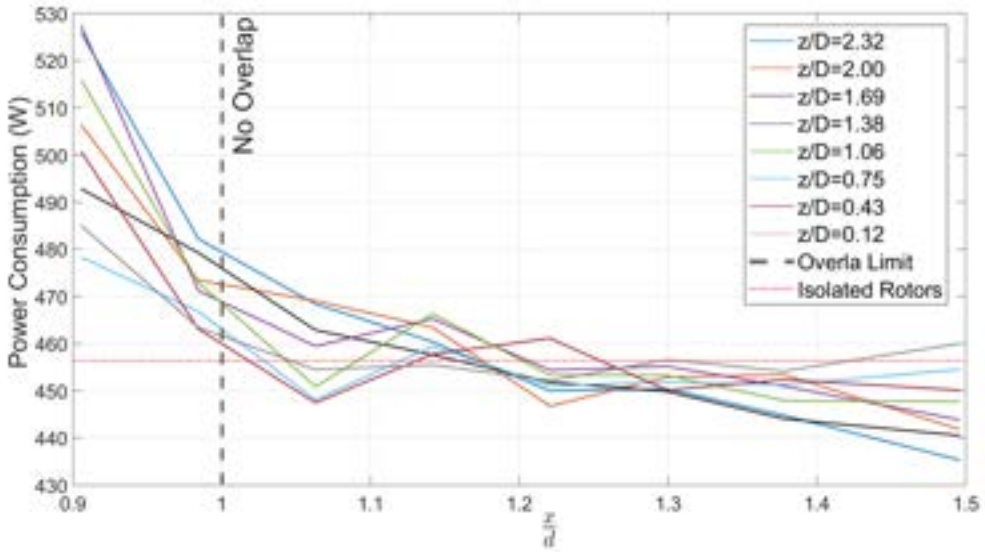

Figure 3.2: Power consumption versus the horizontal separation between the rotors for each vertical separation tested.

3.4 Conclusion

The rotor-rotor interactions generated due to the rotor placement of the novel Tetrahedron rotor configuration are scarcely studied. From the literature review presented, it can be seen that there is a lack of empirical data involving the performance of low Reynolds number rotors that experience rotor-rotor interactions. The data currently available is not sufficient to accurately estimate the optimal configurations of the Tetracopter and the Dodecacopter. There is also a lack of data on the performance of rotor configurations similar

to the semi-coaxial rotor configuration. The lack of available empirical data motivates the work performed in this thesis.

CHAPTER 4
EXPERIMENTAL METHODS

4.1 Summary

This chapter aims to explain the experimental methods used to conduct the thrust stand experiments on the three rotor configurations of interest (i.e., the tandem-rotor, semi-coaxial, and oblique rotor configurations). This data will be used to determine the relationship between the relative positioning of the rotors in these configurations, the *Re* they operate at, and their performance. These relationships will dictate on the best design practices for developing rotorcraft UAS with rotor configurations that experience rotor-rotor interactions. This chapter is broken into six sections: section 4.2 outlines the design, equipment, experimental procedure, and data acquisition the thrust stand used to collect the data that is later presented in this thesis; section 4.3 presents the experimental method used to test tandem-rotor configurations on the thrust stand along with the precision of the thrust stand while collecting data of the tandem rotor configurations; section 4.4 discusses the precision of the thrust stand when collecting data on the semi-coaxial rotor configurations as well as the apparatus used to angle the rotors so that the semi-coaxial rotor configuration could be formed; section 4.5 describes the experimental setup for the oblique rotor configurations. Lastly, the chapter ends with concluding remarks in section 4.7.

4.2 The Automated Thrust Stand

To reduce the number of sources of uncertainty and collect data that encompasses a more extensive design space, a thrust stand that is larger and more precise than the one that gathered the preliminary data presented in Section 3.3.3 is designed and fabricated. Several elements of this thrust stand, such as the propellers, motors, ESCs, and sensors used, reduce

the sources of uncertainty compared to the thrust stand used to collect the preliminary results. A schematic illustrating how the hardware and sensors used on the thrust stand interface with one another is shown in Fig. 4.1.

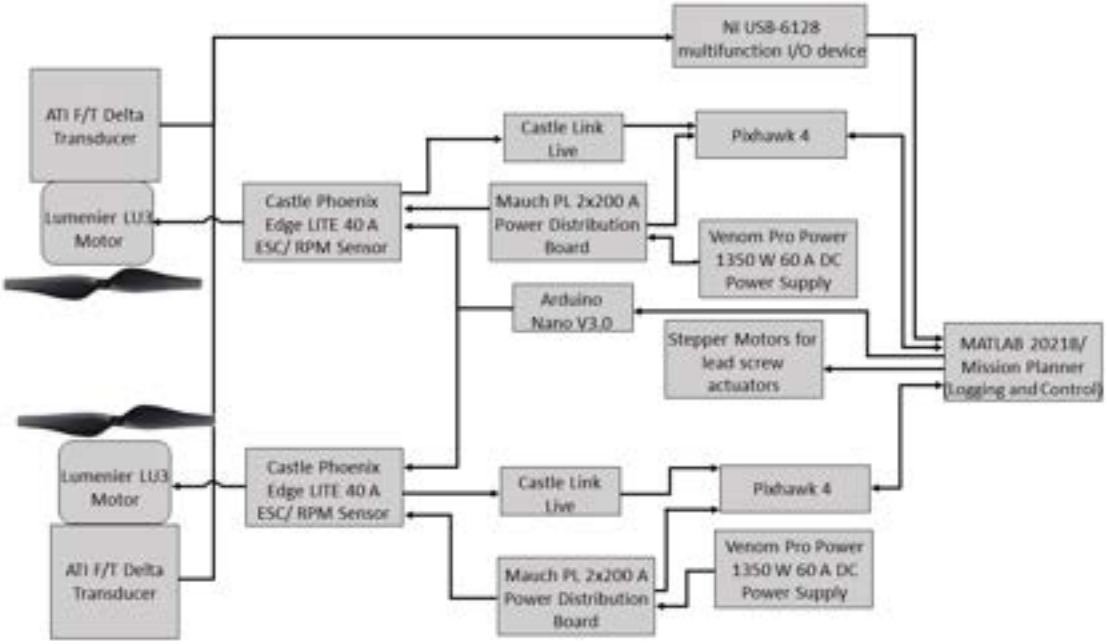

Figure 4.1: Schematic depicting the hardware and sensors used on the thrust stand

4.2.1 Propulsion System

Unlike the preliminary experiments presented in Section 3.3.3 that used 5" polycarbonate tri-blade propellers, this second thrust stand is designed to collect data of 13" carbon fiber propellers, specifically the Tiger Motor 13x4.4" carbon fiber propellers [57]. These propellers are selected because the carbon fiber propellers are more rigid than the smaller polycarbonate tri-blade propellers; thus, the carbon fiber propellers are less likely to suffer from rotor blade flapping than polycarbonate propellers. However, like most COTS propellers, there is little information about the rotor's geometry. The data of the power consumption and thrust generation of the propeller at a given RPM using the same motor that is used in these experiments is provided by the manufacturer and shown in Figs. 4.2 and 4.3.

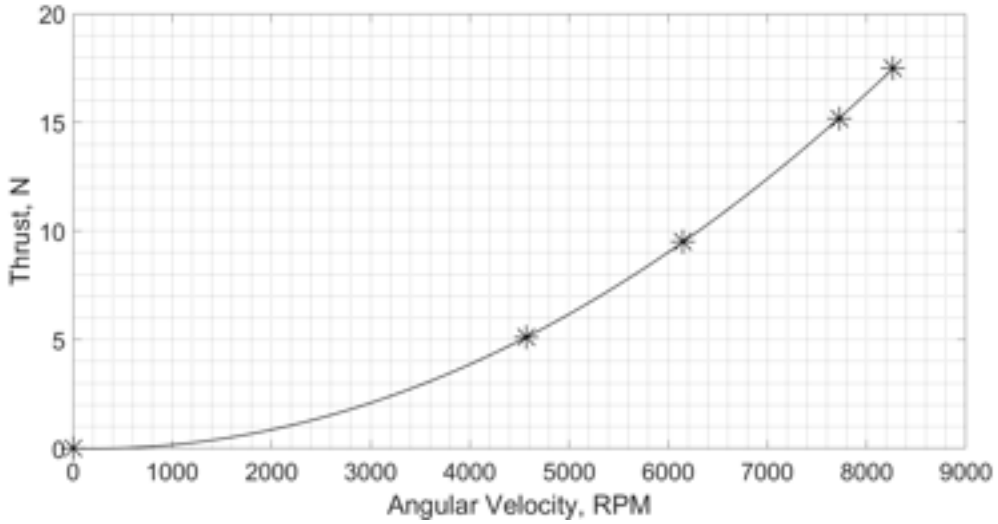

Figure 4.2: Thrust vs. angular velocity data of the T-Motor 13x4.4" carbon fiber propeller provided by T-motor.

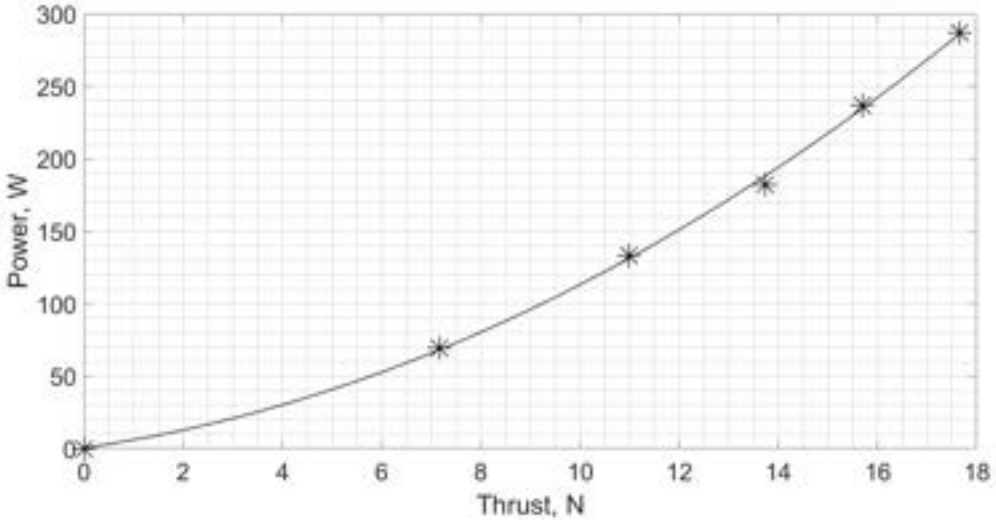

Figure 4.3: Thrust vs. power data of the T-Motor 13x4.4" carbon fiber propeller provided by T-Motor.

4.2.2 Hardware

The COTS hardware used on the thrust stand is selected based on their capabilities and ability to interface with one another. Table 4.1 lists the main hardware used to operate the motors on the thrust stand. The following sections will discuss the properties of the sensors

and hardware used on the thrust stand.

Power Supply and Power Distribution Board

Each rotor is powered by their own power source, a Venom Pro Power 1350 W 60 A DC power supply [58], and are supplied with roughly 24.4 V. Each rotor has a separate power supply to mitigate the possibility of electrical interference. Pulse-width modulation signals (PWM) are generated by an Arduino Nano V3.0 [59] and delivered to the ESC via the Castle Link Live [60]. The command dictating the duty cycle of the PWM signal is given to the Arduino Nano via MATLAB. The power supply delivers power to each ESC through a Mauch PL 2200 A Power Distribution Board (PDB) [61], which is also used to monitor the voltage and current consumption of the rotor.

Motors and ESCs

Each propeller is spun by a Lumenier 700 kV Professional motor [62]. The Electronic Speed Controller (ESC) used is a Castle Phoenix Edge LITE HV 40 A ESC [63], which has a max voltage of 50.4 V and a max continuous amperage of 40 A. This ESC also has logging capabilities for current, voltage, rotor angular velocity, and more.

Table 4.1: Hardware used during the experiments.

Hardware	Type
Power Source	Venom Pro Power 1350 W 60 A DC Power Supply
Propeller	Tiger Motor 13x4.4 Carbon Fiber Propeller
Motor	Lumenier LU3 700 kV Professional Motor
ESC	Castle Phoenix Edge LITE HV 40 A ESC
PDB	Mauch PL 2x200 A Power Distribution Board

Force and Torque Measurements

Data of several parameters are captured during each experiment. These parameters include the angular velocity of each rotor, the voltage and current consumption of each rotor, and the forces and moments created by each rotor. Table 4.2 lists the sensors used. Each rotor is mounted to its own 0.5" steel shaft that is mounted to a 6 degree of freedom ATI Force/Torque Delta Transducer that measures force and torque about three perpendicular axes as shown in Fig. 4.4. The forces and torques about the three axes are measured at a frequency of 2000 Hz. The sensor's resolutions for forces in the Z-axis and X,Y-axes are 0.125 N and 0.0625 N respectively. The sensor's resolution for moments about all three axes is 5/1333 N m. Each sensor has a measurement uncertainty of 1.25 % for forces and torques in all three axes. Data is retrieved from an ATI Force/Torque Delta Transducer via a National Instrument USB-6218 multi-function I/O device and relayed back to a computer that operates and collects data from the sensors via MATLAB.

Angular velocity Measurements

For these experiments, the angular velocity data gathered by the ESC is collected and later used to analyze the performance of the rotors. The ESC measures the rotor's angular velocity by measuring the rotor's counter-electromotive force (counter-EMF). The ESC measured RPM at a frequency of 10 Hz.

Current and Voltage Measurements

The Mauch PDB monitors the voltage and current consumption at 10 Hz. The Mauch PDB uses a hall effect sensor for measuring current and has an uncertainty of roughly 1.2 % over the full range of the sensor, according to the manufacturer. The hall effect sensor is calibrated using manufacturer-provided specifications.

4.2.3 Data Acquisition

The schematic shown in Fig. 4.1, shows that the data gathered by ESC and the PDB are passed to a Pixhawk 4 [64], where it is stored and later downloaded for analysis. The Pixhawk 4 used a customized version of the Ardupilot [65] flight controller software, which allowed the live collection of the voltage, current, and angular velocity measurements. The Castle Link Live allows for the angular velocity data collected by the ESC to be passed to the Pixhawk 4. The data is then downloaded by a computer using the ground control station software, Mission Planner [66], and later analyzed using MATLAB.

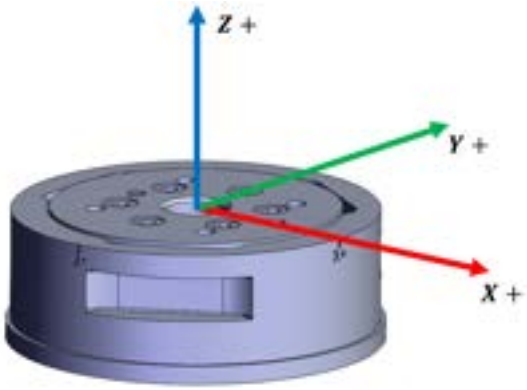

Figure 4.4: The three perpendicular axes that the ATI Force/Torque Delta Transducer measures force and torque.

Table 4.2: Sensors used during the experiments.

Sensor	Type	Parameter Measured
Power Sensor	Mauch PL 2x200 A Power Distribution Board	Current, Voltage
Force/Torque Sensor	6 DoF ATI F/T Delta Transducer	Force, Torque
Angular Velocity Sensor	Castle Phoenix Edge LITE HV 40 A ESC	Angular Velocity

4.2.4 Thrust Stand Design

The structure of the thrust stand is designed to allow for quick and easy changes of the rotor configurations. Moreover, in the tandem-rotor configurations, the vertical and horizontal separation between the rotors can be easily changed via linear actuators. The full thrust stand is shown in Fig. 4.5. Although Fig. 4.5 shows mounting points for four motors, for all experiments discussed in this thesis, only two motors are mounted on the thrust stand. To capture the impact of the downstream rotor operating in the wake of the upstream rotor, the thrust stand is designed so that no external objects are placed between the two rotors allowing the aerodynamic interactions between the rotors to occur with minimum external disturbances. The downstream rotor is lofted roughly 16" (406.4 mm) from the ATI F/T sensor via a steel threaded shaft that is mounted to the ATI F/T sensor. A 3-D printed polyethylene terephthalate glycol (PETG) motor mount connects the motor to the shaft. To ensure that the torque generated by the propeller is transferred to the ATI F/T sensor, the 3-D printed motor mount is fastened to the steel shaft by a carbon steel clamping shaft collar. As can be seen in Fig. 4.5, three linear actuators equipped with lead screws control the vertical distance between the two rotors. Linear actuators are also used to change the horizontal distance between the upstream and downstream rotor. The movement of the linear actuators is controlled by Anaheim Automation 23MD106D stepper motors [67] that have a step size of 1.8° (200 steps per revolution) and a step angle accuracy of 5 %. The lead screw used is a 800 mm lead screw with a 2 mm pitch, 8 mm lead and four starts. The combination of both the stepper motor and the lead screw allows for the vertical and horizontal distance between the rotors can be changed with a resolution of 0.04 mm. For all of the experiments conducted in this thesis, the rotors are mounted in a manner that directs the lift generated toward the floor to avoid operating the rotors in ground effect, meaning the airflow of the rotors is directed toward the ceiling. For all of the thrust stand experiments, the thrust-stand is lofted roughly 2.0' (609.6 mm) above the ground to ensure that the lower rotor does not operate in ceiling effect. All of the experiments are conducted

in an enclosed environment; thus, no significant external airflows are present.

Figure 4.5: Thrust Stand

4.2.5 Experimental Procedure

Although several different rotor configurations are tested using the presented thrust stand, the same experimental procedure is used for all tests. These experiments aim to quantify the effects of the rotor-rotor interactions as a function of the relative position between the rotors. Data is collected from the upstream rotor and downstream rotor operating independently, meaning only one rotor operates at a time and when operated simultaneously for each configuration. The experiments are performed in this manner to mitigate the effects of uncontrollable parameters (i.e., temperature, slight physical differences in the two motors,

propellers, and electronic speed controllers (ESCs), wire lengths, and interference between the rotors' wakes and the thrust stand). When each rotor is operated independently, the propeller of the rotor not being operated is removed. This experimental method allows for the results of each configuration where the rotors operate simultaneously to be compared to the results of each rotor operating independently. For each configuration, the rotors are operated at four different throttle commands. These throttle commands correspond to specific *Re* (75,000, 100,000, 125,000, 135,000) that the rotor operates at when operated independently. This is done because it was found in [26] that the tip vortices and trailing edge vortex sheets in a rotor wake can interact differently depending on the downward velocity of the wake, which in turn may impact the performance of the rotors. The angular velocities that correspond with the chosen *Re* span the full operational window of the rotors used. The rotors operated at these four angular velocities for 30 s each, and the force, voltage, angular velocity, and current data of these time segments are averaged to produce four sets of data points for each rotor configuration in both counter-rotating and co-rotating spin orientations. To change the spin direction of the rotor configurations, the direction of the upstream rotor is changed, and the direction of the downstream rotor remains constant.

Before starting an experiment, force and moment data are collected from both ATI F/T sensors for 30 s. This is done to ensure that the sensors are functioning correctly and that the sensors are not experiencing significant drift. The values collected during this time are averaged and used to tare the sensor. Before starting an experiment, the separation distance between the rotors is verified by manual measurements. The step-by-step protocol used for each experiment is listed below.

Test Procedure.

1. Remove the upstream propeller
2. Verify the location of the downstream rotor with respect to the upstream rotor through manual measurements

3. Take measurements from both ATI F/T sensors for 30 s to ensure that neither sensor is experiencing significant drift
4. Connect both Pixhawk 4 flight controllers to their own instance of Mission Planner
5. Turn on both power sources and ensure that the power source is set to roughly 24
6. Activate both safety switches attached to both PDBs
7. Arm both Pixhawk 4 flight controllers via Mission Planner
8. Run the MATLAB script that begins the experiment
9. After the downstream rotor has stopped, press both safety switches on the PDBs
10. Place the upstream propeller on the motor
11. Remove the propeller from the downstream rotor
12. Activate both safety switches attached to both PDBs
13. Ensure that any disturbances created by removing and attaching the propellers have dissipated
14. Continue the MATLAB script by pressing the ENTER key on the central computer
15. After the upstream rotor has stopped, press both safety switches on the PDBs
16. Place the upstream propeller on the upstream motor
17. Activate both safety switches attached to both PDBs
18. Ensure that any disturbances created by removing and attaching the propellers have dissipated
19. Continue the MATLAB script by pressing the ENTER key on the central computer

20. Wait until both rotors have completed their operations

21. Once both rotors have stopped moving, disarm both Pixhawk 4 flight controllers via Mission Planner

22. Turn off both power sources

It should be noted that before any step that involves operating the rotor (i.e., steps 13 and 18), the ATI F/T sensors collect 30 s of data while neither propeller is operating. This data is averaged and used to tare the sensors.

4.3 Tandem Rotor Experiments

4.3.1 Thrust Stand Alignment

To ensure that the separation between the two rotors of the tandem rotor configuration is accurate, the vertical separation between the rotors is reduced to $\frac{z}{D} = 0.0$, where z is the vertical distance between the rotors and D is the diameter of one rotor, by lowering the downstream rotor so that its propeller is in the same plane as the upstream propeller. The horizontal separation of the rotor is minimized, and the horizontal distance between the center of the rotors is measured using a dial caliper. The minimum horizontal separation is found to be 145 mm.

4.3.2 Thrust Stand Precision

To ensure that the thrust stand can gather repeatable results, ten experiments are conducted whilst the two rotors are in a tandem rotor configuration that can be described by vertical and horizontal separation ratios of $\frac{z}{D} = 0.81$ and $\frac{x}{D} = 0.57$ respectively. This configuration is selected to validate the thrust stand's precision because this configuration is the closest spaced rotor configuration of the constrained rotor configurations tested, and the expected magnitude of rotor-rotor wake interactions are high. The coefficient of variation (CV), the

Table 4.3: The CV for C_T, C_P, and C_Q of the upstream and downstream rotors.

	Upstream Rotor			Downstream Rotor		
Re	C_T (%)	C_P (%)	C_Q (%)	C_T (%)	C_P (%)	C_Q (%)
135,000	0.58	1.92	2.31	2.53	1.06	1.15
125,000	0.47	1.59	2.42	1.97	0.94	0.72
100,000	0.92	2.12	2.78	1.79	1.28	0.79
75,000	1.01	4.80	2.33	1.16	3.53	1.01

standard deviation divided by the mean of the thrust, power, and torque coefficients, for both the upstream and downstream rotors of the ten experiments is shown in Table 4.3. Table 4.4 shows the uncertainty within a 95% confidence interval on the mean of each performance metric for both rotors. The CV of these three parameters shows that even in a configuration with a significant amount of overlap and consequently a significant amount of rotor-rotor wake interactions, the thrust stand can generate repeatable results with a (CV) of 2.53% or less for the thrust coefficient, 2.78% or less for the torque coefficient, and 4.80% or less for the power coefficient for all angular velocities tested. More data supporting the precision of the thrust stand are shown in Figure A.1, located in the Appendix. Figure A.1a - Fig. A.1c show the CV of the thrust, power, and torque coefficients for each set of three experiments for each spin direction and constrained tandem rotor configuration that will be introduced in the next section. Those figures show that even when the relative distance of the rotors on the thrust stand changes, the thrust stand is relatively precise. However, at low *Re*, the CV of C_P, shown in Fig. A.1b, can be as high as 12 %, indicating that the power module struggles to measure the rotors' power consumption when the current draw is low. The lack in the precision of the PDB to measure lower current draw is also seen in Table 4.3. This effect will also be apparent in later sections of this thesis when the results of the experiments are presented and discussed.

Table 4.4: The uncertainty within a 95% confidence interval of the mean of C_T, C_P, and C_Q of the upstream and downstream rotors as a percentage of the mean.

	Upstream Rotor			Downstream Rotor		
Re	C_T ($\pm\%$)	C_P ($\pm\%$)	C_Q ($\pm\%$)	C_T ($\pm\%$)	C_P ($\pm\%$)	C_Q ($\pm\%$)
135,000	0.89	2.98	3.58	3.92	1.64	1.78
125,000	0.73	2.46	3.75	3.05	1.46	1.12
100,000	1.43	3.29	4.31	2.77	1.98	1.22
75,000	1.57	7.44	3.61	1.79	5.47	1.57

4.3.3 Tandem Rotor Configurations

The tested tandem rotor configurations can be broken into two categories, which correspond to the design of the Tetracopter and the Dodecacopter. The first category is tandem-rotor configurations that have a constraint between their vertical and horizontal separation. This constraint is related to the rigidity goal of the Tetracopter and the Dodecacopter. The second category consists of tandem configurations that do not have a constraint relating their vertical and horizontal separation. In total, 35 tandem rotor configurations are tested, five of which are constrained tandem rotor configurations.

Constrained Tandem Rotor Configurations

Five constrained tandem rotor configurations are tested. For each configuration, the relationship between the vertical and horizontal separation is as described by Eq. (1.1). Table 4.5 lists the configurations tested. The configuration index listed in Table 4.5 is linear in relation to the vertical and horizontal separation of the rotor configurations. For each configuration and spin direction, a series of three identical experiments are conducted. Each experiment is conducted as stated in Section 4.2.5.

Table 4.5: Constrained tandem-rotor configurations tested

x (mm)	$\frac{x}{D}$	z (mm)	$\frac{z}{D}$	Configuration Index
190	0.57	268	0.81	1
235	0.71	332	1.00	2
280	0.85	395	1.20	3
325	0.98	459	1.39	4
347	1.05	491	1.58	4.5

As previously mentioned, to change the parameters of the tandem rotor configuration, the downstream rotor (the upper rotor when viewing the thrust stand) is moved both vertically and horizontally away from the upstream rotor (the lower rotor when viewing the thrust stand). To show that changing the position of the downstream rotor does not create significant aerodynamic or vibratory effects that would impact the recorded data, Figs. 4.6 to 4.8 show the thrust, power and torque coefficients of the downstream rotor operating independently (meaning the upstream rotor is not operating) in the five different constrained rotor configurations. The largest difference between the maximum and minimum thrust, power, and torque coefficients at any of the angular velocities tested are 3.39 %, 10.97 %, and 5.46 %, respectively. The second-largest difference in the power coefficient at any angular velocity tested is 1.96 %. The large difference in the power coefficients is caused by the lack in the precision of the PDB to measure low current draw and the fact that the electrical power, not the mechanical power, is being measured. It should be noted that the thrust and power coefficients for a fixed-pitch propeller should be nearly constant throughout the range of angular velocities that the rotors can be operated.

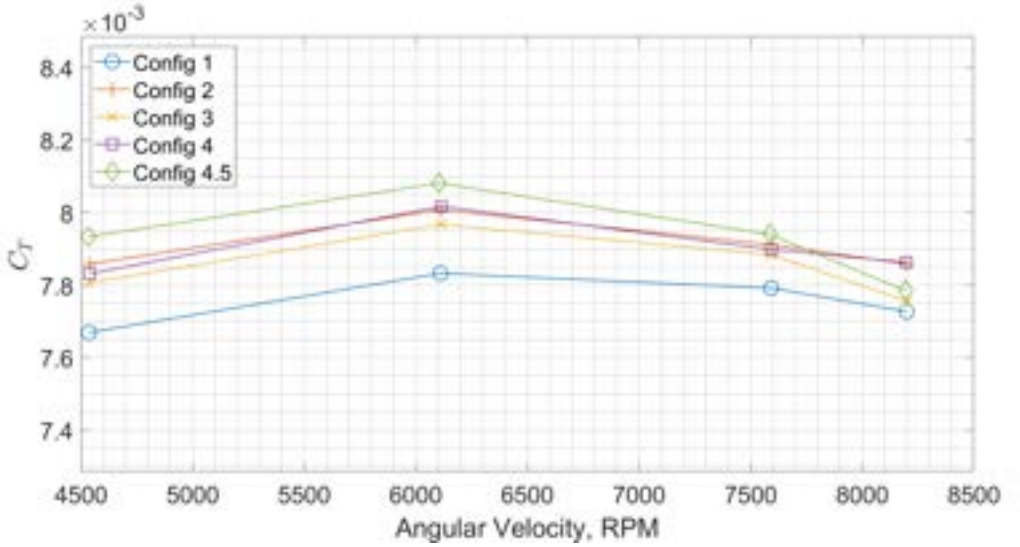

Figure 4.6: Angular Velocity of the downstream rotor versus the thrust coefficient of the downstream rotor operating independently at the different positions of the constrained configurations tested

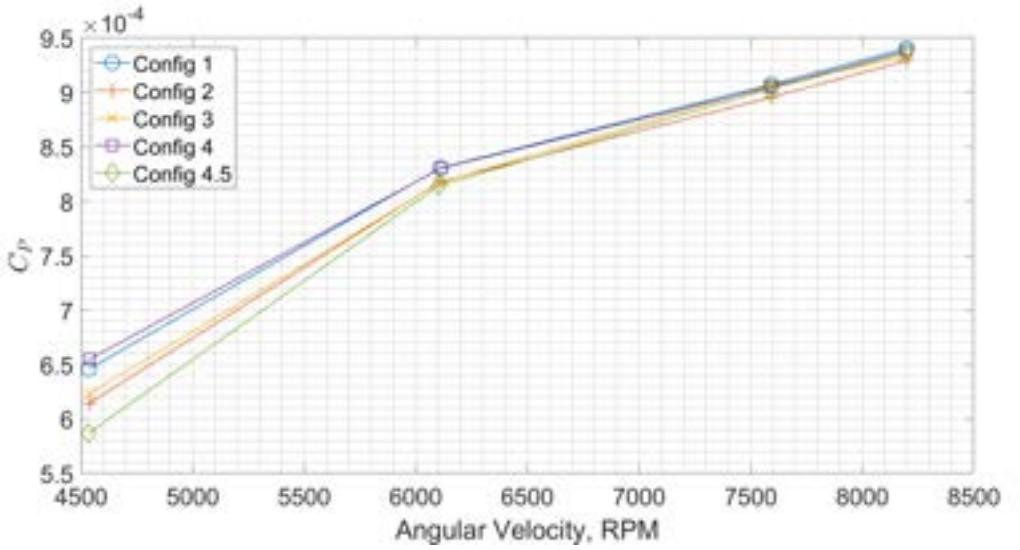

Figure 4.7: Angular Velocity of the downstream rotor versus the power coefficient of the downstream rotor operating independently at the different positions of the constrained configurations tested

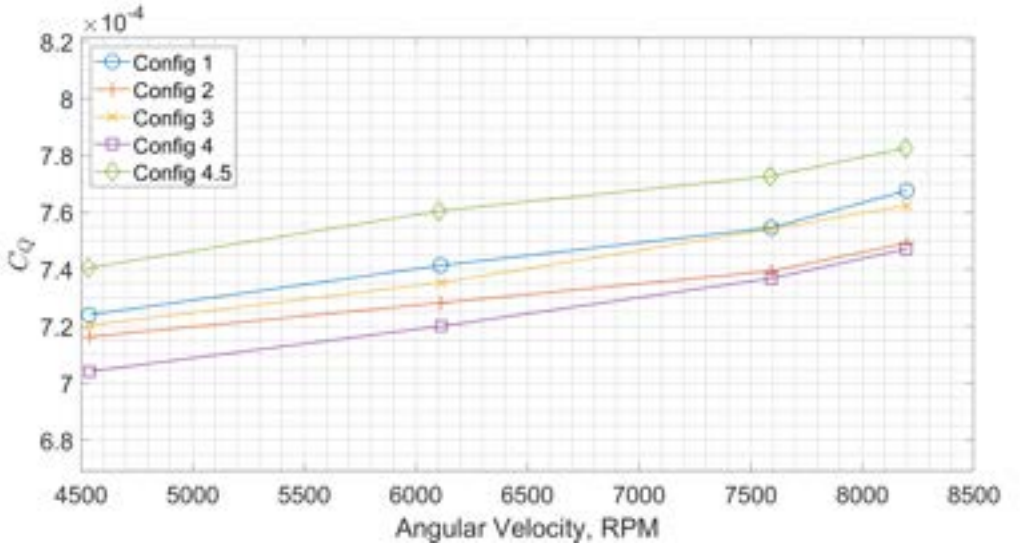

Figure 4.8: Angular Velocity of the downstream rotor versus the torque coefficient of the downstream rotor operating independently at the different positions of the constrained configurations tested

Unconstrained Tandem Rotor Configurations

The 30 unconstrained tandem rotor configurations tested consist of every combination of five vertical and six horizontal separations, which are shown in Table 4.6. These configurations include the minimum horizontal separation and the minimum vertical separation for the safe operation of the thrust stand. The maximum horizontal separation is chosen based on past works that have shown that at a horizontal separation ratio of roughly 1.1 the rotor-rotor interactions of a tandem-rotor system are not significant.

Table 4.6: The parameters of the 30 tandem rotor configurations tested

x (mm)	$\frac{x}{D}$	z (mm)	$\frac{z}{D}$
145.29	0.44	49.53	0.15
198.125	0.60	115.57	0.35
247.65	0.75	165.10	0.50
297.18	0.90	247.65 9	0.75
346.71	1.05	330.20	1.0
379.73	1.15		

4.4 Semi-coaxial Experiments

4.4.1 Thrust Stand Precision

Previous thrust stand experiments performed to ensure the precision of the thrust stand while testing tandem rotor configurations showed that the thrust stand can produce repeatable results while the rotors operate simultaneously. The main difference between the tandem-rotor configurations and the semi-coaxial rotor configurations is that the downstream rotor of the semi-coaxial rotor configurations is mounted to the center of the moving platform rather than a movable track as was done for the tandem-rotor configuration. To ensure that mounting the upstream rotor to the center of the moving platform does not drastically change the precision of the thrust stand, ten experiments are conducted where the upstream and downstream rotors are operated independently. Table 4.7 shows the CV of thrust and power coefficients for the downstream and upstream rotors operating independently while in a semi-coaxial rotor configuration. These experiments show that the variation in the measurements of the downstream rotor operating independently while in the semi-coaxial rotor configuration is slightly larger than the measurements of the downstream rotor operating in the wake of the upstream rotor while in the tandem-rotor configuration. These results suggest that the vibratory effects of the thrust stand may be slightly more

severe when the downstream rotor is mounted to the center of the thrust stand's moving platform.

Table 4.7: The CV for C_T and C_P of the upstream and downstream rotors while in the semi-coaxial configuration.

	Upstream Rotor		Downstream Rotor	
Re	C_T CV (%)	C_P CV (%)	C_T CV (%)	C_P CV (%)
135,000	0.51	0.63	2.13	0.76
125,000	0.30	0.73	2.78	1.27
100,000	0.65	0.94	2.51	0.96
75,000	0.83	1.33	1.4	1.77

4.4.2 Semi-coaxial Rotor Configurations

In total, 21 semi-coaxial configurations are tested. The downstream rotor of nine of the tested semi-coaxial configurations have a dζ_D, that is set to 0°, excluding the traditional coaxial rotor configurations. Hereinafter, these nine configurations will be referred to as semi-coaxial-B configurations, while semi-coaxial configurations where $\zeta_U = \zeta_D$ will be referred to as semi-coaxial-A configurations. For both semi-coaxial configurations, three vertical separations are tested ($s_D = 0.88, 0.96, 1.5$). In order to compare the performance of the semi-coaxial configurations to a traditional coaxial rotor configuration, coaxial rotor configurations are tested at each vertical separation. In total, for each vertical separation, the seven configurations listed in Table 4.8 are tested. The values of the vertical separations tested include the minimum distance the rotors could safely operate at when $\zeta_{U,D} = 45°$. For each configuration, both the co-rotating and the counter-rotating spin orientations are tested. In total, 42 thrust stand experiments are completed for the semi-coaxial rotor configuration. To enable the semi-coaxial rotor configuration to be placed on the thrust stand, a custom mechanism, as shown in Fig. 4.9, is designed to ensure that the angles (ζ) between the rotor blades and the horizontal plane are accurate. An example of how the semi-coaxial

configuration is orientated on the thrust stand can be seen in Figures 4.10 and 4.11.

Table 4.8: Semi-coaxial configurations tested

ζ_U^o	ζ_D^o	Configuration Number
0	0	1
15	15	2
30	30	3
45	45	4
15	0	5
30	0	6
45	0	7

Figure 4.9: Apparatus that allows the value of ζ to be changed in 15^o increments.

Figure 4.10: The Thrust stand used for all experiments.

Figure 4.11: A semi-coaxial configuration on the thrust stand.

4.5 Oblique Rotor Configurations

For the oblique rotor configurations, two horizontal separations represented by the variable x in Fig. 1.14 are tested. For each horizontal separation, four angles, described as ζ in Fig. 1.14, are tested. For these experiments, the angle of the rotors, ζ, are equal to one another. The values of ζ tested are 0°, 15°, 30° and 45° at horizontal separation ratios, $\frac{x}{D}$, of 1.1 and 1.5.

4.6 Thrust Stand Limitations

The previously described thrust stand and the experimental methods used have limitations and downfalls that should be considered when discussing the results gathered from using them. The data generated from the experiments conducted to show the precision of the thrust stand showed that the power measurement of the downstream rotor at low current has more variability than other measurements. This variability can be seen throughout the

results that will be later presented and can be seen in Fig. 4.7. The magnitude of the variability may be caused by the length of the wires between the DC power supply and the Mauch Power Monitor connected to the ESC of the downstream rotor. It must also be noted that the power measurements for both the downstream and upstream rotor are measurements of the electrical power consumption, not just the mechanical power consumption of the propeller, meaning that the measurements may be slightly higher than power consumption estimations derived from momentum theory or other computational methods. The size of the thrust stand limits the horizontal separation to $0.45 < \frac{x}{D}$. Vibration caused by the rotational motion of the rotors, the aerodynamic interaction between the rotors, and the aerodynamic interaction between the rotors and the structure of the thrust stand is also a factor that could skew the measurements of the sensors used. To mitigate the effects of vibration, each rotor configuration and angular velocity is maintained for 30s. Although these limitations exist, the precision statistics presented show that the thrust stand can gather repeated results. The experimental method chosen for these experiments achieves the goal of quantifying the effects of the rotor-rotor interactions as a function of the relative position between the rotors; however, it does not provide data for when the rotor configurations are torque balanced, which is how the rotors would operate while on a vehicle that is maintaining a steady hover. To overcome this limitation, an estimation method that predicts the performance of the tandem-rotor configurations under different operating parameters (i.e., different angular velocities and relative positions) is presented in this thesis and validated.

4.7 Conclusion

The methods used to perform the experiments on the three aforementioned rotor configurations are meant to allow for the collection of performance data that shows the impact of the rotor-rotor interactions between the upstream and downstream rotors. Steps, such as operating each rotor for 30 s and operating each rotor independently before operating them both simultaneously, were taken to normalize any vibratory effects or aerodynamic

effects caused by the components of the thrust stand. Experiments were conducted, and the CV of the performance parameters gathered from those experiments were presented, which showed that the thrust stand can produce repeatable results.

CHAPTER 5
THRUST STAND RESULTS AND OPTIMIZATION

5.1 Summary

This chapter presents the results of the thrust stand experiments for the three previously mentioned rotor configurations and the metrics used to analyze the configurations. This chapter also presents the methods used to determine the optimal rotor configuration of the Tetrahedron Dodecacopter and the optimal rotor configuration of the Tetracopter. The two goals of this chapter regarding the tandem-rotor configuration are to quantify the relationship between the relative position of the rotors in a tandem rotor system and the performance of the rotors and to use this data to find the optimal Tetracopter and Dodecacopter vehicle design. The results of the tandem-rotor experiments are presented in several different ways using several different metrics. The results of these experiments are also compared to the predictions derived from the momentum theory, which show that, in general, the results and the momentum theory have similar trends. However, the results from the tandem-rotor experiments show that the momentum theory solution underpredicts the interaction between the rotors of closely spaced tandem-rotor configurations.

A novel estimation method that uses the thrust stand data to estimate the performance of non-coplanar overlapping rotors while torque-balanced is introduced in this chapter. The novel estimation method is then used to find the optimal rotor configuration of both the Tetracopter and Dodecacopter. The results of optimizing the vehicles' design using the estimation method show that the weight of the vehicles can influence the design of the vehicles more than the degradation in performance of the rotors due to rotor-rotor interactions. The novel estimation method used to find the optimal vehicle designs is discussed in detail and validated.

Regarding the semi-coaxial rotor configuration, this section aims to show the relationship between the vertical separation, the angle of the rotors, and the rotors' performance in the different semi-coaxial rotor configurations. The semi-coaxial data presented suggests that under specific parameters, the semi-coaxial rotor configuration is more efficient than a traditional coaxial rotor configuration. Lastly, the results of the oblique rotor configurations are presented, which shows that there are no significant performance changes due to oblique flows where only the slipstream of both rotors interacts with one another. In this chapter, each subsection presenting the results of the thrust stand experiments is followed by a discussion of the results.

5.2 Results of the Constrained Rotor Configurations

As discussed in Section 4.3, five constrained rotor configurations are tested on the thrust stand. Each of these configurations is constrained such that the vertical and horizontal separations between the rotors are as described in Eq. (1.1).

5.2.1 Performance Metrics

The thrust, power, and torque coefficient

A few analysis methods are used to see the effects of the rotor configuration on the performance of the rotors. The first analysis uses the thrust, power, and torque coefficients as well as the ratio of C_T/C_P of the downstream rotor of each constrained rotor configuration. To mitigate any minor vibratory effects that the downstream rotor experiences due to it operating at different positions on the thrust stand, the percent difference of the performance coefficients between the downstream rotor operating independently and simultaneously (i.e., in the wake of the upstream rotor) are used as a performance metric. The percent decrease in the performance coefficients is calculated using the data gathered from the downstream rotor operating independently and simultaneously in the same position on the thrust stand (i.e., in the same position relative to the upstream rotor). As previously

mentioned, the angular velocity of the downstream rotor changes due to it operating in the wake of the upstream rotor. This increase in angular velocity is no more than 2.42 % than when the downstream rotor operates independently. Although the increase in angular velocity is minor, to make a fair comparison, the performance coefficients of the downstream rotor operating independently are calculated by creating three polynomial regressions relating the angular velocity and the thrust, power, and torque of the downstream rotor operating independently. These polynomial regressions are evaluated at the angular velocity recorded when the downstream rotor operates simultaneously with the upstream rotor. This is done because, as is shown in Figs. 4.6 to 4.8, there is a slight change in the coefficients based on the angular velocity of the rotor. This analysis requires the least amount of data manipulation; however, when both rotors are operating simultaneously at the highest throttle value tested, the *Re* of the downstream rotor exceeds 135,000. In these cases, the estimated performance coefficients are extrapolated from the previously mentioned three polynomial regressions; however, this extrapolation is no more than 2.42 % more than the highest data points collected when the downstream rotor operates independently. The sum squared error (SSE), coefficient of determination (R^2), and the root mean squared error (RMSE) of each polynomial regression used in this analysis are shown in Section A.1. Only the downstream rotor is of interest because the vertical separation between the rotors is always large enough so that the downstream rotor does not impact the upstream rotor. The results of this analysis are shown in Figs. 5.2 to 5.5 for the counter-rotating spin direction and the results of the co-rotating spin direction can be found in Chapter A of the Appendix.

The overlap interference factor performance metric

Although the performance coefficients show a clear relationship between the reduction in performance of the downstream rotor as a function of the relative position between the downstream and upstream rotor, it does not provide a clear understanding of how the rotor-rotor interactions reduce the functionality (i.e., the amount of thrust generated) of the tan-

dem rotor system. Also, using the performance coefficients as metrics does not allow the thrust stand results to be compared to the momentum theory derived results. A metric that can provide this information is the overlap interference factor, κ_{ov}, as calculated in Eq. (5.1). Note, the same principle of the overlap interference described in Eq. (2.11) is used when defining it as shown in Eq. (5.1). This analysis aims to estimate the performance impact of the rotor-rotor interactions on the tandem rotor system while it operates as if it would on a multirotor vehicle in hover, meaning when the system is torque balanced. As previously mentioned, during the experiments, the tandem rotor system is not torque balanced; therefore, the angular velocity of the downstream rotor required to create a torque balanced system is found mathematically. This is done by using the thrust stand data and the calculated thrust, torque, and power coefficients of the downstream rotor while operating in the wake of the upstream rotor.

The process used to estimate the performance of the torque balanced tandem rotor configurations is shown in Fig. 5.1. In Fig. 5.1, the subscripts U and D denote that the value corresponds to either the upstream or downstream rotor. The superscripts I and S indicate if the value is for the rotor operating independently or simultaneously. Function blocks that do not have a function symbol (i.e., $C_Q(\Omega, T)$) indicate that a known equation is used where the inputs are given and the variable outside the brackets is calculated. Function blocks that do have the function symbol indicate that a polynomial regression is created to relate the two variables of interest. For example, $f^I_{DP}(T)$ indicates that a polynomial regression relating the thrust generation and power consumption for the downstream rotor operating independently is used, and a thrust value is the input into this regression which will provide an estimate of the power consumption at that thrust value. This estimation method is based on two assumptions. The first assumption is that the thrust coefficient of a downstream rotor of a tandem-rotor system is mainly a function of the relative position between the two rotors. The second assumption is that the power coefficient would also be constant as it relates to the angular velocity of the rotor if mechanical power is used in the

calculation of the coefficient; however, since electrical power is measured, losses due to the lengths of the wires between the power source, ESC, and motor, as well as the devices themselves, must be accounted for. This can be seen by the slight change in the power coefficient as a function of the angular velocity of the downstream rotor shown in Fig. 4.7. To account for these losses, the coefficient of power of the downstream rotor operating in the wake of the upstream rotor must be estimated as a function of the *Re* of the upstream rotor, the angular velocity of the downstream rotor itself, and the relative position between the rotors.

$$k_{ov} = \frac{P_{U,simu} + P_{D,simu}}{P_{U,iso} + P_{D,iso}} \tag{5.1}$$

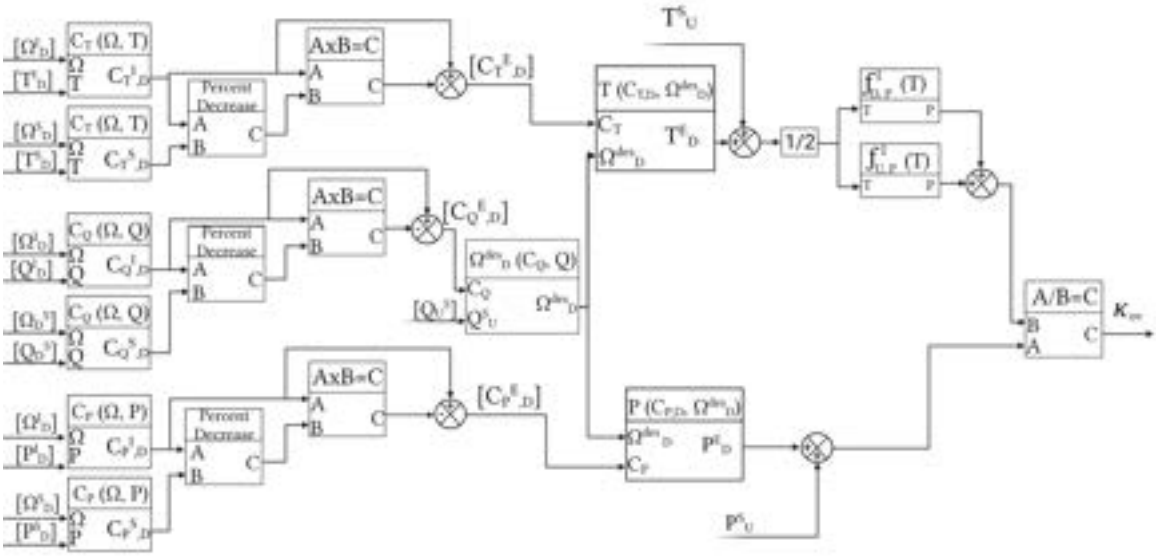

Figure 5.1: Block diagram describing how the overlap interference factor is calculated for each constrained rotor configuration where the system is torque balanced but not producing a specified thrust (*Case 1*).

The overlap interference factor is used in two ways when analyzing the constrained rotor configurations, *Case 1* and *Case 2*. For *Case 1*, the collective thrust of each config-

uration is not the same; however, the collective thrust between an individual tandem rotor configuration and the thrust of the two isolated rotors whose power consumption is used in the denominator of the overlap interference factor is the same. For *Case 2*, the overlap interference factor is calculated for a mathematically torque balanced system, and each rotor configuration is mathematically generating the same collective thrust. The configurations are analyzed using both cases because they both involve different amounts of data processing, thus different amounts of estimation and possible error. Setting each upstream rotor at a *Re* number that is tested in the thrust stand experiments as is done in *Case 1* allows for the effects of the downstream rotor operating in the wake to be calculated directly from the unprocessed data of the thrust stand experiments. Whereas in *Case 2*, the angular velocity of the upstream rotor is allowed to change so that the configuration can produce a specified amount of thrust while remaining torque balanced. In *Case 2*, the effects of the downstream rotor operating in the wake of the upstream rotor have to be estimated using a polynomial regression relating the angular velocity of the upstream rotor and the percent decrease in the thrust, power, and torque coefficients between the downstream rotor operating simultaneously with the upstream rotor and independently. Of course, this estimation is only as accurate as the polynomial regressions that describe the relationships. In both cases, rotor configurations with an overlap interference factor equal to unity indicate that the configuration consumes the same power as two isolated rotors producing an equivalent amount of thrust; thus, the rotors do not experience significant performance impacts due to wake interactions. For the co-rotating spin direction, the values used to calculate the overlap interference factor are for a system where both rotors produce the same torque.

The Figure of Merit performance metric

The last metric used to analyze the performance of each configuration is the Figure of Merit (FM), as shown in Eq. (5.2). The FM is a commonly used rotor efficiency metric and is essentially the ratio of the ideal power required to hover as calculated using the simple

momentum theory to the actual power required to hover. There is one important caveat to using the FM, which is that it can only be used when the rotors being compared are operating at roughly the same disk loading, the ratio of thrust to rotor disk area, (T/A). If using the FM to compare coaxial or tandem rotor systems, the disk loading of the entire system must be equal for each system being compared, even if the individual rotors of the system have different disk loading values. This is because a higher disk loading can lead to the calculation of a misleadingly high FM, which is further explained in [22, 68]. However, since fixed pitch propellers are used in these experiments, and the thrust and power coefficients are generally constant, the FM of the downstream rotor is essentially a function of the rotor configuration.

$$FM = \frac{C_T^{3/2}}{\sqrt{2}C_P} \tag{5.2}$$

5.2.2 Results and Discussion

The thrust, torque, power consumption, and angular velocity data from the three identical experiments completed for both counter and co-rotating spin directions of each rotor configuration listed in Table 4.5 are averaged; this unprocessed data can be accessed using the link in the footnotes[1].

Analysis using Performance Coefficients

Figures 5.2 to 5.5 depict the percent decrease in the thrust, power, C_T/C_P, and torque coefficient of the downstream rotor operating simultaneously with the upstream rotor in the counter-rotating spin direction relative to the downstream rotor operating independently in the same configuration (i.e., at the same position on the thrust stand). Each trend shown in Figs. 5.2 to 5.5 corresponds with an angular velocity at which the upstream rotor is operating at. Note that the angular velocity of the downstream rotor is also increased as the

[1] https://www.dropbox.com/sh/y9o0g327eyyy6u2/AADqSNEGEOzYyfIReEIX5hEDa?dl=0

angular velocity of the upstream rotor increases. The same results but for the co-rotating spin direction can be seen in Section A.2 of the Appendix.

As shown in Fig. 5.2, the percent decrease in the thrust coefficient decreases towards zero as the space between the two rotors increases, meaning at configuration 4.5 the rotors operate as if they are isolated. This result is expected and related to the geometry of the wake created by the upstream rotor. Since the vertical and horizontal separations are constrained by Eq. (1.1), the results do not suggest which parameter drives the performance of the thrust coefficient. However, it should be noted that the ratio of the horizontal separation between the rotors and the propeller diameter at configuration 4.5 is 1.05, meaning that there is no overlap between the rotors. This result corresponds with the momentum theory analysis for both cases of a tandem-rotor system, one with virtually no vertical separation between the rotors and a tandem rotor system with significant vertical separation between the rotors. The rate at which the percent decrease in the thrust coefficient changes varies between the different rotor configurations. This rate of change will play an important role when determining the optimal configuration of the Tetrahedron Dodecacopter. The results shown in Fig. 5.2 also seem to suggest that as the angular velocity of the upstream rotor increases, the percent decrease in the thrust coefficient increases; however, the difference in the values is nearly negligible.

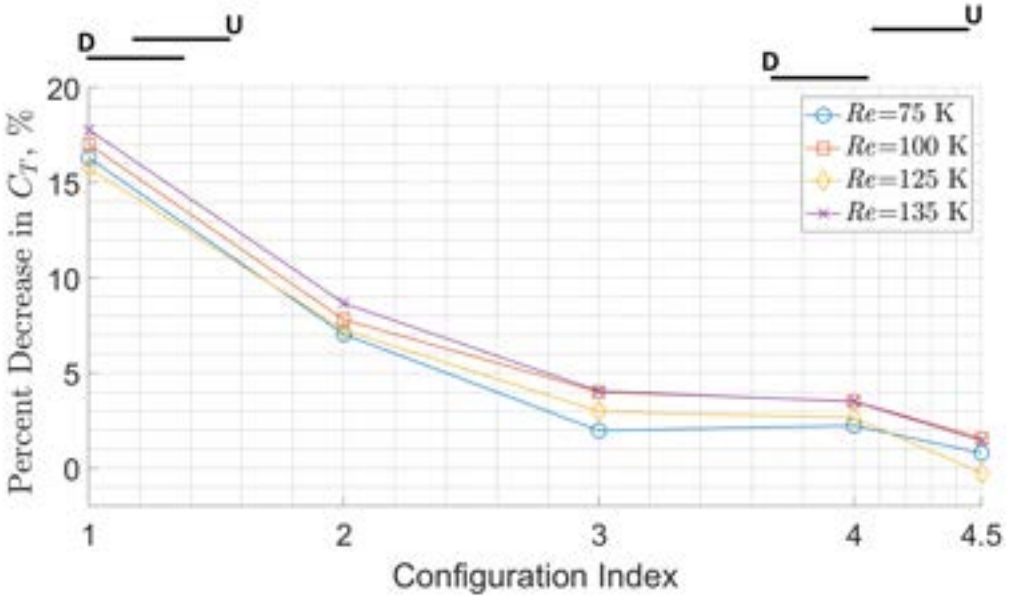

Figure 5.2: The percent difference in the thrust coefficient of the downstream rotor operating independently and simultaneously in the counter-rotating spin direction.

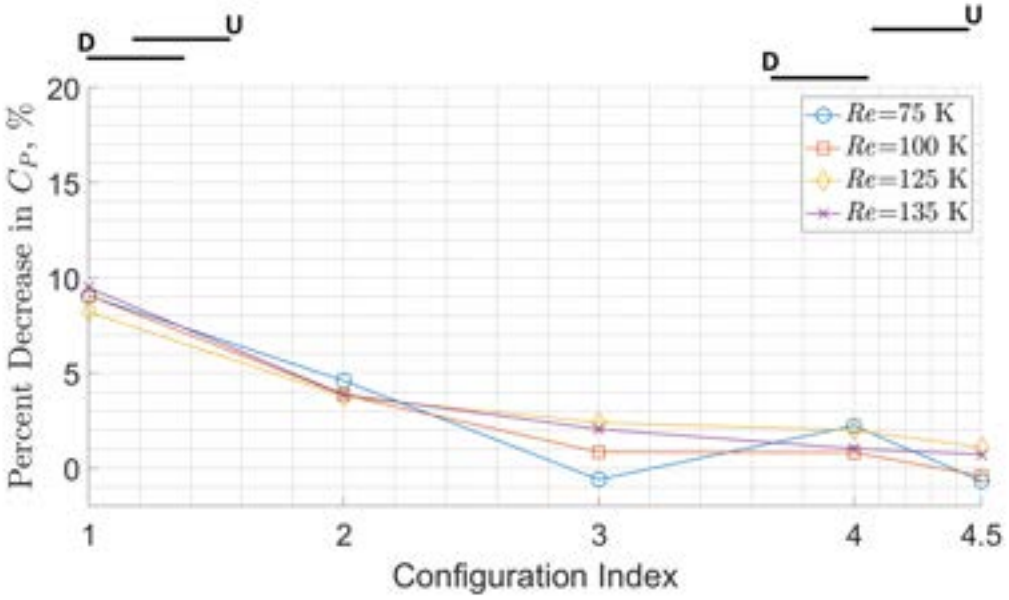

Figure 5.3: The percent difference in the power coefficient of the downstream rotor operating independently and simultaneously in the counter-rotating spin direction.

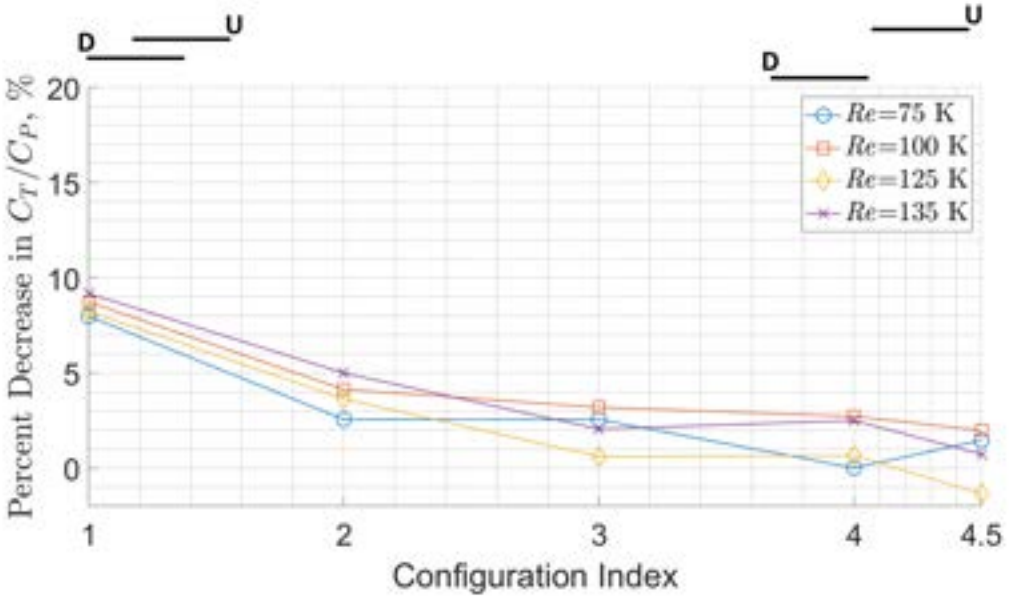

Figure 5.4: The percent difference in the ratio of the thrust and power coefficient of the downstream rotor operating independently and simultaneously in the counter-rotating spin direction.

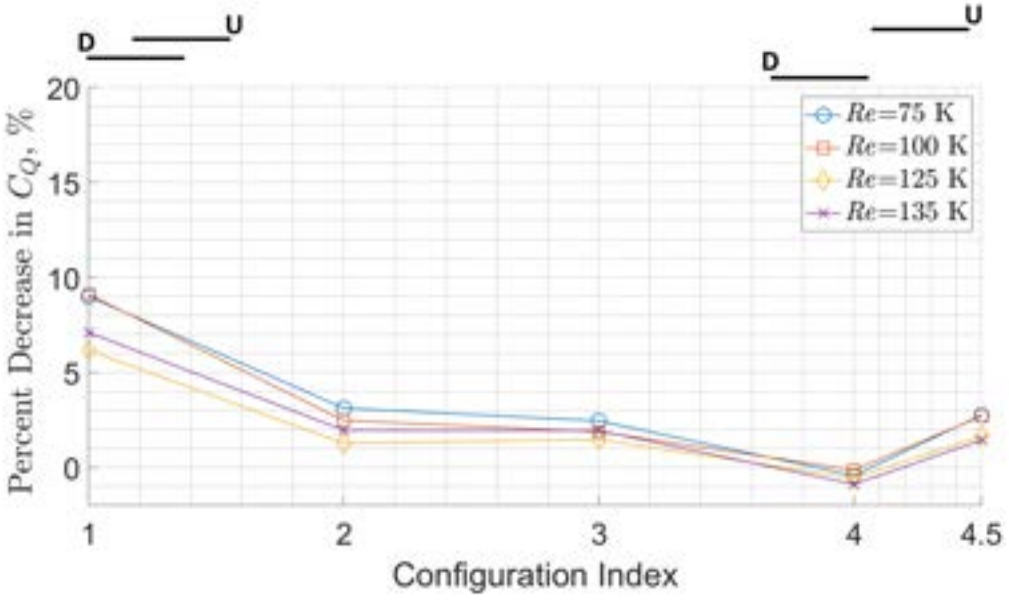

Figure 5.5: The percent difference in the ratio of the thrust and power coefficient of the downstream rotor operating independently and simultaneously in the counter-rotating spin direction.

The percent decrease of the power coefficient, C_T/C_P and the torque coefficient, shown

in Figs. 5.3 to 5.5 respectively, all show that as the downstream rotor moves further away from the upstream rotor, it begins to perform much more like it is operating independently, which is expected. However, for all of these plots, the most drastic improvement in performance is the change from configuration 1 to configuration 2. As the separation between the rotors changes from configuration 3 to 4.5, the percent decrease in the coefficients is relatively small. Although the optimal constrained tetrahedron rotor configuration is obviously the configuration that has the furthest separation between the rotors, configuration 4.5, this may not mean the optimal design of the Tetrahedron Dodecacopter has this rotor separation. This is because as the separation between the rotors increase, so does the weight of the vehicle, thus raising the amount of thrust needed to hover along with the power required to hover. This will be further investigated later in this thesis. The coefficients of the co-rotating configurations follow the same trends.

Analysis using Overlap Interference Factor: Case 1

Figures 5.6 to 5.9 show the results of analyzing each configuration using the overlap interference factor in the manner described as *Case 1* in Section 5.2.1. Figures 5.6 and 5.7 shows the results for the counter and co-rotating spin directions when the upstream rotor operates at a rotor *Re* of 135,000. Figures 5.8 and 5.9 shows the results for the counter and co-rotating spin direction when the upstream rotor operates at a *Re* of $75,000$. Since each rotor configuration and spin direction is tested three times, the results of this analysis are shown as box and whisker plots that allow the reader to see the variation caused by rotor-rotor interaction generated from the downstream rotor operating in the wake of the upstream rotor. The results of this analysis when the upstream rotor operates at a rotor *Re* of 125,000 and 100,000 can be seen in Section A.3 of the Appendix.

The results of this analysis show that at all *Re* tested, the overlap interference factor decreases towards $k_{ov} = 1$ as the configuration number, and in turn, the vertical and horizontal separation between the rotors increases. These results correspond with the previously pre-

sented results of the coefficients of the downstream rotor. Similar to the percent difference in the coefficients of the downstream rotor, Fig. 5.6 shows that the largest change in performance is from configuration 1 to configuration 2 and that between configuration 3 and configuration 4.5, there is little change. Figure 5.6 also shows that at most, the configuration with the most overlap, configuration 1, requires 12 % more power to create a torque balanced system when compared to the two rotors operating independently. However, as shown in Figs. 5.8 and 5.9, when the rotors operate at an angular velocity corresponding to a *Re* of 75,000 the tandem rotor system requires less power, which may indicate that a rotor operating within the wake of another rotor performs worst as the angular velocity of the rotor generating the wake increases. The configurations operating in the co-rotating spin direction generally show the same trends as those operating in the counter-rotating spin direction. The box and whisker plots also show a maximum variation in the overlap interference factor of roughly 0.11 for the experiments where the upstream rotor operates at a *Re* $>$75,000. The variation increases for the experiments where the *Re* of the rotors equals 75,000, which may be caused by the lack of precision in the PDB's ability to measure low current draw.

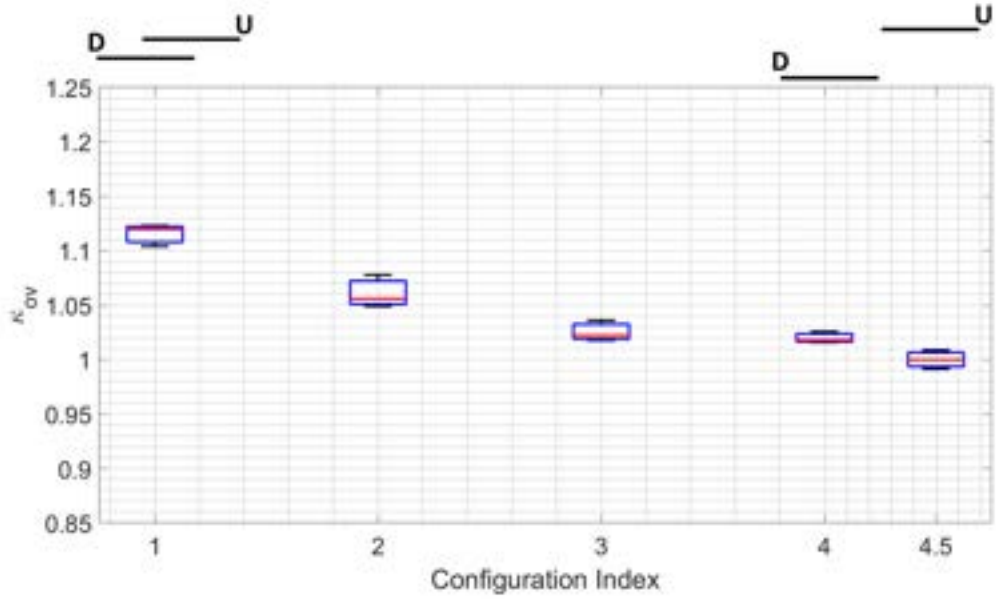

Figure 5.6: A box and whisker plot of the interference factor of mathematically torque balanced configurations while the upstream rotor operates at a *Re* of 135,000 for the counter-rotating spin direction.

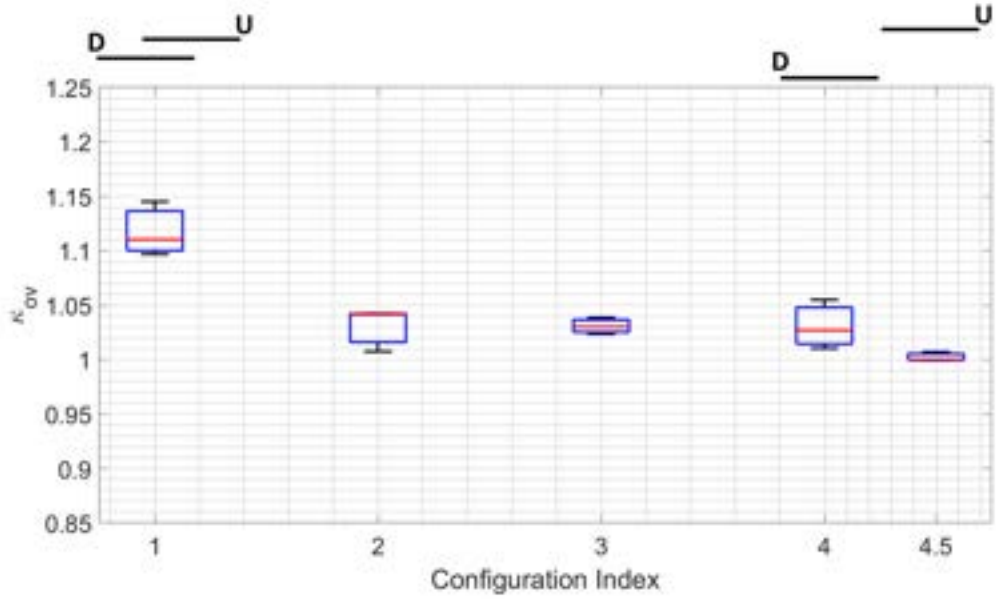

Figure 5.7: A box and whisker plot of the interference factor of mathematically torque balanced configurations while the upstream rotor operates at a *Re* of 135,000 for the co-rotating spin direction.

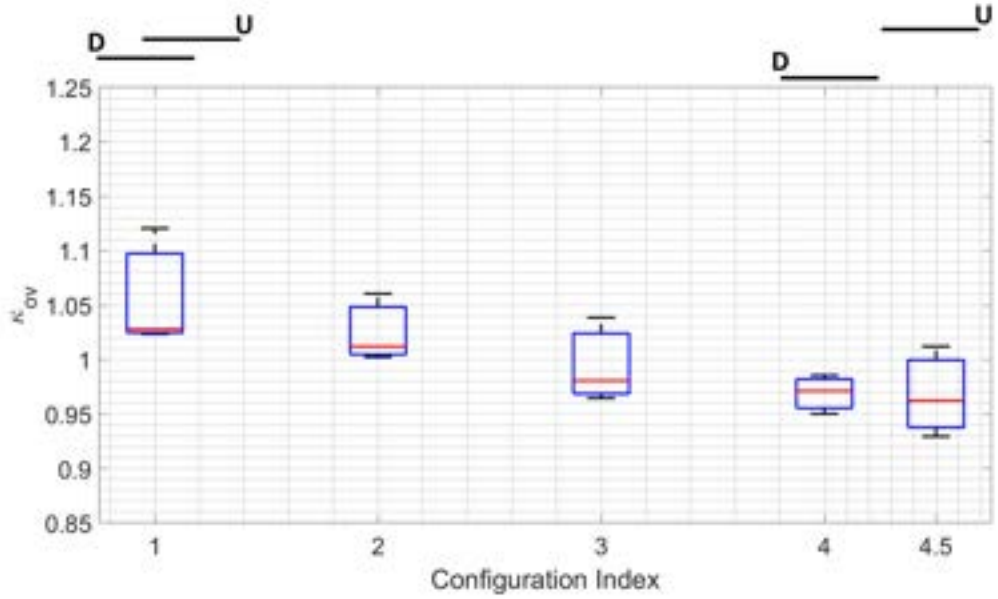

Figure 5.8: A box and whisker plot of the interference factor of mathematically torque balanced configurations while the upstream rotor operates at a *Re* of 75,000 for the counter-rotating spin direction.

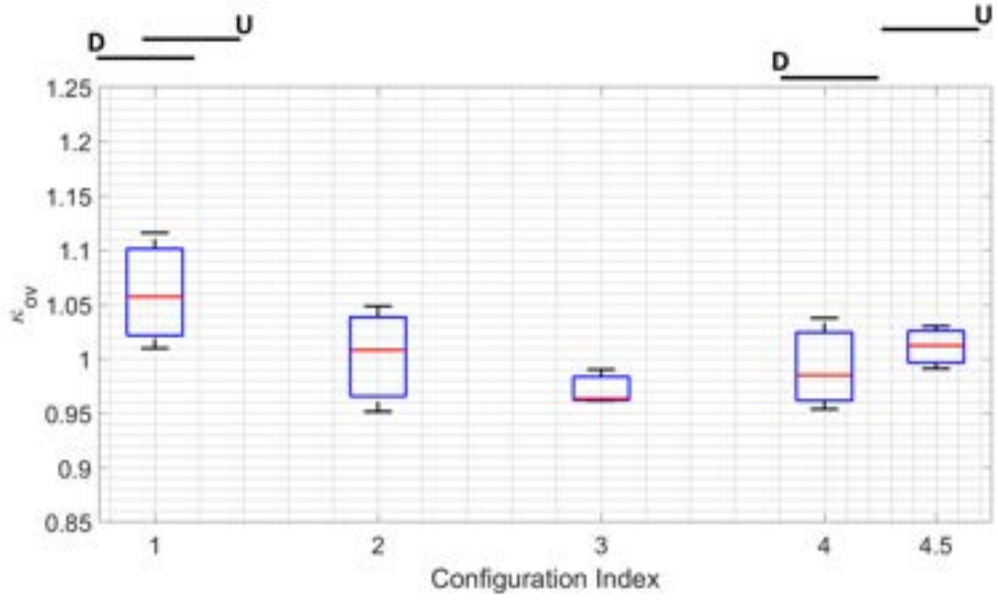

Figure 5.9: A box and whisker plot of the interference factor of mathematically torque balanced configurations while the upstream rotor operates at a *Re* of 75,000 for the co-rotating spin direction.

Figures 5.10 and 5.11 shows the calculated overlap interference factor in comparison

with both cases of the induced overlap interference factor as derived in the momentum theory. As a reminder, *Case 1* of the momentum theory derivation calculates the induced overlap interference factor for two tandem rotors that operate in the same plane while *Case 2* is for two rotors where the downstream rotor operates in the fully developed slipstream of the upstream rotor. From past flow visualization works, it is known that a wake's contraction occurs before $\frac{z}{D} = 0.20$, with the majority of the contraction happening within $\frac{z}{D} = 0.125$ of the rotor [69]. The trends between the thrust stand data and the induced power overlap interference factor derived by momentum theory seem to correlate. It should be noted that this analysis does not show the vertical separation between the rotors at the different configurations, yet the trends still are relatively similar. Although the trends between both cases and the thrust stand data are similar, the thrust stand data matches the *Case 1* derivation of the momentum theory more closely than *Case 2*, even though the vertical separation between the rotors at these configurations are high enough for the downstream rotor to be considered as operating in the fully developed wake of the upstream rotor. This may be because, in the experiments, electrical power is measured and not just mechanical power. For both spin directions, the results show that when both rotors are operating at lower angular velocities, the overlap interference factor is less than it is at higher angular velocities. Similar results can be found in other studies that produced empirical data of tandem rotor configurations [70, 13]. Each author states different reasons behind this phenomenon. In [70], the author states this may be due to swirl recovery, which is most noticeable at lower values of disc loading. However, in the presented results, the lower overlap interference factor is seen even when $\frac{x}{D} > 1.0$, which indicates there is still some form of positive aerodynamic effect when the rotors are not overlapping yet closely spaced. In [13], the author attributes this effect to less interactions between the rotors' wakes since the tip vortices and vortex sheets of the wake are convected down at a slower rate than they are when the rotors are operating at a higher angular velocity. As previously mentioned, the accuracy of the current measurements at lower angular velocities is less than the accuracy of measur-

ing higher values of current, which may also be impacting the results shown in Figs. 5.10 and 5.11.

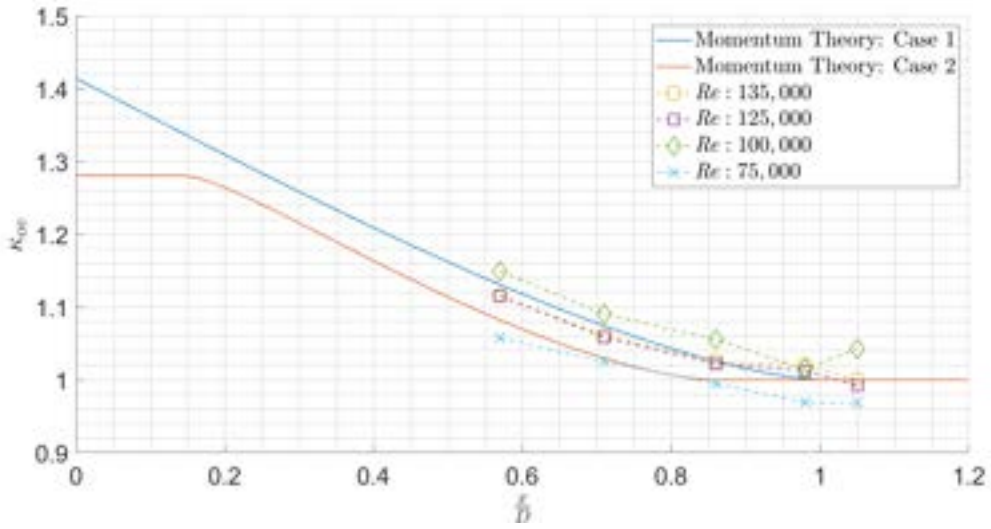

Figure 5.10: A comparison of the momentum theory derived induced overlap interference factor to the calculated overlap interference factor of the constrained rotor configurations operating in the counter-rotating spin direction.

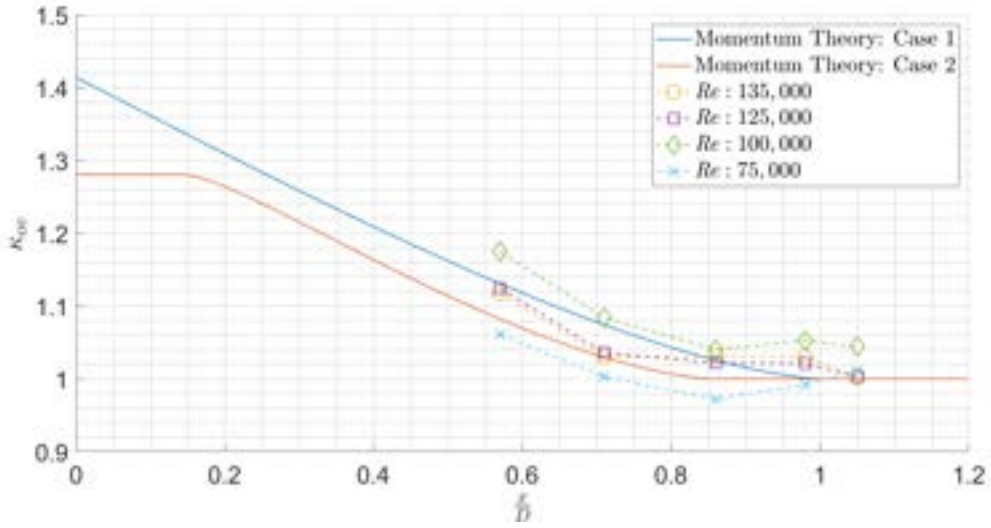

Figure 5.11: A comparison of the momentum theory derived induced overlap interference factor to the calculated overlap interference factor of the constrained rotor configurations operating in the co-rotating spin direction.

Analysis using Overlap Interference Factor: Case 2

Figures 5.12 and 5.13 show the results of analyzing the thrust stand data using the overlap interference factor in the manner discussed in Section 5.2.1 as *Case 2*. For both the counter-rotating and co-rotating spin directions, the collective thrust value used to calculate the overlap interference factor are such that the collective thrust of the configurations is 29 N. This value is selected because it is the maximum collective thrust that could be used without extrapolating the thrust stand data. At any value higher than 29 N, the estimated angular velocity of either rotor is higher than the angular velocity that the rotors were operated at during the thrust stand experiments. Fig. 5.14 shows the comparison between the momentum theory derived induced power overlap interference factor and the overlap interference factor of the constrained rotor configurations when they are torque balanced and producing a thrust of 29 N.

The results shown in Figs. 5.12 and 5.13 do not drastically differ from the overlap interference factor calculated in Section 5.2.2 when the upstream rotor operates at a *Re* of 135,000 . This indicates that there is not much difference between the two methods of calculating the overlap interference factor. Comparing these results to the results of the momentum theory, as seen in Fig. 5.14, shows that the trends between the two results are similar. However, once again, the thrust stand results follow *Case 1* of the momentum theory analysis more closely than Case 2.

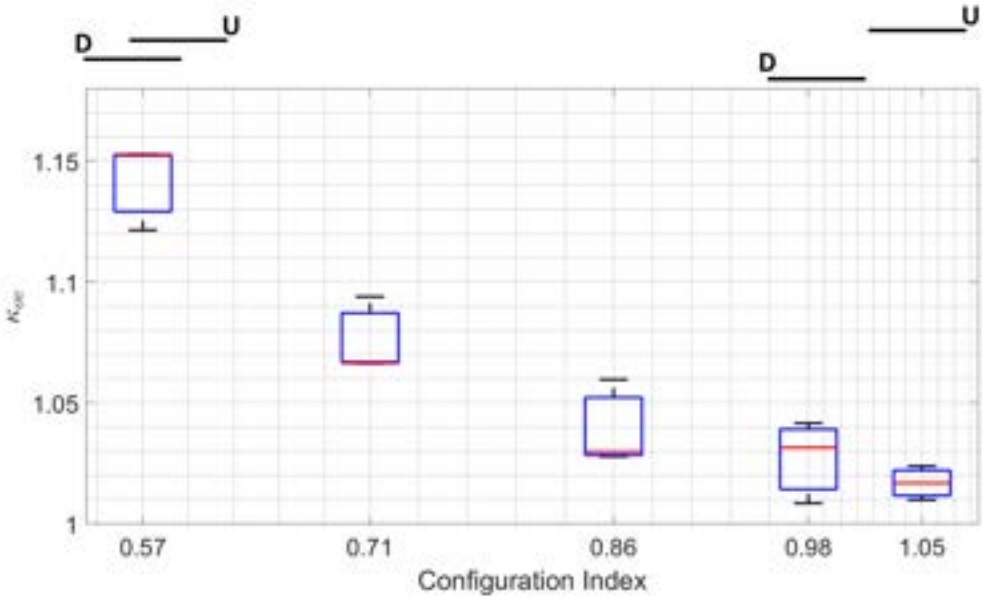

Figure 5.12: A box and whisker plot of the overlap interference factor of the constrained rotor configurations operating in the counter-rotating spin direction while each rotor generates equivalent torque and while each configuration produces 29 N of thrust.

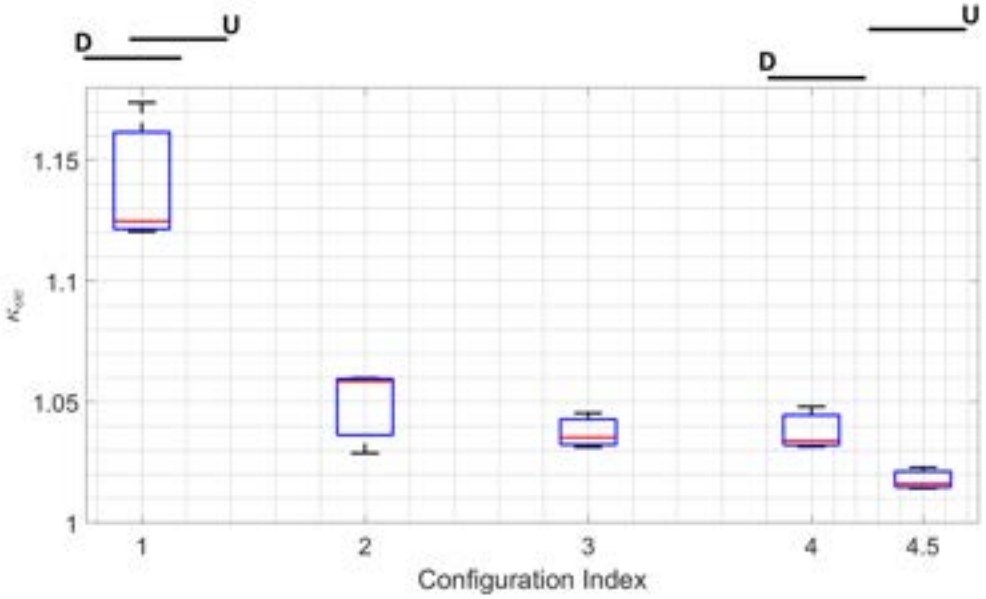

Figure 5.13: A box and whisker plot of the overlap interference factor of the constrained rotor configurations operating in the co-rotating spin direction while each rotor generates equivalent torque and while each configuration produces 29 N of thrust.

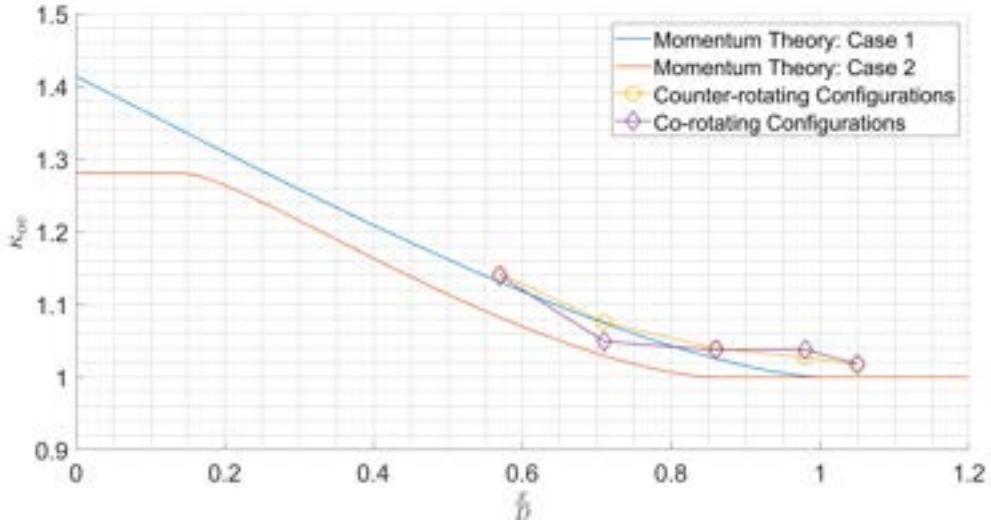

Figure 5.14: A comparison between the induced power overlap interference factor and the overlap interference factor calculated while each configuration is mathematically torque balanced and generating a collective thrust of 29 N. Note, the rotors of the co-rotating configurations generate equal torque.

Analysis using the Figure of Merit

To analyze the configurations using the FM, the FM of each of the three experiments for each configuration and spin direction are averaged to produce one FM for each spin direction and rotor configuration. Figure 5.15 shows the results of analyzing the efficiency of the upstream rotor while it operates simultaneously with the downstream rotor. These results show that the downstream rotor does not effect the performance of the upstream rotor. Figure 5.16 shows the FM of the downstream rotor operating simultaneously with both rotors operating roughly at *Re* of 135,000 and the FM of the downstream rotor operating independently. This result shows an approximately 20 % difference in the FM of the downstream rotor in configuration 1 than in the rotor operating independently at the same position on the thrust stand. This analysis clearly shows that at configuration 4.5 there are no significant rotor-rotor wake interactions. The change in the FM for each rotor configuration at the different *Re* tested can be seen in Figs. 5.17 and 5.18. Similarities in the results shown in Figs. 5.17 and 5.18 and the percent difference in the thrust coefficient as a func-

tion of the rotor configuration, Fig. 5.2, are quite apparent, which shows that the rotor-rotor interactions change the thrust coefficient far more than the power coefficient. According to Fig. 5.17, the change in the FM of the downstream rotor does not vary significantly with a change in *Re*. However, for the co-rotating spin direction, Fig. 5.18, the variation in the decrease in FM of the downstream rotor is slightly higher between the different *Re* tested. This may be because vibratory effects from the co-rotating rotor configurations are higher than that of the counter-rotating configurations.

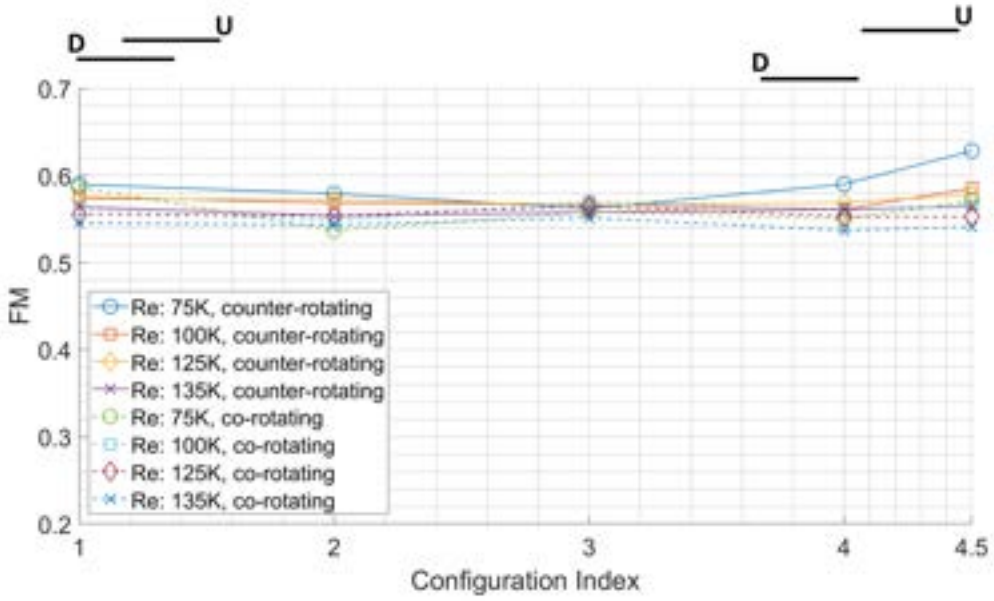

Figure 5.15: The Figure of Merit of the upstream rotor operating at the *Re* specified simultaneously with the downstream rotor.

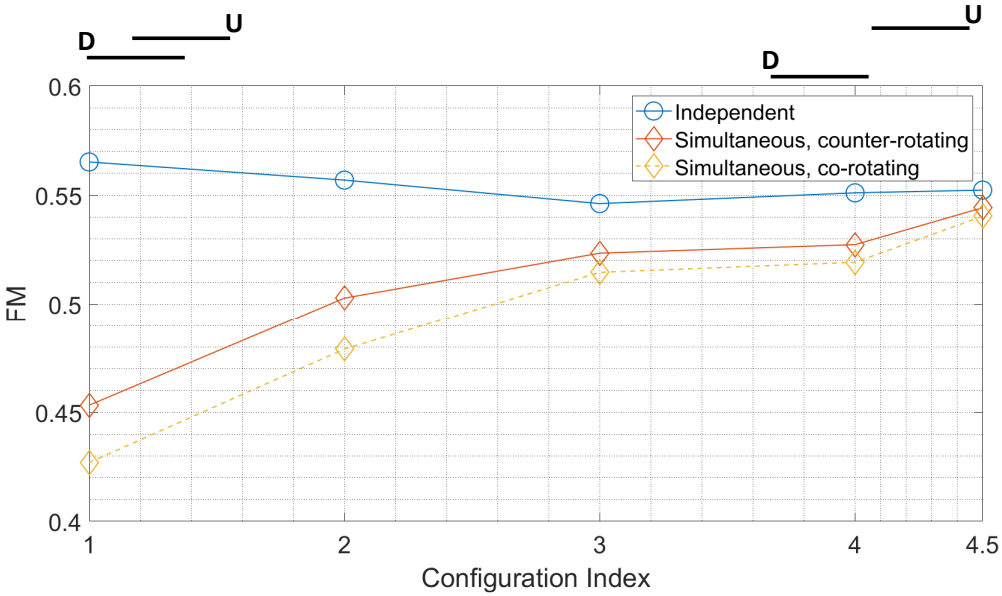

Figure 5.16: The Figure of Merit of the downstream rotor operating in the wake of the upstream rotor that has a *Re* of $135,000$.

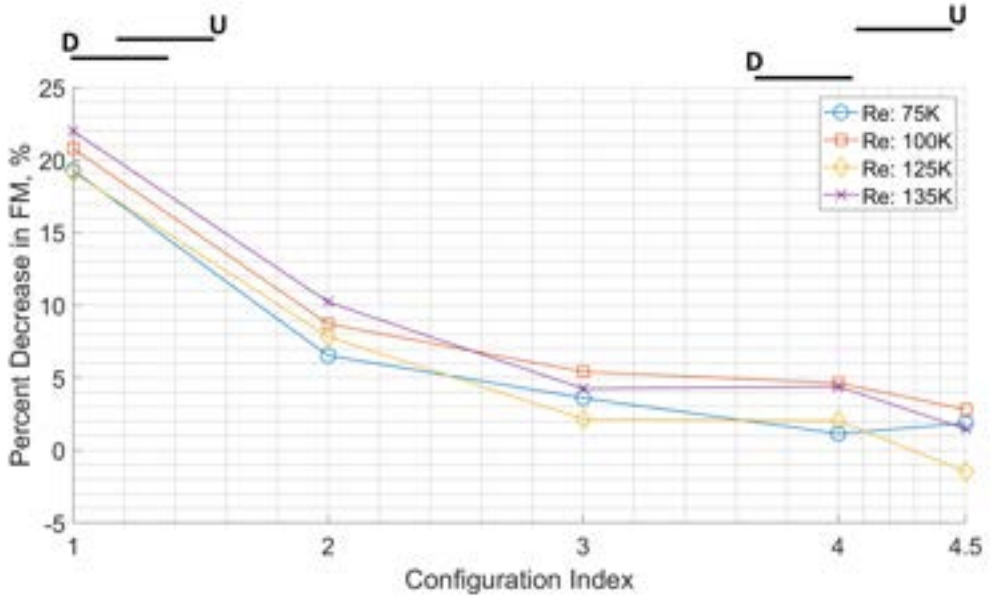

Figure 5.17: The percent decrease in the FM of the downstream rotor operating in the wake of the upstream rotor at the specified *Re* as a function of the configuration index for the counter-rotating spin direction.

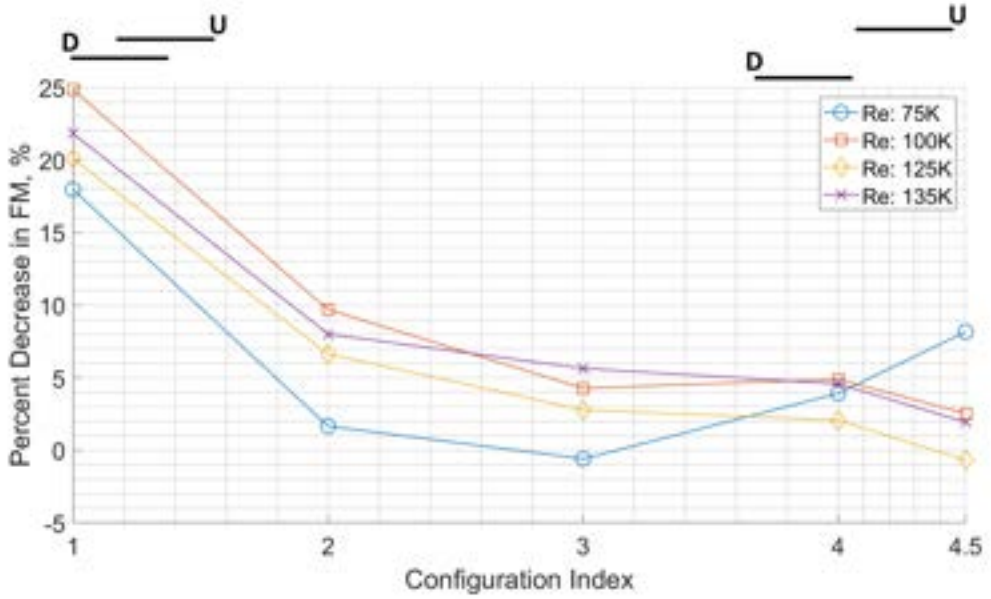

Figure 5.18: The percent decrease in the FM of the downstream rotor operating in the wake of the upstream rotor at the specified *Re* as a function of the configuration index for the co-rotating spin direction.

Overall these results support the estimates derived by the momentum theory; however, other studies have shown that at a horizontal separation ratio of $\frac{x}{D} = 1.03$, the tandem rotor system begins to perform better than two rotors operating in an isolated manner [71, 72]. The results of the constrained tandem rotor configurations do not indicate that the rotors receive any performance benefits from the rotor-rotor or wake interactions. However, it should be noted that these previous studies were conducted using much larger rotors operating at higher *Re* and the vertical separation of the constrained rotor configurations are far larger than those in [71, 72] with respect to the diameter of the rotors used. Overall, all of these results show that at configuration 4.5 there is little to no rotor-rotor impact that changes the performance of the downstream rotor. Without accounting for the vehicle's weight, these results suggest that the best rotor configuration is one where the rotors have no overlap. As previously mentioned, the optimal rotor configuration does not inherently correspond to the optimal tetrahedron rotor configuration because the weight of the vehicle must be taken into account. The next section will estimate the optimal design of the Tetrahedron Dodecacopter by using the results of the constrained tandem rotor experiments and accounting for the weight of the vehicle.

5.2.3 Optimization Problem and Solution

To achieve Objective 4 of this thesis, the optimization of the Tetrahedron Dodecacopter, two aspects of the Tetrahedron Dodecacopter are taken into account, the efficiency of the vehicle at hover (i.e., the power required for hover) and the rigidity of the vehicle. The efficiency of the vehicle accounts for the weight of the vehicle and any changes in the performance of the vehicle's rotors caused by rotor-rotor interactions. To simplify this optimization problem, the assumption is made that the most rigid dodecahedron is a regular dodecahedron, which consists of 12 regular pentagonal faces. Mathematically, this optimization problem can be written as Eq. (5.3), where $f(\epsilon(x, z, \Omega_U, \Omega_D), w(x, z))$ is a function describing the power consumption at hover of the Tetrahedron Dodecacopter as a function of the weight

of the vehicle, $w(x, z)$, and the vehicle's hover efficiency, $\epsilon(x, z, \Omega_U, \Omega_D)$, which is a function of the separation between the rotors. It should be noted that the weight of the vehicle dictates the angular velocity that the rotors must operate at, which influences the magnitude of performance degradation due to the rotor-rotor interactions. The first equality constraint of the optimization equation is derived from the constraint on the airframe of the Dodecacopter modules, which places a constraint on the relative position between the upstream rotor and three downstream rotors of the vehicle. The second equality constraint of the optimization problem ensures that the vehicle is torque balanced, meaning there is no yaw moment and that the vehicle is at a steady hover.

$$\begin{aligned} \min_{x,z} \quad & f(\epsilon(x, z, \Omega_U, \Omega_D), w(x, z)) \\ \text{s.t.} \quad & z - \sqrt{2}x = 0 \\ & \dot{\psi}(\Omega_D, \Omega_U) = 0 \\ & \dot{\theta}(\Omega_D) = 0 \\ & \dot{\phi}(\Omega_D) = 0 \\ & x_l \leq x \leq x_u \\ & z_l \leq z \leq z_u \end{aligned} \tag{5.3}$$

Given that the airframe of each module is in the shape of a regular dodecachedron, the size of the Dodecacopter modules are linearly related to the weight of the vehicle. Observing the design of the Dodecacopter modules, it can be seen that the two elements of the module that change with its overall size are the exterior carbon fiber rods creating the airframe of the module and the three interior larger carbon fiber rods that attach the motor and avionics to the airframe of the module as shown in Fig. 5.19.

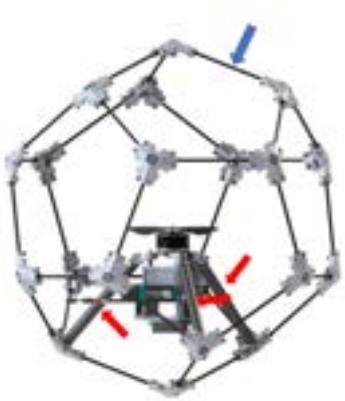

Figure 5.19: The carbon fiber rods creating the airframe (identified by the blue arrow) and the carbon fiber rods attaching the motor and avionics to the airframe (identified by the red arrows

A function relating the weight of the Dodecacopter module with the vertical and horizontal separation between the upstream rotor and the three downstream rotors of the Dodecacopter is created by manipulating the equations describing the size of a regular dodecahedron. The relationship between the length of the airframe's carbon fiber rods, represented by the variable a in Eqs. (5.4) and (5.5), and the vehicle's rotor configuration is derived from the inscribed radius equation of a dodecahedron, Eq. (5.4). The inscribed radius equation describes the radius of an inscribed sphere that is tangent to all of the faces of the regular dodecahedron. Manipulating Eq. (5.4) so that the edge length is a function of the vertical and horizontal separation of the rotors generates Eq. (5.5). To find the distance from the center of the dodecahedron to the dodecahedron's vertices, where the larger carbon fiber tubes attach the motor to the airframe, the edge length found in Eq. (5.5) can be inserted into Eq. (5.6). Equation (5.6) is the circumscribed radius equation that describes the radius of a sphere that intersects the regular dodecahedron at all of its vertices. Combining Eqs. (5.5) and (5.6), along with the weight per unit length of the carbon fiber tubes of the airframe and those attaching the motor to the airframe, represented by c_F and c_A, a weight equation relating the separation between the rotors and the weight of the vehicle can be created as shown in Eq. (5.7). The base weight of the Dodecacopter module, meaning the weight of

the components that do not change with the size of the Dodecacopter module, is represented by the variable b, and in practice is roughly 1.40 kg.

$$r_i = a\frac{1}{2}\sqrt{\frac{5}{2} + \frac{11}{10}\sqrt{5}} \tag{5.4}$$

$$a = \frac{\sqrt{x^2 + z^2}}{\sqrt{\frac{5}{2} + \frac{11}{10}\sqrt{5}}} \tag{5.5}$$

$$r_u = a\frac{\sqrt{3}}{4}(1 + \sqrt{5}) \tag{5.6}$$

$$w(x, z) = \frac{\sqrt{x^2 + z^2}}{\sqrt{\frac{5}{2} + \frac{11}{10}\sqrt{5}}} * c_F + \frac{\sqrt{x^2 + z^2}}{\sqrt{\frac{5}{2} + \frac{11}{10}\sqrt{5}}} * \frac{\sqrt{3}}{4}(1 + \sqrt{5}) * c_A + b \tag{5.7}$$

The exact relationship between the power consumption of each Tetrahedron Dodecacopter configuration and the separation of the vehicle's rotors is not known. However, a pseudo-surrogate model, or estimation, of this relationship is created using the thrust stand data. The optimization problem requires that the vehicle is at a steady hover, meaning there is no significant yaw moment. However, during the thrust stand experiments, the tandem-rotor systems are not operated in a manner similar to what the rotors on the Tetrahedron Dodecacopter would need to be operated at in order to not create a net yaw moment. In order to estimate the performance of the downstream rotor, an estimation method similar to what is used to calculate the overlap interference factor in Section 5.2.1 is used. As previously mentioned, for each rotor configuration tested on the thrust stand, the rotors are operated independently and then simultaneously. This allows for the calculation of the percent decrease in the thrust, power, and torque coefficient of the downstream rotor operating within the wake of the upstream rotor versus operating independently. Functions relating the percent decrease in these three coefficients and the relative position and angular velocity of both rotors are created. An example of how these relationships are created is shown

in Fig. 5.20 as a block diagram for the percent decrease in the torque coefficient. The variable $C_{Q\%135}$ represents the percent decrease in the torque coefficient of the downstream rotor when the upstream rotor is operating at a *Re* of 135,000 versus the downstream rotor operating independently.

Several other second-degree polynomials are created so that the pseudo-surrogate model of the objective function can be created. Each of these estimation models is created using the thrust stand data, and the pseudo-surrogate model of the objective function is created from sampling the second-degree polynomials. The full process of creating the pseudo-surrogate model of the objective function is depicted as a block diagram in Fig. 5.21. It should be noted that for all calculations, the data used is sampled from the second-degree polynomials and the pseudo-surrogate models within the bounds of the results of the thrust stand test, meaning that there was no extrapolation of the surrogate models. The superscript E used in Fig. 5.21 denotes that the function is estimating the value of the specified rotor based on the thrust stand data. One obvious downfall to using this method to determine the optimum rotor configuration is that the pseudo-surrogate model of the objective function is only as accurate as the second-degree polynomials describing the relationship of other parameters. The second-degree polynomials used to create the pseudo-surrogate model of the objective function can be seen in Figs. A.4 and A.5.

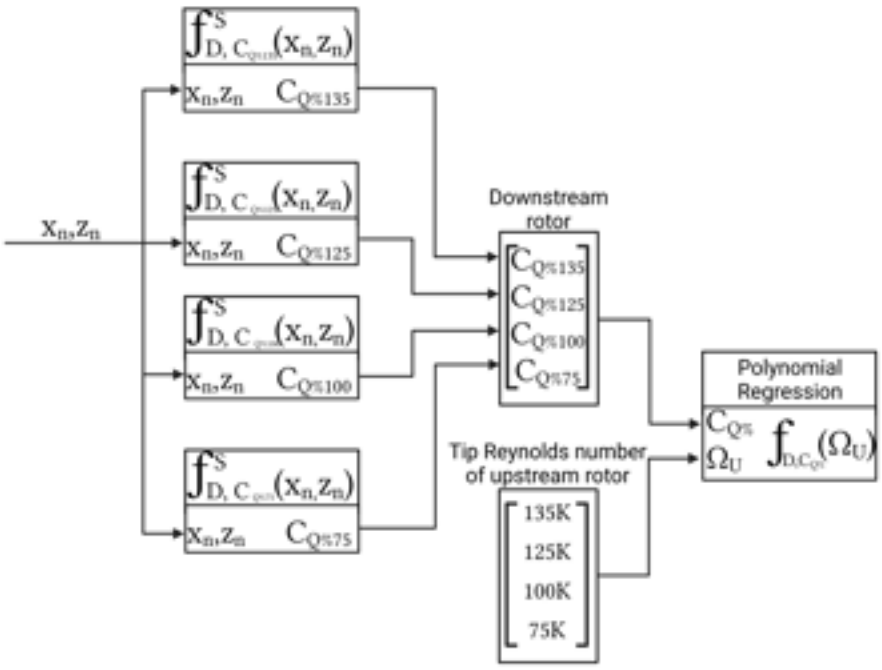

Figure 5.20: A block diagram illustrating how the relationship between the angular velocity of the upstream rotor and the percent decrease in the downstream rotor's torque coefficient is created.

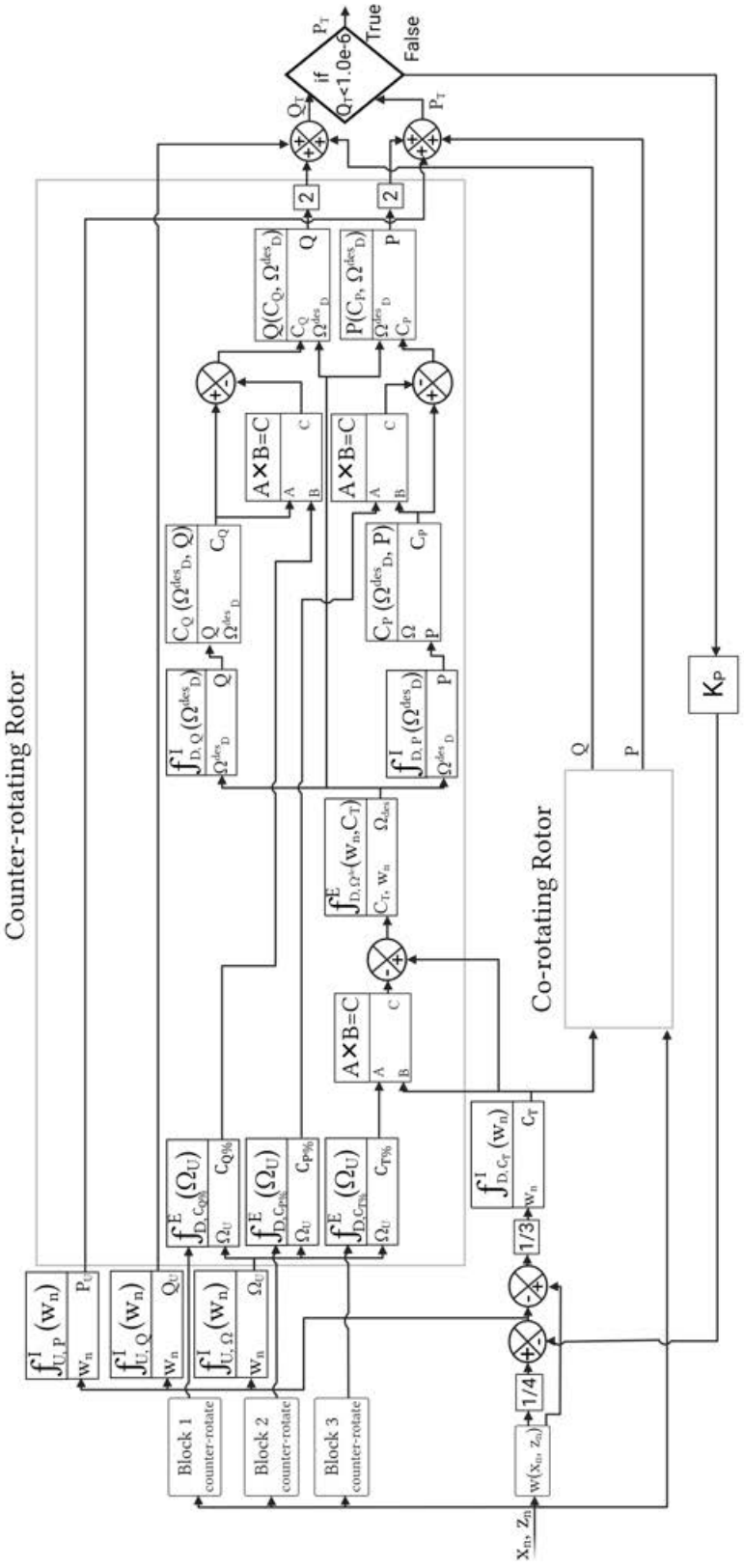

Figure 5.21: A block diagram describing how the power required for each configuration is calculated, thus creating a pseudo-surrogate model of the objective function. (Created with BioRender.com)

Figure 5.22, shows the pseudo-surrogate model of the objective function compared to the power consumption of a traditional quadcopter that has the same weight as the Tetrahedron Dodecacopter in the specified configuration. Minimizing the pseudo-surrogate model indicates that the optimum tetrahedron configuration corresponds to a configuration index of 2.66, which has a vertical and horizontal separation of $\frac{x}{D} = 0.80$ and $\frac{z}{D} = 1.13$. This positioning places the downstream rotor within the wake of the upstream rotor; however, the shape of the objective function indicates that the vehicle's weight becomes the driving factor if the distance between the rotors becomes any greater. Fig. 5.23, shows that the estimated interference factor of the optimum design is 1.06, meaning that the optimum design requires roughly 6% more power for hover compared to a traditional quadcopter with four isolated rotors. It should be noted that when referring to the Tetrahedron Dodecacopter, the overlap interference factor is the ratio of the vehicle's total power required for hover to the total power required for hover for a traditional quadcopter, which is assumed to have four rotors operating in an isolated manner. This result illustrates that although rotor-rotor wake interactions negatively impact the performance of a system, in a practical design, all factors must be accounted for to determine the optimum design. This optimization method can also be used for other vehicle designs that involve non-coplanar, parallel rotors that experience rotor-rotor wake interactions, as long as the relationship between the vehicle's weight and the separation of the rotors is known.

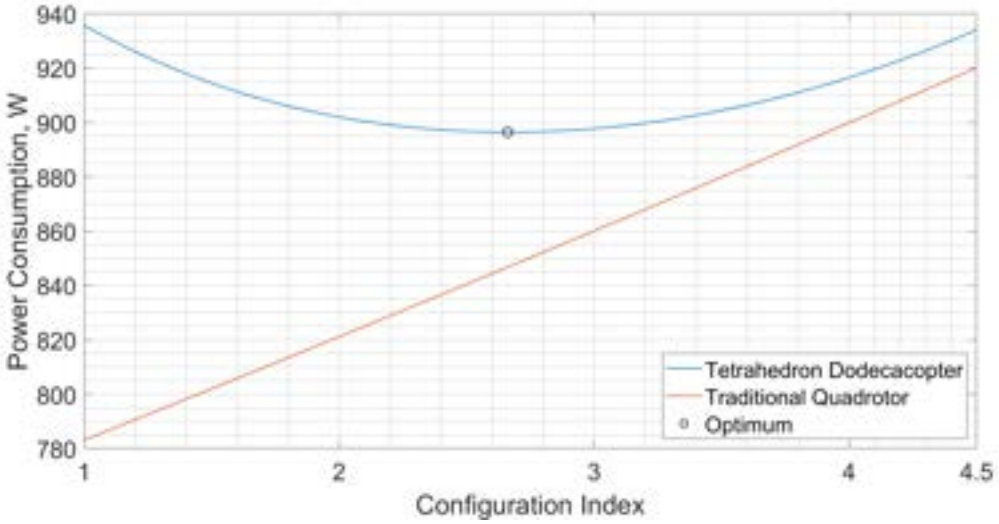

Figure 5.22: The pseudo-surrogate model of the power consumption at hover of the Tetrahedron Dodecacopter along with the power consumption of a traditional quadrotor of the same weight with no rotor-rotor interactions.

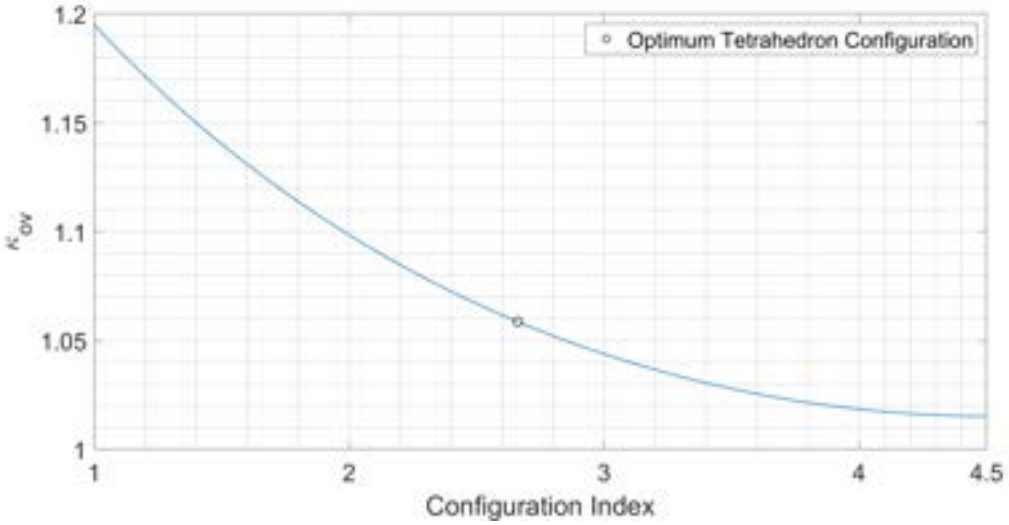

Figure 5.23: The interference factor of each Tetrahedron Dodecacopter configuration. The interference factor of the optimum configuration is indicated by the black circle.

Weight Sensitivity Analysis

An analysis of the effects of the change in the base weight of the vehicle, the change in the weight per unit length of the carbon fiber rods, and the optimum Tetrahedron Dodecacopter configuration is also performed using the presented optimization method. Increasing the

weight per unit length of the carbon fiber rods causes the optimum Tetrahedron Dodecacopter configuration to be smaller in size, thus creating more overlap between the upstream rotor and the three downstream rotors causing more rotor-rotor interactions. The size of the optimum configuration increases if the weight per unit length of the carbon fiber rods decreases, which is expected. However, if the base weight of the Tetrahedron Dodecacopter module increases, the size of the optimum configuration increases, as shown in Fig. 5.24. This result seems counter-intuitive because one may think that as the base weight of the vehicle increases, the driving factor in the optimization problem would become the weight of the vehicle, meaning that the rotor separation of the optimum configuration would decrease as the base weight of the vehicle increases. However, as shown in Fig. 5.24, as the base weight increases by 50 $\%$, the overall separation between the rotors increases by 9.7 $\%$. These results may be caused by the increase in the thrust of the upstream rotor needed for the vehicle to hover at a higher base weight, which decreases the efficiency of the downstream rotor as shown in Fig. 5.4. Figure 5.25 shows that the estimated FM of a downstream rotor of the optimal Tetrahedron Dodecacopter decreases as the base weight increases, while Fig. 5.26 shows the increase in the angular velocity of the upstream rotor as the base weight of the optimal Tetrahedron Dodecacopter increases. This decrease in the efficiency of the downstream rotors drives the optimization technique to increase the distance between the rotors in order to avoid rotor-rotor interactions. This result shows that the relationship between the angular velocity of the upstream rotor and the efficiency of the downstream rotor must be considered when designing a vehicle with overlapping rotors.

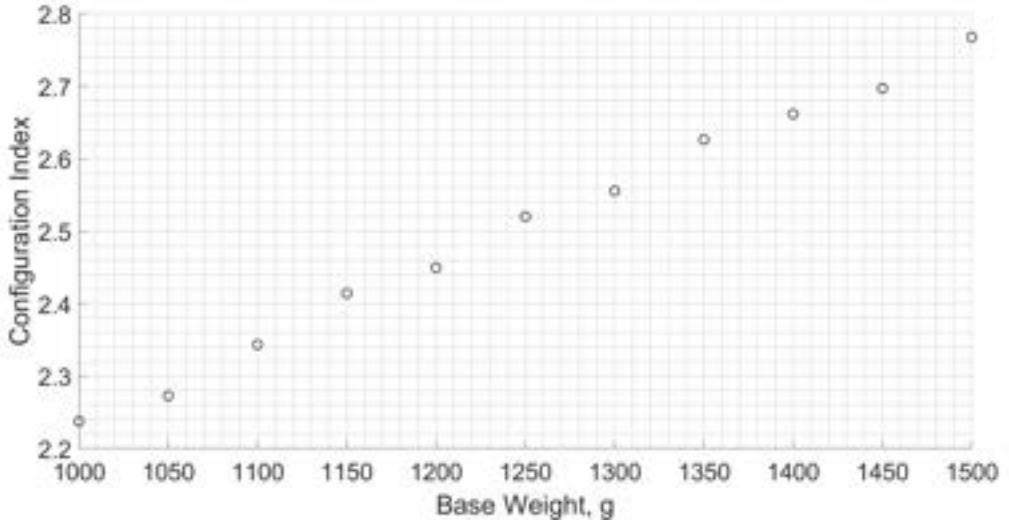

Figure 5.24: The change in the optimal configuration of the Tetrahedron Dodecacopter as a function of the vehicle's base weight.

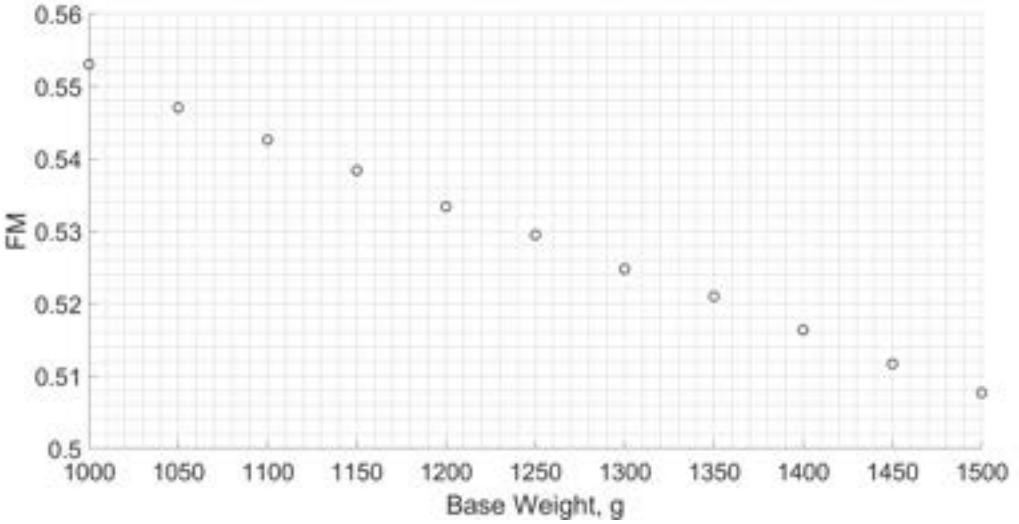

Figure 5.25: The FM of a downstream rotor of the optimal Tetrahedron Dodecacopter designs as the base weight of the designs change.

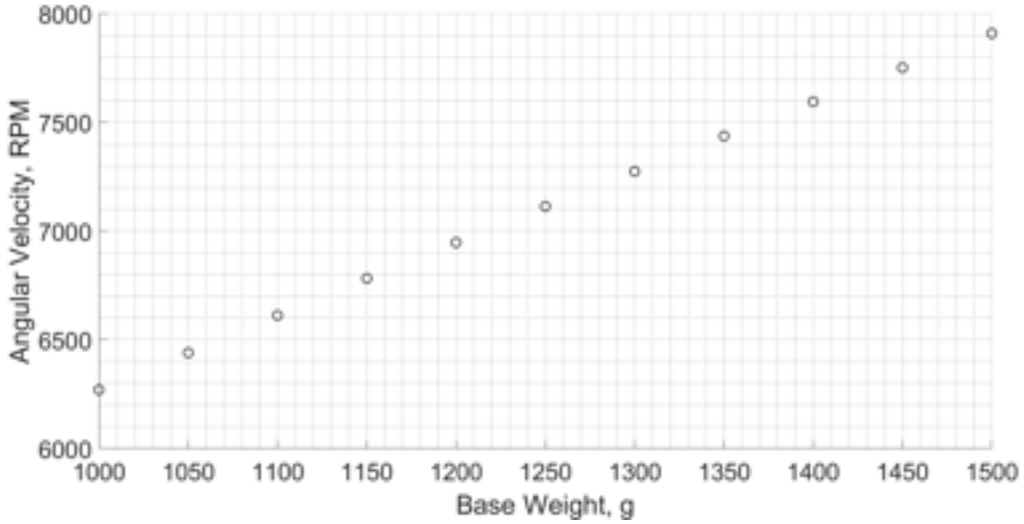

Figure 5.26: The change in the angular velocity of the upstream rotor as a function of the base weight of the optimal Tetrahedron Dodecacopter configuration while in a steady hover.

Momentum Theory Comparison

A comparison between the interference factor of the Tetrahedron Dodecacopter and the interference factor derived for a tandem-rotor system using momentum theory is completed and shown in Fig. 5.27. As a reminder, the interference factor calculated for the Tetrahedron Dodecacopter is the ratio of the estimated total power required to hover for the Tetrahedron Dodecacopter and the estimated total power required for hover for a traditional quadcopter. In contrast, the interference factor calculated using the momentum theory is the ratio of the total power required for a given thrust of a tandem-rotor system and the total power required for two isolated rotors to generate the same amount of thrust.

Figure 5.27 shows that the estimated overlap interference factor of the Tetrahedron Dodecacopter is always higher than both *Case 1* and *Case 2* of the results of the momentum theory derivation. It should be noted that although the x-axis of Fig. 5.27 only shows the horizontal separation between the rotors, the vertical separation between the rotors is also increasing as a function of the horizontal separation, which is in contrast with the vertical separation of both cases of the momentum theory derivation. At the smallest separation

distance of the Tetrahedron Dodecacopter, the difference between the estimated interference factor and the interference of *Case 1* and *Case 2* of the momentum theory derivation is 9.69 % and 5.17 % respectively. The difference between momentum theory derivation of the interference factor and the estimated interference factor at the largest rotor separation is 1.49 %. The difference in the results of the momentum theory and the estimated interference factor is mostly attributed to the goodness of fit of the surrogate models used to estimate the power required for hover for the Tetrahedron Dodecacopter in the different constrained configurations.

Figure 5.28 shows the estimated power consumption of the Tetrahedron Dodecacopter using both cases of the momentum theory and the estimated power consumption of the vehicle using the pseudo-surrogate model. When calculating the power consumption estimated by the momentum theory, the estimated power of the downstream and upstream rotors are found using a polynomial regression relating the thrust generated by an isolated rotor and that rotor's power consumption. Using this relationship, each rotor is set to produce thrust equal to one-quarter of the vehicle's weight. For three of the rotors, the overlap interference factor for both cases of momentum theory is multiplied by the amount of power required to produce the specified amount of thrust, and these three power estimates, as well as the power estimate for one rotor operating completely isolated, are summed. This is done because the thrust stand data shows that the performance of the upstream rotor of all constrained tandem rotor configurations tested is not affected by the downstream rotor. Note that this analysis also takes into account changes in the weight of the vehicle as the rotor configuration changes. However, this analysis is not for a torque balanced system, since it is not possible to estimate the torque of the downstream rotors using the momentum theory. The result shows that according to the momentum theory, the optimum configuration should be the configuration with the closest spaced rotors. However, the pseudo-surrogate model estimates that the optimum configuration balances both the vehicle's weight and the performance impact of the downstream rotors caused by operating in the wake of the

upstream rotor. This difference in the estimated total power consumption is caused by the difference in the rate of change of the estimated interference factor as the separation between the rotors of the Tetrahedron Dodecacopter increases.

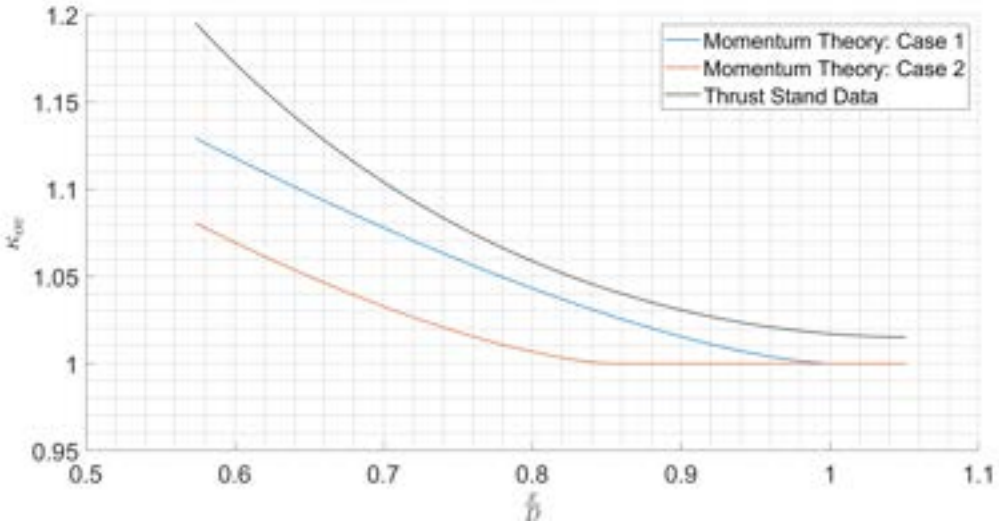

Figure 5.27: A comparison between the interference factor derived by momentum theory and the interference factor calculated using the pseudo-surrogate model.

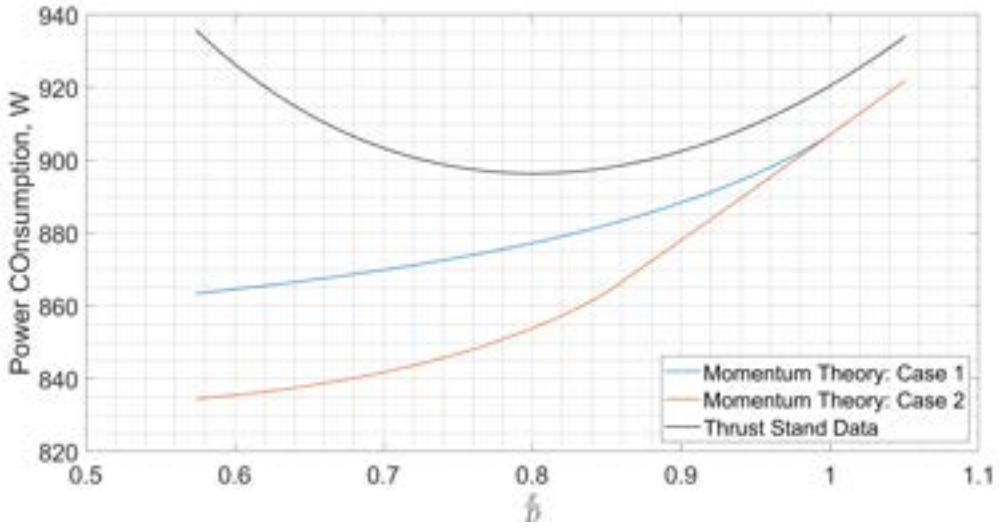

Figure 5.28: A comparison between the power required to hover using the interference factor derived by momentum theory and the power required to hover calculated by using the pseudo-surrogate model.

5.2.4 Summary of Results

The results presented in this section cover the constrained rotor configurations listed in Table 4.5, which have a horizontal and vertical separation such that the rotors are in the shape of a regular tetrahedron, where the center of each rotor is at the vertex of the regular tetrahedron. The results include an analysis of the thrust stand experiments as well as the optimization of the Tetracopter design based on these thrust stand experiments. The thrust stand experiments show that the configuration where the rotors are farthest apart performs the best due to the lack of interaction between the wake of the upstream rotor and the downstream rotor. However, when accounting for the weight of the Tetracopter, depending on the base weight of the vehicle and the weight per unit increase of the vehicle, a vehicle design with rotor overlap and possible wake interactions is optimum. The inability of the momentum theory to estimate the optimum configuration shows the importance of the empirical data. This optimum design accounts for efficiency as well as the rigidity of the vehicle. If the vehicle's rigidity is sacrificed, the optimum design is unknown based on the results presented in this section.

5.3 Results of the Unconstrained Tandem Rotor Configurations

Thirty tandem rotor configurations are tested in both the counter and co-rotating spin directions. The results of testing these configurations show the individual influence of the vertical and horizontal separation between the rotors of the tandem-rotor configuration on the system's performance.

5.3.1 Performance Metrics

The metrics used to analyze the performance of the unconstrained tandem rotor configurations are the same as those used to analyze the constrained rotor configurations. This includes the thrust, power, and torque coefficients of the downstream rotor and the thrust

and power coefficients ratio. Secondly, the overlap interference factor is used to describe the performance of the rotors, and lastly, an analysis using the FM of the downstream rotor is completed. The manner in which these metrics are calculated is also identical to that of the constrained rotor configurations. Given that the minimum vertical separation of the unconstrained tandem rotor configurations is less than that of the constrained tandem rotor configurations, the performance of the upstream rotor is also analyzed.

5.3.2 Results and Discussion

Analysis using Performance Coefficients

Figs. 5.29 to 5.32 show the percent decrease of the thrust, power, the ratio of the two, and the torque of the downstream rotor operating in the wake of the upstream rotor when the upstream rotor's *Re* is 135,000, compared to the performance coefficients of the downstream rotor operating independently. The change in the performance coefficients of both rotors operating simultaneously with respect to each rotor operating independently in each rotor configuration at each angular velocity and spin direction tested are shown in Section B.1 of the Appendix.

These results generally support the simple momentum theory analysis of the tandem-rotor configurations where the downstream rotor operates in the fully contracted wake of the upstream rotor. These results confirm that a tandem-rotor configuration can have roughly 10 % overlap between the rotors without experiencing a significant degradation in performance. This remains true as the vertical separation varies from $0.15 < \frac{z}{D} < 1.0$. As the overlap between the rotor increases such that $\frac{x}{D} = 0.75$, the results show that the performance impact becomes non-negligible. Although the horizontal separation between the rotors is far more influential to the performance of the downstream rotor, Figs. 5.29 to 5.31 shows that when $\frac{x}{D} = 0.75$ an increase in the vertical separation improves the efficiency of the downstream rotor. As the horizontal separation between the rotors decreases, the results show that the downstream rotor performs better when the vertical separation is minimized

rather than increased. Viewing the performance coefficients of the upstream rotor, Figs. B.5 to B.7, it can be seen that the rotor's performance decreases as the vertical separation decreases when the horizontal separation is minimal, opposite of what the downstream rotor experiences. Both of these effects have been found in other studies that produced empirical data [13, 73]. One phenomenon that is not clearly seen in these results is the performance benefit of swirl recovery. The benefits of swirl-recovery have been captured in experiments such as those performed by Shukla et al. [14, 70], which states that swirl recovery has a greater effect on rotor configurations operating at a lower *Re*, and should improve the performance of the upstream rotor. However, the results of the thrust stand experiments where the rotors operate at a *Re* of 75,000, shown in Figs. B.5 to B.7, show that in nearly all the configurations where there is significant overlap the upstream rotor performs worst than it would if they were operated independently.

Another notable result is the change in the torque coefficient of both the downstream and upstream rotors as a function of their relative position. Figure 5.32 shows the change in torque coefficient of the downstream rotor when the rotors operate at a *Re* of 135,000, and Fig. B.7 shows the change in the torque coefficient of the upstream rotor at all *Re* tested. This change in torque coefficient must be considered when accounting for the control authority of a vehicle with overlapping rotors. For the Tetracopter and the Tetrahedron Dodecacopter, three of its four rotors operate in the wake of its upstream rotor, meaning that the maximum torque that the lower three rotors can produce is reduced, which in turn reduces the maximum moment that the vehicle can generate. This reduces the overall maneuverability of the vehicles in comparison with a traditional quadrotor design that has four rotors operating in an isolated manner.

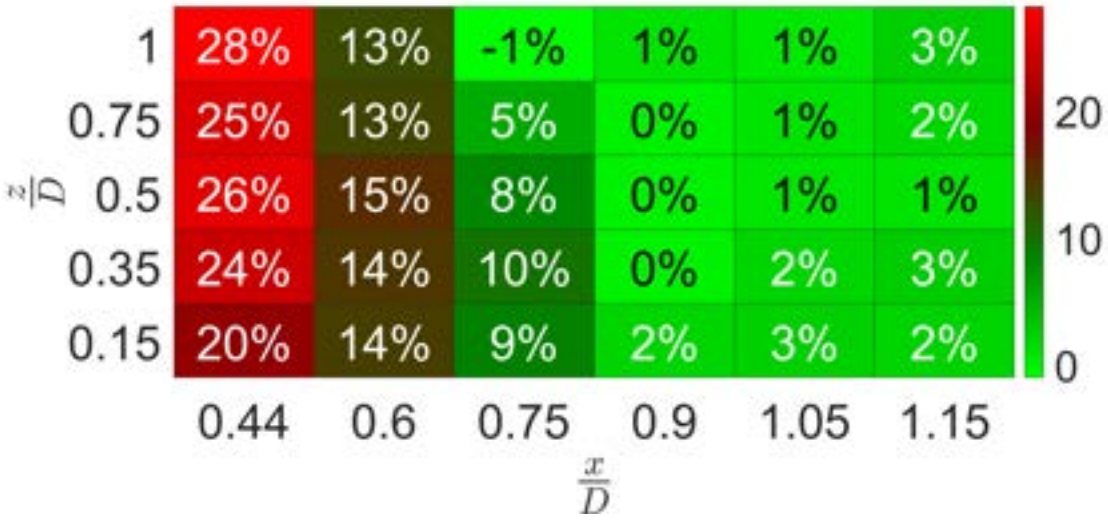

Figure 5.29: The percent decrease in C_T of the downstream rotor at each configuration tested while the upstream rotor operates at a *Re* of 135,000.

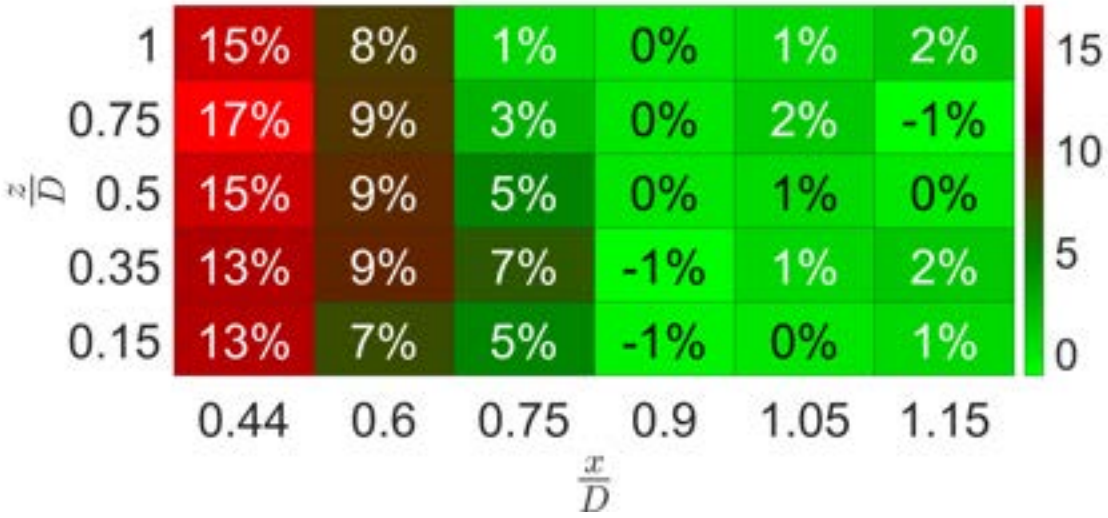

Figure 5.30: The percent decrease in C_P of the downstream rotor at each configuration tested while the upstream rotor operates at a *Re* of 135,000.

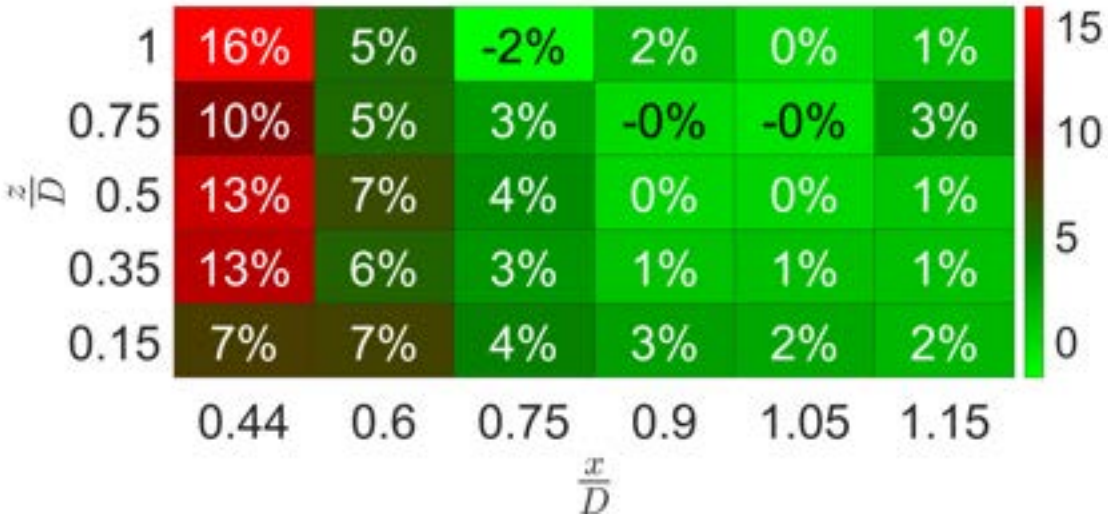

Figure 5.31: The percent decrease in C_T/C_P of the downstream rotor at each configuration tested while the upstream rotor operates at a *Re* of 135,000.

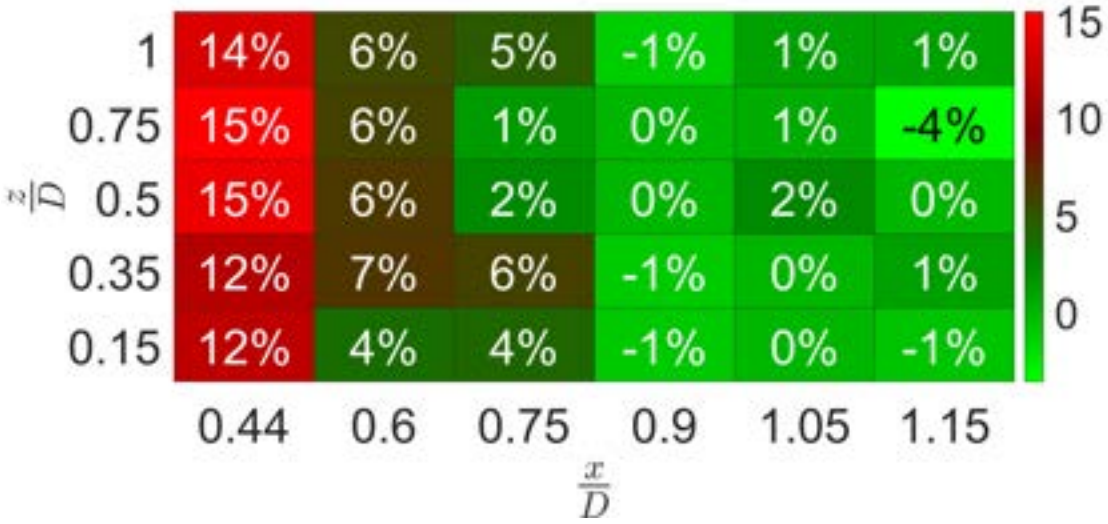

Figure 5.32: The percent decrease in C_Q of the downstream rotor at each configuration tested while the upstream rotor operates at a *Re* of 135,000.

Analysis using Overlap Interference Factor: Case 1

The results shown in Figs. 5.33 to 5.36 depict the overlap interference factor of each unconstrained rotor configuration when the rotors are operated at a *Re* of 135,000 and 100,000 and the overlap interference factor is calculated in the manner previously described as *Case 1*.

The results of this analysis for the experiments where the rotors operates at a *Re* of 75,000 and 125,000 can be seen in Section B.2.

These results shown in Figs. 5.33 and 5.34 have the same trends as the analysis of the unconstrained rotor configurations using the percent difference of C_T/C_P. The performance of the rotors when $\frac{x}{D} \geq 0.9$ and $\frac{z}{D} \geq 0.15$ are roughly constant, so it can be expected that when accounting for the weight of the vehicle, the optimal configuration will have overlapping rotors. There is not a drastic difference in the results with respect to a change in *Re* or spin direction, which is shown in Figs. 5.33 to 5.36.

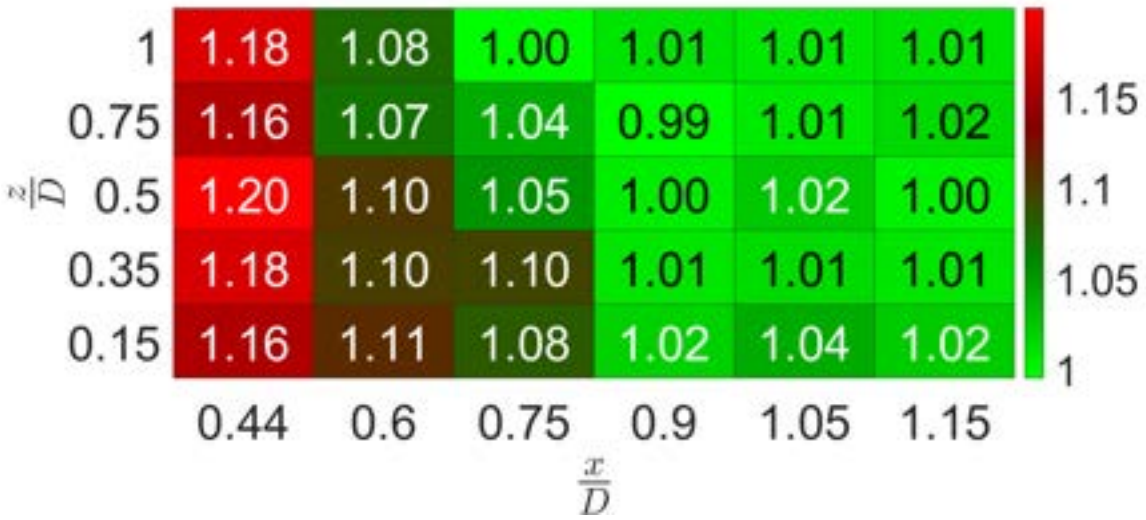

Figure 5.33: The overlap interference factor for each unconstrained tandem rotor configuration in a counter-rotating spin direction when the upstream rotor is operating at a *Re* of $135,000$ and the system is mathematically torque balanced.

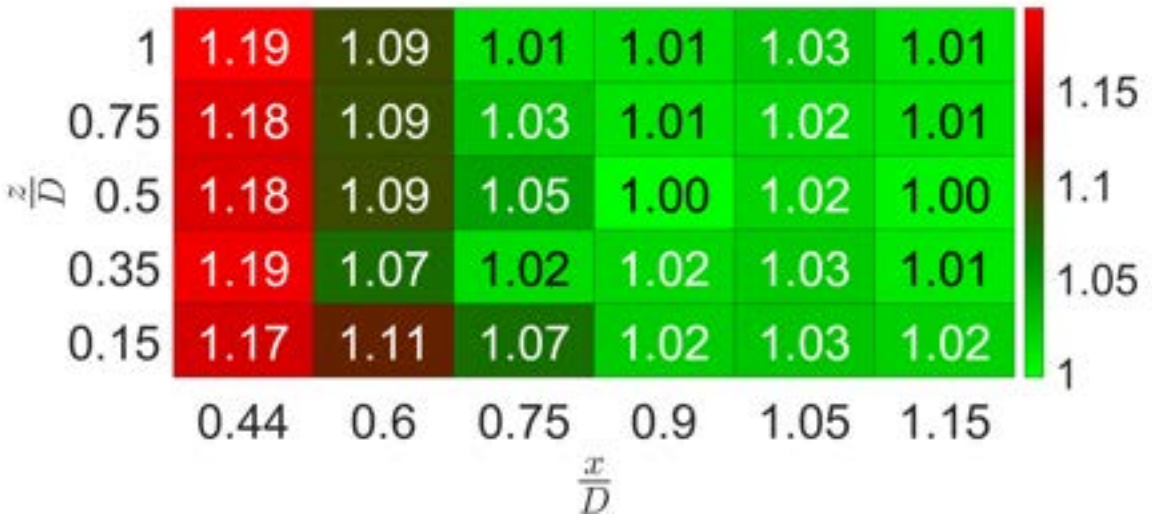

Figure 5.34: The overlap interference factor for each unconstrained tandem rotor configuration in a co-rotating spin direction when the upstream rotor is operating at a *Re* of $135,000$ and each rotor is mathematically producing equivalent amounts of torque.

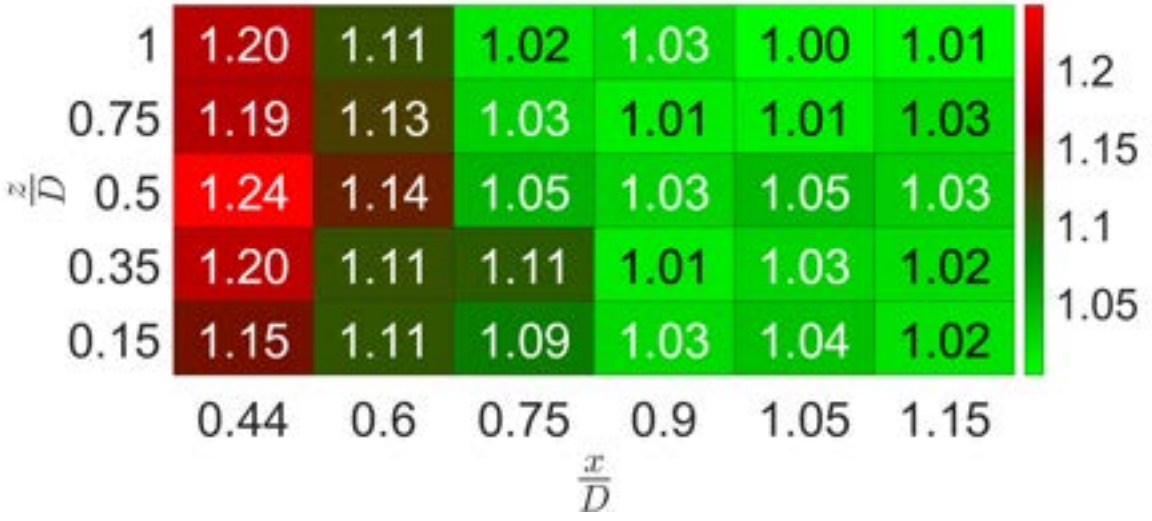

Figure 5.35: The overlap interference factor for each unconstrained tandem rotor configuration in a counter-rotating spin direction when the upstream rotor is operating at a rotor *Re* of 100,000 and the system is mathematically torque balanced.

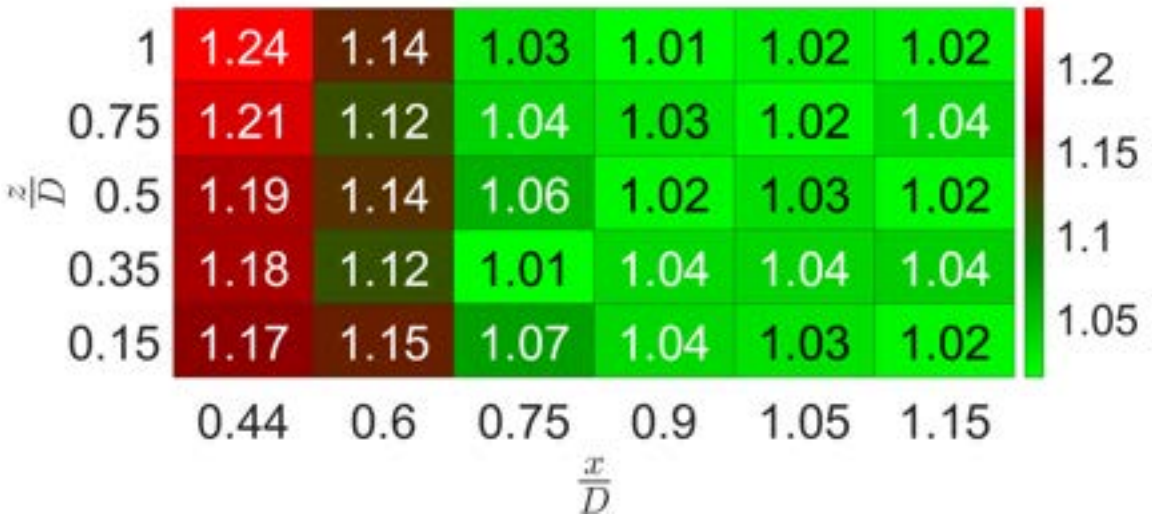

Figure 5.36: The overlap interference factor for each unconstrained tandem rotor configuration in a co-rotating spin direction when the upstream rotor is operating at a rotor *Re* of 100,000 and each rotor is mathematically producing equivalent amounts of torque.

Figures 5.37 and 5.38 shows a comparison between the momentum theory derived overlap interference factor for a tandem-rotor configuration and the results of the mathematically torque balanced unconstrained tandem rotor configurations when the rotors operates at a *Re* of 135,000 for both the counter and co-rotating spin directions respectively. As can be seen, the results of the experiments have the same trend as both *Case 1* and *Case 2* of momentum theory. Moreover, the results of the tandem-rotor configurations where $\frac{z}{D} = 0.15$ follow *Case 1* of the momentum theory, and the results tend to be more similar to *Case 2* of the momentum theory as the vertical separation between the rotors increase, which confirms the momentum theory prediction of the overlap interference factor. Figs. 5.39 and 5.40 show the comparison between the momentum theory and the results of the torque balance tandem rotor configuration where the upstream rotor operates at a *Re* of 100,000. In these figures, the overlap interference factor calculated from the thrust stand data is overestimated compared to the momentum theory derived overlap interference factor, which is most likely caused by the method used to mathematically torque balance the tandem rotor system. As previously mentioned, the power and thrust coefficients of the downstream

rotor are estimated based on the unprocessed data generated by the thrust stand. As a reminder, the tandem rotor system is not torque balanced during the experiments, so when mathematically torque balancing the system, the change in the power, torque, and thrust coefficients are estimated, which may contribute to the overestimation of the overlap interference factor. For comparison, Fig. B.10 shows the overlap interference factors of the unconstrained configurations if they are not mathematically torque balanced. In these figures, the unprocessed data of each unconstrained tandem rotor configuration is compared to the two rotors operating independently while torque balanced and producing the same collective thrust generated by the tandem-rotor configuration. The results of this analysis fit more closely with the momentum theory results than the results presented in Figs. 5.37 to 5.40.

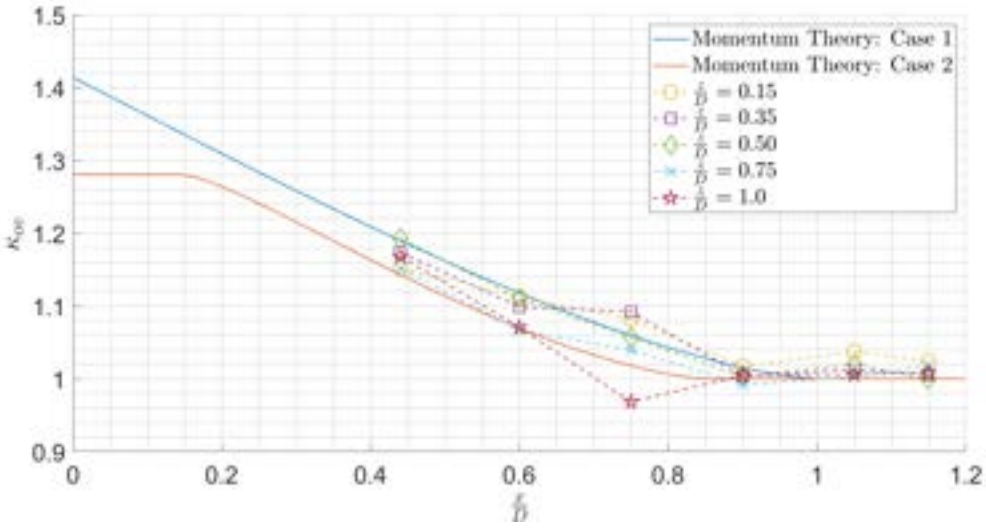

Figure 5.37: A comparison between the momentum theory derived induced overlap interference factor and overlap interference factor for each unconstrained tandem rotor configuration in a counter-rotating spin direction when the upstream rotor is operating at a *Re* of 135,000 and the system is mathematically torque balanced.

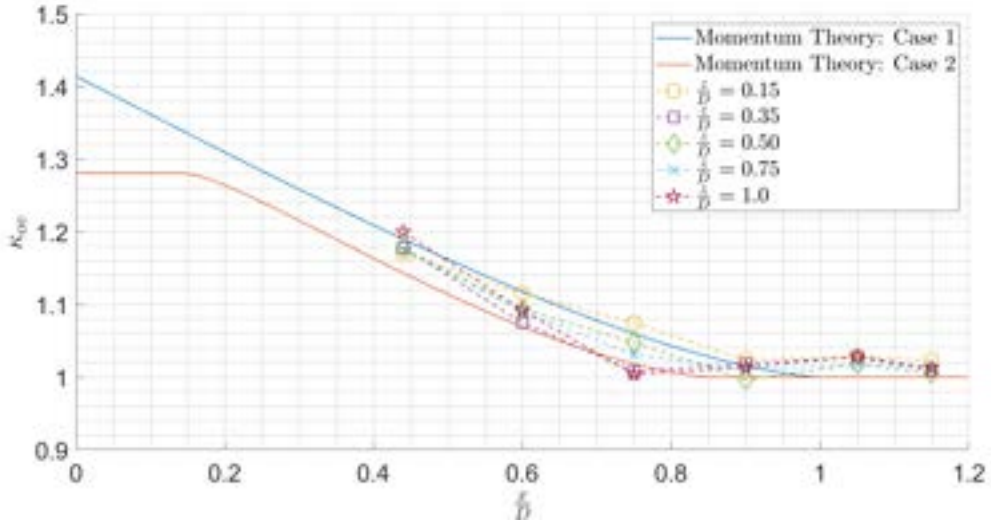

Figure 5.38: A comparison between the momentum theory derived induced overlap interference factor and overlap interference factor for each unconstrained tandem rotor configuration in a co-rotating spin direction when the upstream rotor is operating at a *Re* of 135,000 and the system is mathematically torque balanced.

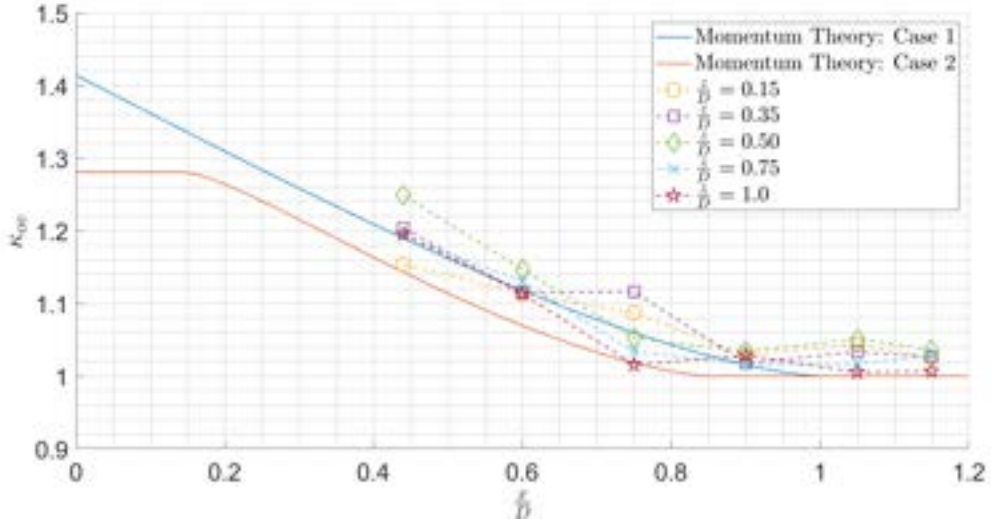

Figure 5.39: A comparison between the momentum theory derived induced overlap interference factor and overlap interference factor for each unconstrained tandem rotor configuration in a counter-rotating spin direction when the upstream rotor is operating at a *Re* of 100,000 and the system is mathematically torque balanced.

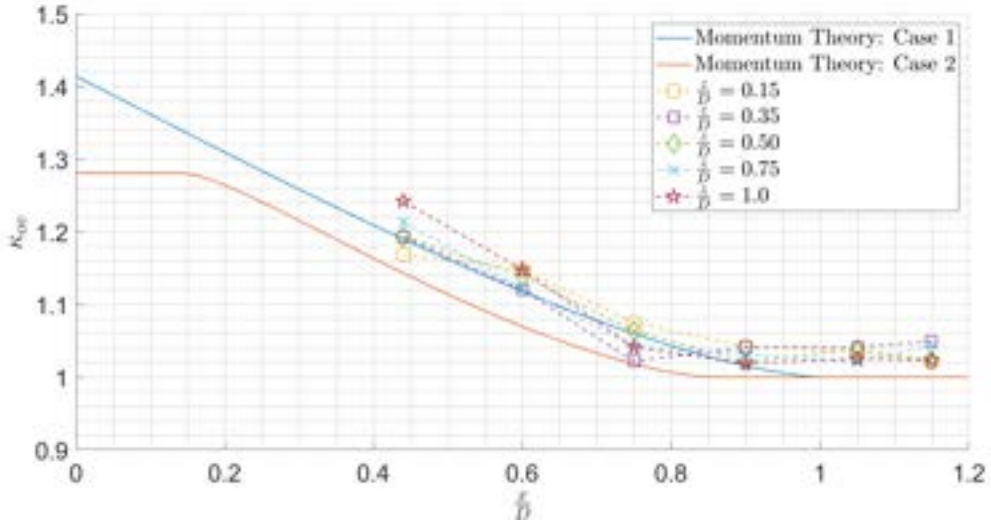

Figure 5.40: A comparison between the momentum theory derived induced overlap interference factor and overlap interference factor for each unconstrained tandem rotor configuration in a co-rotating spin direction when the upstream rotor is operating at a *Re* of 100,000 and the system is mathematically torque balanced.

Comparing the results shown in Figs. 5.37 to 5.40, to similar experiments performed using tandem rotor configurations, such as those shown in [52], shows that there is no major difference between the overlap interference factor of a tandem rotor system that uses smaller rotors that operate at a lower *Re* and larger rotors that operate at a higher *Re* (i.e., 325,000-275,000). Experiments performed in [52] consisted tandem rotor configurations that implement twisted and untwisted blades with a diameter of roughly 4.34 ’. The vertical separations of the configurations tested are $\frac{z}{D} = 0.07$ and $\frac{z}{D} = 0.0$, which is significantly smaller than the vertical separations of the tandem rotor configurations used in the presented work. The maximum overlap interference factor of the tandem rotor configurations operating at a horizontal and vertical separation ratio of $0.9 \leq \frac{x}{D} \leq 1.02$ and $\frac{z}{D} = 0.07$ using untwisted blades is roughly 1.05 , which is only slightly higher than the results presented in this work despite the difference in the vertical separation ratios tested. One major difference between the results shown in [52] and the presented results is the overlap interference factor for tandem rotor configurations where $0.5 \leq \frac{d}{D} = 1.02$. In [52], untwisted blades were implemented in the tandem rotor configurations tested and the estimated over-

lap interference factor derived using the momentum theory consistently underestimates the overlap interference factor compared to the results. Moreover, the trend of the results differ from both the momentum theory results and the results presented in this thesis.

Analysis using Overlap Interference Factor: Case 2

In this section, the same method of calculating the overlap interference factor for the constrained configurations in *Case 2* is used to calculate the overlap interference factor of the unconstrained configurations. The calculated overlap interference factor for the counter-rotating and co-rotating configurations with a collective thrust of 24 N while mathematically torque balanced is shown in Figs. 5.41 and 5.42 respectively.

This analysis does not drastically vary from the *Case 1* calculation of the overlap interference factor. The configurations where $\frac{z}{D} > 0.15$ and $\frac{x}{D} = 0.9$ have an overlap interference factor slightly greater than one, which is most likely due to an error in the estimation method used to calculate the overlap interference factor for this case. Figures 5.43 and 5.44 show that the estimation method overpredicts the overlap interference factor compared to the momentum theory derived result. Since this use of the overlap interference factor requires the upstream rotor to change its angular velocity, the estimation of the performance degradation in the downstream rotor has more error than the *Case 1* estimations of the overlap interference factor. However, other experiments that have collected data on torque balanced tandem rotor systems have also produced empirical data that shows a higher overlap interference factor than the momentum theory predicts [73], suggesting that the estimation method used does not produce unrealistic results. Figures 5.43 and 5.44 also shows that the results of this analysis do not show a strong correlation between the performance of the system and the vertical separation between the rotors when $\frac{x}{D} > 0.44$. This result indicates that the aerodynamic effects between the rotors caused by changing the vertical separation between the rotors will not drastically influence the performance of the system if the horizontal separation ratio is larger than 0.44.

Another notable conclusion from the data shown in Figs. 5.33 to 5.36, 5.41 and 5.42, is that the when the horizontal separation is minimal, $\frac{x}{D} = 0.44$, the configurations with a minimal vertical separation perform slightly better than configurations with larger vertical separation ratios. To the author's knowledge, there is no published data that investigates the relationship between the vertical separation between the rotors of a tandem rotor system with minimal horizontal separation and its performance. However, a contrast is seen when comparing the presented data to empirical data of coaxial rotor configurations presented in [13, 73]. The data in these publications show that minimizing the vertical separation between the upstream and downstream rotors of a coaxial rotor system produces the same trends regarding the performance impact on the individual rotors as minimizing the vertical separation between the rotors of a tandem rotor system where $\frac{x}{D} = 0.44$. However, the data from these studies shows that the overall performance of the coaxial system decreases when the vertical separation is minimal, which contrasts the data shown in Figs. 5.33 to 5.36, 5.41 and 5.42. This is most likely due to the inflow of the downstream rotor having less impact on the upstream rotor when in a tandem rotor configuration as opposed to a coaxial rotor configuration. The downstream rotor of a closely space coaxial rotor system increases the upstream rotor's inflow angle, which in turn decreases the upstream rotor's angle of attack, thus decreasing the amount of thrust the upstream rotor generates. The increased inflow angle also increases torque generation, corresponding to an increase in power consumption. An in depth explanation of this phenomenon can be found in [73]. The results shown in Fig. B.6, show that the power coefficient of the upstream rotor decreases when both the horizontal and vertical separation ratios are minimal, which contradicts the performance impact the upstream rotor of a coaxial rotor system experiences. This difference in the change in the power coefficient causes the contrast between the overall performance of a closely spaced coaxial rotor system and a closely spaced tandem rotor system where $\frac{x}{D} = 0.44$ To understand why the power coefficient of the upstream rotor in a closely spaced tandem rotor system decreases, flow visualization experiments would need to be

conducted.

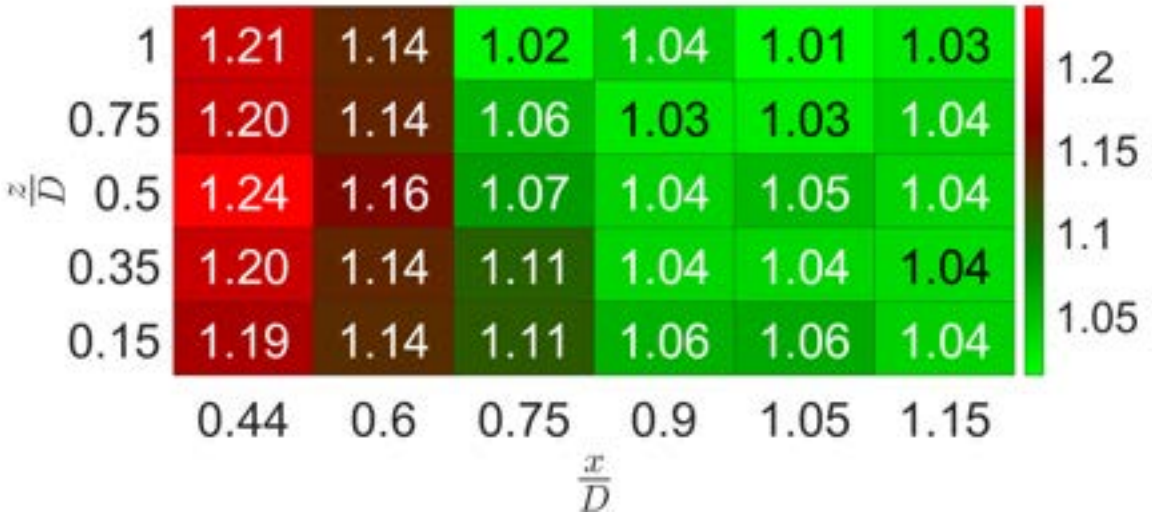

Figure 5.41: The overlap interference factor for each unconstrained tandem rotor configuration in the counter-rotating spin direction generating a thrust of 24 N while mathematically torque balanced.

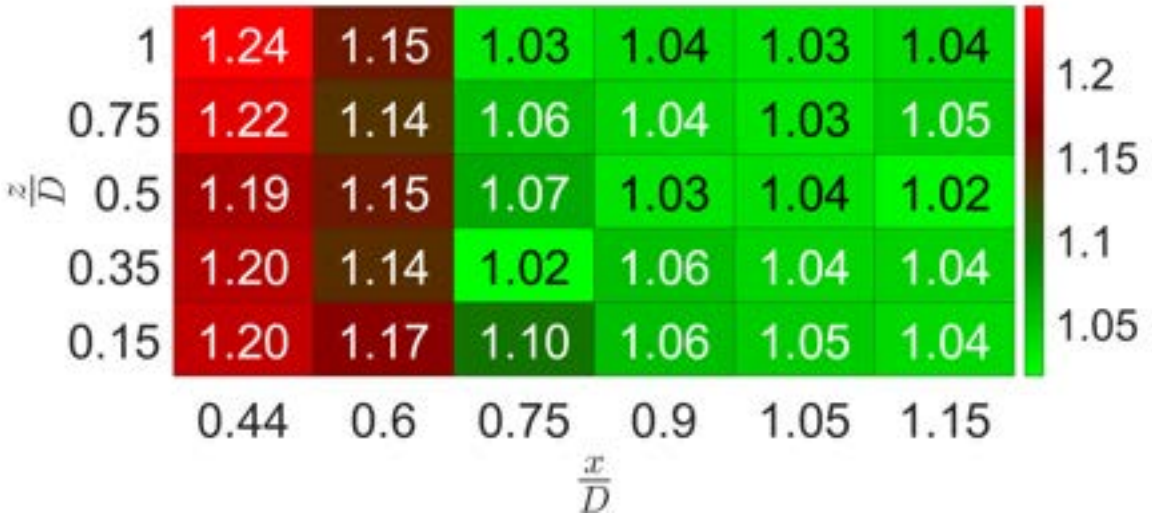

Figure 5.42: The overlap interference factor for each unconstrained tandem rotor configuration in the co-rotating spin direction generating a thrust of 24 N while mathematically torque balanced.

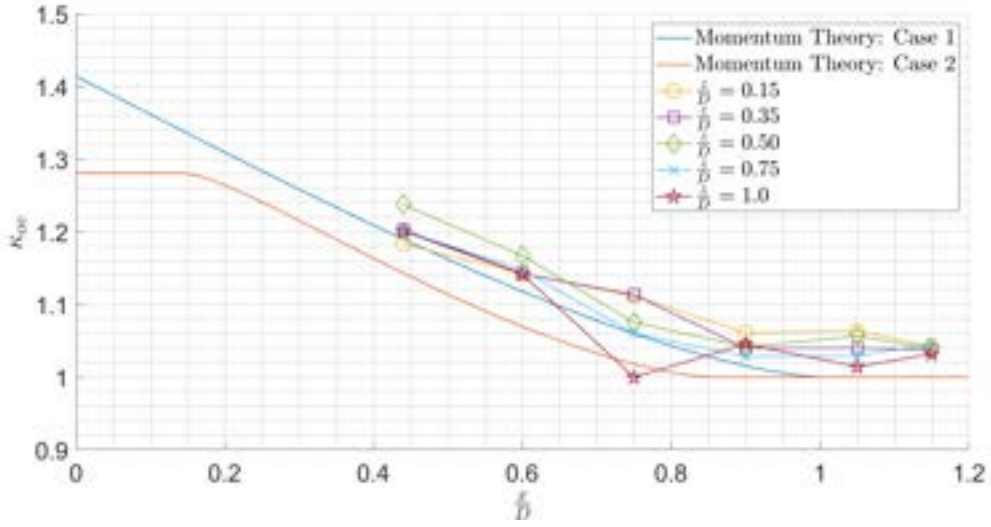

Figure 5.43: Momentum theory derived induced overlap interference factor compared to the overlap interference factor for each unconstrained tandem rotor configuration in the counter-rotating spin direction generating a thrust of 24 N while mathematically torque balanced.

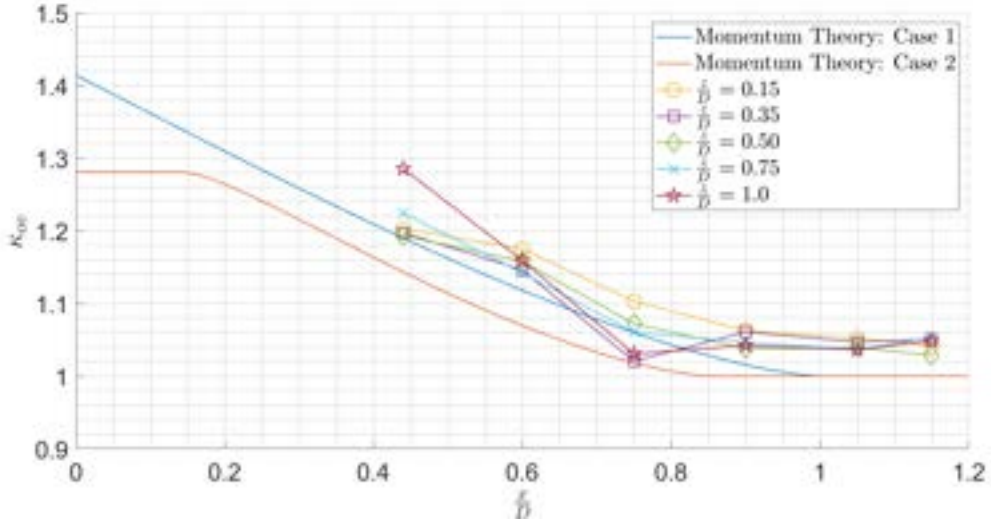

Figure 5.44: Momentum theory derived induced overlap interference factor compared to the overlap interference factor for each unconstrained tandem rotor configuration in the co-rotating spin direction generating a thrust of 24 N while mathematically torque balanced.

Analysis using the Figure of Merit

The percent decrease of the FM of the downstream rotor operating while the upstream rotor operates at a *Re* of 135,000 and 100,000 compared to the downstream rotor operating inde-

pendently is shown in Figs. 5.45 and 5.46, respectively. The results show that the decrease in the FM does not drastically vary in relation to the angular velocity of the upstream rotor, which contradicts the results found in [26], where two closely spaced rotors in a side-by-side rotor configuration experienced a change in performance attributed to the change in the interaction between the vortex cores of each rotor relative to the angular velocity of the rotors. Although the side-by-side configuration is not tested in the presented work, it is expected that results similar to what is found in [49, 26] would have been found for the tandem-rotor configurations where $\frac{x}{D} = 1.05$. This may be because the vertical separation of the configurations tested is not small enough to cause an efficiency boost. Based on past works, it is suggested that an increase in performance of a closely spaced tandem rotor system with no rotor overlap can occur when the contraction of both rotors' wakes is reduced, meaning the wakes contract less than they would if they operated independently. This would cause the induced velocity at the rotor to be reduced, thus reducing the induced power.

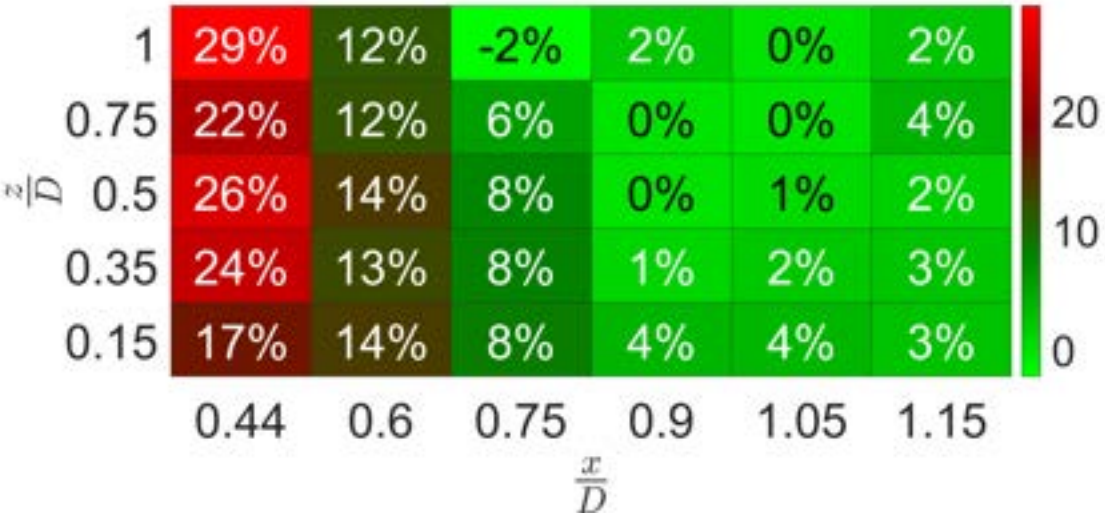

Figure 5.45: The percent decrease in the FM of the downstream rotor operating simultaneously with the upstream rotor operating at a *Re* of 135,000 in the counter-rotating spin direction.

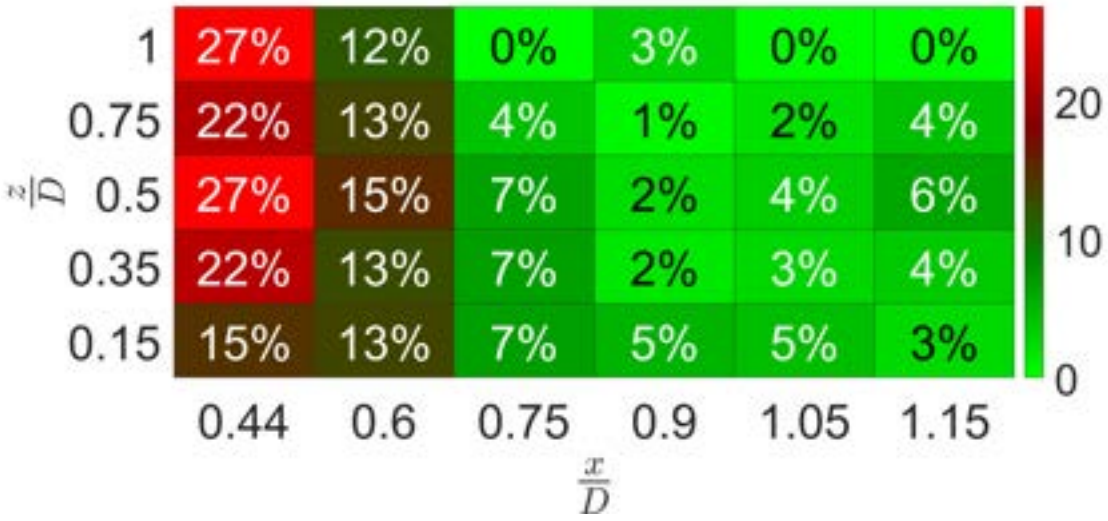

Figure 5.46: The percent decrease in the FM of the downstream rotor operating simultaneously with the upstream rotor operating at a *Re* of 100,000 in the counter-rotating spin direction.

The decrease in the FM of the unconstrained tandem rotor configurations operating in the co-rotating spin direction when the upstream rotor is operating at a *Re* of 135,000 and 100,000 are shown in Figs. 5.47 and 5.48, while the same figures for when the upstream rotor operates at a *Re* of 125,000 and 75,000 are shown in Fig. B.11. The FM of the upstream rotor can be seen in Fig. B.12. For configurations where $\frac{x}{D} = 0.44$, the results show that the percent decrease of the FM is slightly higher than when the rotors are operating in the co-rotating spin direction rather than the counter-rotating spin direction. For configurations where $\frac{x}{D} = 0.44$, the largest differences between the two spin directions in the percent decrease of the FM are at vertical separations of $\frac{z}{D} = 0.15$ and $\frac{z}{D} \geq 0.75$. Comparing the results of the experiments in [26] with the results shown in Figs. 5.45 to 5.48, it is safe to conclude that the performance difference between the counter-rotating and co-rotating systems is not caused by swirl recovery, given that the results presented in [26] suggested that swirl recovery occurs between tandem-rotor systems that have minimal vertical separation.

Results of similar experiments involving tandem rotor configurations that implemented larger rotor blades [52], with a vertical separation of $\frac{z}{D} = 0.07$, and that operate at higher

Re, show that the FM of the upstream rotor decreases roughly $0.9 \leq \frac{x}{D} \leq 1.02$ compared to the rotor operating in an isolated state. Although the decrease in the FM of the upstream rotor in the unconstrained rotor configurations, shown in Fig. B.12, does not show an apparent significant decrease in the FM, the results do show a significant decrease in the FM of the upstream rotor when the horizontal separation is decreased while $\frac{z}{D} = 0.15$. Comparing the performance of the downstream rotor of the presented experiments and the the experiments conducted in [52] shows a significant difference. The results shown in [52] suggest that the upstream rotor of a tandem rotor configuration where $0.95 \leq \frac{x}{D} \leq 1.0$ performs more efficiency than an isolated rotor, which contradicts the results shown in Figs. 5.45 and 5.46. The difference in these results may be because the vertical separation of the tandem rotor configuration in [52] is quite small, $\frac{z}{D} = 0.07$, compared to the minimum vertical separation tested in the presented work, $\frac{z}{D} = 0.15$. As discussed in Section 5.3.2, empirical results have shown that minimizing the vertical separation between coaxial rotor configuration improves the performance of the downstream rotor and degrades the performance of the upstream rotor. This could also cause the difference in results between the presented work and the work performed in [52].

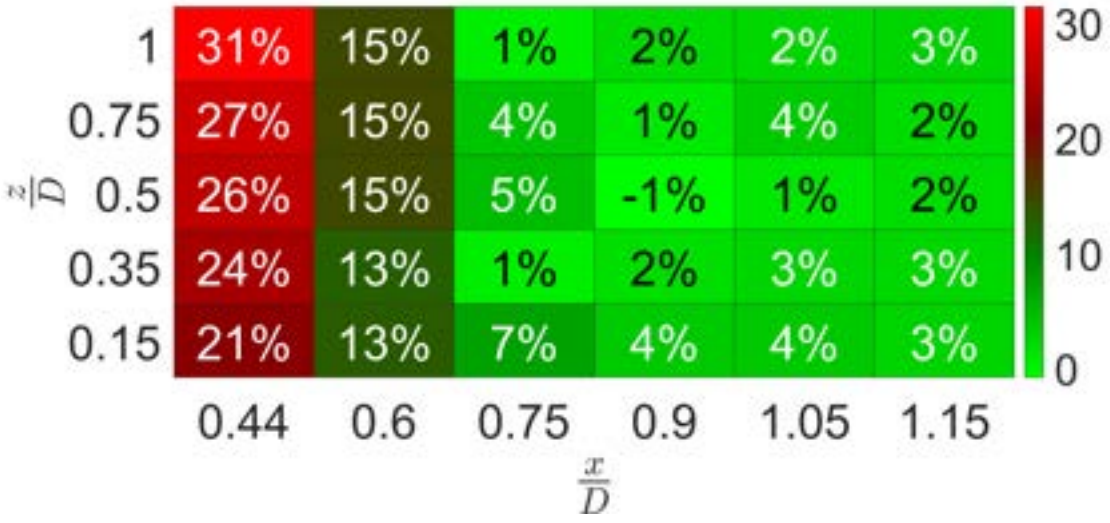

Figure 5.47: The percent decrease in the FM of the downstream rotor operating simultaneously with the upstream rotor operating at *Re* of 135,000 in the co-rotating spin direction.

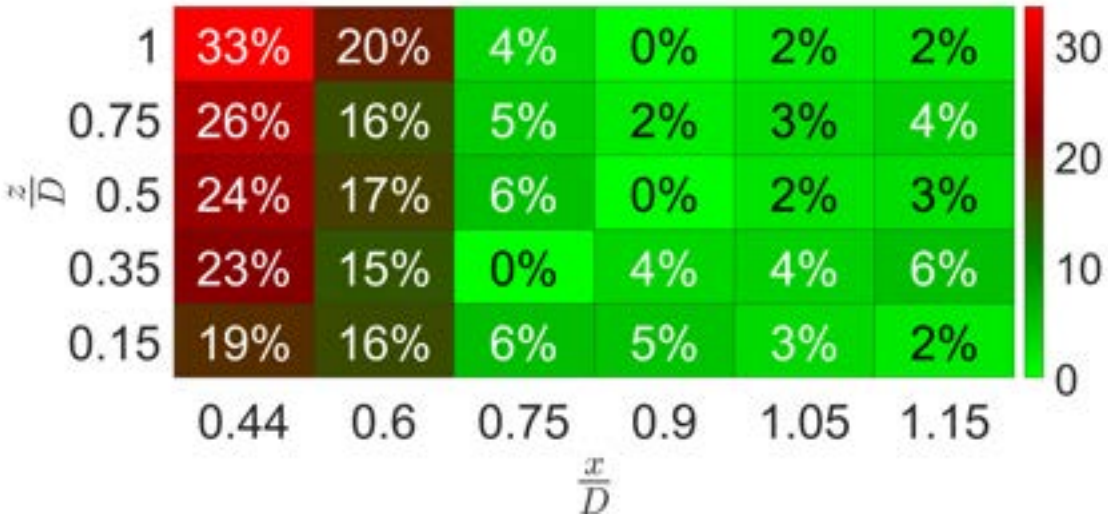

Figure 5.48: The percent decrease in the FM of the downstream rotor operating simultaneously with the upstream rotor operating at *Re* of 100,000 in the co-rotating spin direction.

5.3.3 Optimization of Unconstrained Rotor Configurations

Changing the height of a dodecahedron without changing the width creates a strange shape that can be complicated to fabricate. On the other hand, the height and width of a tetrahedron can be changed quite easily. For this reason, the thrust stand data of the unconstrained tandem rotor configurations are used to optimize the design of the Tetracopter. To determine the optimal design of the Tetracopter, without a constraint on the rotor configuration, a method similar to the optimization method used in Section 5.2.3 is implemented. However, unlike the optimization problem used to estimate the optimal Tetrahedron Dodecacopter design, the optimization problem for the Tetracopter does not have a constraint on the relative position between the rotors of the Tetracopter. The optimization problem can be seen in standard form in Eq. (5.8). The relationship between the Tetracopter's rotor configuration and the weight of each module is shown in Eq. (5.9), where c_F is the mass per unit length of the carbon fiber rods used to form the Tetracopter's airframe, which is $3g/mm$. The first term is the weight of the lower three carbon fiber rods of a Tetracopter module, while the second term is the weight of the upper three carbon fiber rods of a Tetracopter module, as

shown in Fig. 5.49.

$$\begin{aligned} \min_{x,z} \quad & f(\epsilon(x,z,\Omega_U,\Omega_D), w(x,z)) \\ & \dot{\psi}(\Omega_D,\Omega_U) = 0 \\ & \dot{\theta}(\Omega_D) = 0 \\ & \dot{\phi}(\Omega_D) = 0 \\ & x_l \leq x \leq x_u \\ & z_l \leq z \leq z_u \end{aligned} \tag{5.8}$$

$$w(x,z) = 6x\cos 30^o c_F + 3\sqrt{x^2+z^2}c_F \tag{5.9}$$

Figure 5.49: A module of the Tetracopter with the lower three carbon fiber rods identified by the red arrows and the upper three carbon fiber rods identified by the blue arrows.

As was stated for the optimization of the Tetrahedron Dodecacopter, the objective function is not known, which is due to the fact that tandem-rotor configurations tested on the thrust stand are not torque balanced. An estimation method similar to what was is shown in Fig. 5.21 is used to estimate the power required for multiple designs of the Tetracopter.

Figure 5.50 shows the power required for 100 Tetracopter configurations, all of which have a vertical and horizontal separation between their rotors that is within the ranges of the unconstrained tandem rotor configurations tested on the thrust stand. It should be noted that this estimation method accounts for the aerodynamic effects on both the upstream and downstream rotors due to their relative position. The surface shown in Fig. 5.50 is a surrogate model created using the outputs of the estimation method used to predict the power required of the Tetracopter configurations. A detailed discussion of this estimation method is given in Section 5.3.4. Using a basic optimization technique, the optimal design based on the surrogate model is found to have a horizontal separation ratio of $\frac{x}{D} = 0.93$, a vertical separation ratio of $\frac{z}{D} = 1.0$, with an estimated power required to hover of 277 W. Out of the 100 configurations that are input into the estimation method, the optimal configuration is found to have a horizontal and vertical separation ratio of $\frac{x}{D} = 0.91$ and $\frac{z}{D} = 0.90$, with an estimated power required to hover of 278 W.

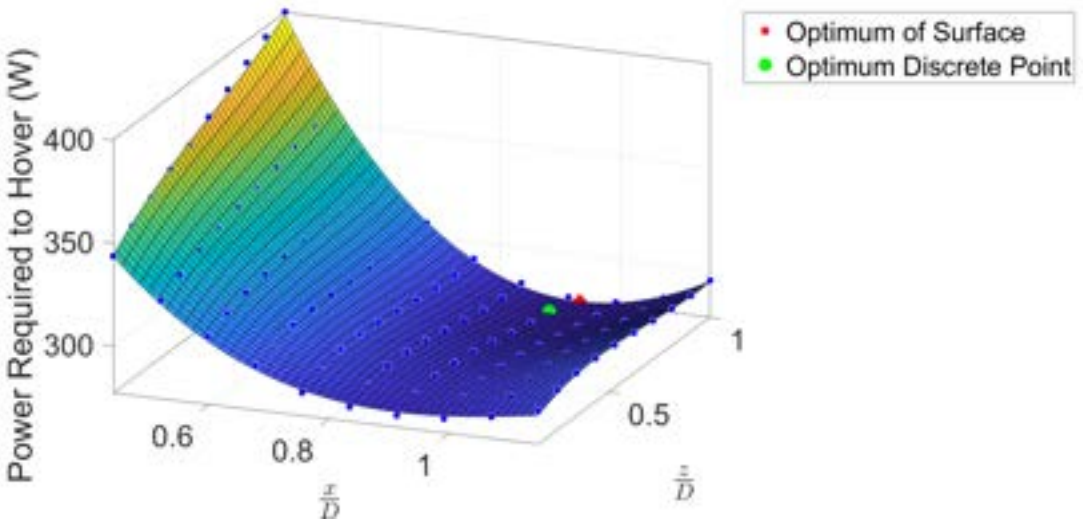

Figure 5.50: Power versus horizontal and vertical rotor separation ratio for the Tetracopter design

Both optimal configurations containing a horizontal separation ratio close to unity are expected because both the thrust stand results and the momentum theory derived results of a tandem-rotor system show that the rotors perform better when there is little to no overlap

between the rotors. However, both of these configurations also have a vertical separation close to the maximum vertical separation tested on the thrust stand. One would think that the optimal configuration would have a minimal vertical separation so that the vehicle's weight is reduced. This is caused by the relationship between the vehicle's weight and the vertical separation of the rotors. Viewing Eq. (5.9), it can be seen that the horizontal separation between the rotors has a greater impact on the weight of the vehicle because x is in both terms, whereas the vertical separation only drives the second term of the equation. For example, the difference in the weight of the vehicle with a rotor configuration of $\frac{x}{D} = 0.91$ and $\frac{z}{D} = 1$ and a vehicle with a rotor configuration of $\frac{x}{D} = 0.91$ and $\frac{z}{D} = 0.15$ is roughly 34 g, a 1 % difference.

Since the rotors of the Tetracopter are not constrained, the influence of the vertical and horizontal separation between the rotors and the power required to hover can be isolated. Figure 5.51 shows the relationship between the horizontal separation of the rotors in the Tetracopter and the overlap interference factor for every vertical separation tested on the thrust stand. The trends of each vertical separation follow that of the momentum theory; however, when the horizontal separation between the rotors is minimal, the results of the estimation method far overpredict the overlap interference factor compared to the momentum theory. There may be several reasons why the interference factor is overpredicted. Firstly, the majority of the vertical separations of the configurations tested are much larger than the vertical separations used to gather results that closely match the results of the momentum theory [48, 73, 49]. The second reason may be the error in the method used to estimate the performance of the rotors of the Tetracopter. One noticeable result is that the estimation method predicts that the configurations with a larger vertical separation have a higher overlap interference factor when the horizontal space between the rotors is minimal. This corresponds to the results found when investigating the effects of increasing the base weight of the Tetrahedron Dodecacopter in Section 5.2.3. However, as previously mentioned, the weight of the Tetracopter is not drastically changed by a change in the vertical separation

between the rotors, meaning that the increase in the estimated overlap interference factor is mainly due to the downstream rotor's location in the slipstream of the upstream rotor. Figure 5.51 shows that this effect dissipates once the horizontal separation ratio increases to $\frac{x}{D} \geq 0.60$. Figure 5.52 depicts the predicted power consumption as a function of the horizontal separation. Comparing Fig. 5.24 and Fig. 5.52, it can be seen that the Tetracopter design with the highest overlap interference factor corresponds to the design that requires the most power to hover.

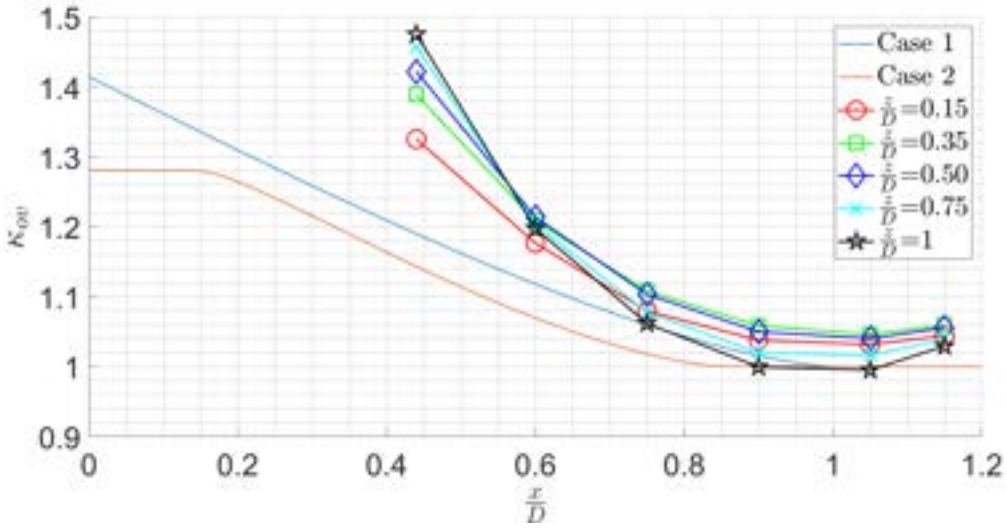

Figure 5.51: The horizontal separation of all Tetracopter designs versus the estimated overlap interference factor calculated using the thrust stand data.

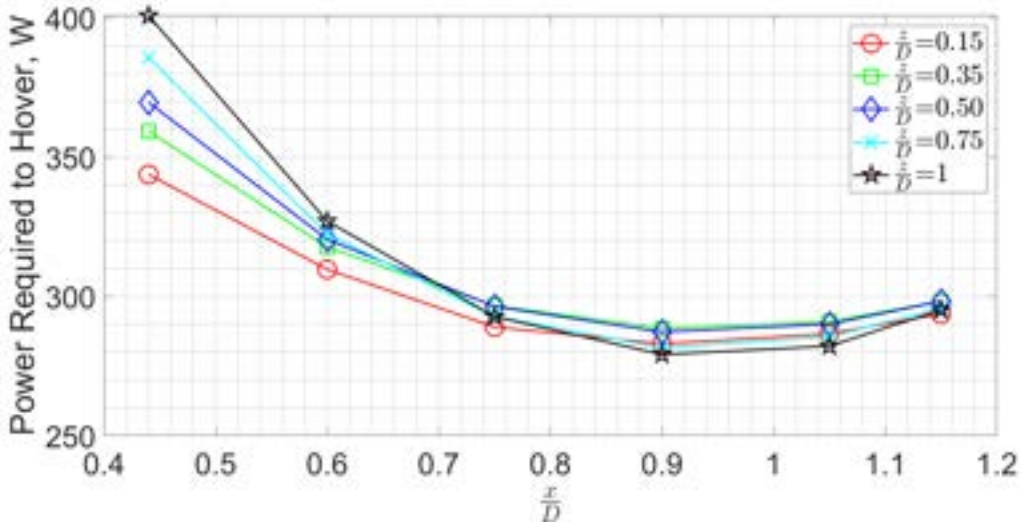

Figure 5.52: The relationship between the horizontal separation of the Tetracopter's rotors and the estimated power consumption of the Tetracopter designs.

Figures 5.53 and 5.54 show the relationship between the estimated overlap interference factor, the estimated power consumption, and the vertical separation of the Tetracopter designs. Figure 5.53 shows that the vertical separation of the rotors affects the performance of the Tetracopter designs with the highest amount of rotor overlap, $\frac{x}{D} = 0.44$. In contrast, the effects of the vertical separation are more subtle for configurations with greater horizontal separation. The overall power consumption of the configurations as a function of vertical separation, Fig. 5.54 has the same trends as the effects of vertical separation on the overlap interference factor.

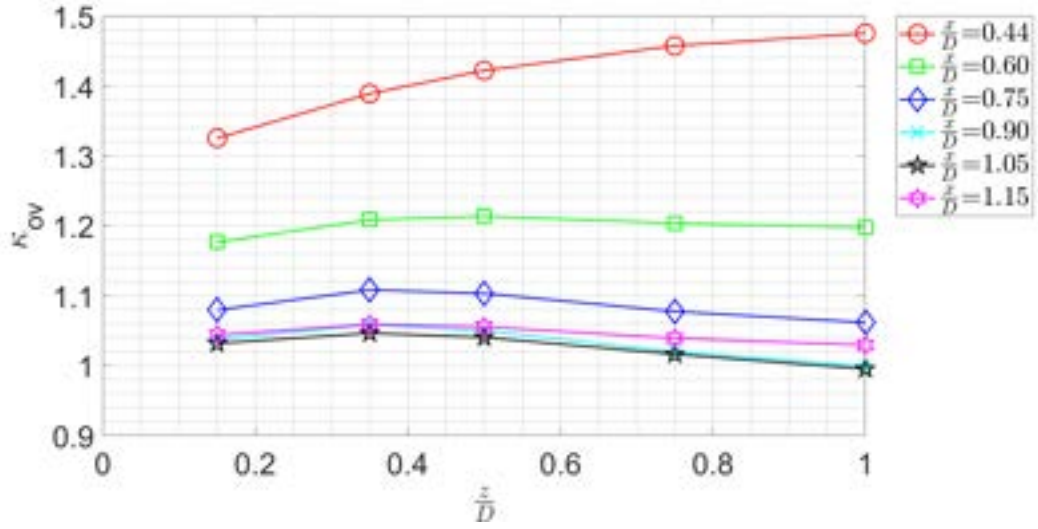

Figure 5.53: The relationship between the vertical separation of the Tetracopter's rotors and the estimated overlap interference factor of the design.

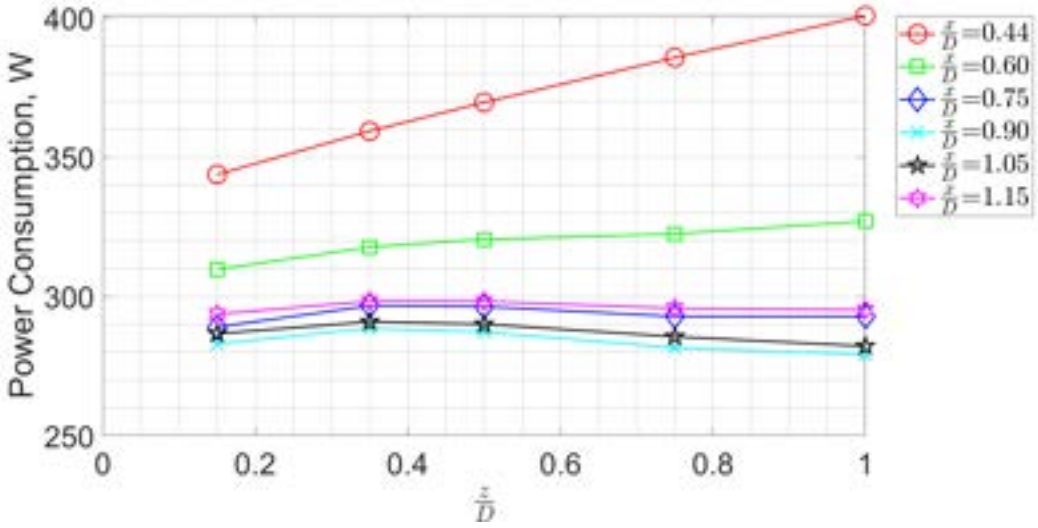

Figure 5.54: The relationship between the vertical separation of the Tetracopters rotor's and the estimated power consumption of the design.

5.3.4 Estimation and Validation

To the author's knowledge, the method used in this thesis to predict the performance of overlapping rotors has not been used in other works. As previously discussed, this method allows for the performance of both rotors of a tandem-rotor system operating at different an-

gular velocities and relative rotor positions to be estimated using empirical data. As stated in Section 5.2.1, this method is based on the relationship between the percent decrease of the performance coefficients (C_T, C_P, C_Q) of both rotors operating independently with respect to both rotors operating simultaneously. This relationship accounts for the relative position between the rotors and the angular velocity of both rotors. An example of this relationship can be seen in Fig. 5.55, which depicts the decrease in C_T of the downstream rotor while both rotors operate at a *Re* of 135,000.

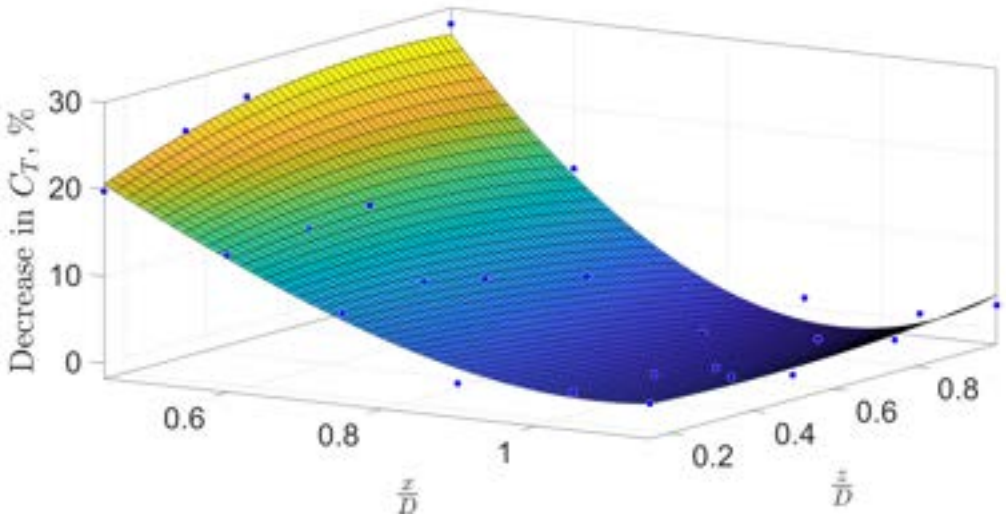

Figure 5.55: The decrease in C_T between the downstream rotor operating independently versus operating in the wake of the upstream rotor as a function of rotor position while both rotors are operating at a *Re* of 135,000.

For each coefficient, four polynomial surface regressions are created. These polynomial regressions have three degrees of freedom for the vertical separation and two degrees of freedom for the horizontal separation. As with any regression, the possibility of overfitting is present, which is why a higher-order polynomial is not used. Data describing each surface and how well they fit the data collected from the thrust stand is given in Tables C.2 and C.4. When estimating the performance of a tandem-rotor system, the relative position of the rotors is required. Given the relative position, each surface of each coefficient is evaluated at those given values of $\frac{x}{D}$ and $\frac{z}{D}$, which produces four points for each coefficient, one

for each angular velocity given by the training data. For each coefficient, a second-degree polynomial is then used to develop a relationship between the decrease in the coefficient and the angular velocity of the opposite rotor. Meaning, when estimating the performance of the downstream rotor, the relationship between the decrease in the coefficient of the downstream rotor and the angular velocity of the upstream rotor is used. Figure 5.56 shows the relationship between the decrease in the thrust coefficient of the upstream rotor and the angular velocity of the upstream rotor. The second-degree polynomial is then evaluated at the given angular velocity of the upstream rotor, which produces an estimated percent decrease in C_T, C_P, and C_Q. This percent decrease is subtracted from the performance coefficients of the downstream rotor operating in an isolated manner, which in most cases is given by the manufacturer of the rotor.

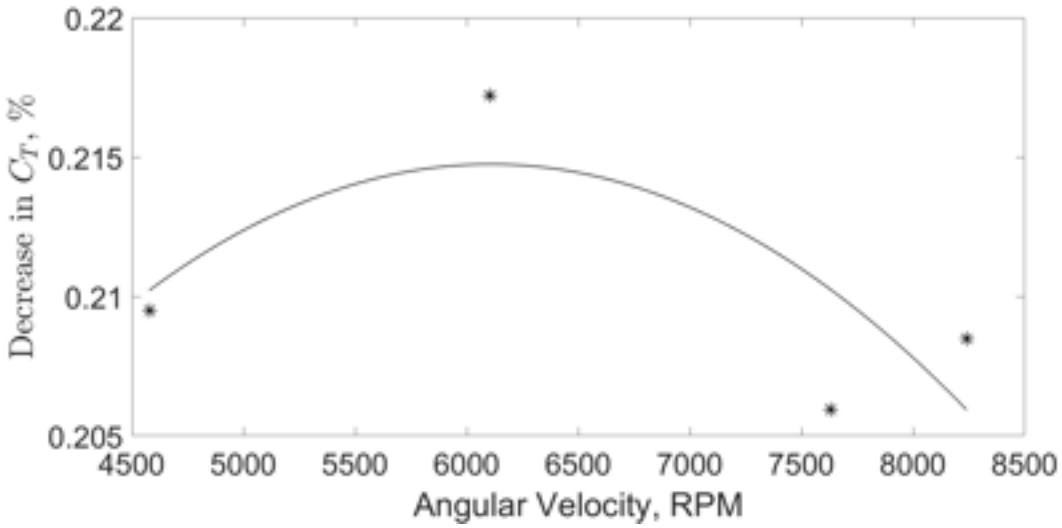

Figure 5.56: The decrease in C_T between the downstream rotor operating independently versus operating in the wake of the upstream rotor as a function of the angular velocity of the upstream rotor.

Since this estimation method has not been used in prior work, the accuracy of the method must be validated in order for the results in Sections 5.2.3 and 5.3.3 to be valid. To show the accuracy of this method, the performance of the downstream rotor of two tandem rotor configurations that have not been tested on the thrust stand is estimated using

the method and verified via thrust stand experiments. The data collected from the unconstrained tandem rotor thrust stand experiments are used as training data to create several regressions to estimate the thrust and power consumption of the downstream rotor of the two test tandem rotor configurations. The angular velocities of both rotors of these two test configurations are changed so that they do not match the angular velocity of the rotors in the training data. These tests aim to show that the thrust, torque, and power consumption of the downstream rotor in a tandem rotor configuration that experiences rotor-rotor interactions can be estimated. To simulate this case, the only known information about the test tandem rotor configurations is the angular velocity of both the upstream and downstream rotor, their position relative to one another, and the performance of the rotor operating in an isolated manner, which in practice is usually given by the motor or propeller manufacturer.

Table C.5 in Section C.2 of the Appendix lists test sets that are used to test the accuracy of the estimation method. Table C.7 in Section C.2 of the Appendix shows the percent error of the estimated performance of the downstream rotor relative to the actual data recorded by the sensors of the thrust stand. The average percent error in the thrust estimation is under 5 % while the average torque estimation error is under 6 % and the average power estimation is under 10 %. The R^2 of the test configurations is greater than 0.95 for all three coefficients. The torque estimation of the co-rotating configurations, labeled with an index of 20 to 24, has a higher percent error, which may point to the volatility of the aerodynamic interaction. The error in the power consumption estimation seems to grow when the current draw of the downstream rotor is lower, which may be attributed to the lack of precision in the PDB's ability to measure low current draw. The optimization of the Tetrahedron Dodecacopter used a similar method as described above, except the training data for that method consisted of only the data collected from the thrust stand experiments of the constrained tandem rotor configurations.

This method of estimation is limited by the training data it uses. Like most estimation methods that are based on empirical data, extrapolating the training data will lead to inac-

curacy in the estimation. This is somewhat seen in this estimation method. The training data included the data from all of the unconstrained tandem rotor configurations, where the *Re* of the upstream and downstream rotors are roughly equivalent at all times. The test sets that show higher error in estimation (test set 6, 7, 14, 15 and 16) are those with a 10,000 or more difference between *Re* of the upstream and downstream rotor. Improvements in the polynomial surface regressions would also produce more accurate results. This should be considered when viewing the results of this method. Overall, the pseudo-surrogate model can provide a rough estimate of the thrust, torque, and power consumption of the downstream rotor, given the angular velocity of both rotors and their position relative to one another.

5.4 Results of the Semi-Coaxial and Oblique Rotor Configuration

5.4.1 Semi-Coaxial and Oblique Rotors Performance Metrics

The oblique rotor configurations are only analyzed using the overlap interference factor. The performance metrics used to analyze the efficiency of the semi-coaxial rotor configuration are the same as those used to analyze the previously discussed tandem rotor configurations. However, there are slight differences in how the metrics are calculated.

The performance metric: C_T/C_P

The percent decrease in C_T/C_P of the downstream rotor is calculated the same as was done for the tandem-rotor configurations. One downfall of using this metric to analyze the semi-coaxial rotor configuration is that the percent decrease of C_T/C_P only accounts for the aerodynamic effects from the wake of the upstream rotor onto the downstream rotor and not the reduction in Z-force due to the angles $\zeta_{U,D}$.

The overlap interference factor performance metric

To account for both the degradation in performance of the downstream rotor due to aerodynamic effects of operating in the wake of the upstream rotor and the decrease in Z-force caused by increasing $\zeta_{U,D}$, the overlap interference factor is calculated in a different manner than was done for the tandem-rotor configurations. There are two differences in the calculation of the overlap interference factor for the semi-coaxial rotor configuration. Firstly, the interference factor is calculated as the ratio of power consumption needed to generate a collective force along the z-axis (i.e., opposing gravity), which will be referred to as Z-force hereinafter. Meaning, that the numerator of the interference factor is the power required for the semi-coaxial configuration to create a certain Z-Force, not overall thrust. Secondly, the denominator is the power required for two isolated rotors to generate an equivalent Z-force; however, unlike the semi-coaxial, the isolated rotors are parallel with the ground, meaning $\zeta = 0$. As was done for the tandem-rotor configurations, the power consumption of the semi-coaxial configuration and the two isolated rotors used in the overlap interference factor should be for a given collective Z-force, F_{des}. During the experiments, since the rotors of each configuration tested are not operating at angular velocities that produce precisely the desired collective Z-force, the power consumption of each configuration at the selected collective Z-force is calculated mathematically using the force, angular velocity, and power consumption data gathered during the experiments along with the calculated thrust and power coefficients. Similar to the method used when calculating the overlap interference factor for the tandem-rotor configurations, a method is used to estimate the power consumption of the downstream rotor when operating simultaneously with the upstream rotor, $P_{D,simu}$, based on the unprocessed data collected of the two rotors operating. In contrast, the upstream rotor operates at a specified ***Re***. This is first done by calculating the amount of Z-force the downstream rotor is required to create, which is the difference between the collective desired Z-force and the Z-force generated by the upstream rotor, as shown in Eq. (5.10). Note that the Z-force of the upstream rotor, F_U, and the power

consumption of the upstream rotor, $P_{U,simu}$, are gathered from the unprocessed thrust stand data. Using the desired Z-force of the downstream rotor, the desired angular velocity of the downstream rotor can be found using Eqs. (5.11) and (5.12). The thrust coefficient used in Eq. (5.12) is calculated using the thrust stand data of the downstream rotor as it operates in the wake of the upstream rotor while the upstream rotor operates at the specified *Re* in the given semi-coaxial configuration. Using the thrust coefficient of the downstream rotor in these conditions ensures that the aerodynamic effects caused by the downstream rotor operating in the wake of the upstream rotor are captured in the analysis. The power consumption of the downstream rotor is calculated by quantifying the relationship between the angular velocity of the upstream rotor and the percent decrease in the power coefficient of the downstream rotor operating independently versus operating in the wake of the upstream rotor. The power coefficient of the downstream rotor operating independently is adjusted to correspond to the angular velocity that the downstream rotor operates at when operating simultaneously with the upstream rotor. This percent decrease is then multiplied by the power coefficient of the downstream rotor operating independently at the desired angular velocity. The reason that the power coefficient is calculated differently than the thrust coefficient is because electrical power is being measured, not mechanical power; thus, unlike the thrust coefficient, which is relatively constant regardless of the angular velocity of the rotor being measured, the power coefficient changes slightly as a function of angular velocity. The desired collective Z-forces used for these analyses are 23 N, 21 N, 16 N, and 12 N which correspond to the *Re* of the upstream rotor operating at a *Re* of 135,000, 125,000, 100,000, and 75,000 respectively. These values for the collective Z-force are chosen so that the data used to estimate the percent decrease in the power coefficients are not extrapolated. The power consumption of the isolated rotors, $P_{U,iso}$ and $P_{D,iso}$, are found through the creation of polynomial regressions using the thrust stand data of the rotors operating independently while $\zeta_{U,D} = 0^o$. The two polynomials (one for each rotor) are then solved for $F_{des}/2$ to calculate $P_{U,iso}$ and $P_{D,iso}$. As previously mentioned, the goal of using the

overlap interference factor as a metric is to account for both the wake interactions and the direction of the thrust generated by each rotor of the semi-coaxial configuration.

$$F_{D,des} = F_{des} - F_U \tag{5.10}$$

$$T_{D,des} = \frac{F_{D,des}}{cos(\zeta_D)} \tag{5.11}$$

$$\Omega_{des} = \sqrt{\frac{T_{D,des}}{C_T \rho A}} \frac{1}{R} \tag{5.12}$$

5.4.2 Presentation of Results and Discussion

The unprocessed data generated from each experiment can be accessed using the link in the footnotes[2]. This data includes plots showing the relationship between thrust generation in the Z-axis and power consumption and the relationship between the angular velocity of the rotors and their power consumption for each semi-coaxial and oblique rotor configuration.

Analysis using C_T/C_P

The results of analyzing the configurations using the percent decrease in C_T/C_P are shown in Figs. 5.57 to 5.59, while the results of the co-rotating configurations can be found in Fig. D.5. The results show that the rate at which the percent decrease in C_T/C_P changes as a function of $\zeta_{U,D}$ and $\frac{z}{D}$ for semi-coaxial-A configurations is not constant. Excluding the configurations that operate at a *Re* of 75,000, the semi-coaxial-A configurations where $\frac{z}{D} = 1.5$ experience a linear improvement in the percent decrease of C_T/C_P up until $\zeta_{U,D} = 30^o$, where the downstream rotor performs as well as it does when isolated. This suggests that the wake of the upstream rotor is directed far enough away from the downstream rotor such that the performance of the downstream rotor is not impacted and that any

[2]https://www.dropbox.com/sh/8ggngisxn3k54mp/AAAqgWjFklQESD1WvvglPINya?dl=0

semi-coaxial-A configurations with $\zeta_{U,D} > 30^o$ would experience no further performance benefits. As the vertical separation decreases between the rotors of the semi-coaxial-A configuration, Fig. 5.58 and Fig. 5.59 show that the rate of change of the percent decrease in C_T/C_P is more drastic between $\zeta_{U,D} = 15^o$ and $\zeta_{U,D} = 30^o$ than between the other angles. Moreover, the rate of change between $\zeta_{U,D} = 0^o$ and $\zeta_{U,D} = 15^o$ for semi-coaxial-A configurations is less when the $\frac{z}{D} = 0.96, 0.88$ than when $\frac{z}{D} = 1.5$, indicating the sensitivity of the rotor configurations performance on the vertical separation between the rotors. For semi-coaxial-A configurations where $\frac{z}{D} = 0.88$ and $\zeta_{U,D} = 45^o$, the results suggest that the downstream rotor operating simultaneously with the upstream performs slightly better than when it operates in an isolated manner (i.e., independently) for both counter-rotating and co-rotating configurations. This can be seen in the results of the counter-rotating and co-rotating semi-coaxial configurations. This improvement in efficiency may be a result of the downstream rotor operating in a similar condition as a rotor in forward flight, which could be caused by the relative angle between the rotors being 90^o. The well-documented and proven simple momentum theory states that the induced power required by a rotor in forward flight is inversely related to the free stream velocity [22]. This relationship would explain why the improvement in the efficiency of semi-coaxial-A rotor configurations where $\zeta_{U,D} = 45^o$ is greater when the $\frac{z}{D}$ is smallest, which in turn places the downstream rotor in a free stream velocity of higher magnitude than it would experience if $\frac{z}{D}$ is greater while $\zeta_{U,D} = 45^o$. However, there are clear differences between the free stream air that a rotor experiences in forward flight and the rotating slipstream created by another rotor. More experiments will need to be completed to confirm if the downstream rotor experiences an improvement in efficiency in these conditions.

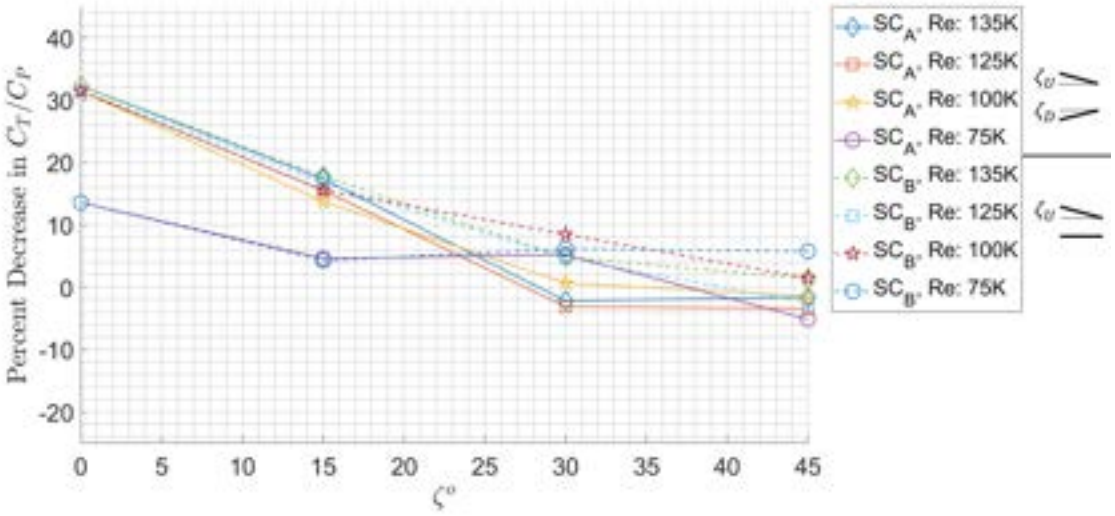

Figure 5.57: The percent decrease in C_T/C_P of the downstream rotor versus the rotor angle for both semi-coaxial configurations at a vertical separation of $\frac{z}{D} = 1.5$ for the counter-rotating spin direction.

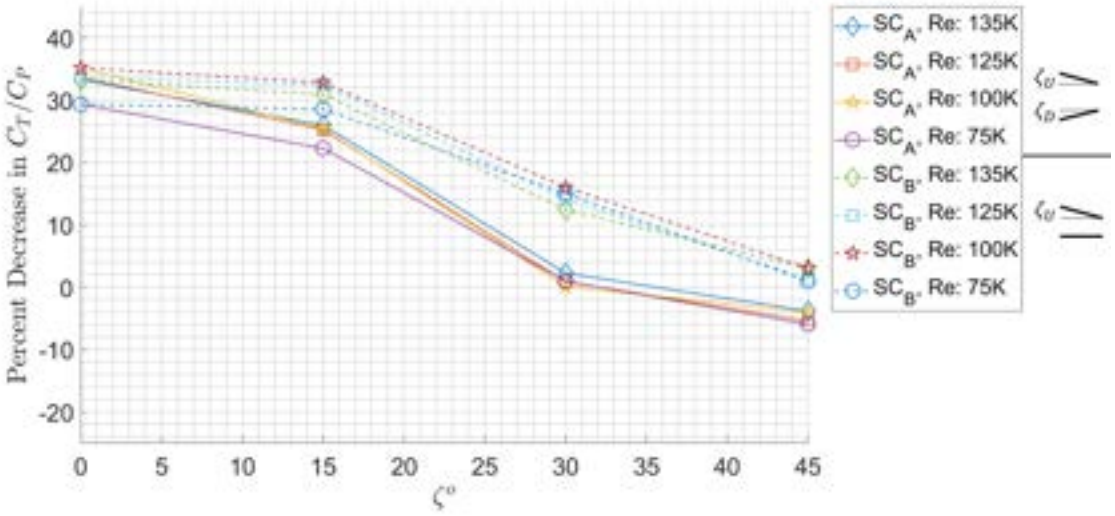

Figure 5.58: The percent decrease in C_T/C_P of the downstream rotor versus the rotor angle for both semi-coaxial configurations at a vertical separation of $\frac{z}{D} = 0.96$ for the counter-rotating spin direction.

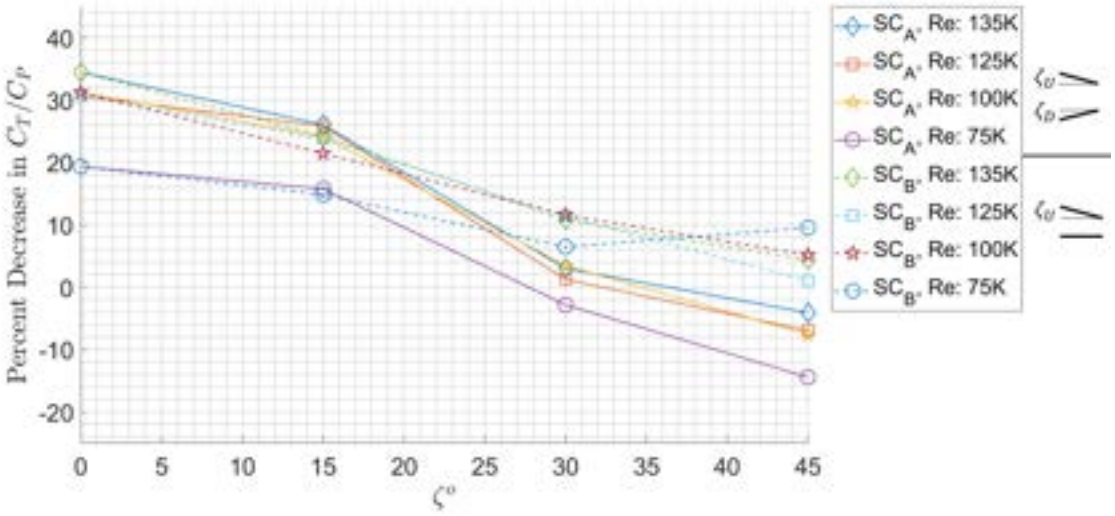

Figure 5.59: The percent decrease in C_T/C_P of the downstream rotor versus the rotor angle for both semi-coaxial configurations at a vertical separation of $\frac{z}{D} = 0.88$ for the counter-rotating spin direction.

Unlike semi-coaxial-A configurations, the downstream rotor of Semi-coaxial-B configurations operating simultaneously with the upstream rotor reaches a performance equivalent to a rotor operating in an isolated manner when $\zeta_U = 45^o$, not $\zeta_U = 30^o$, which suggest that the downstream rotor is ingesting some portion of the wake of the upstream rotor up until $\zeta_U = 45^o$. The rate at which the percent decrease in C_T/C_P changes as a function of ζ_U for the semi-coaxial-B configurations is linear for all vertical separations tested. The results of the co-rotating semi-coaxial configurations, Fig. D.5, show that there is little difference between co-rotating and counter-rotating semi-coaxial configurations. Lastly, as shown in Figs. D.5, 5.57 and 5.59, the rotor configurations where the *Re* is 75,000, perform very different than the configurations operating at higher *Re*, which is most likely attributed to the PDB's inaccuracy in measuring low current draw. Overall, the results show that the downstream rotor of both semi-coaxial rotor configurations benefits from an increase in $\zeta_{U,D}$ compared to a traditional coaxial rotor configuration; however, as previously mentioned, this analysis does not account for the decrease in maximum Z-force due

to the increase in $\zeta_{U,D}$. Data showing the percent decrease in C_T and C_P as a function of $\zeta_{U,D}$ for the semi-coaxial-A configurations and a function of ζ_U for the semi-coaxial-B configurations can be seen in Figs. D.2 and D.4. Both variables have similar trends as the analysis using C_T/C_P.

Analysis using the Overlap Interference Factor

Figures 5.60 to 5.62 show the results of analyzing the performance of the semi-coaxial rotor configurations using the overlap interference factor for each vertical separation when the upstream rotor operates at a *Re* of $100,000$ and the collective Z-force is 16 N. The results of the other three iterations of this analysis can be found in Section D.2 of the appendix.

The results in Fig. D.6 shows that for each vertical separation tested, when $15^o \leq \zeta_{U,D} \leq 30^o$ and the upstream rotor operates at a *Re* of $135,000$ the efficiency of both semi-coaxial configurations are roughly equal to the efficiency of a traditional coaxial rotor configuration. This shows that even when the upstream rotor operates at its highest possible angular velocity, both semi-coaxial rotor configurations can provide oblique capabilities with no significant efficiency loss. As $\zeta_{U,D}$ increases for the semi-coaxial-A configurations, Figs. D.6 to D.8 and Figs. 5.60 to 5.62 show that the efficiency drastically decreases. This illustrates that even though the previously discussed results of the percent decrease in C_T/C_P of the downstream rotor indicate that there are little to no aerodynamic effects between the rotors of the semi-coaxial-A configuration when $\zeta_{U,D} = 45^o$, the overall efficiency of the configuration in generating Z-force is degraded due to the high angles of $\zeta_{U,D}$. The benefits of not angling the downstream rotor, semi-coaxial-B configurations, are apparent. Although Fig. D.6 shows that the semi-coaxial-B configurations may have a slight decrease in efficiency when $\zeta_U = 45^o$, Figs. 5.60 to 5.62 shows that the semi-coaxial-B configurations are either as efficient or more efficient than the coaxial rotor configuration. This result also illustrates how significant the performance degradation of the downstream operating in the wake of the upstream rotor is while in a coaxial rotor configuration. The

performance of the downstream rotor in a coaxial rotor configuration is nearly equivalent to the decrease in Z-force between a rotor that is generating thrust completely parallel to the gravity vector and a rotor where roughly only 70 $\%$ (caused by $\zeta_U = 45^o$) of its thrust opposes gravity. This also leads to a conclusion that the angle placed on the downstream rotor in the semi-coaxial-A configuration has little impact on improving the system's efficiency in creating Z-force once $\zeta_D > 15^o$. The vertical separation between the rotors does not seem to have a significant impact on the overall performance of the system. These results show that a vehicle that implements either semi-coaxial rotor configuration where $\zeta \leq 30^o$ will be as efficient and, in some cases, more efficient than a coaxial rotor configuration in generating Z-force. However, it should be noted that unlike the semi-coaxial-A configuration, the semi-coaxial-B configurations will not have the capability of generating pure forces in the lateral direction or pure moments about the roll and pitch axis.

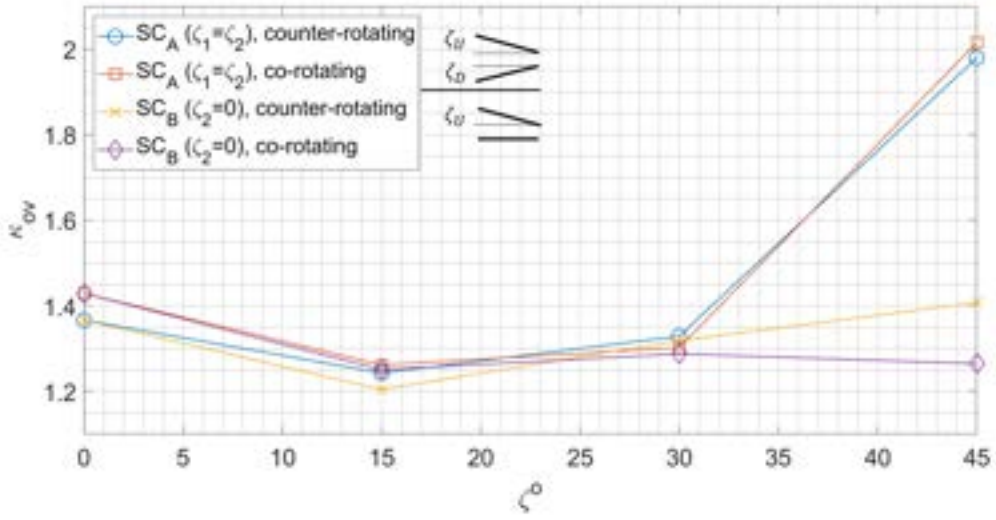

Figure 5.60: Rotor angle vs. overlap interference factor while $\frac{z}{D} = 1.5$ and the upstream rotor operates at a *Re* of $100,000$

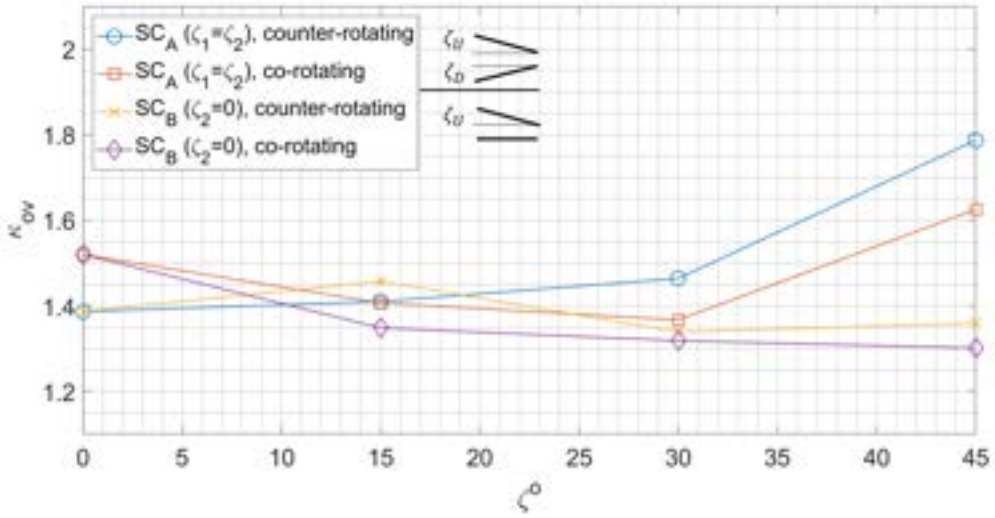

Figure 5.61: Rotor angle vs. overlap interference factor while $\frac{z}{D} = 0.96$ and the upstream rotor operates at a *Re* of $100,000$

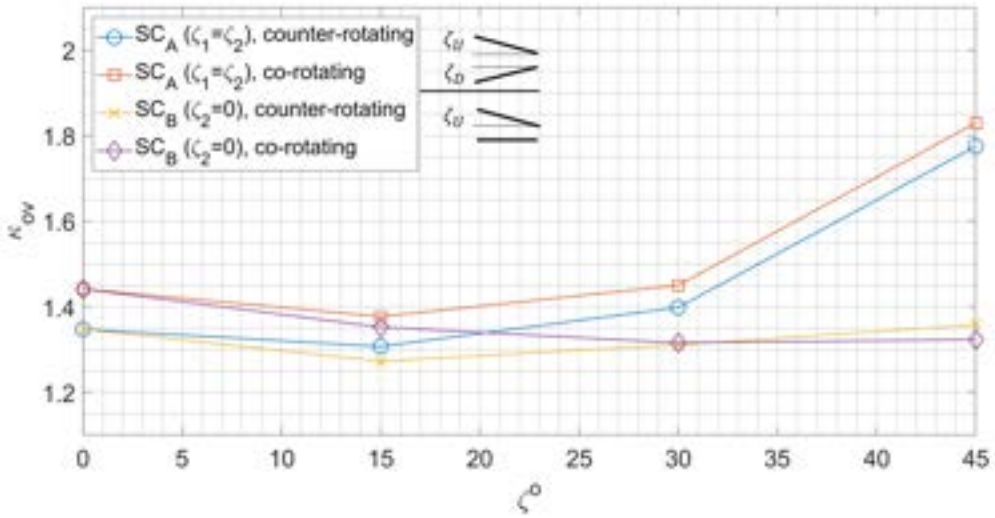

Figure 5.62: Rotor angle vs. overlap interference factor while $\frac{z}{D} = 0.88$ and the upstream rotor operates at a *Re* of $100,000$

Oblique Rotor Configuration Results

The oblique rotor configurations are analyzed using only the overlap interference factor. Using the overlap interference factor the results of the performance of the oblique rotor configurations are shown in Figs. 5.63 and 5.64. For this analysis, the power consumption values used in the overlap interference factor equation are for a Z-force value of 2.25 lbf (10 N), and the oblique configurations are compared to two isolated rotors generating 2.25 lbf (10 N) each and have a rotor angle of $\zeta_{1,2} = 0$. The Z-force value of 2.25 lbf is chosen so that the data used in this analysis is interpolated from the data collected on the thrust stand rather than extrapolated. Also shown on Figs. 5.63 and 5.64 are two rotors operating independently at the rotor angle, ζ, specified in the figure, meaning that there are no interactions between the wakes of both rotors. Figs. 5.63 and 5.64 show that there is a negligible difference in performance between the rotors operating simultaneously and isolated until $\zeta_{1,2} = 45^o$ for both separations, $x_D = 1.1, 1.5$. There is also little to no difference in the performance of the oblique rotor configurations in regard to the change in separation distance.

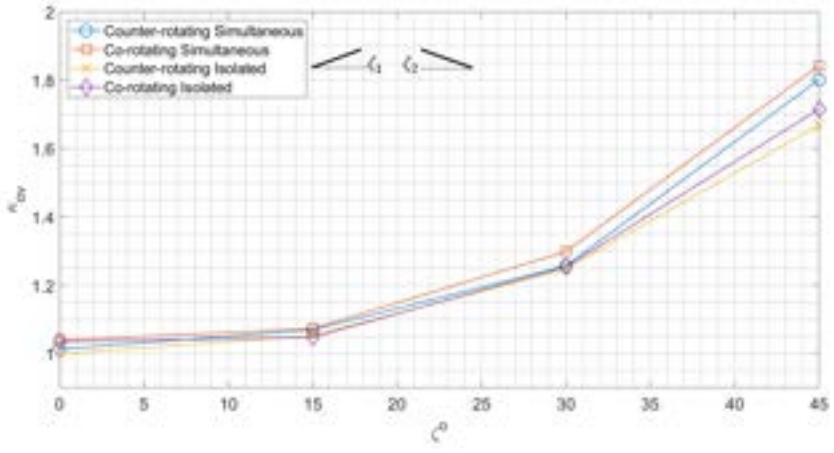

Figure 5.63: Rotor angle vs. overlap interference factor for oblique rotor configurations when $x_D = 1.5$

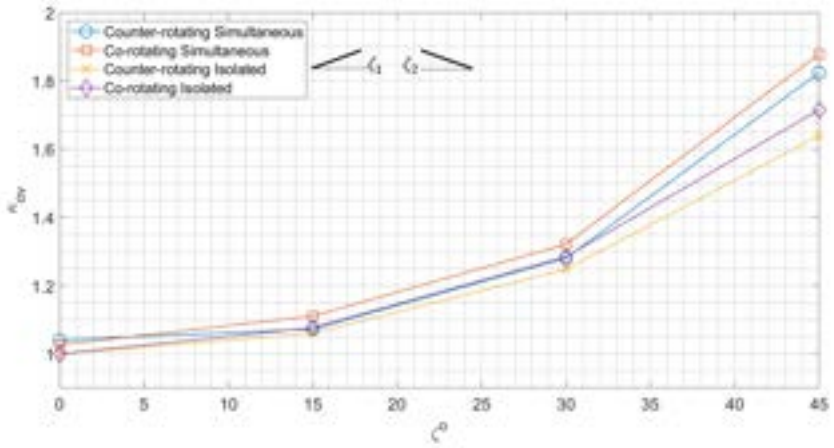

Figure 5.64: Rotor angle vs. overlap interference factor for oblique rotor configurations when $x_D = 1.1$

5.5 Conclusion

The performance of the constrained and unconstrained tandem rotor configurations and the semi-coaxial and oblique rotor configurations have been presented in this chapter. Each rotor configuration is analyzed using one or more performance metrics discussed in detail before presenting the results. The optimization of the Tetrahedron Dodecacopter and the Tetracopter have also been presented in this chapter, along with the method used to estimate the performance of the downstream rotor using the thrust stand data. The method used to estimate the performance of the downstream rotor in each configuration has been discussed in-depth, along with its limitations. Overall the results of the thrust stand experiments match those of previously published work. The estimated optimal vehicle designs for the Tetracopter and the Tetrahedron Dodecaocpter correspond with the results of similar studies that investigated the performance of overlapping rotors. However, to the author's knowledge, using empirical data to optimize the design of a vehicle that can have overlapping rotors is novel. The results of the semi-coaxial rotor configuration showed that the configuration is either as efficient or more efficient than a traditional coaxial rotor config-

uration depending on the angle of the rotors. Results show that the novel semi-coaxial-B configuration provides enhanced efficiency compared to the semi-coaxial-A configuration. The oblique rotor configurations showed no efficiency benefits or deficits due to wake interactions. Overall, the thrust stand tests have provided a vast amount of data that has allowed for a thorough analysis of the three rotor configurations.

CHAPTER 6
FLIGHT TESTS

6.1 Summary

Flight tests of the four-module Tetrahedron Dodecacopter, the Gen-1 Dodecacopter, and the 16 module Tetrahedron Dodecacopter, the Gen-2 Dodecacopter, are performed. These flight tests aim to capture and quantify the effects of rotor-rotor interactions of overlapping non-coplanar rotors in a less ideal environment than a thrust stand. To do this, each vehicle is flown at a relatively steady hover for several seconds. For these tests, angular velocity measurements of the rotors are used to estimate the overall thrust generated by the vehicle. Using the angular velocity data of each rotor along with the weight of the vehicle and the known performance of the rotor operating in isolation, the performance impact of the rotor-rotor interactions can be quantified. Comparisons between the Gen-1 Dodecacopter, which has one layer of non-coplanar overlapping rotors, and the Gen-2 Dodecacopter, which has four layers of non-coplanar rotors, are also presented in this section. This comparison aims to investigate if the degradation in performance for multiple layers of non-coplanar, overlapping rotors is scaled with the number of layers of non-coplanar rotors. Parallels between the thrust stand data and the flight test data are also discussed in this chapter.

6.2 Dodecacopter Design

6.2.1 Airfame

As previously mentioned, the shape of the airframe of each module of the Dodecacopter is the shape of a dodecahedron. The airframe is made of 5 mm carbon fiber tubes that are connected to one another using custom joints 3D printed from Polyethylene terephthalate glycol (PETG). The ends of the carbon fiber tubes are fitted with 3D printed end pieces

made of FlexFill thermoplastic polyurethane (TPU). The carbon fiber tubes and PETG joints are connected by compressing FlexFill end pieces between the two pieces of the PETG joint. It must be noted that the motors, blades, and ESCs used on the thrust stand differ from those used with the Dodecacopter. This is an unfortunate result of conducting the thrust stand experiments prior to properly sizing the modules of the Dodecacopter. The avionics of each module is mounted in the center of the module's airframe, using three carbon fiber tubes with a larger diameter than those used to build the exterior airframe, as shown in Fig. 6.1. The vertical and horizontal separation ratios between the rotors of the Tetrahedron Dodecacopter are $\frac{x}{D} = 0.65$ and $\frac{z}{D} = 0.86$, respectively. Note, based on the thrust stand experiments; the Dodecacopter should experience performance degradation due to rotor-rotor interactions. The weight of the Gen-1 Dodecacopter is roughly 6.57 kg (64.49 N).

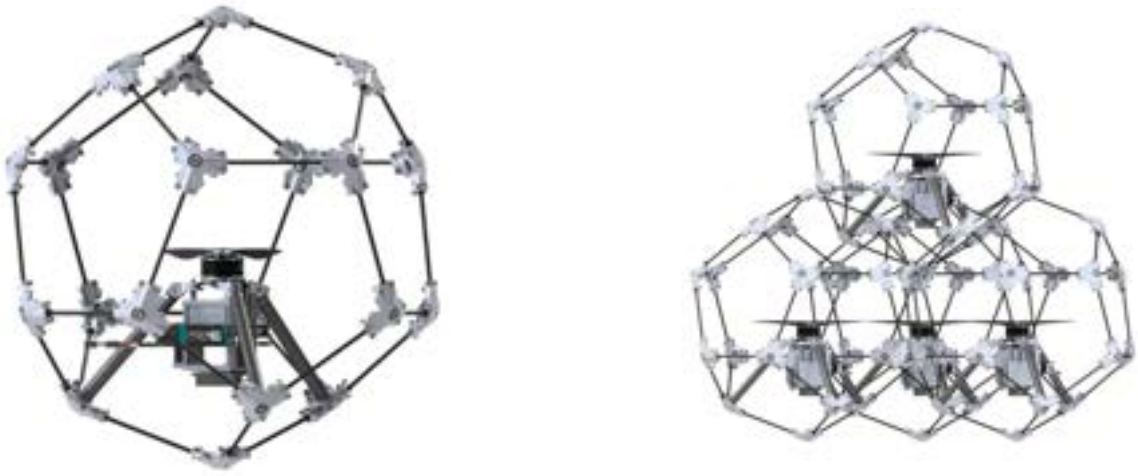

Figure 6.1: Computer Aided Design models of the Dodecacopter module (left) and the Gen-1 Dodecacopter (right).

6.2.2 Propulsion and Power Supply

Each module is equipped with a KDE4215XF-465 brushless motor paired with a KDEXF-UAS55 electronic speed controller (ESC), and a tri-blade 15.5" propeller that uses KDE-CF155-TP rotor blades. Each motor of the Dodecacopter is powered by a Tattu R-Line

22.2 V 95 C 1300 mA h battery.

6.2.3 Flight Controller

Each module of the Gen-1 Dodecacopter is equipped with a Pixhawk4 flight controller; however, only one flight controller, which is on the module that lies on the upper vertex of the Gen-1 Dodecacopter, is used during flight. A custom version of the ArduPilot [65] flight controller software is installed on each Pixhawk4 [74] flight controller. For the ArduPilot firmware to work properly, two custom motor allocation matrices, one for the Gen-1 Dodecacopter and another for the Gen-2 Dodecacopter, were added to the firmware.

6.2.4 Sensors

A Hobbywing RPM sensor is soldered to each motor of the Gen-1 Dodecacopter. Select motors of the Gen-2 Dodecacopter are also equipped with a hobbywing RPM sensor. These RPM sensors pass data to either the Pixhawk4 or an Arduino Mega 2560, which stores the data.

6.2.5 Communication

Each vehicle uses a FrSky X8R receiver that receives radio commands from the pilots via the FrSky Taranis transmitter. Each vehicle also has a wifi module that communicates with the motion capture system used.

6.3 Flight Test Setup

Due to the limited space to place the flight controller on each Dodecacopter module, the flight controller is placed underneath the rotor; more specifically, the flight controller is placed in the slipstream of the rotor. This is an issue because the flight controller uses barometric pressure to measure its altitude; thus, the pressure differentiation caused by the rotor causes the altimeter to produce incorrect altitude data. To solve this problem,

and improve the vehicle's ability to maintain a specific altitude and position, an OptiTrack Motion Capture system [75] is used. The vehicle is flown indoors in an area with sufficient space so that no significantly unique aerodynamic effects are present. The stability of the vehicle is not ideal, so for the safety of the operators as well as the vehicle, the vehicle is tethered to the ceiling of the room in which it is flown in, as shown in Fig. 6.2.

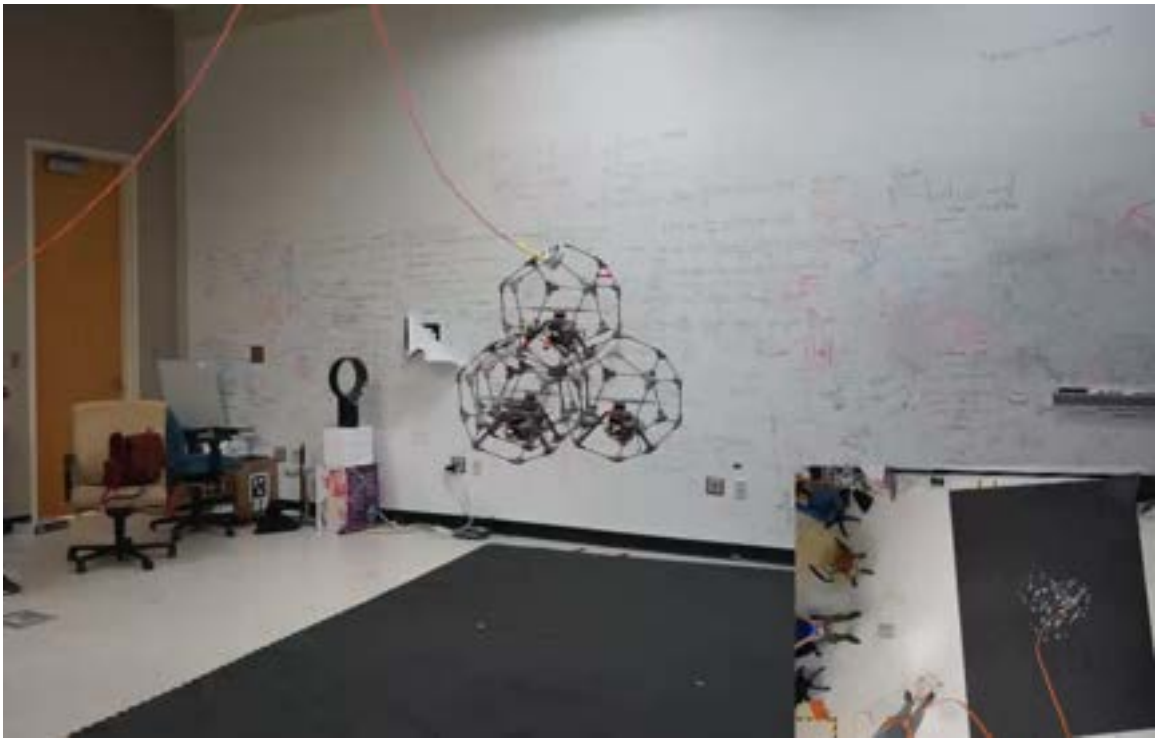

Figure 6.2: The Gen-1 Dodecacopter flight test. The lower right corner of the image shows a top view of the vehicle during the flight test.

6.4 Results of the Tetrahedron Dodecacopter Flight

The vehicle's controller gains are tuned so that the vehicle is stable enough to allow for a relatively steady hover; however, the hover is not ideal. The attitude angles of the vehicle during the flight are shown in Fig. 6.4. The altitude of the vehicle remained roughly at 1.2 m for the majority of the flight, as shown in Fig. 6.3. The angular velocity measurements of each rotor are shown in Fig. 6.5. Figure 6.5 shows that the upstream rotor operated at a higher angular velocity than the three downstream rotors. The rotor's angular velocity is

determined by the flight controller, which uses the user-defined motor matrix along with the attitude and position data measured by the internal inertial measurement unit (IMU). Based on the thrust stand data gathered from the tandem-rotor configurations, a higher angular velocity of the upstream rotor should degrade the performance of the downstream rotors slightly more than if the upstream rotor is operated at a lower angular velocity, strengthening the chances of the degradation in the downstream rotors being captured during the flight test.

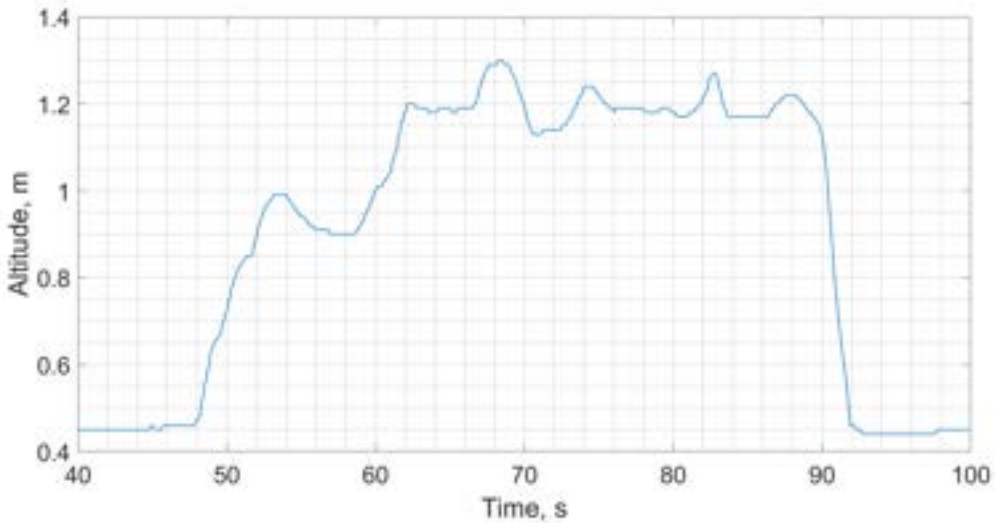

Figure 6.3: Altitude of the Gen-1 Dodecacopter

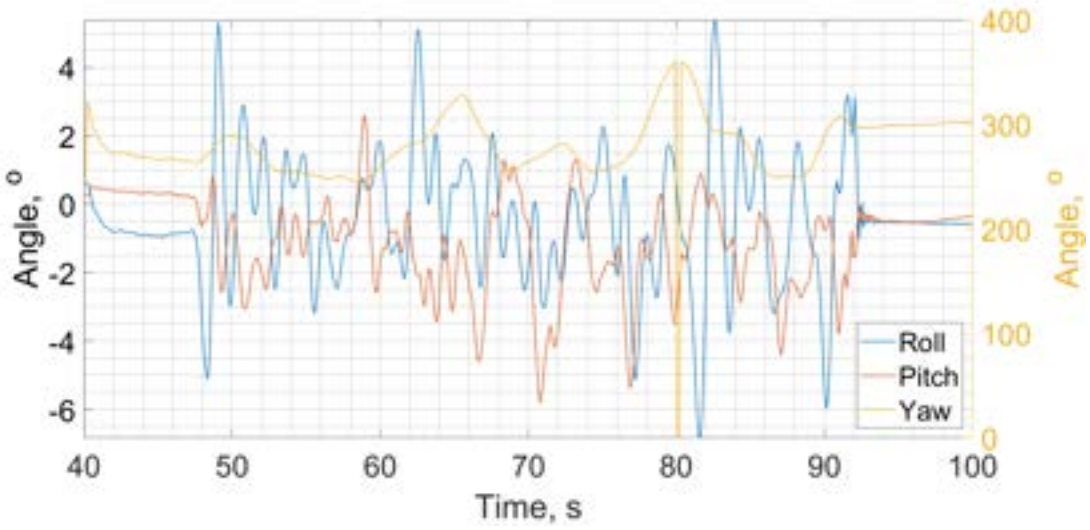

Figure 6.4: Attitude angles of the Gen-1 Dodecacopter during the flight test

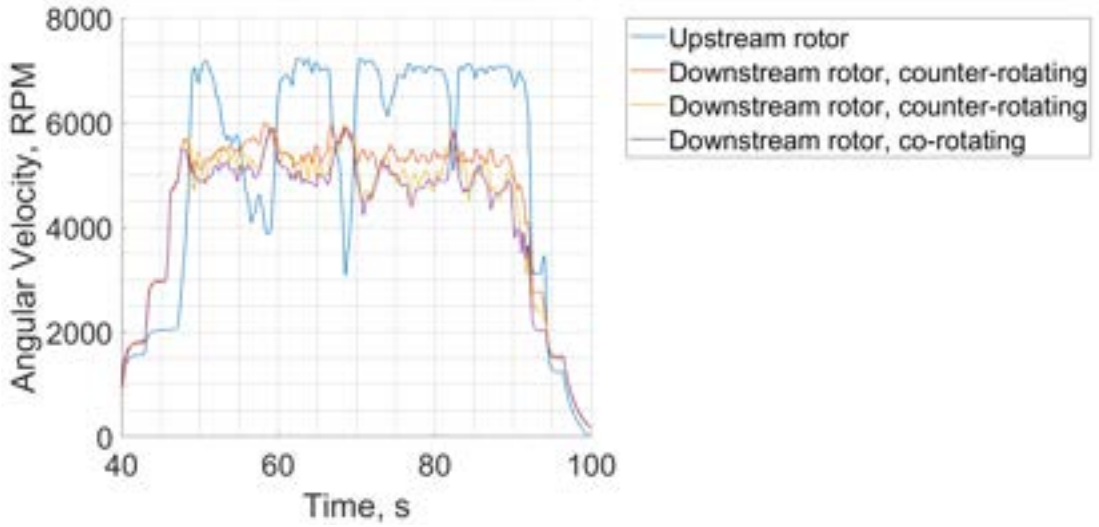

Figure 6.5: The angular velocity of each rotor during the flight test

Two analyses are performed using the gathered angular velocity data. The first analysis estimates the total thrust generation by the vehicle using the manufacturer-provided performance data of the rotor. This analysis ignores the aerodynamic rotor-rotor effects and estimates the total thrust production if each rotor operates as if they are isolated. The results of this analysis shown in Fig. 6.6, indicate that the average of the estimated thrust is 91 N, which is 41 % more than the weight of the vehicle. This result suggests that the

angular velocity of the rotors is higher than what is needed to produce thrust equal to the weight of the vehicle if the rotors are operating in an isolated manner.

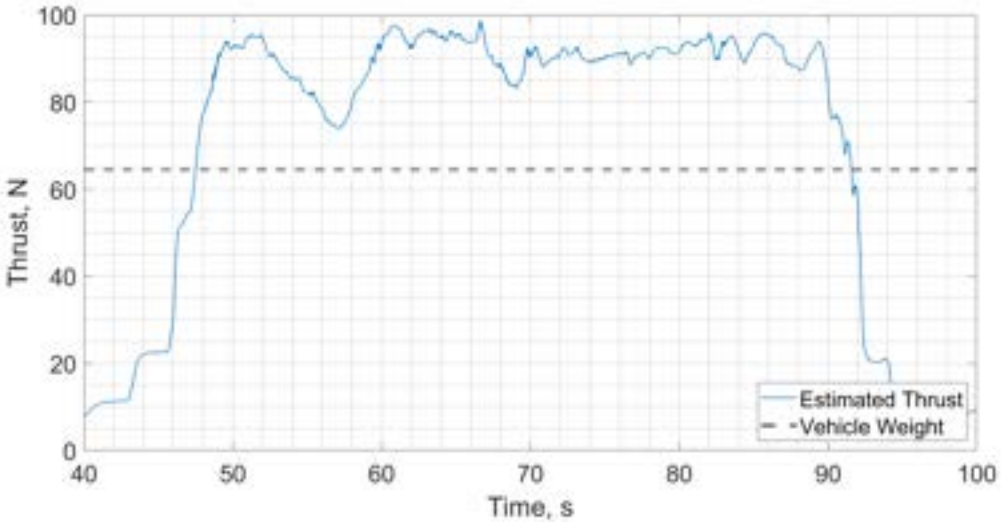

Figure 6.6: The estimated thrust generation of the Gen-1 Dodecacopter

The second analysis uses the angular velocity measurements of the rotors as well as the manufacturer's performance specifications of the rotor to estimate the thrust and thrust coefficient of each of the Gen-1 Dodecacopter's rotors. This is done using several assumptions. The first assumption is that the downstream rotors do not affect the performance of the upstream rotor. This is assumed based on the results of the thrust stand experiments. The second assumption is that all three downstream rotors produce the same thrust. This assumption is based on the fact that the vehicle is at a relatively steady hover and is not rolling nor pitching, which is roughly true as seen in Fig. 6.4. Using the manufacturer's performance specifications of the Gen-1 Dodecacopter's rotors and the measured angular velocity of the upstream rotor, the thrust and thrust coefficient of the upstream rotor are estimated. Using acceleration data measured by the IMU, the total thrust produced by all four rotors can be calculated given the vehicle's weight. The estimated thrust of the upstream rotor is then subtracted from the calculated thrust of the vehicle, which produces the estimated thrust of the three downstream rotors. Using the second previously mentioned assumption, the estimated thrust of the three downstream rotors is equally distributed amongst the three

rotors. Using the estimated thrust value of the three downstream rotors along with their measured angular velocities, their thrust coefficients are calculated as shown in Fig. 6.7.

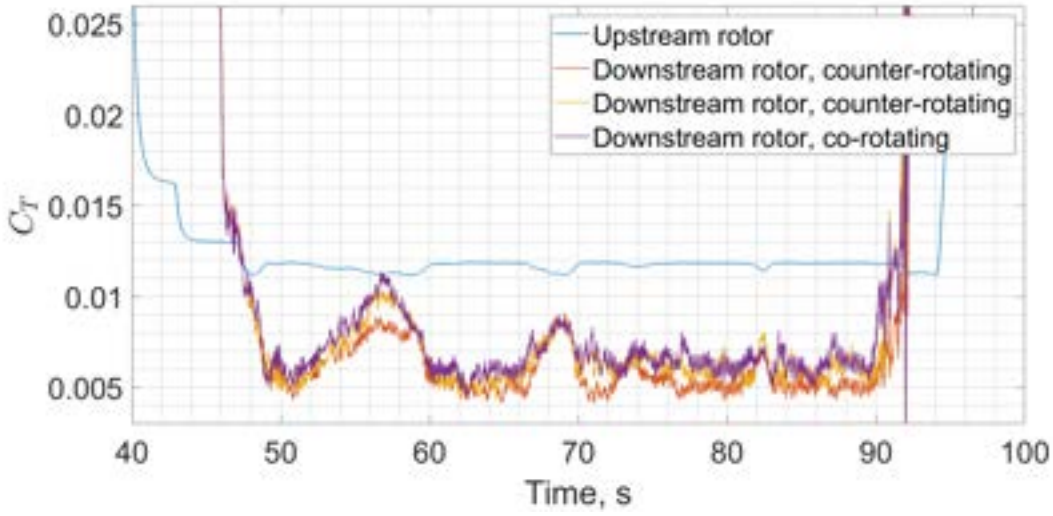

Figure 6.7: The estimated C_T of the Gen-1 Dodecacopter's rotors

Figure 6.7 shows that the downstream rotors have thrust coefficients that are roughly 45 % to 55 % less than the thrust coefficient of the upstream rotor, which is a much more drastic decrease than what was found through the thrust stand experiments. This is most likely due to the rotors used on the Gen-1 Dodecacopter being larger and the propeller being a tri-blade instead of the two-bladed propellers used in the thrust stand experiments. The *Re* that the Gen-1 Dodecacopter propellers operate at during the flight test are between 100,000 and 143,000 which is slightly higher than the range of *Re* that the rotors used on the thrust stand are operated at. The increase in the number of blades impacts the velocity at which tip vortices convect axially away from the plane of the propeller [32], meaning that the velocity of the slipstream that the downstream rotors of the Gen-1 Dodecacopter operate in is higher than the slipstream of the downstream rotor on the thrust stand. This explains why the estimated thrust coefficient of the downstream rotors of the Gen-1 Dodecacopter is degraded more than the downstream rotor used on the thrust stand.

6.5 Comparison between Dodecacopter Generations

The Gen-2 Tetrahedron Dodecacopter is flown in the same indoor environment as the Gen-1 Tetrahedron Dodecacopter, as shown in Fig. 6.8. Similar to the flight test of the Gen-1 Tetrahedron Dodecacopter, the OptiTrack system and a tether is also used in this flight test. During the flight, the Gen-2 Tetrahedron Dodecacopter maintained an altitude of roughly 1.6 m, but as shown in Fig. 6.9, the hover was not ideal.

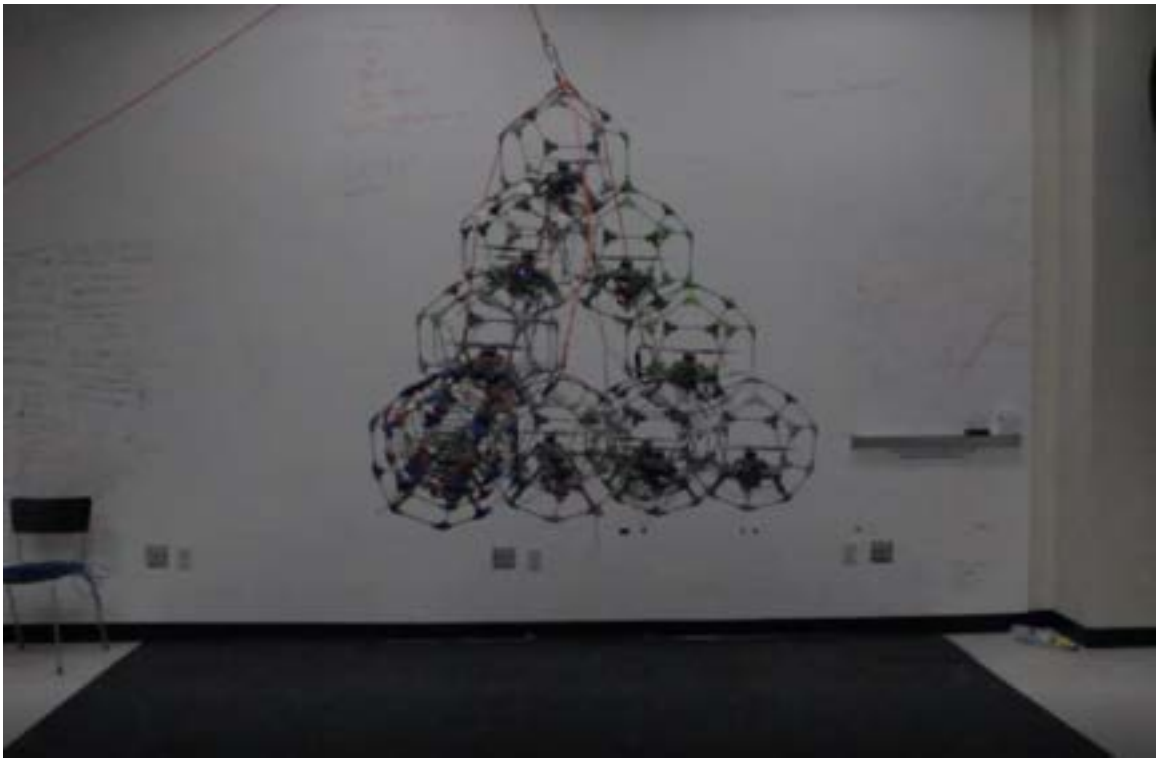

Figure 6.8: The Gen-2 Tetrahedron Dodecacopter flight test.

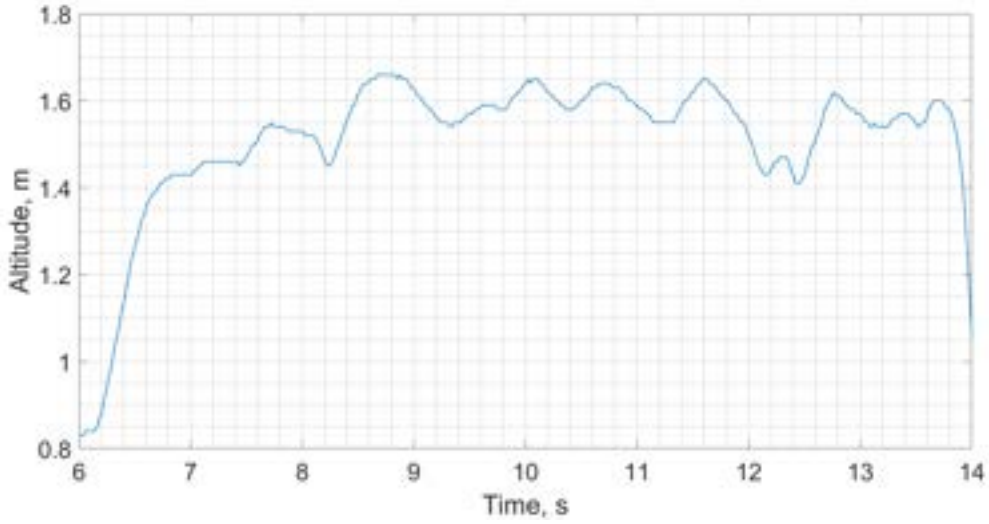

Figure 6.9: Altitude of the 16 rotor Tetrahedron Dodecacopter during the flight.

The Gen-2 Tetrahedron Dodecacopter weighs roughly 27.3 kg (267.8 N), which is roughly four times the weight of the Gen-1 Tetrahedron Dodecacopter. Using the same method as was used to estimate the thrust of the Gen-1 Tetrahedron Dodecacopter, the average estimated thrust of the Gen-2 Tetrahedron Dodecacopter in hover is 407 N, nearly 52 % more than the weight of the vehicle, which is slightly higher than the estimated thrust of the Gen-1 Tetrahedron Dodecacopter compared to its weight. This is expected because the Gen-2 Tetrahedron Dodecacopter has three layers of overlapping rotors as opposed to one layer of overlapping rotors on the Gen-1 Tetrahedron Dodecacopter. Using the assumption that any rotor operating in the slipstream of another rotor on the Gen-2 Tetrahedron Dodecacopter is only affected by the aerodynamic effects created by the rotor directly above it, the thrust of the Gen-2 Tetrahedron Dodecacopter should be equal to fourfold the estimated thrust of the Gen-1 Tetrahedron Dodecacopter once the thrust coefficient of the three rotors on the third layer of modules (third from the top-most module) is decreased by roughly 45 %. Using the angular velocity measurements of the Gen-2 Tetrahedron Dodecacopter, the thrust generated by each rotor is estimated along with their thrust coefficients. The percent decrease in the thrust coefficient of the three rotors on the third layer of the Gen-2 Tetrahedron Dodecacopter needed for the estimated thrust of the Gen-2 Tetrahedron Dodecacopter to equal

the estimated thrust of four Gen-1 Tetrahedron Dodecacopters operating independently of one another is calculated to be 39.5 % with respect to the thrust coefficient calculated using the manufacturer's performance data. The difference in the expected percent decrease of 45 % and the calculated decrease of 39.5 % could be attributed to the unsteady nature of the hover of both the Gen-1 and Gen-2 Dodecacopter. The results of this comparison suggest that the degradation in performance of the rotors in the Gen-2 Tetrahedron Dodecacopter rotor configuration, where there are multiple non-coplanar layers of rotors, is not a function of the number of layers of non-coplanar rotors in the configuration, which means that the rotors of the third or fourth layer of modules (third and fourth from the top) are only impacted by the rotors directly above them.

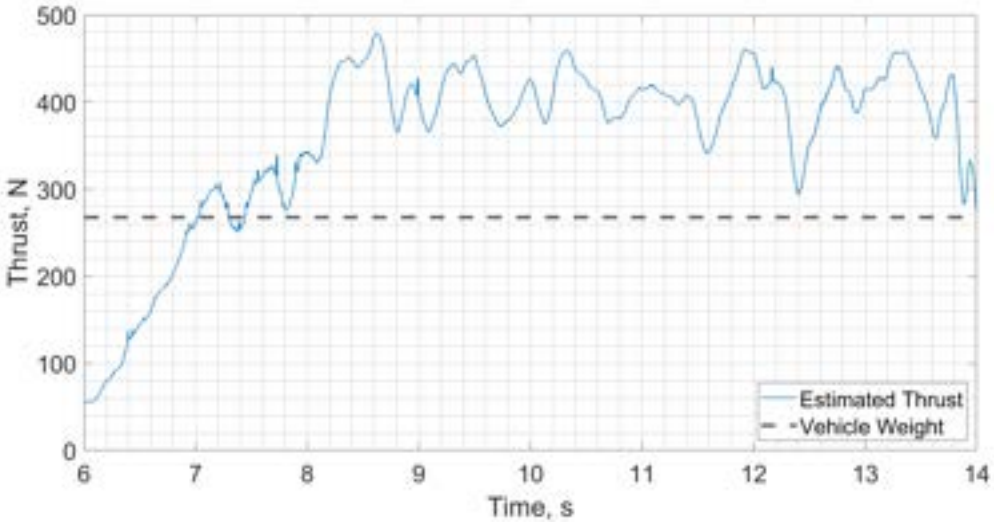

Figure 6.10: The estimated thrust generation of the Gen-2 Tetrahedron Dodecacopter during the flight test.

6.6 Conclusion and Improvements

Both generations of the novel Tetrahedron Dodecacopter were fabricated and flown. The angular velocity of each motor was recorded, and the thrust generation of both vehicles was estimated using the performance data of the rotors provided by the manufacturer. The estimated degradation in performance of the downstream rotors of either generation Do-

decacopter is more than the degradation in performance measured during the thrust stand experiments, which is largely attributed to the increase in the number of blades of the propeller used on the Dodecacopters versus the propeller used on the thrust stand. Based on the comparison between the Gen-1 and Gen-2 Dodecacopter, it seems as if the performance of the Gen-2 Dodecacopter is worse because 15 of the 16 , 93.7 %, rotors operate in the slipstream of another rotor, as opposed to 75 % of the rotors in the Gen-1 Dodecacopter operating in the wake of another rotor. The results of the analysis also suggest that the downstream rotors of the Gen-2 Dodecacopter are only impacted by the rotor immediately above it. However, the limitations of this analysis should be noted, such as the quality of the hover that each vehicle maintained while the presented data was collected. Another aspect that is not captured is the aerodynamic effects of the rotors operating in the airframe as opposed to operating in an isolated manner. Another factor that may have impacted the results of the flight test is the imperfect alignment between the planes of each rotor of the Gen-1 and Gen-2 Dodecacopter. Lastly, the effects of the vehicles' rotors rapidly changing angular velocity needed to maintain a steady hover also impact the results of the tests and are known to degrade the efficiency of a rotor compared to the rotor being operated on a thrust stand [76].

CHAPTER 7
RESEARCH CONCLUSIONS

7.1 Design Implications

The data gathered from the thrust stand experiments as well as the flight tests provide insight into the best design practices for vehicles with overlapping rotors. For vehicles with non-coplanar rotors, if possible, given the goal of the vehicle, the overlap between the rotors of the vehicle should be minimized; however, if the vehicle's rotors must have some amount of overlap, the effects of rotor-rotor interactions due to rotor overlap is minimal when $\frac{x}{D} \geq 0.75$. The vertical overlap between the rotors of said vehicle has little to no impact on the performance of the rotors as long as the horizontal separation ratio is $\frac{x}{D} \geq 0.75$. In the case where the vehicle must have a significant amount of overlap, $\frac{x}{D} = 0.44$, the vertical separation should be minimized in order to improve the vehicle's hover efficiency. When optimizing these vehicles, the airframe's weight as the separation between the rotors increases must be accounted for to achieve optimal hover efficiency. Changing the empty weight of these vehicles may change the optimal rotor separation of the vehicle. If one would like to measure the change in a vehicle's hover efficiency due to rotor-rotor interference, using the measured angular velocity of the vehicle and the manufacturer-provided performance data of the propeller can provide an estimate of the performance degradation of the rotors.

For vehicles that currently implement coaxial rotor configurations, for a simple rearrangement of the relative angles between the rotors, the semi-coaxial rotor configuration can be implemented, which allows the vehicle to enable DFC. The efficiency of the vehicle is maintained or improved depending on the operational angular velocity of the rotors and the time required for the vehicle to respond to disturbances is reduced.

7.2 Summary of Contributions

The following itemized list discusses the key contributions of this thesis.

1. The design and development of two novel rotorcraft, the Tetracopter and Tetrahedron Dodecacopter, are presented in this thesis. These vehicles show that the Tetrahedron rotor configuration is feasible. These vehicles are created with the goal of being more structurally rigid than a traditional multi-agent UAS array. To date, these two multi-agent UAS are the only of their kind that have a rotor configuration that involves overlapping rotors. The development of these vehicles spurred the investigation into the hover efficiency of their design related to their rotor placement and weight.

2. Data of overlapping non-coplanar tandem rotor configurations are presented in this thesis. This data covers a broader design space regarding the vertical and horizontal separation between the rotors than any other published work. The relationship between the relative position of the rotors in a tandem rotor system and their efficiency is quantified and compared to the momentum theory. The comparison shows that, in general, the trends provided by the momentum theory are accurate despite the assumptions of the theory limiting the aerodynamic effects that are captured. The data also shows that the vertical separation between overlapping rotors has little impact on their performance.

3. The data from the thrust stand experiments are used to estimate an optimal configuration for both the Tetracopter and the Gen-1 Dodecacopter. The data shows that the weight of the vehicle and the amount of overlap between the vehicle's rotors must be accounted for when designing a vehicle with overlapping rotors, such as the Tetracopter or the Tetrahedron Dodecacopter. The optimal Gen-1 Dodecacopter design, where the vertical and horizontal separation between the rotors is constrained such that $z = \sqrt{2}x$, has a horizontal and vertical separation of $\frac{x}{D} = 0.80$ and $\frac{z}{D} = 1.13$, respectively. In this configuration, the Gen-1 Dodecacopter requires roughly 6 % more

power than a UAS with coplanar rotors; however, the Gen-1 Dodecacopter has the added benefit of being structurally rigid and, by using two or more systems, can carry payloads above its rotors. The optimal Tetracopter design, $\frac{x}{D} = -0.93$ and $\frac{z}{D} = 1.0$, has minimal rotor overlap between the upstream and three downstream rotors, and the vertical separation between the rotors does not have a significant impact on the performance of the vehicle if the rotors have minimal overlap.

4. A method that can estimate the performance of both rotors of a tandem rotor system and the optimal configuration of a vehicle with overlapping rotors is presented. This estimation method uses the thrust stand data presented in this thesis and relates the percent decrease in C_T, C_P and C_Q of the downstream rotor operating independently and simultaneously with the relative position of the upstream and downstream rotor along with the angular velocity of both rotors. This method is shown to be relatively accurate; however, the limitations of this method are based on the training data used, which in this case is the thrust stand data.

5. Data from the flight test of the Gen-1 Tetrahedron Dodecacopter and the Gen-2 Tetrahedron Dodecacopter are presented. The analysis performed using this data shows that the performance degradation of a vehicle with overlapping rotors can be captured by measuring the angular velocity of the rotors during flight. The analysis of the flight test data of the Gen-2 Dodecacopter suggests that the performance of the downstream rotors of the vehicle is only impacted by the rotor immediately upstream.

6. The efficiency of the semi-coaxial rotor configuration is investigated, and the configuration is found to be as efficient or, in some cases, more efficient than the traditional coaxial rotor configuration depending on the parameters of the semi-coaxial configuration. A vehicle using the semi-coaxial rotor configuration is able to generate thrust in the lateral directions while still being as efficient as a coaxial rotor configuration. The angle at which the semi-coaxial configuration is most efficient in generating

thrust in the z-axis is found to be $\zeta < 30^o$.

7. A different semi-coaxial configuration is presented, the semi-coaxial-B configuration, which only changes the orientation of the upstream rotor of a traditional coaxial rotor configuration. The semi-coaxial-B configuration is found to be more efficient than both a traditional coaxial rotor configuration and the already established semi-coaxial rotor configuration. The thrust stand results also show that the semi-coaxial-B configuration mitigates the issue of reduced thrust generation in the z-axis, which is an issue for the established semi-coaxial rotor configuration.

7.3 Recommendations

Recommendations for future work and additions to the presented work are as follows:

1. To further validate the estimated optimal rotor configuration of the Tetrahedron Dodecacopter, a vehicle with a tetrahedron rotor configuration where the relative position between the rotors can be easily changed could be built. This vehicle could then be flown using different rotor configurations, and data can be collected and compared to the data collected from the presented thrust stand experiments.

2. Although the analysis of the Gen-2 Dodecacopter flight test data suggests that the downstream rotors of the vehicle are only affected by the rotor immediately upstream of itself, thrust stand experiments of at least three layers of overlapping rotors should be performed. The goal of these thrust stand tests would be to quantify the relationship between the vertical and horizontal separation of the three rotors, the rotors' angular velocity, and the rotors' performance degradation due to the rotor-rotor interactions between them.

3. To further optimize the design of a vehicle that implements the Tetrahedron rotor configuration, the required flight time of the vehicle could be added to the optimization equation. Adding a required flight time, which impacts the size and weight of

the vehicle's battery, would impact the gross take-off weight of the vehicle. In turn, a change in the weight of the battery would impact the vehicle's efficiency because the upstream rotor, as well as the downstream rotors, will need to generate more thrust, meaning that the downstream rotors will operate in a stronger slipstream. A brief analysis of these effects has been shown in Section 5.3.2.

4. In this work, the metric used to measure the performance degradation of the Dodecacopter's rotors is the thrust coefficient; however, with a properly calibrated power sensors, the power coefficient of the vehicle and the FM of each rotor on the vehicle can be calculated. This data would provide a more comprehensive analysis of the vehicle.

Appendices

APPENDIX A

CONSTRAINED ROTOR CONFIGURATION DATA

A.0.1 Thrust Stand Precision Data

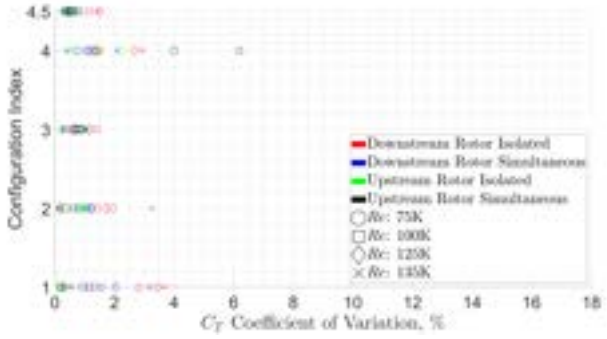

(a)

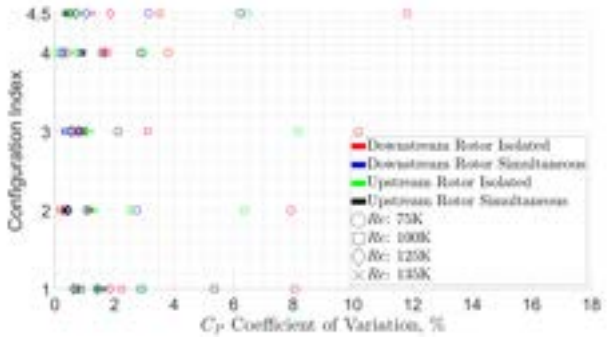

(b)

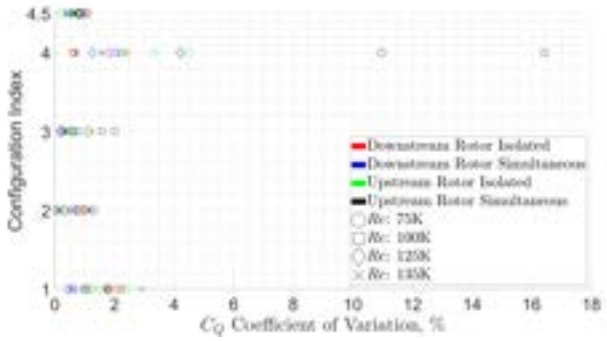

(c)

Figure A.1: The coefficient of variation of (a) C_T, (b) C_P, and (c) C_Q for each rotor in the constrained tandem rotor configurations.

A.1 Polynomial Regressions for Constrained Configurations

Table A.1: Goodness of fit data for polynomial regressions relating the angular velocity of the downstream rotor and its thrust generation when operating independently

Configuration Index	SSE	R^2	RMSE
1	0.0010	0.9999	0.0316
2	0.0014	0.9999	0.0370
3	0.0036	0.9999	0.0596
4	0.0008	0.9999	0.0278
4.5	0.0036	0.9999	0.0600

Table A.2: Goodness of fit data for polynomial regressions relating the angular velocity of the downstream rotor and its power consumption when operating independently.

Configuration Index	SSE	R^2	RMSE
1	9.3636	0.9997	3.0600
2	9.1107	0.9998	3.0183
3	6.3476	0.9998	2.5194
4	8.9668	0.9998	2.9945
4.5	8.2569	0.9998	2.8735

Table A.3: Goodness of fit data for polynomial regressions relating the angular velocity of the downstream rotor and its torque generation when operating independently.

Configuration Index	SSE	R^2	RMSE
1	1.8×10^{-6}	0.9999	0.0013
2	1.1×10^{-6}	0.9999	0.0011
3	6.7×10^{-7}	0.9999	8.2×10^{-4}
4	9.7×10^{-7} 8	0.9998	9.8×10^{-4}
4.5	1.1×10^{-6}	0.9998	0.0011

A.2 Results: Performance Coefficients

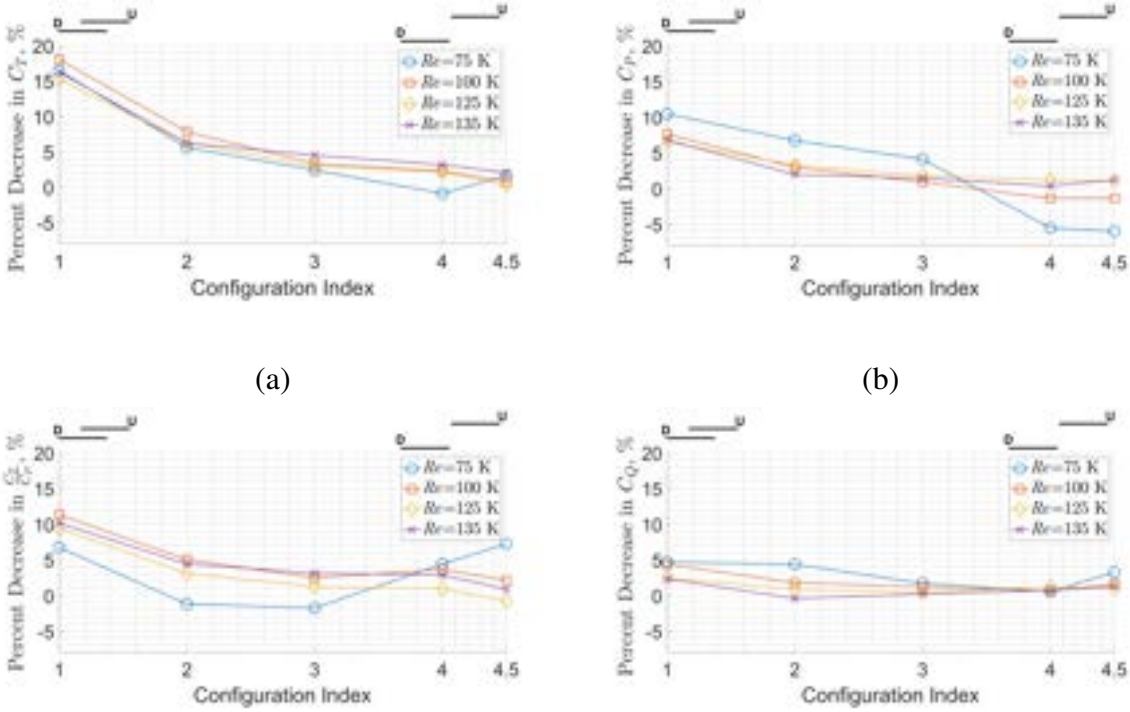

Figure A.2: The percent decrease in the ratio of the (a) thrust coefficient, (b) power coefficient, (c) ratio of thrust and power coefficient and (d) torque coefficient of the downstream rotor operating independently and simultaneously in the co-rotating spin direction.

A.3 Results: Overlap Interference Factor of Constrained Configurations

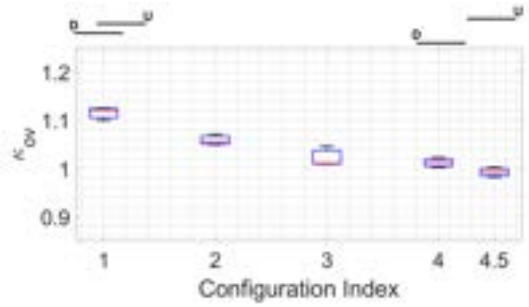

(a) $Re = 125,000$, counter-rotating

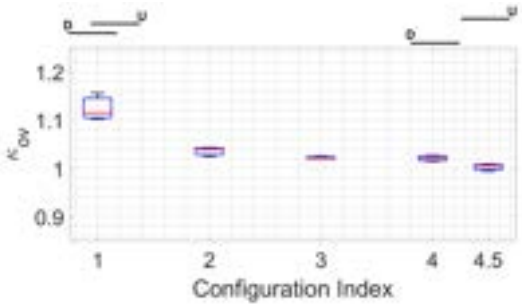

(b) $Re = 125,000$, co-rotating

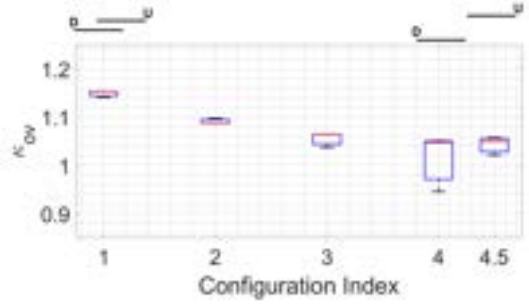

(c) $Re = 100,000$ counter-rotating

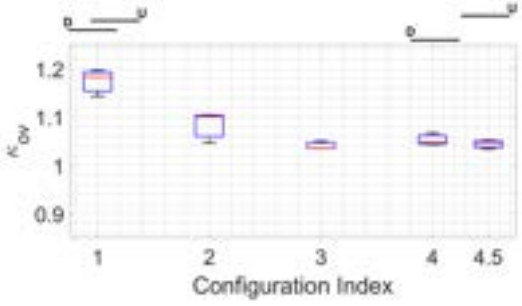

(d) $Re = 100,000$, co-rotating

Figure A.3: The box and whisker plots of the interference factor of mathematically torque balanced configurations while the upstream rotor operates at the specified *Re* and spin direction.

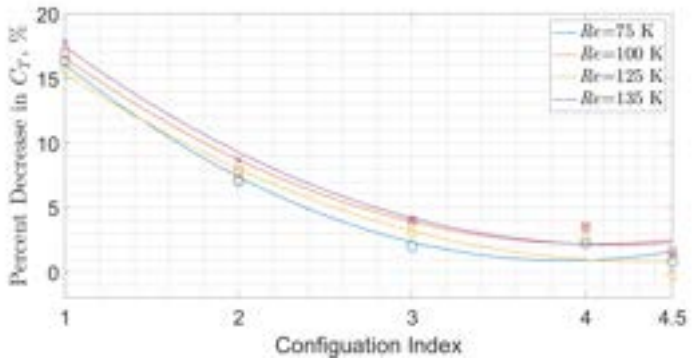

(a)

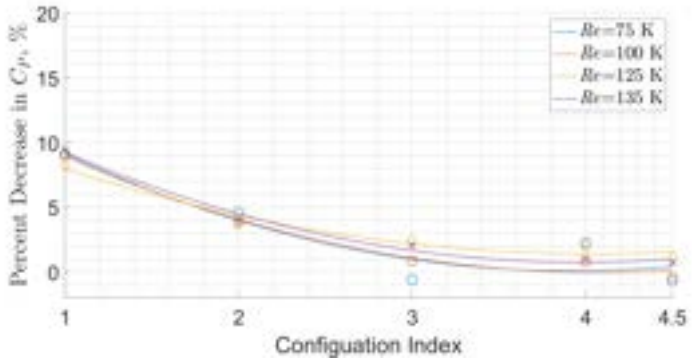

(b)

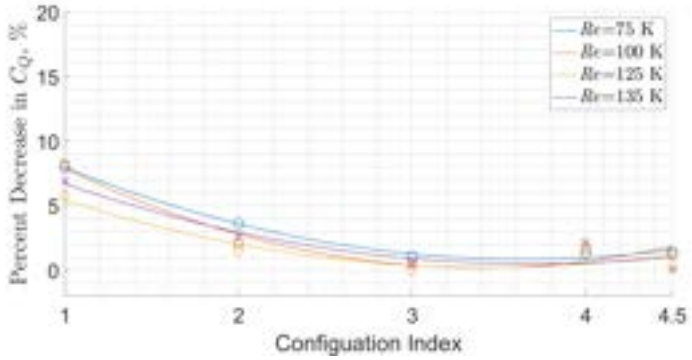

(c)

Figure A.4: Second degree polynomial regressions of the percent decrease in the (a) thrust (b) power and (c) torque coefficients of the downstream rotor while operating simultaneously with the upstream rotor in the counter-rotating spin direction.

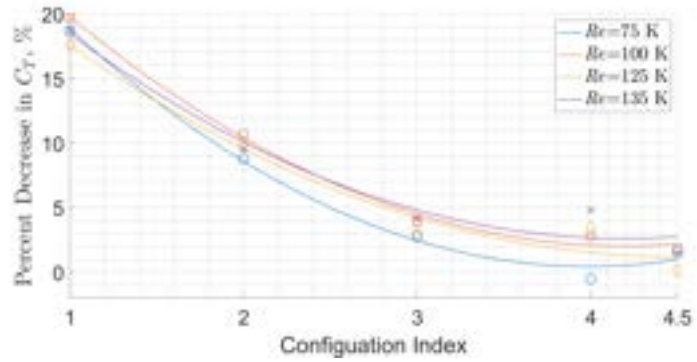

(a)

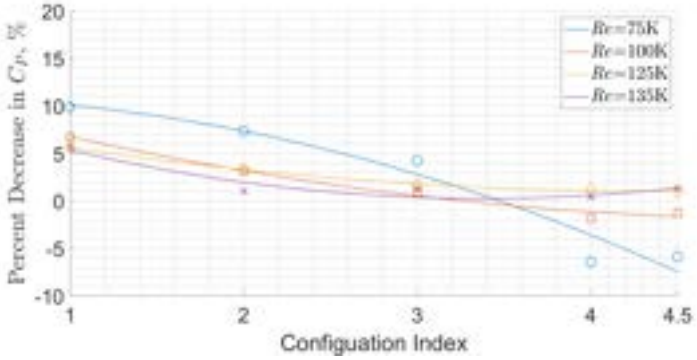

(b)

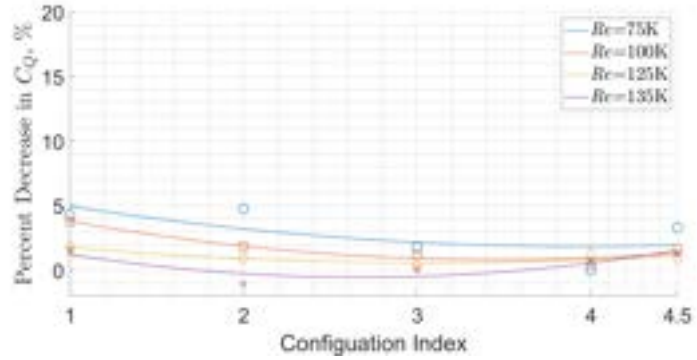

(c)

Figure A.5: Second degree polynomial regressions of the percent decrease in the (a) thrust (b) power and (c) torque coefficients of the downstream rotor while operating simultaneously with the upstream rotor in the co-rotating spin direction.

APPENDIX B

UNCONSTRAINED ROTOR CONFIGURATION DATA

B.1 Performance Coefficients

B.1.1 Percent Decrease in C_T: Downstream Rotor

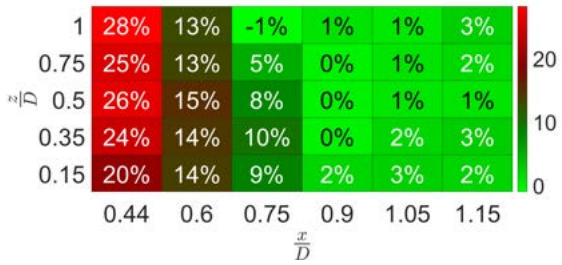

(a) *Re*: $135,000$, counter-rotating

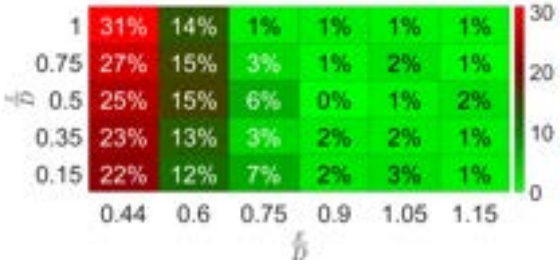

(b) *Re*: $135,000$, co-rotating

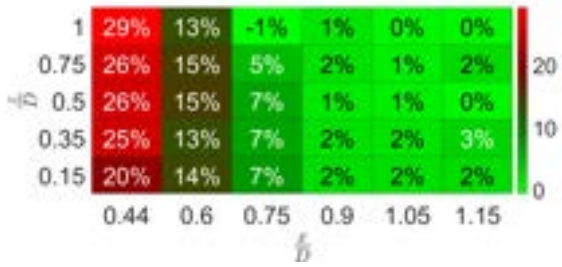

(c) *Re*: $125,000$, counter-rotating

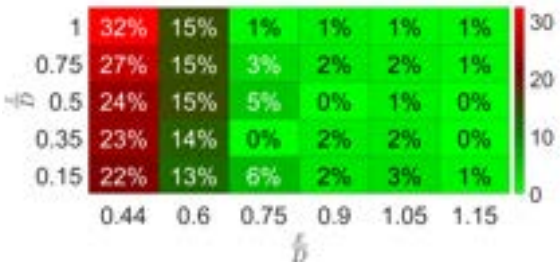

(d) *Re*: $125,000$, co-rotating

Figure B.1: The percent decrease in C_T of the downstream rotor while operating simultaneously with the upstream rotor at the specified *Re* and spin direction.

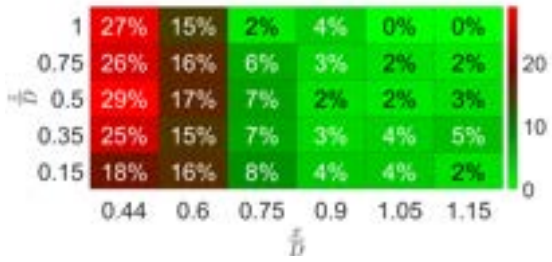

(e) *Re*: $100,000$, counter-rotating

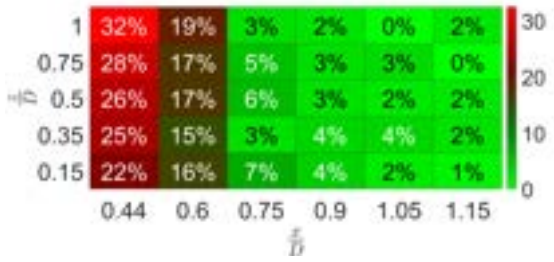

(f) *Re*: $100,000$, co-rotating

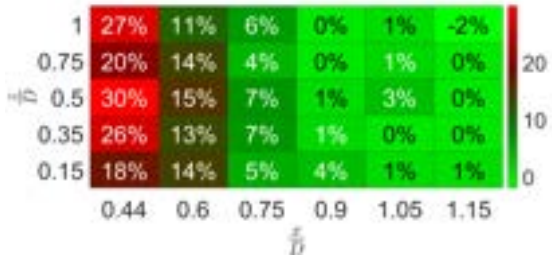

(g) *Re*: $75,000$, counter-rotating

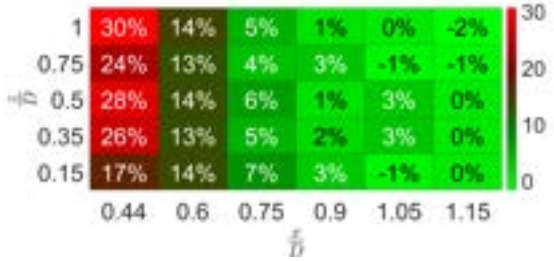

(h) *Re*: $75,000$, co-rotating

Figure B.2: The percent decrease in C_T of the downstream rotor while operating simultaneously with the upstream rotor at the specified *Re* and spin direction (cont.).

B.1.2 Percent Decrease in C_P: Downstream Rotor

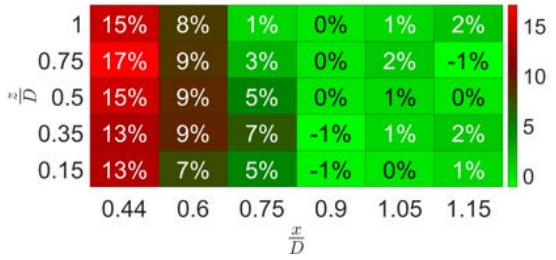

(a) *Re*: $135,000$, counter-rotating

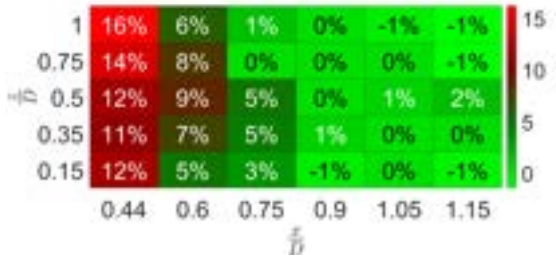

(b) *Re*: $135,000$, co-rotating

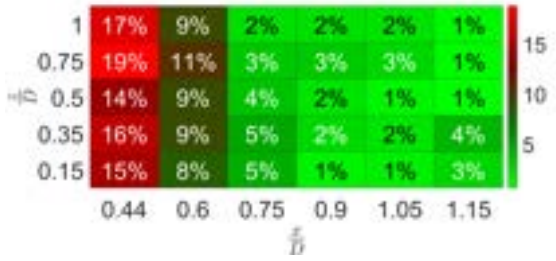

(c) *Re*: $125,000$, counter-rotating

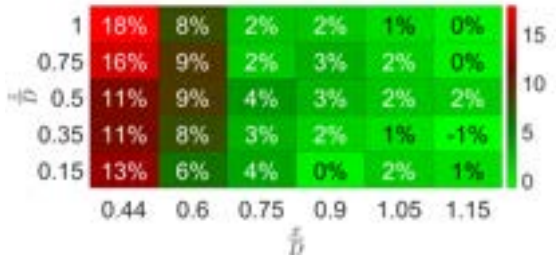

(d) *Re*: $125,000$, co-rotating

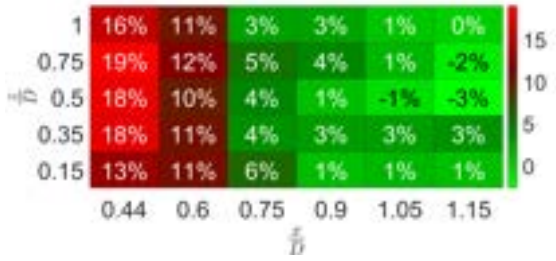

(e) *Re*: $100,000$, counter-rotating

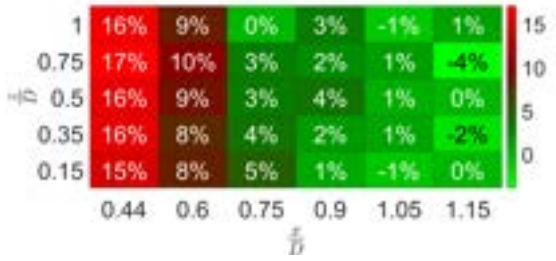

(f) *Re*: $100,000$, co-rotating

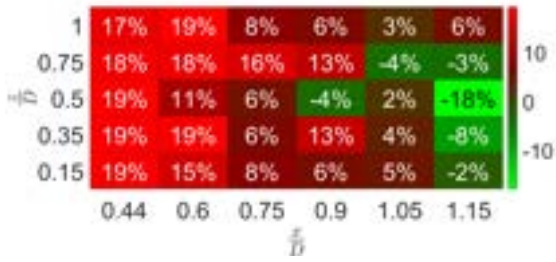

(g) *Re*: $75,000$, counter-rotating

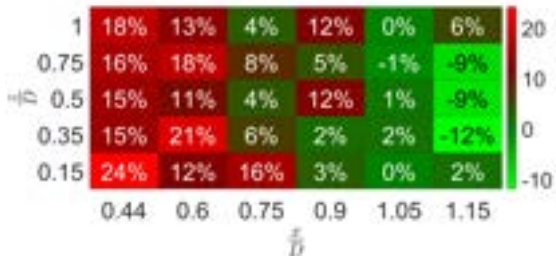

(h) *Re*: $75,000$, co-rotating

Figure B.3: The percent decrease in C_P of the downstream rotor while operating simultaneously with the upstream rotor at the specified *Re* and spin direction

B.1.3 Percent Decrease in C_Q: Downstream Rotor

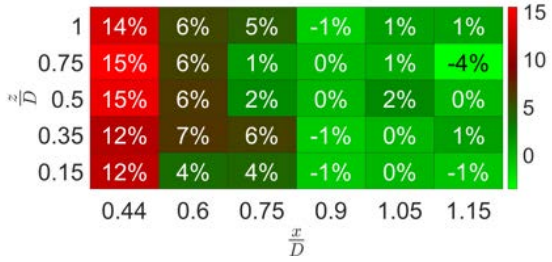

(a) *Re*: $135,000$, counter-rotating

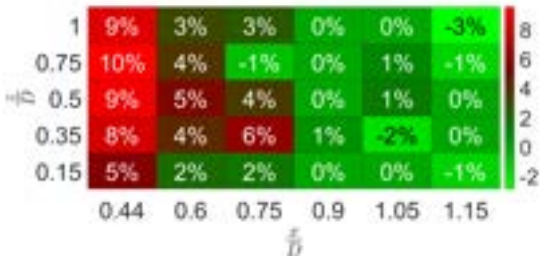

(b) *Re*: $135,000$, co-rotating

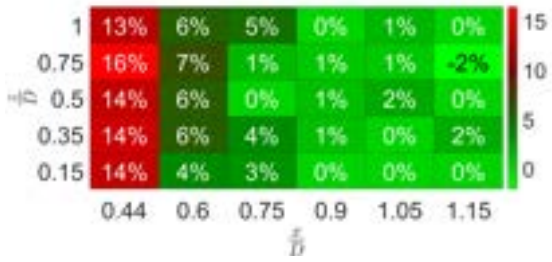

(c) *Re*: $125,000$, counter-rotating

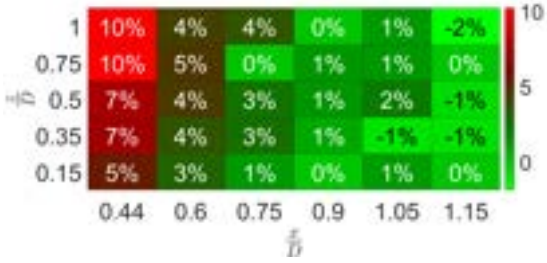

(d) *Re*: $125,000$, co-rotating

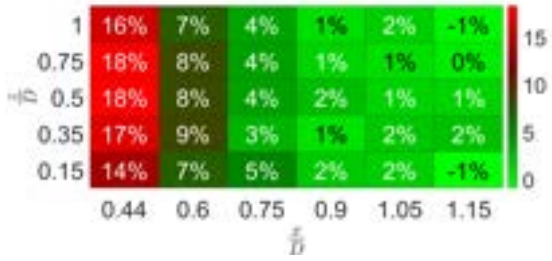

(e) *Re*: $100,000$, counter-rotating

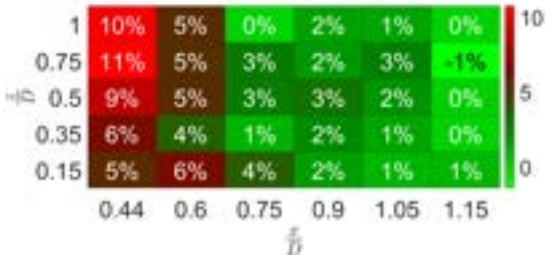

(f) *Re*: $100,000$, co-rotating

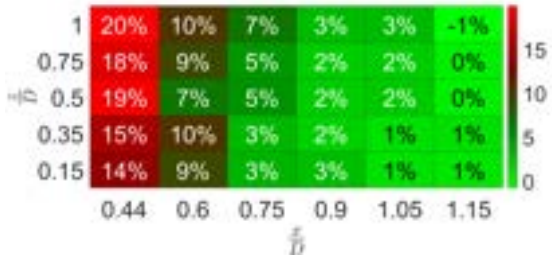

(g) *Re*: $75,000$, counter-rotating

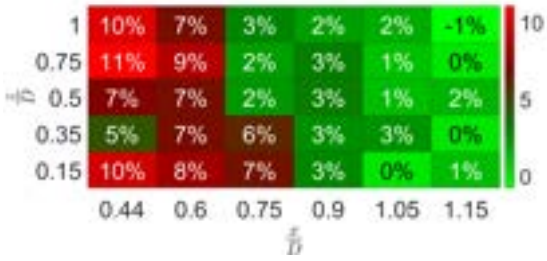

(h) *Re*: $75,000$, co-rotating

Figure B.4: The percent decrease in C_Q of the downstream rotor while operating simultaneously with the upstream rotor at the specified *Re* and spin direction

B.1.4 Percent Decrease in C_T: Upstream Rotor

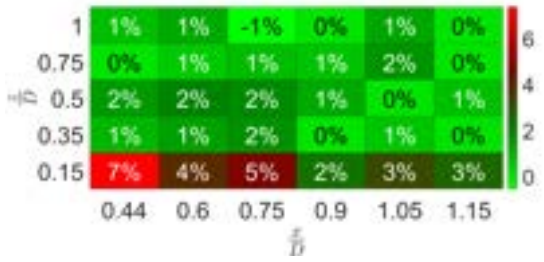

(a) *Re*: $135,000$, counter-rotating

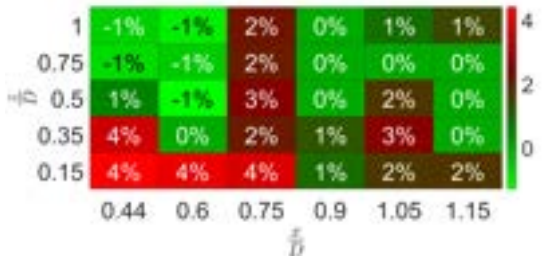

(b) *Re*: $135,000$, co-rotating

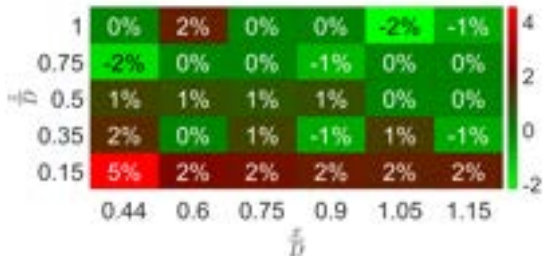

(c) *Re*: $125,000$, counter-rotating

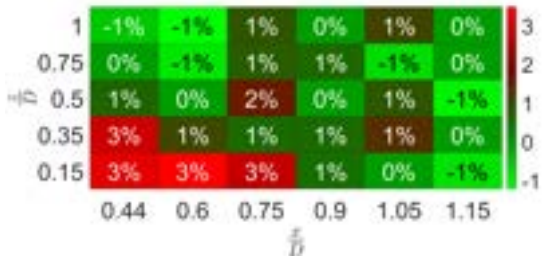

(d) *Re*: $125,000$, co-rotating

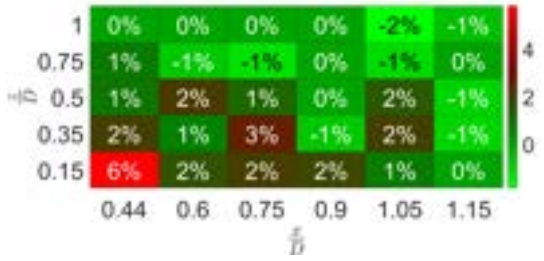

(e) *Re*: $100,000$, counter-rotating

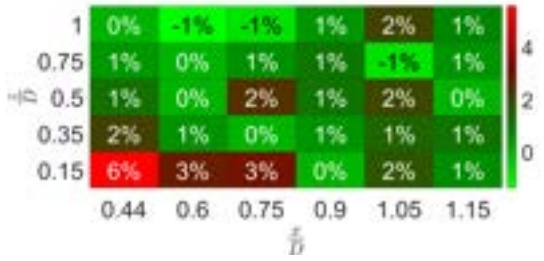

(f) *Re*: $100,000$, co-rotating

(g) *Re*: $75,000$, counter-rotating

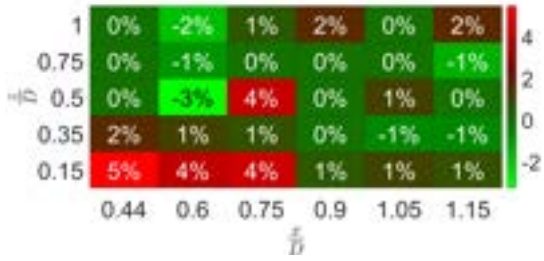

(h) *Re*: $75,000$, co-rotating

Figure B.5: The percent decrease in C_T of the upstream rotor while operating simultaneously with the downstream rotor at the specified *Re* of the upstream rotor and spin direction

B.1.5 Percent Decrease in C_P: Upstream Rotor

(a) *Re*: $135,000$, counter-rotating

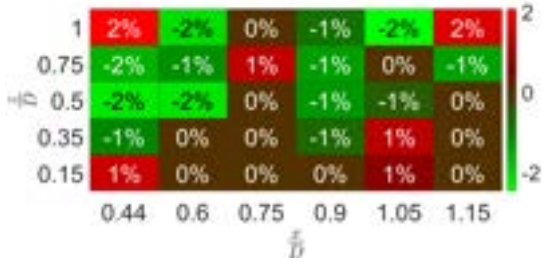

(b) *Re*: $135,000$, co-rotating

(c) *Re*: $125,000$, counter-rotating

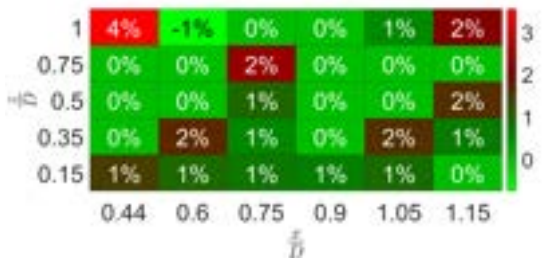

(d) *Re*: $125,000$, co-rotating

(e) *Re*: $100,000$, counter-rotating

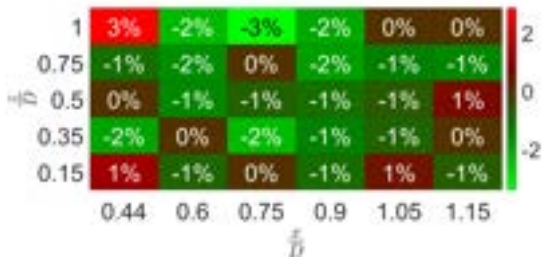

(f) *Re*: $100,000$, co-rotating

(g) *Re*: $75,000$, counter-rotating

(h) *Re*: $75,000$, co-rotating

Figure B.6: The percent decrease in C_P of the upstream rotor while operating simultaneously with the downstream rotor at the specified *Re* of the upstream rotor and spin direction

B.1.6 Percent Decrease in C_Q: Upstream Rotor

(a) *Re*: $135,000$, counter-rotating

(b) *Re*: $135,000$, co-rotating

(c) *Re*: $125,000$, counter-rotating

(d) *Re*: $125,000$, co-rotating

(e) *Re*: $100,000$, counter-rotating

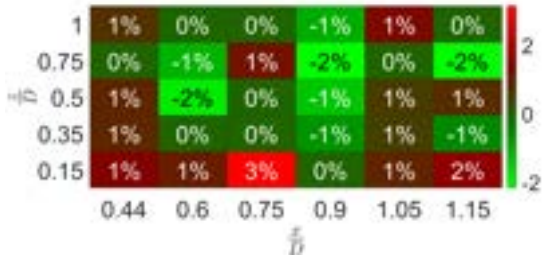

(f) *Re*: $100,000$, co-rotating

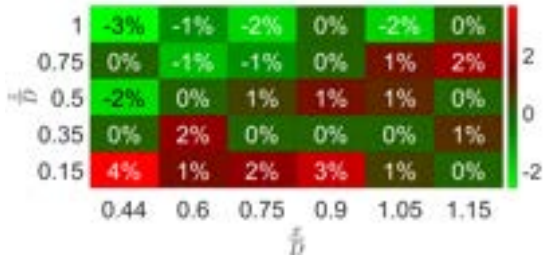

(g) *Re*: $75,000$, counter-rotating

(h) *Re*: $75,000$, co-rotating

Figure B.7: The percent decrease in C_Q of the upstream rotor while operating simultaneously with the downstream rotor at the specified *Re* of the upstream rotor and spin direction

B.2 Overlap Interference Factor: Case 1

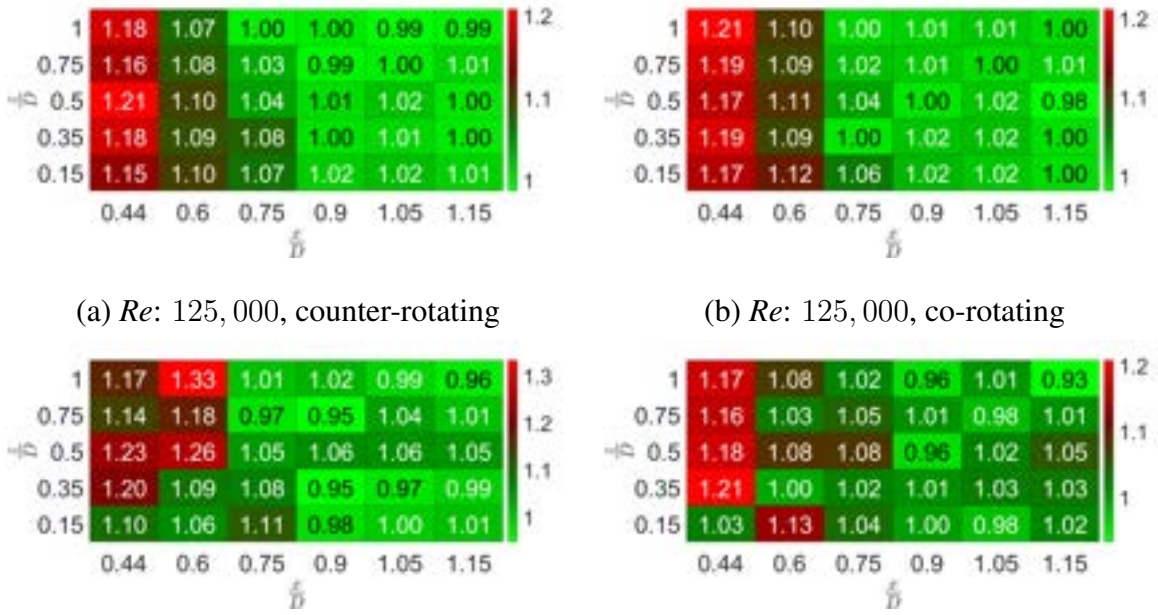

(a) *Re*: $125,000$, counter-rotating

(b) *Re*: $125,000$, co-rotating

(c) *Re*: $75,000$ counter-rotating

(d) *Re*: $75,000$, co-rotating

Figure B.8: The overlap interference factor (*Case 1*) for unconstrained rotor configurations.

B.3 Overlap interference factor for non-torque balanced systems

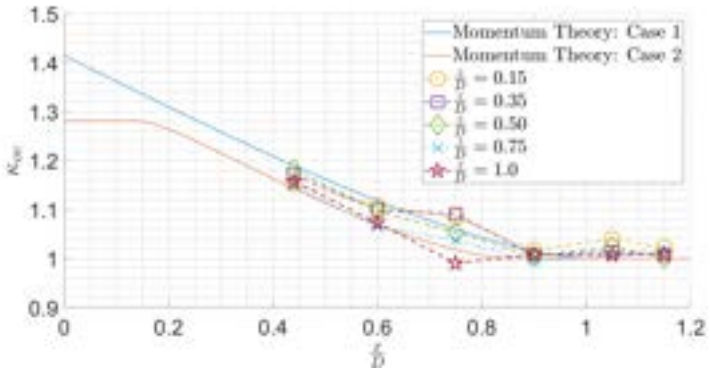

(a)

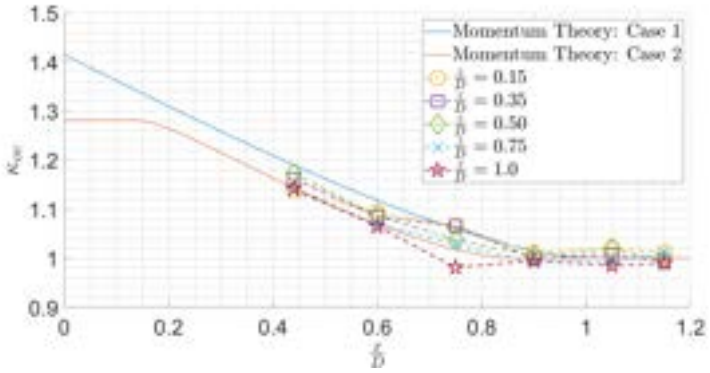

(b)

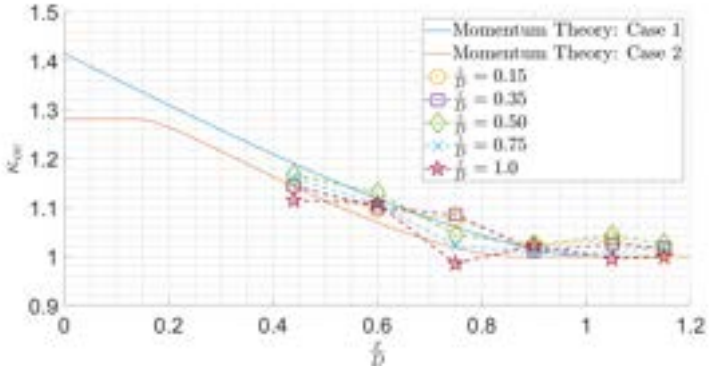

(c)

Figure B.9: The overlap interference factor for unconstrained tandem rotor systems that are not mathematically torque balanced and are in a counter-rotating spin direction while operating at a *Re* of (a) 135,000, (b) 125,000, (c) 100,000.

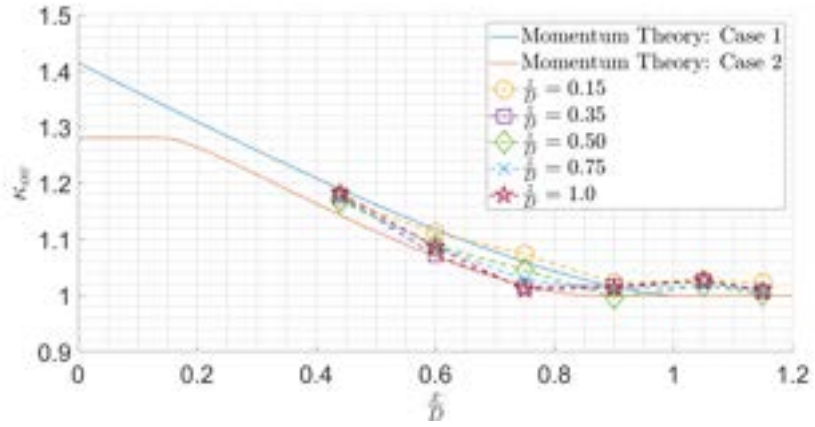

(a)

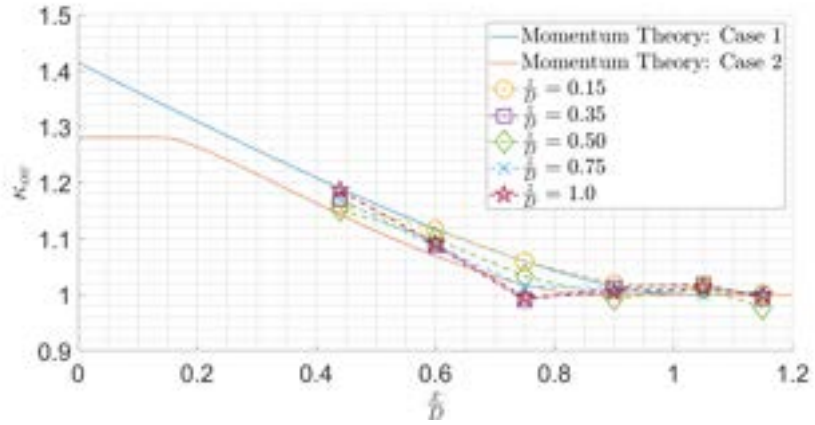

(b)

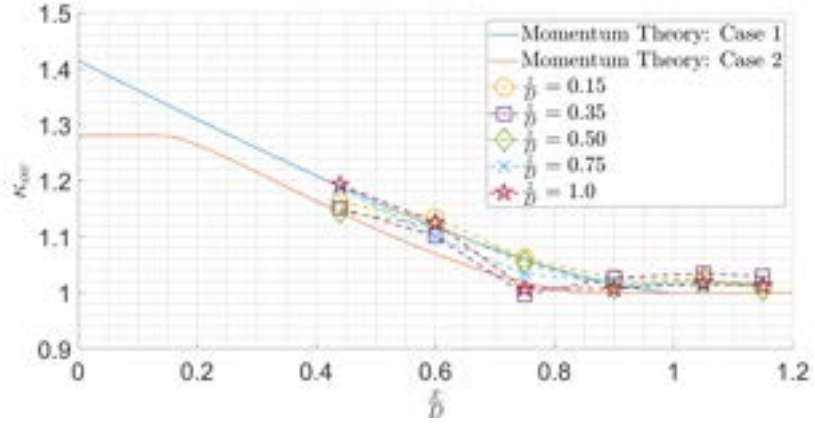

(c)

Figure B.10: The overlap interference factor for unconstrained tandem rotor systems that are not mathematically torque balanced and are in a co-rotating spin direction while operating at a *Re* of (a) 135,000, (b) 125,000, (c) 100,000.

B.4 Figure of Merit Analysis

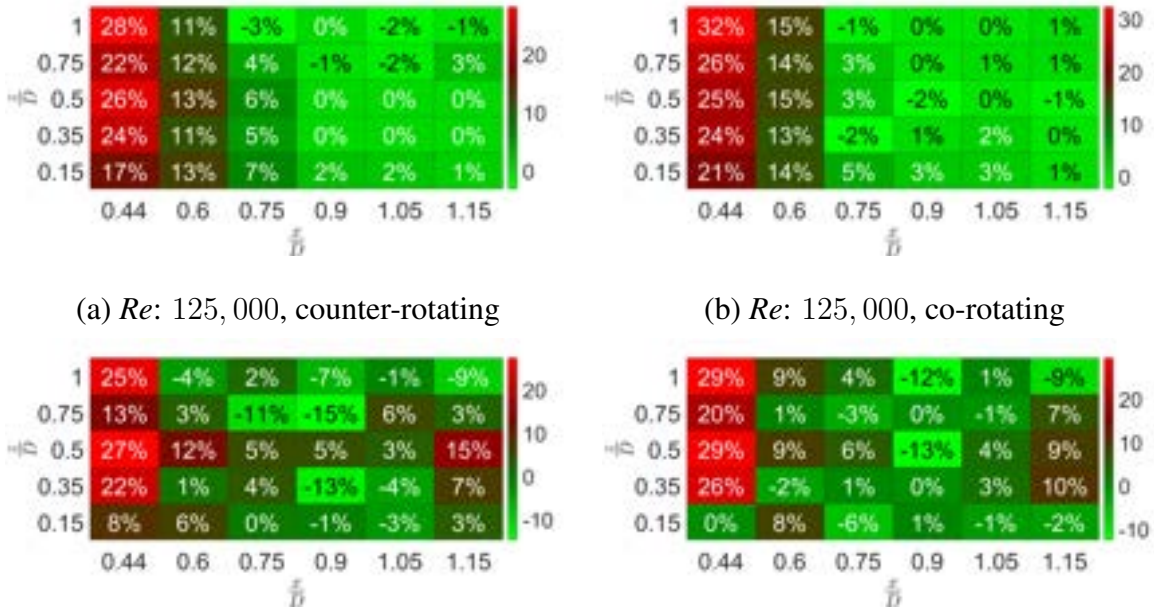

(a) *Re*: $125,000$, counter-rotating

(b) *Re*: $125,000$, co-rotating

(c) *Re*: $75,000$, counter-rotating

(d) *Re*: $75,000$, co-rotating

Figure B.11: The percent decrease in the FM of the downstream rotor operating simultaneously with the upstream rotor.

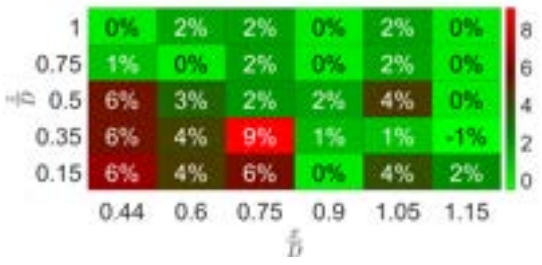

(a) *Re*: $135,000$, counter-rotating

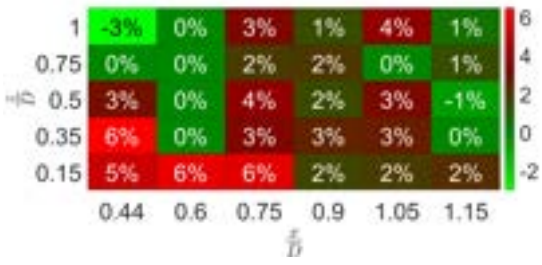

(b) *Re*: $135,000$, co-rotating

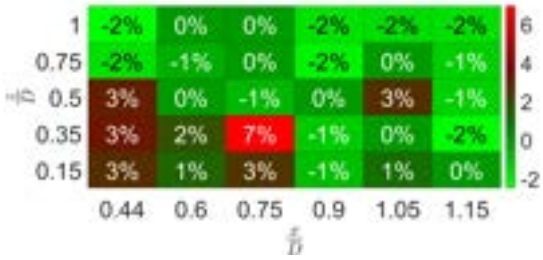

(c) *Re*: $125,000$, counter-rotating

(d) *Re*: $125,000$, co-rotating

(e) *Re*: $100,000$, counter-rotating

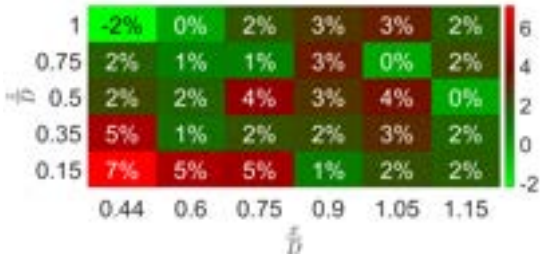

(f) *Re*: $100,000$, co-rotating

(g) *Re*: $75,000$, counter-rotating

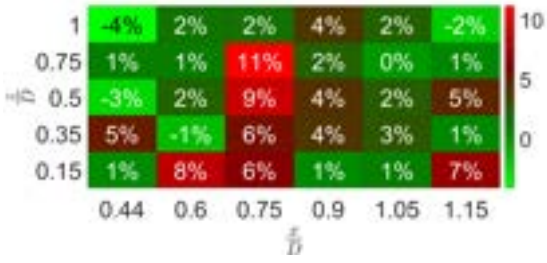

(h) *Re*: $75,000$, co-rotating

Figure B.12: The percent decrease in the FM of the upstream rotor operating simultaneously with the downstream rotor.

APPENDIX C

PERFORMANCE ESTIMATION VALIDATION DATA

C.1 Goodness of Fit Information

Table C.1: Goodness of fit data for the polynomial regression describing the relationship between the relative position between the rotors and the percent decrease of the performance coefficients of the downstream rotor operating simultaneously in the counter-rotating spin direction versus independently.

Coefficient	*Re* (K)	R^2	NRMSE	Range
C_T	135	0.97	0.049	29
C_T	125	0.98	0.040	29
C_T	100	0.97	0.054	29
C_T	75	0.95	0.061	32
C_P	135	0.95	0.065	18
C_P	125	0.96	0.056	18
C_P	100	0.95	0.064	22
C_P	75	0.78	0.11	37
C_Q	135	0.92	0.075	19
C_Q	125	0.93	0.071	18
C_Q	100	0.97	0.052	19
C_Q	75	0.97	0.056	20

Table C.2: Goodness of fit data for the polynomial regression describing the relationship between the relative position between the rotors and the percent decrease of the performance coefficients of the upstream rotor operating simultaneously in the counter-rotating spin direction versus independently.

Coefficient	*Re* (K)	R^2	NRMSE	Range
C_T	135	0.79	0.095	8
C_T	125	0.71	0.105	7
C_T	100	0.66	0.117	7
C_T	75	0.59	0.129	9
C_P	135	0.46	0.148	11
C_P	125	0.40	0.157	9
C_P	100	0.33	0.149	12
C_P	75	0.25	0.148	95
C_Q	135	0.46	0.168	4
C_Q	125	0.24	0.181	5
C_Q	100	0.47	0.161	6
C_Q	75	0.66	0.132	6

Table C.3: Goodness of fit data for the polynomial regression describing the relationship between the relative position between the rotors and the percent decrease of the performance coefficients of the downstream rotor operating simultaneously in the co-rotating spin direction versus independently.

Coefficient	*Re* (K)	R^2	NRMSE	Range
C_T	135	0.97	0.042	31
C_T	125	0.97	0.050	32
C_T	100	0.97	0.051	31
C_T	75	0.97	0.052	32
C_P	135	0.96	0.057	17
C_P	125	0.95	0.057	18
C_P	100	0.94	0.065	21
C_P	75	0.79	0.110	36
C_Q	135	0.87	0.096	12
C_Q	125	0.89	0.080	12
C_Q	100	0.87	0.090	12
C_Q	75	0.86	0.104	11

Table C.4: Goodness of fit data for the polynomial regression describing the relationship between the relative position between the rotors and the percent decrease of the performance coefficients of the upstream rotor operating simultaneously in the co-rotating spin direction versus independently.

Coefficient	*Re* (K)	R^2	NRMSE	Range
C_T	135	0.57	0.176	6
C_T	125	0.73	0.136	5
C_T	100	0.57	0.125	7
C_T	75	0.55	0.139	8
C_P	135	0.27	0.221	5
C_P	125	0.28	0.184	4
C_P	100	0.44	0.138	6
C_P	75	0.46	0.142	20
C_Q	135	0.34	0.189	5
C_Q	125	0.33	0.190	4
C_Q	100	0.37	0.173	5
C_Q	75	0.44	0.179	6

C.2 Estimation Accuracy

Table C.5: The validation configurations tested.

Test Set Index	$\frac{x}{D}$	$\frac{z}{D}$	Re Upstream	Re Downstream	Spin Direction
1	0.5	0.43	134792	137133	Counter
2	0.5	0.43	125602	125998	Counter
3	0.5	0.43	100227	100924	Counter
4	0.5	0.43	74958	74740	Counter
5	0.5	0.43	135043	127927	Counter
6	0.5	0.43	126051	105598	Counter
7	0.5	0.43	100267	89863	Counter
8	0.5	0.43	75064	74886	Counter
9	0.5	0.43	131686	137602	Counter
10	0.5	0.43	117011	126108	Counter
11	0.5	0.43	109240	101725	Counter
12	0.5	0.43	84672	75688	Counter
13	0.5	0.43	131888	127795	Counter
14	0.5	0.43	117015	105192	Counter
15	0.5	0.43	109227	90301	Counter
16	0.5	0.43	84628	75552	Counter

Table C.6: The validation configurations tested (cont.).

Test Set Index	$\frac{x}{D}$	$\frac{z}{D}$	Re Upstream	Re Downstream	Spin Direction
17	0.7	0.63	129842	128846	Counter
18	0.7	0.63	121369	120709	Counter
19	0.7	0.63	112444	112377	Counter
20	0.7	0.63	88443	85965	Counter
21	0.7	0.63	130469	129425	Co
22	0.7	0.63	121777	121210	Co
23	0.7	0.63	112867	112732	Co
24	0.7	0.63	88328	86364	Co

Table C.7: The percent error of the thrust, torque, and power estimates of the validation configurations.

Test Set Index	Error in Thrust	Error in Torque	Error in Power
1	5.05%	4.32%	4.60%
2	0.53%	0.13%	2.31%
3	3.52%	2.69%	15.11%
4	5.00%	5.03%	10.09%
5	2.12%	0.72%	0.31%
6	15.32%	10.67%	6.03%
7	8.71%	6.46%	13.49%
8	5.54%	3.73%	15.81%
9	5.34%	3.19%	5.46%
10	1.89 %	0.27%	4.04%
11	8.97%	8.42%	12.03%
12	0.18%	0.60%	7.13%
13	1.18%	1.43%	0.32%
14	9.81%	8.12%	9.32%
15	13.62%	11.58%	8.29%
16	1.16%	0.47%	7.04%

Table C.8: The percent error of the thrust, torque, and power estimates of the validation configurations (cont.).

Test Set Index	Error in Thrust	Error in Torque	Error in Power
17	3.62%	1.43%	3.64%
18	1.99%	0.88%	8.44%
19	0.28%	2.84%	12.47%
20	3.07%	2.33%	24.73%
21	1.74%	6.58%	1.79%
22	1.35%	20.76%	5.70%
23	1.63%	31.94%	10.43%
24	1.78%	14.51%	20.69%
SSE	4.99	0.004	2191.59
SST	318.11	0.09	156978
R^2	0.98	0.95	0.98

APPENDIX D

SEMI-COAXIAL DATA

D.1 Performance Coefficients

D.1.1 Percent Decrease in C_T: Downstream Rotor

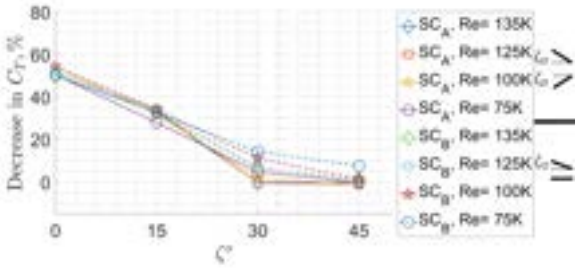

(a)

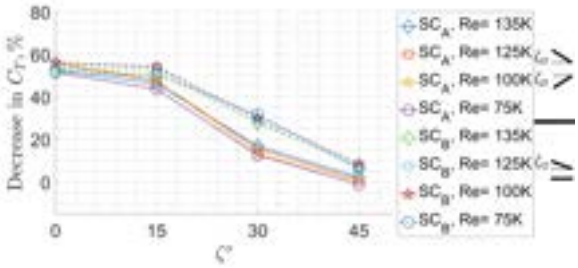

(b)

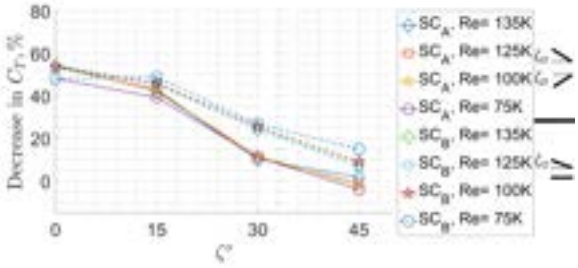

(c)

Figure D.1: The percent decrease in C_T of the semi-coaxial rotor configurations operating in the counter-rotating spin direction at a vertical separation at (a) $\frac{z}{D} = 1.5$, (b) $\frac{z}{D} = 0.96$, (c) $\frac{z}{D} = 0.88$.

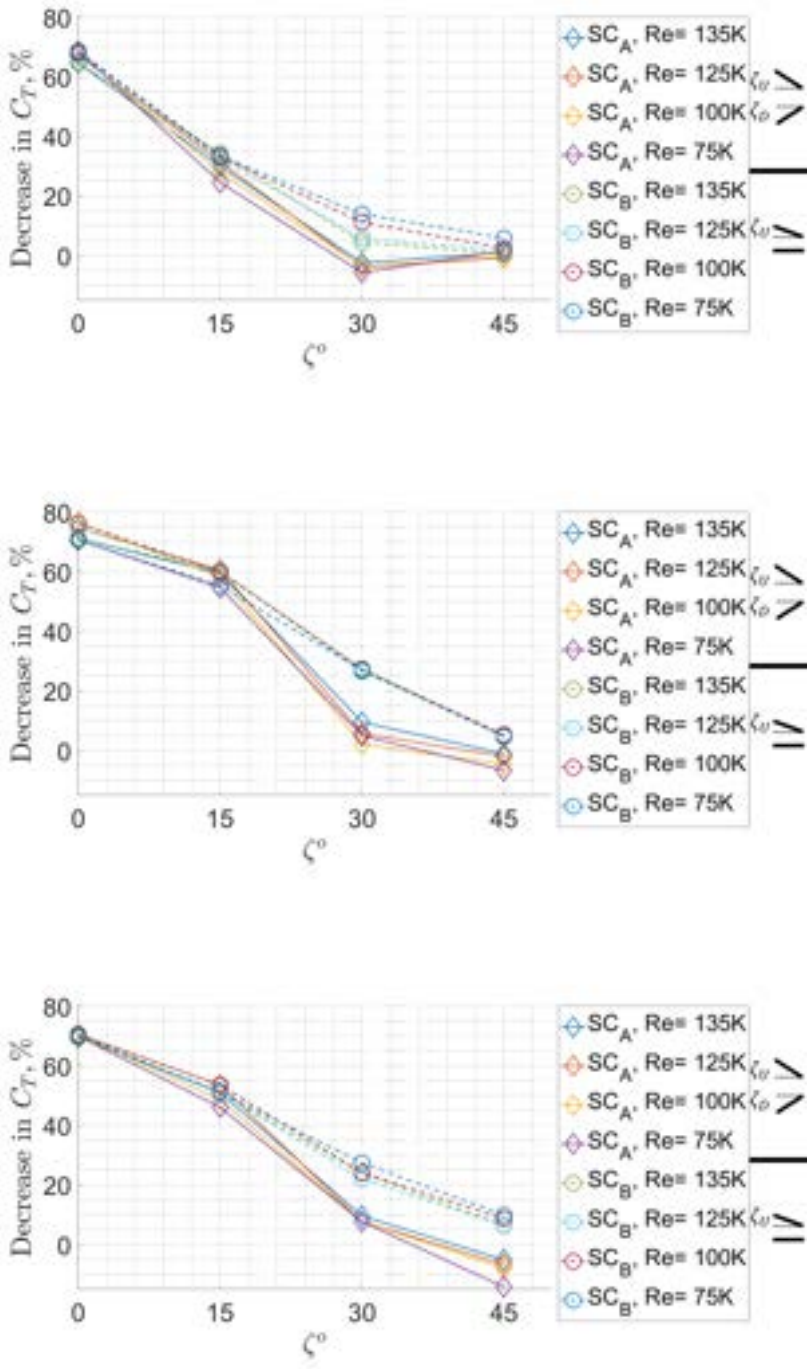

(c)

Figure D.2: The percent decrease in C_T of the semi-coaxial rotor configurations operating in the co-rotating spin direction at a vertical separation at (a) $\frac{z}{D} = 1.5$, (b) $\frac{z}{D} = 0.96$, (c) $\frac{z}{D} = 0.88$.

D.1.2 Percent Decrease in C_P: Downstream Rotor

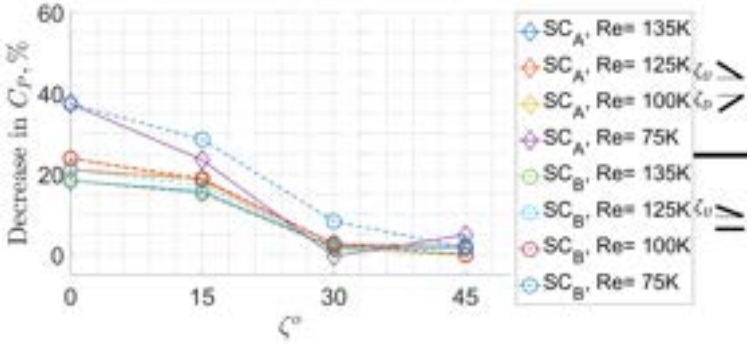

(a)

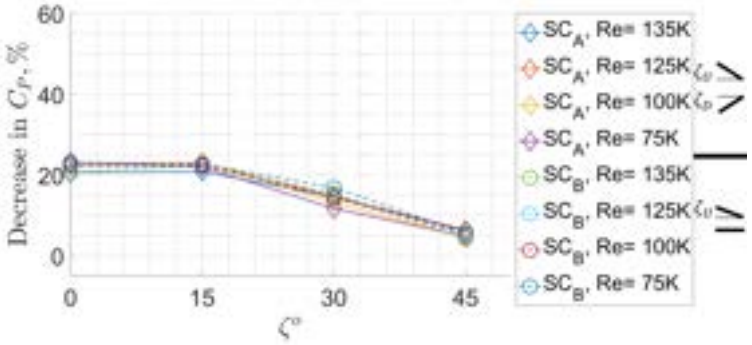

(b)

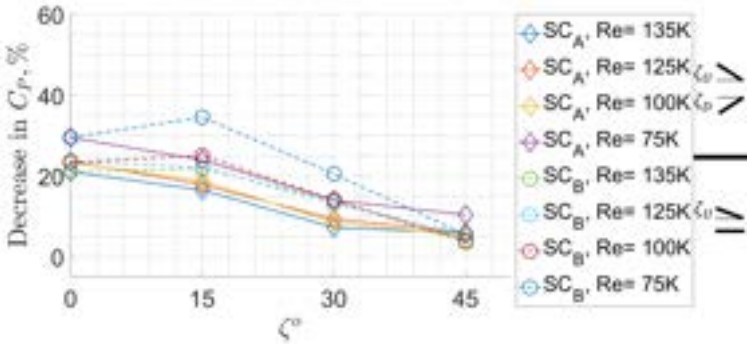

(c)

Figure D.3: The percent decrease in C_P of the semi-coaxial rotor configurations operating in the counter-rotating spin direction at a vertical separation at (a) $\frac{z}{D} = 1.5$, (b) $\frac{z}{D} = 0.96$, (c) $\frac{z}{D} = 0.88$

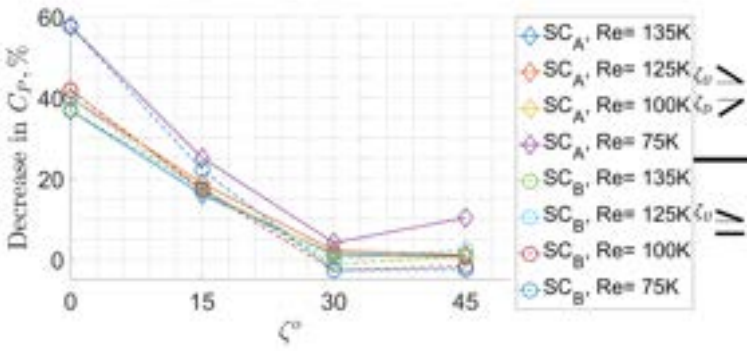

(a)

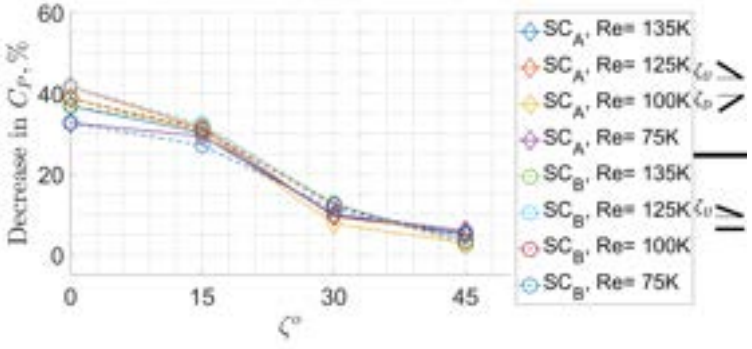

(b)

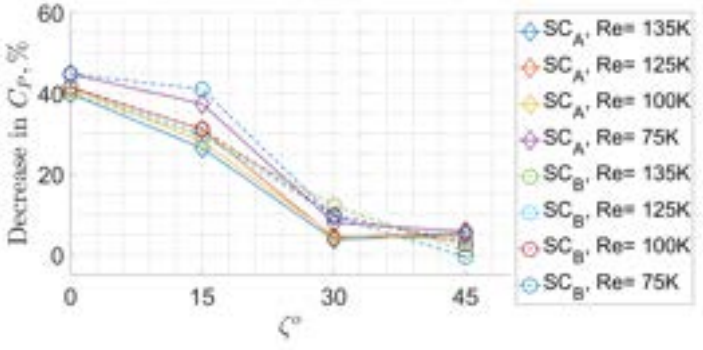

(c)

Figure D.4: The percent decrease in C_P of the semi-coaxial rotor configurations operating in the co-rotating spin direction at a vertical separation at (a) $\frac{z}{D} = 1.5$, (b) $\frac{z}{D} = 0.96$, (c) $\frac{z}{D} = 0.88$

D.1.3 Percent Decrease in C_T/C_P: Downstream Rotor

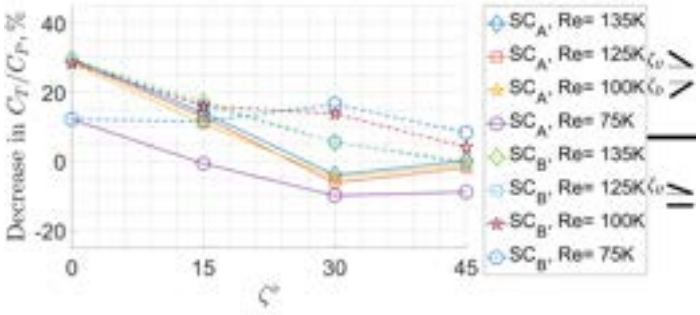

(a)

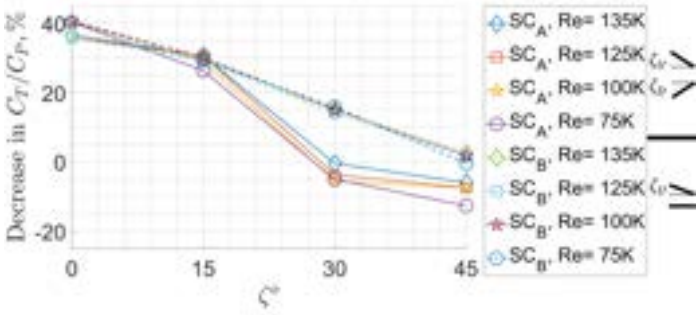

(b)

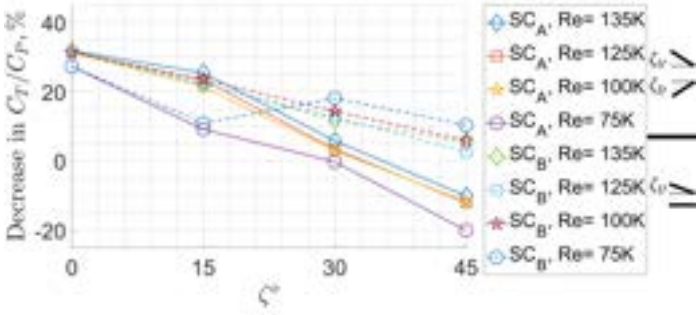

(c)

Figure D.5: The percent decrease in C_T/C_P of the downstream rotor versus the rotor angle for both semi-coaxial configurations at a vertical separation of (a) $\frac{z}{D} = 1.5$, (b) $\frac{z}{D} = 0.96$, and (c) $\frac{z}{D} = 0.88$ for the co-rotating spin direction.

D.2 Semi-Coaxial Overlap Interference Factor Analysis

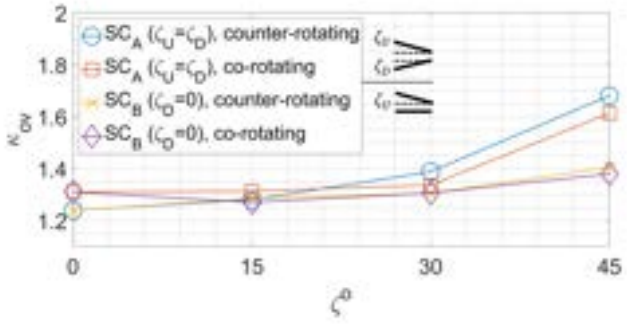

(a)

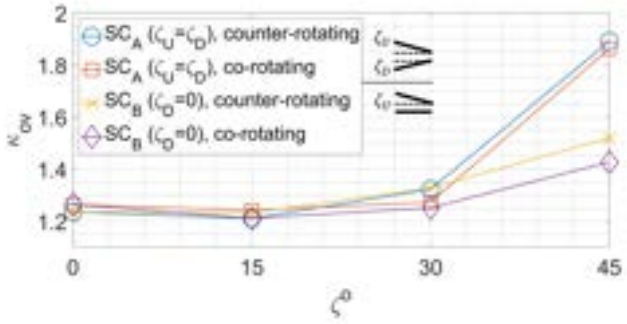

(b)

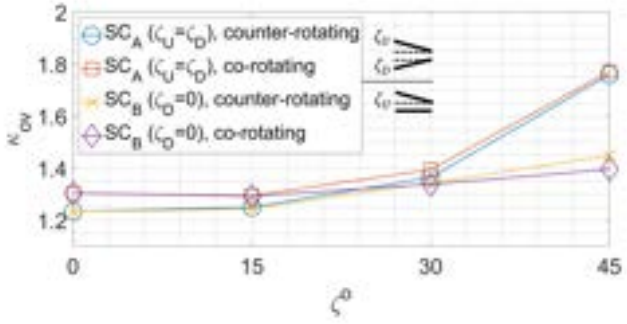

(c)

Figure D.6: The overlap interference factor versus ζ when rotor 1 is operated at a *Re* of $135,000$ and the collective force of the configurations are 26 N for each vertical separation tested (a) $\frac{z}{D} = 1.5$, (b) $\frac{z}{D} = 0.96$, (c) $\frac{z}{D} = 0.88$.

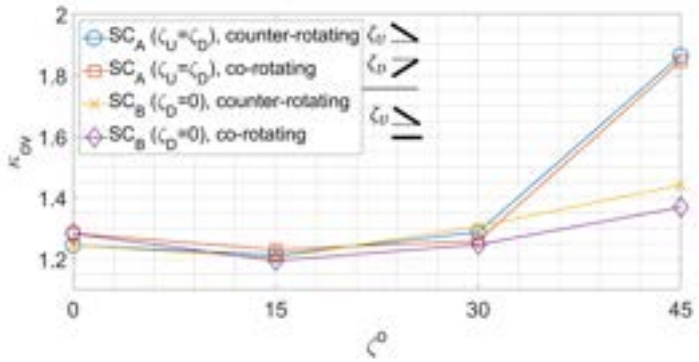

(a)

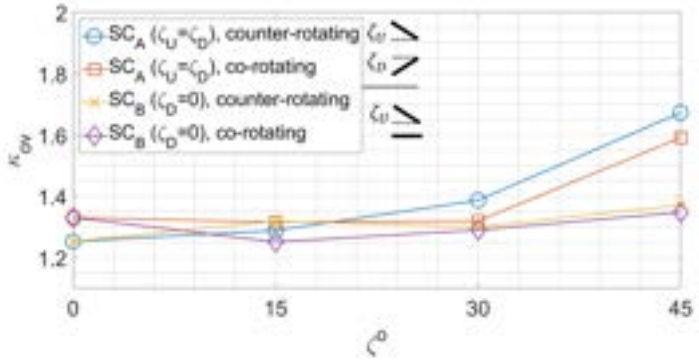

(b)

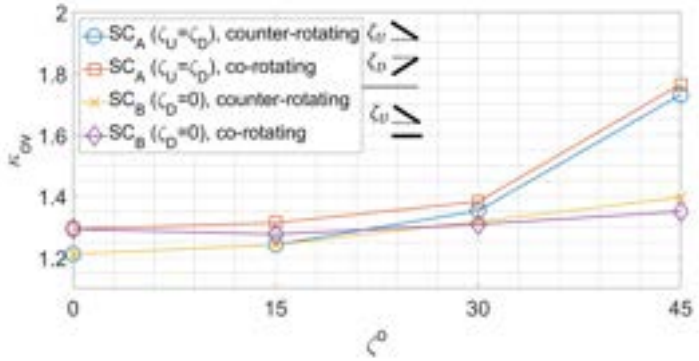

(c)

Figure D.7: The overlap interference factor versus ζ when rotor 1 is operated at a *Re* of $125,000$ and the collective force of the configurations are 21 N for each vertical separation tested (a) $\frac{z}{D} = 1.5$, (b) $\frac{z}{D} = 0.96$, (c) $\frac{z}{D} = 0.88$.

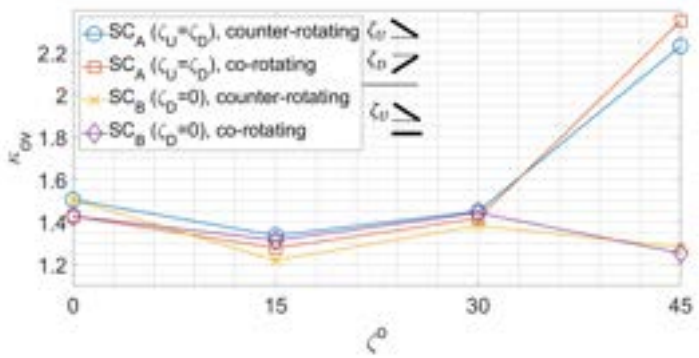

(a)

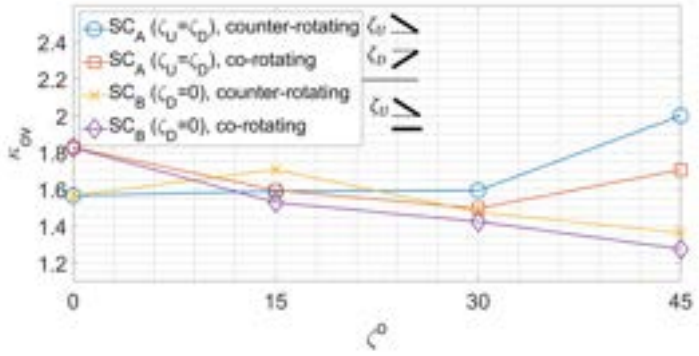

(b)

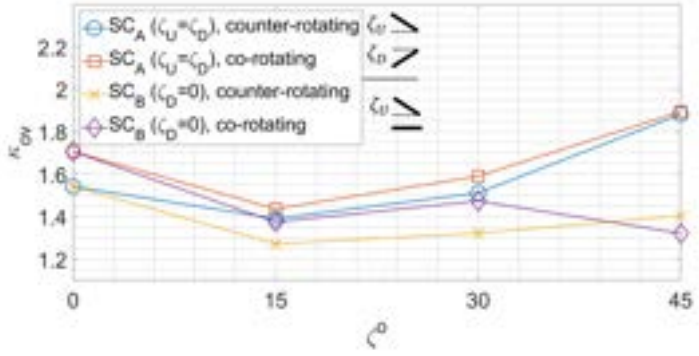

(c)

Figure D.8: The overlap interference factor versus ζ when rotor 1 is operated at a *Re* of $75,000$ and the collective force of the configurations are 12 N for each vertical separation tested (a) $\frac{z}{D} = 1.5$, (b) $\frac{z}{D} = 0.96$, (c) $\frac{z}{D} = 0.88$.

REFERENCES

[1] H. Mehmood, T. Nakamura, and E. N. Johnson, "A maneuverability analysis of a novel hexarotor uav concept," in *2016 International Conference on Unmanned Aircraft Systems (ICUAS)*, IEEE, 2016, pp. 437–446.

[2] F. Augugliaro, A. Mirjan, F. Gramazio, M. Kohler, and R. D'Andrea, "Building tensile structures with flying machines," in *Intelligent Robots and Systems (IROS), 2013 IEEE/RSJ International Conference on*, IEEE, 2013, pp. 3487–3492.

[3] D. Brescianini and R. D'Andrea, "Design, modeling and control of an omni-directional aerial vehicle," in *2016 IEEE international conference on robotics and automation (ICRA)*, IEEE, 2016, pp. 3261–3266.

[4] D. Kaya, A. T. Kutay, and O. Tekinalp, "Experimental investigation of optimal gap distance between rotors of a quadrotor uav," in *AIAA Atmospheric Flight Mechanics Conference*, 2017, p. 3894.

[5] R. Oung and R. D'Andrea, "The distributed flight array," *Mechatronics*, vol. 21, no. 6, pp. 908–917, 2011.

[6] M. J. Duffy and A. Samaritano, "The lift! project-modular, electric vertical lift system with ground power tether," in *33rd AIAA Applied Aerodynamics Conference*, 2015, p. 3013.

[7] D. Saldana, B. Gabrich, G. Li, M. Yim, and V. Kumar, "Modquad: The flying modular structure that self-assembles in midair," in *2018 IEEE International Conference on Robotics and Automation (ICRA)*, IEEE, 2018, pp. 691–698.

[8] K. Garanger, J. Epps, and E. Feron, "Modeling and experimental validation of a fractal tetrahedron uas assembly," in *2020 IEEE Aerospace Conference*, IEEE, 2020, pp. 1–11.

[9] D. Bershadsky, S. Haviland, and E. N. Johnson, "The semi-coaxial multirotor," 2018.

[10] J. T. Epps, K. Garanger, T. Khamvilai, and E. Feron, "An empirical analysis of the wake interactions of a novel multi-agent uas," in *AIAA SCITECH 2022 Forum*, 2022, p. 0280.

[11] K. Garanger, J. Epps, E. Feron, and T. Khamvilai, *Dodecahedron-shaped rotorcraft modules for versatile aerial robotic systems*, U.S. Patent Application No. 63/303,205, Jan. 2022.

[12] J. G. Leishman and S. Ananthan, "An optimum coaxial rotor system for axial flight," *Journal of the American Helicopter Society*, vol. 53, no. 4, pp. 366–381, 2008.

[13] M. Brazinskas, S. D. Prior, and J. P. Scanlan, "An empirical study of overlapping rotor interference for a small unmanned aircraft propulsion system," *Aerospace*, vol. 3, no. 4, p. 32, 2016.

[14] D. Shukla and N. Komerath, "Low reynolds number multirotor aerodynamic wake interactions," *Experiments in Fluids*, vol. 60, no. 4, pp. 1–14, 2019.

[15] H. Otsuka and K. Nagatani, "Thrust loss saving design of overlapping rotor arrangement on small multirotor unmanned aerial vehicles," in *2016 IEEE International Conference on Robotics and Automation (ICRA)*, IEEE, 2016, pp. 3242–3248.

[16] A. R. Schenk, "Computational investigation of the effects of rotor-on-rotor interactions on thrust and noise," Ph.D. dissertation, Brigham Young University, 2020.

[17] A. Bennetts, *Aerodynamic interactions of non-planar rotors*. The University of Manchester (United Kingdom), 2019.

[18] K. Garanger, J. Epps, E. Feron, and M. Miller, *Fractal tetrahedron uas assembly*, U.S. Patent Application No. 62/947,865, Jan. 2020.

[19] M. Frame and A. Urry, *Fractal worlds: Grown, built, and imagined*. Yale University Press, 2016.

[20] A. G. Bell, *Aerial vehicle or other-structure*, US Patent 770,626A, 3 1904.

[21] A. G. Bell, *The tetrahedral principle in kite structure*. Judd & Detweiler, 1903.

[22] G. J. Leishman, *Principles of helicopter aerodynamics with CD extra*. Cambridge university press, 2006.

[23] J. Epps, D. Bershadsky, S. Haviland, E. Johnson, and J. Irizarry, "The development and flight testing of a group-3 ultra-lift uas for the research and development sector," in *AIAA Aviation 2022 Forum*, AIAA Aviation Forum, 2022.

[24] G. Jiang and R. Voyles, "A nonparallel hexrotor uav with faster response to disturbances for precision position keeping," in *Safety, Security, and Rescue Robotics (SSRR), 2014 IEEE International Symposium on*, IEEE, 2014, pp. 1–5.

[25] G. Jiang and R. Voyles, "Hexrotor uav platform enabling dextrous interaction with structures-flight test," in *Safety, Security, and Rescue Robotics (SSRR), 2013 IEEE International Symposium on*, IEEE, 2013, pp. 1–6.

[26] D. Shukla and N. Komerath, "Multirotor drone aerodynamic interaction investigation," *Drones*, vol. 2, no. 4, p. 43, 2018.

[27] A. J. Landgrebe, "An analytical method for predicting rotor wake geometry," *Journal of the American Helicopter Society*, vol. 14, no. 4, pp. 20–32, 1969.

[28] J. D. Kocurek and J. L. Tangler, "A prescribed wake lifting surface hover performance analysis," *Journal of the American Helicopter Society*, vol. 22, no. 1, pp. 24–35, 1977.

[29] A. Bagai and J. G. Leishman, "Rotor free-wake modeling using a pseudo implicit relaxation algorithm," *Journal of Aircraft*, vol. 32, no. 6, pp. 1276–1285, 1995.

[30] A. Bagai and G. Leishman, "Free-wake analysis of tandem, tilt-rotor and coaxial rotor configurations," *Journal of the American Helicopter Society*, vol. 41, no. 3, pp. 196–207, 1996.

[31] T. R. Quackenbush, D. B. Bliss, and D. A. Wachspress, "New free-wake analysis of rotorcraft hover performance using influence coefficients," *Journal of Aircraft*, vol. 26, no. 12, pp. 1090–1097, 1989.

[32] J. G. Leishman, "Measurements of the aperiodic wake of a hovering rotor," *Experiments in Fluids*, vol. 25, no. 4, pp. 352–361, 1998.

[33] J. G. Leishman, A. Baker, and A. Coyne, "Measurements of rotor tip vortices using three-component laser doppler velocimetry," *Journal of the American Helicopter Society*, vol. 41, no. 4, pp. 342–353, 1996.

[34] A. J. Landgrebe, "The wake geometry of a hovering helicopter rotor and its influence on rotor performance," *Journal of the American Helicopter society*, vol. 17, no. 4, pp. 3–15, 1972.

[35] T. R. Norman and J. S. Light, "Rotor tip vortex geometry measurements using the wide-field shadowgraph technique," *Journal of the American Helicopter Society*, vol. 32, no. 2, pp. 40–50, 1987.

[36] J. G. Leishman and A. Bagai, "Challenges in understanding the vortex dynamics of helicopter rotor wakes," *AIAA journal*, vol. 36, no. 7, pp. 1130–1140, 1998.

[37] B. Crowther, A. Lanzon, M. Maya-Gonzalez, and D. Langkamp, "Kinematic analysis and control design for a nonplanar multirotor vehicle," *Journal of Guidance, Control, and Dynamics*, vol. 34, no. 4, pp. 1157–1171, 2011.

[38] E. Kaufman, K. Caldwell, D. Lee, and T. Lee, "Design and development of a free-floating hexrotor uav for 6-dof maneuvers," in *Aerospace Conference, 2014 IEEE*, IEEE, 2014, pp. 1–10.

[39] S. Rajappa, M. Ryll, H. H. Bülthoff, and A. Franchi, "These," in *Robotics and Automation (ICRA), 2015 IEEE International Conference on*, IEEE, 2015, pp. 4006–4013.

[40] Y. Lei, Y. Ji, C. Wang, Y. Bai, and Z. Xu, "Aerodynamic design on the non-planar rotor system of a multi-rotor flying robot (mfr)," in *2017 IEEE 3rd International Symposium in Robotics and Manufacturing Automation (ROMA)*, 2017, pp. 1–5.

[41] Y. Lei and J. Wang, "Aerodynamic performance of quadrotor uav with non-planar rotors," *Applied Sciences*, vol. 9, no. 14, 2019.

[42] A. Nikou, G. C. Gavridis, and K. J. Kyriakopoulos, "Mechanical design, modelling and control of a novel aerial manipulator," in *Robotics and Automation (ICRA), 2015 IEEE International Conference on*, IEEE, 2015, pp. 4698–4703.

[43] S. Park, J. Her, J. Kim, and D. Lee, "Design, modeling and control of omni-directional aerial robot," in *Intelligent Robots and Systems (IROS), 2016 IEEE/RSJ International Conference on*, IEEE, 2016, pp. 1570–1575.

[44] M. Allenspach *et al.*, "Design and optimal control of a tiltrotor micro-aerial vehicle for efficient omnidirectional flight," *The International Journal of Robotics Research*, vol. 39, no. 10-11, pp. 1305–1325, 2020.

[45] M. Kamel *et al.*, "The voliro omniorientational hexacopter: An agile and maneuverable tiltable-rotor aerial vehicle," *IEEE Robotics Automation Magazine*, vol. 25, no. 4, pp. 34–44, 2018.

[46] J. Epps and D. Bershadsky, *Semi-coaxial-b configuration*, U.S. Patent Application No. 63/268,010, Feb. 2022.

[47] B. T. Gabrich, "Flying modular robots: From self-assembling structures in midair to embedding grasping capabilities," Ph.D. dissertation, University of Pennsylvania, 2021.

[48] J. G. Leishman, M. J. Bhagwat, and A. Bagai, "Free-vortex filament methods for the analysis of helicopter rotor wakes," *Journal of aircraft*, vol. 39, no. 5, pp. 759–775, 2002.

[49] J. Lee, K. Yee, and S. Oh, "Aerodynamic characteristic analysis of multi-rotors using a modified free-wake method," *Transactions of the Japan Society for Aeronautical and Space Sciences*, vol. 52, no. 177, pp. 168–179, 2009.

[50] E. J. Alvarez and A. Ning, "High-fidelity modeling of multirotor aerodynamic interactions for aircraft design," *AIAA Journal*, vol. 58, no. 10, pp. 4385–4400, 2020.

[51] S. S. McGowen, *Helicopters: an illustrated history of their impact*. ABC-CLIO, 2005.

[52] M. Ramasamy, "Hover performance measurements toward understanding aerodynamic interference in coaxial, tandem, and tilt rotors," *Journal of the American Helicopter Society*, vol. 60, no. 3, pp. 1–17, 2015.

[53] A. Dimanlig, E. Meadowcroft, R. Strawn, and M. Potsdam, "Computational modeling of the ch-47 helicopter in hover," in *2007 DoD High Performance Computing Modernization Program Users Group Conference*, 2007, pp. 98–103.

[54] B. Theys, G. Dimitriadis, P. Hendrick, and J. De Schutter, "Influence of propeller configuration on propulsion system efficiency of multi-rotor unmanned aerial vehicles," in *2016 international conference on unmanned aircraft systems (ICUAS)*, IEEE, 2016, pp. 195–201.

[55] C. McCutchen, "A theorem on swirl loss in propeller wakes," *Journal of Aircraft*, vol. 22, no. 4, pp. 344–346, 1985.

[56] J. Epps, K. Garanger, and E. Feron, "Wake interactions of a tetrahedron quadcopter," in *2020 International Conference on Unmanned Aircraft Systems (ICUAS)*, IEEE, 2020, pp. 1852–1859.

[57] M. Tiger, *P13x4.4 prop-2pcs/pair*, https://store.tmotor.com/goods.php?id=379.

[58] D. Camps RC, *Venom - pro power 1350w dc power supply (vnr0692)*, https://www.dronecamps.com/product-page/venom-pro-power-1350w-dc-power-supply-vnr0692.

[59] T. A. Team, *Nano: Arduino documentation*, https://docs.arduino.cc/hardware/nano.

[60] C. Creations, *Castle live link*, https://www.castlecreations.com/castle-link-live.

[61] M. Technology, *Mauch unparalleled electronics*, https://www.mauch-electronic.com/apps/webstore/products/show/7863063.

[62] G. LLC, *Lumenier lu3 700kv professional motor*, https://www.getfpv.com/lumenier-lu3-700kv-professional-motor.html.

[63] C. Creations, *Phoenix edge lite hv 40 amp esc, 12s / 50.4v, no bec*, https://www.castlecreations.com/en/phoenix-edge-lite-hv-40-esc-010-0116-00.

[64] Holybro, *Pixhawk 4*, http://www.holybro.com/product/pixhawk-4/.

[65] A. D. Team, *Ardupilot autopilot suite*, http://ardupilot.org, 2016.

[66] A. Team, *Mission planner*, https://ardupilot.org/planner/.

[67] A. Aneheim, *23md-stepper motors with integrated drivers*, https://www.anaheimautomation.com/products/stepper/stepper-integrated-item.php?sID=49&pt=i&tID=132&cID=50.

[68] J. G. Leishman and M. Syal, "Figure of merit definition for coaxial rotors," *Journal of the American Helicopter Society*, vol. 53, no. 3, pp. 290–300, 2008.

[69] W. Zhou, Z. Ning, H. Li, and H. Hu, "An experimental investigation on rotor-to-rotor interactions of small uav propellers," in *35th AIAA applied aerodynamics conference*, 2017, p. 3744.

[70] D. Shukla, N. Hiremath, and N. M. Komerath, "Low reynolds number aerodynamics study on coaxial and quad-rotor," in *2018 Applied Aerodynamics Conference*, 2018, p. 4118.

[71] R. C. Dingeldein, *Wind-tunnel studies of the performance of multirotor configurations*. National Advisory Committee for Aeronautics, 1954, vol. 3236.

[72] D. A. Griffiths, "A study of dual-rotor interference and ground effect using a free-vortex wake model," in *American Helicopter Society 58th Annual Forum, Montreal, Canada, June 11-13, 2002*, 2002.

[73] M. Ramasamy, "Measurements comparing hover performance of single, coaxial, tandem, and tilt-rotor configurations," in *AHS 69th Annual Forum*, vol. 31, 2013, p. 32.

[74] L. Meier, P. Tanskanen, F. Fraundorfer, and M. Pollefeys, "Pixhawk: A system for autonomous flight using onboard computer vision," in *2011 IEEE International Conference on Robotics and Automation*, 2011, pp. 2992–2997.

[75] *Motion capture systems*, https://optitrack.com/, 2021.

[76] D. Bershadsky, "Electric multirotor design and optimization," Ph.D. dissertation, Georgia Institute of Technology, 2017.

VITA

Jeremy Epps was born in Hanover, VA, on June 15, 1994. As a young child and adolescent, Jeremy spent a number of his summers working at his father's automotive repair shop, which sparked his interest in engineering. Jeremy's formal education in engineering began at North Carolina Agricultural and Technical State University, where he earned a Bachelor of Science in Mechanical Engineering with a concentration in Aerospace Engineering in 2016. While at North Carolina A&T State University, Jeremy accepted several summer research positions at NASA's Jet Propulsion Laboratory, MIT, and MIT Lincoln Labs, which spurred his interest in unmanned aerial vehicles. In 2016, he joined the graduate study program in the school of Aerospace Engineering at the Georgia Institute of Technology as part of the Unmanned Aerial Vehicle Research Facility. He received a Master of Science in Aerospace Engineering from the Georgia Institute of Technology in 2019 and is continuing in the Ph.D. program.